UNIVERSITY OF SOUTHAMPTON

Gallium Lanthanum Sulphide Glasses for Near-infrared Photonic Applications

by

Marco N. Petrovich

A thesis submitted in partial fulfillment for the degree of Doctor of Philosophy

in the
Faculty of Engineering and Applied Science
Optoelectronics Research Centre
Department of Electronics and Computer Science

July 2003

This thesis was submitted in July 2003.
It does not necessarily represent the final form of the thesis as deposited in the University after examination.

UNIVERSITY OF SOUTHAMPTON

Gallium Lanthanum Sulphide Glasses for Near-infrared Photonic Applications

by

Marco N. Petrovich

A thesis submitted in partial fulfillment for the degree of Doctor of Philosophy

in the
Faculty of Engineering and Applied Science
Optoelectronics Research Centre
Department of Electronics and Computer Science

July 2003

UNIVERSITY OF SOUTHAMPTON

ABSTRACT

FACULTY OF ENGINEERING AND APPLIED SCIENCE
OPTOELECTRONICS RESEARCH CENTRE
DEPARTMENT OF ELECTRONICS AND COMPUTER SCIENCE

Doctor of Philosophy

by Marco N. Petrovich

This thesis investigates gallium lanthanum oxysulphide (GLS) glasses for potential fibre device applications. GLS glasses have low phonon energy and high rare earth solubility, which makes them candidates for rare earth-doped devices, and in particular for the 1.3 μm praseodymium-doped optical fibre amplifier. In addition, they have one of the highest nonlinear figures of merit among optical glasses, and therefore have potential for all-optical switching and other nonlinear devices. Practical applications, however, have been prevented by the impossibility, to date, of achieving single mode fibres with low attenuation. Previous efforts were concentrated on fabrication and especially tried to address the known issues of glass purity and thermal stability. The present work is focussed on assessing the fundamental glass transparency and on the mechanisms affecting the transmission loss of GLS glasses.

The optical absorption at 1.55 and 1.7 μm was measured for the first time by laser absorption calorimetry using a tunable free-electron laser source. To this end, a calorimeter was designed and commissioned and an improved model for the heat flow analysis of laser calorimetry was also developed. Our measurements identified optical absorption as the principal near-IR loss mechanism for GLS glasses. The extrinsic absorption due to transition metal ion impurities was also measured, and the presence of the weak absorption tail, due to absorption from gap states, was investigated. The occurrence of photoinduced effects and their impact on the material's transmission was also analysed. A thorough characterisation of the photodarkening and photoinduced absorption due to bandgap illumination, including its dependence on the excitation wavelength, and the kinetics of its formation, decay and reversibility, was achieved. Finally, the response of GLS glasses to high-intensity irradiation in the 1 μm region was studied and photoinduced darkening was observed to occur in low oxide undoped and Pr^{3+}-doped GLS.

All these topics are of great practical relevance. The present work clearly demonstrates that, in addition to the known fabrication challenges of monomode GLS fibres, careful consideration of the intrinsic transparency and photoinduced effects is essential for their successful application in fibre devices.

Contents

Nomenclature

Symbols

$\mathcal{A}$	Optical absorptivity
α	Optical absorption coefficient $[m^{-1}, dB \cdot m^{-1}]$
α_R	Temperature coefficient of resistivity
α_T	Coefficient of thermal expansion $[K^{-1}]$
β	Branching ratio
β_2	Nonlinear absorption coefficient $[W \cdot m^{-2}]$
γ_{NL}	Nonlinear factor of merit $[W^{-1} \cdot m^{-1}]$
$\mathbf{C}$	Complex numbers
C_p	Specific heat (constant pressure) $[J \cdot kg^{-1} \cdot K^{-1}]$
δ_{op}	Optical penetration depth $[\mu m]$
E_g	Band-gap energy $[eV]$
ϵ	Integral emissivity
η	Viscosity $[poise]$
F	Small signal figure of merit $[dB \cdot mW^{-1}]$
FOM	Nonlinear figure of merit
$\mathcal{F}$	View factor
G	Optical gain $[dB]$
$G(\mathbf{r}, t\|\mathbf{r}', \tau)$	Green's function
h	Heat exchange coefficient $[W \cdot m^{-2} \cdot K^{-1}]$
k	Thermal conductivity $[W \cdot m^{-1} \cdot K^{-1}]$
κ	Thermal diffusivity $[m^2 \cdot s^{-1}]$
λ	Wavelength $[\mu m]$
n	Refractive index
n_2	Nonlinear refractive index $[m^2 \cdot W^{-1}]$
NA	Numerical aperture
NF	Noise figure [dB]
ν	Frequency $[s^{-1}]$
$\mathbb{Q}$	Radiative quantum efficiency
$\mathbf{R}$	Real numbers
$\mathcal{R}$	Reflectivity

ρ	Specific gravity $[kg \cdot m^{-3}]$
σ	Surface absorptivity
σ_s, $\sigma_{i,j}$	Stimulated cross section $[cm^{-2}]$
σ_{SB}	Stefan-Boltzmann constant [5.67 10^{-8} $Wm^{-2}K^{-4}$]
T	Reduced temperature $[K, °C]$
$\mathcal{T}$	Transmissivity
T_g	Glass transition temperature $[°C]$
T_x	Onset of crystallisation $[°C]$
T_p	Peak of crystallisation $[°C]$
T_m	Onset of melting $[°C]$
τ, τ_r, τ_{nr}	Total, radiative, nonradiative lifetime [s]
$\mathbf{V}$	3-d Volume $[m^3]$
υ	viscosity $[Pa \cdot s]$
w	Stimulated transition rates $[s^{-1}]$
x	Mole fraction
x_w	Weight fraction
Z	Atomic number

Acronyms

AOS	All-Optical Switching
ASE	Amplified Stimulated Emission
BVP	Boundary Value Problem
CRD	Cavity Ring-Down (spectroscopy)
CVD	Chemical Vapor Deposition
CVCM	Collected Volatile Condensable Materials (percent)
DSC	Differential Scanning Calorimetry
DTA	Differential Thermal Analysis
DDFA	Dysprosium-Doped Fibre Amplifier
DSF	Dispersion Shifted Fibre (silica)
DWDM	Dense Wavelength Division Multiplexing
EDFA	Erbium-Doped Fibre Amplifier
EMF	Electromotive Force
ES	Excited State
ESA	Excited State Absorption
EXAFS	Extended X-ray Absorption Fine Structure
FEL	Free-Electron Laser
FHL	First-Harmonic Lasing (FEL)
FWHM	Full Width Half Maximum
GDMS	Glow Discharge Mass Spectroscopy
GS	Ground State
GSA	Ground State Absorption
GLS	Gallium and Lanthanum Sulphide glass
GLSO	Gallium and Lanthanum Sulphide Oxide glass
GNS	Gallium and Sodium Sulphide glass
GVD	Group Velocity Dispersion
HF	Holey Fibre
HMO, HMF	Heavy Metal Oxide, Fluoride glass
HI-PD	High-intensity photoinduced darkening
IR	Infrared
JLFEL	Free-Electon Laser source at the Jefferson Labs
LD	Laser Diode
LIDT	Laser-Induced Damage Threshold
LWP	Long Wavelength-Pass (filter)
MCT	Mercury Cadmium Telluride (infrared detector)
MEMS	Micro Electro-Mechanical System
MIR	Mid-Infrared [2-20 μm]
MM	Multimode (fibre)
MP	Multiphonon (decay)

MPRR	Micropulse Repetition Rate
MQW	Multi Quantum Wells
NBP	Narrow Band Pass (filter)
NDFA	Neodymium-Doped Fibre Amplifier
NIR	Near-Infrared [0.7-2 μm]
OA	Optical Amplifier
OPM	Optical Power Meter
OSA	Optical Spectrum Analyser
PD	Photodarkening
PDFA	Praseodymium-Doped Fibre Amplifier
PDS	Photothermal Deflection Spectroscopy
PLD	Pulsed Laser Deposition
PM	Photo-Multiplier tube (detector)
PTFE	Poly-Tetra-Fluoro-Ethylene
RA	Raman Amplifier
RBS	Rutherford Backscattering Spectroscopy
rBS	Resonant Backscattering Spectroscopy
RE	Rare Earths (Lanthanides)
RQE	Radiative Quantum Efficiency
RT	Room Temperature
RTD	Resistance Temperature Detector
SEM	Scanning Electron Microscope
SI	Side Illumination
SM	Single Mode (fibre)
TEM	Transmission Electron Microscope
SOA	Semiconductor Optical Amplifier
STE	Self-Trapped Exciton
THL	Third Harmonic Lasing (FEL)
TL	Thermal Lens
TM	[3d] Transition Metals
TGS	Triglycine Sulfate (detector)
TTT	Time-Temperature Transformation (curves)
UV	Ultraviolet
WAT	Weak Absorption Tail
WL	White Light
WDM	Wavelength Division Multiplexing
YAG	Yttrium Aluminum Garnet (laser)
ZBLAN	Fluorozirconate (Zr-Ba-La-Al-Na fluoride) glass

Acknowledgements

I wish to express my gratitude to all the people who helped and supported my work. I am very grateful to my supervisors, Prof. Harvey Rutt and Dr. Dan Hewak for their moral and technical support. In particular, I wish to thank Harvey Rutt for making the exciting project of laser calorimetry and the visit to the Jefferson Labs possible. I am also very grateful to Pirelli Cavi e Sistemi, who funded my PhD position and project. Sincere thanks to Dr. Eleanor Tarbox, the 'Pirelli auntie', who helped me to 'carry on regardless' through the ups and, unfortunately, the downs of the project and of the telecoms market; thank you, Eleanor, also for pointing out to me countless 'italish' imperfections within this thesis. I am also very grateful to Dr. Filippo De Monte for the helpful discussion and for encouraging my modeling work of laser calorimetry. Many thanks to Dr. George Neil, Dr. Michelle Shinn and all the people at the FEL facility, Jefferson Labs, who provided precious assistance during the measurement runs. Thanks to Roger Moore for teaching me how to draw a fibre, and thanks to Ken Frampton and Eric Webb for their technical support. I am grateful to my colleagues and friends Gilberto, Daniele, Vittoria, Huai Hoo, Costantino, Fabio, Angelique, Katia and Francesco for the helpful discussion as well as for the good time. Finally, I am truly grateful to my family for their continued moral support and patience. This thesis is dedicated to my dear wife Fariba.

Chapter 1

Introduction.

1.1 Novel Materials for Optical Fibre Telecommunications

The impressive growth of the optical telecommunications industry in the last decade has its foundations on silica-based fibre optics that is now established as a mature technology. Silica glass is universally referred to as the ultimate material for long-haul optical fibre telecommunications as well as for a number of other photonic applications, ranging from fibre lasers to optical sensing, power delivery and imaging. Moreover, driven by the revolutionary invention of the erbium doped fibre amplifier (EDFA) in 1985 (1), a strong impact has been made in recent years by other ground-breaking discoveries, such as photoinscripted fibre gratings and microstructured and photonic crystal fibres. These developments clearly reaffirm that the potential of silica as a photonic material has yet to be fully exploited.

Silica has significant advantages over other optical materials because it is cheap and easy to fabricate, remarkably stable and, especially, because it has very low transmission loss. The continued progress in silica glass fabrication technologies has allowed it to come closer to the intrinsic limits of transparency, than any other optical glass (2). Light signals in optical fibre networks can travel for a few hundred kilometers before becoming significantly attenuated. However, when it comes to optical devices, the attenuation is only one of the factors affecting their performance. For applications where a shorter device length (a few meters to tens of meters) is required, other factors also become relevant, and a greater variety of material properties and structures may be desirable in order to realise devices with superior characteristics.

In all-optical and opto-electronic based communication systems there are several instances where extension of the state-of-the-art requires novel materials, justifying the cost of developing a new technology and the inevitable difficulties in matching it with the existing ones. Perhaps the most cited instance is that of broadband optical fibre amplifiers. In the EDFA, erbium doped silica constitutes a unique 'ideal match', where

erbium has a highly efficient laser transition in the region of maximum transparency of silica. To date, the performance of the EDFA is unrivaled and it has been the only commercially viable optical amplifier for at least a decade; however its gain spectrum bandwidth is small as compared to the width of the region of low attenuation of silica optical fibre networks.

Historically, due to the presence of the overtone absorption of the hydroxyl impurity around 1400 nm, the region of lowest attenuation of silica used to be divided into two separate windows, conventionally indicated as the second and third communication window (see figure 1.1). The second window, centered at 1310 nm, had the advantage, apart from the low loss, of coinciding with the region of minimum chromatic dispersion in standard silica fibres. The first long-haul transmission systems, based on electro-optical repeaters, operated in this window. From the mid-'90s, the development of EDFAs and the progress in wavelength dispersion engineering completely overturned the advantage in favour of the third, lowest attenuation window centered at 1550 nm. Although still pertinent to a fraction of the installed fibre networks, the division into second and third window is now rapidly becoming obsolete; in the last generation of ultra-dry telecom fibres, such as the MagniLight^{TM} fibre developed by Pirelli Cables or the AllWave^{TM} fibre developed by Lucent Technologies, the OH^- band is virtually absent and one continuous, low-loss window, spanning about 1260 to 1675 nm, is available for data transmission. This window is now subdivided in six conventional bands as shown in figure 1.1. Conventional EDFAs work in the 'conventional' C band between 1530 and 1565 nm, while gain-shifted EDFAs cover the 'long' L band (1565-1625 nm). The current DWDM channel capacity of most optical fibre networks is determined by the bandwidth of these erbium-doped amplifiers; the other bands are currently not exploited in DWDM systems mainly due to the lack of suitable amplifiers. The trend towards communications networks with larger capacity, faster rates and improved flexibility requires the development of new devices to exploit more of the available bandwidth; technological forecasts and telecommunication roadmaps have anticipated that amplifiers will be eventually developed, covering the whole region from 1260 to 1675 nm, which would accommodate several times the DWDM channel capacity of the present technology.

Apart from erbium, there are other trivalent rare-earth ions with optical transitions in the region of minimum attenuation of silica, which therefore offer amplification schemes for devices alternative to EDFAs. Fluorescent emissions from neodymium, praseodymium and dysprosium ions have a significant overlap with the 'original' O-band (1260-1360 nm), which coincides with the second telecom window in the old terminology; thulium is relevant for the 'short' S-band (1460-1530 nm) and 'ultra-long' U-band (1625-1675 nm), while holmium has a transition covering the 'extended' E band (1360-1460 nm). Unfortunately, silica is not suitable as a host for any of these rare earths, since its high phonon energy compromises their fluorescent properties. Thus, other glass systems with lower phonon energy, such as tellurites and heavy metal oxides (HMO)

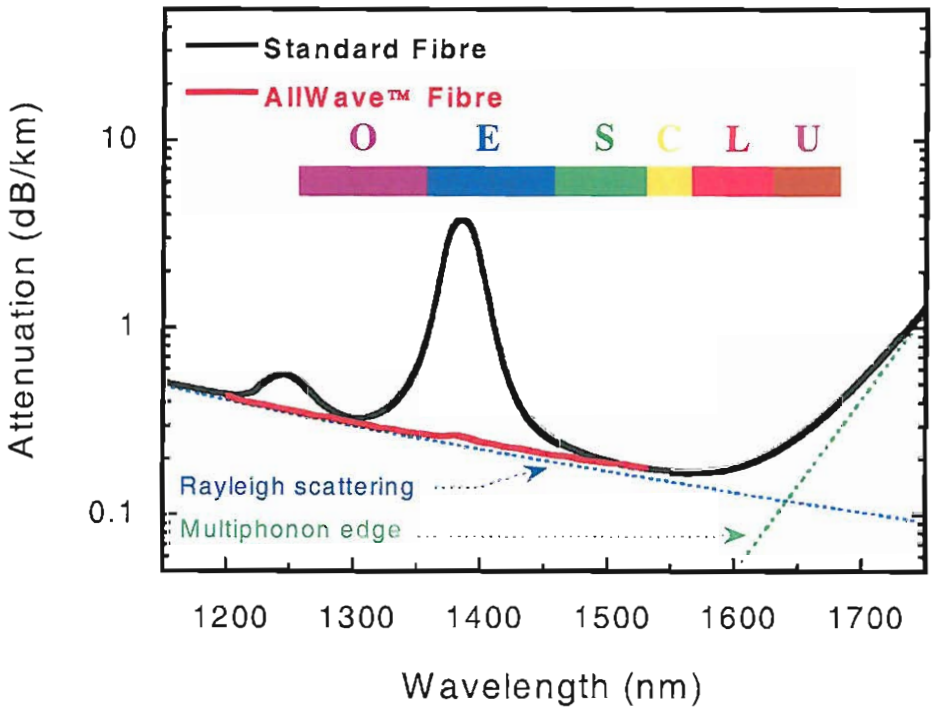

FIGURE 1.1: Transmission of silica fibres showing the region of minimum attenuation and the six conventional bands of optical telecommunications.

glasses, fluoride glasses and chalcogenide glasses, have been investigated as alternative hosts for rare-earth doped devices. These are typically multicomponent glasses, where mixing compounds with different physical properties provides extra flexibility in engineering the material's properties. Multicomponent chalcogenide glasses have very low phonon energy and are also attractive because of unique properties, because they can be prepared in a variety of ways, and they can be compositionally adjusted in order to produce a variety of optical responses. This opens the possibility of integrating different devices on the same optical material. For instance, chalcogenides have the highest third order nonlinearity among optical glasses (3). In these materials, high intensity light pulses can efficiently drive the glass properties with ultra-fast (ps or sub-ps) response time. Third-order nonlinearity can be used to manipulate optical pulses at very high rates and exploited to fabricate components such as all-optical switches, modulators and wavelength converters.

1.2 Chalcogenide Glasses

Chalcogenides are defined as the compounds formed by the 'chalcogen' elements from Group VI of the Periodic Table, i.e. sulphides, selenides and tellurides. Several chalcogenide compounds are excellent glass formers, and the vitreous materials, generally

obtained by melt-quenching, are referred as to the Chalcogenide glasses. These constitute a very large class of materials, which includes elemental chalcogens (Se, Te, $Se{:}S$), several binary V-VI ($As{:}S$, $As{:}Se$), IV-VI (GeS_2) and III-VI compounds and alloys (B_2S_3, $In{:}Se$), some transition metal chalcogenides (MoS_2), and a large number of ternary (or higher multinary) combinations of the above ($As{:}S{:}Se$, $Ge{:}Ga{:}S$, $Ge{:}As{:}Se$, $Ge{:}As{:}Se{:}Te$, etc.). The fabrication, properties and applications of several chalcogenide glass systems have been extensively described in the books by Kokorina (4), Sanghera (5), and Hewak (6).

From a materials standpoint, chalcogenide glasses are rather different from oxide and halide glasses, due principally to the different character of the chemical bonds within their glassy network. A comparative overview of optical, mechanical and thermal properties is presented in table 1.1 as a guide. Oxide and halide glasses are in their vast majority stoichiometric compounds where ionic contribution to bonding is significant (oxides), or the chemical bonds are totally ionic (halides). Chalcogenide glasses can either be stoichiometric or non-stoichiometric, i.e. alloys, and are covalent materials in nature. Consequently, while oxides and halides are generally insulators, with large bandgap energies (e.g., $\approx$ 10 eV for silica and ZBLAN), chalcogenide glasses behave like amorphous semiconductors, having their electronic absorption edge at the red-end of the visible spectrum or in the near-infrared (NIR). Furthermore, the lower average binding energy and larger mass of chalcogen anions cause their characteristic vibrational energies to be very low and lead to enhanced infrared transmission. The transmission window depends to a large extent on the chalcogen anion: sulphides have larger bandgap and transmit to shorter wavelengths, while tellurides have the lowest phonon energy and transmit to the longest wavelengths, but are totally opaque in the visible (figure 1.3).

Besides the infrared transparency, the chalcogenide glasses show a number of other properties which are interesting both fundamentally and from the point of view of device applications. These optical media have high refractive index, high third-order nonlinearity (7), and strong magneto-optic (8) and acousto-optic effects (9). Comparing the thermal and mechanical properties of oxides and chalcogenides (table 1.1), it is clear that the latter are softer and mechanically less tough materials (lower glass transition temperature, smaller elastic moduli and larger expansion coefficients). This correlates with weaker chemical bonds and the lower average co-ordination number of chalcogenides, which in turn cause their glass network to be typically 'floppy' and susceptible to metastable configurational modifications. These modifications, that can be induced externally for instance by bandgap illumination or by temperature changes, are generally accompanied by modifications of physical properties such as optical transmission, density, etching rate and charge transport properties. A number of photoinduced phenomena have been reported, including photodarkening (PD), photobleaching and photoexpansion; reviews on this topic have been presented by Pfeiffer (10) and Tanaka (11). Depending on the chalcogenide material, on the fabrication procedure and on the intensity and wavelength

TABLE 1.1: Selected physical properties of GLS, fluorozirconate and silica glass.

	GLS	ZBLAN	Silica
Optical			
Electronic Bandgap (eV)	2.6	8.9	9
Phonon energy (cm^{-1})	425	600	1150
Transmission window (μm)	$0.53 - 5.0$	$0.22 - 4.0$	$0.16 - 2.0$
Refractive Index (†)	2.38	1.48	1.44
Non-linear Refr. Index ($10^{-20}\ m^2\ W^{-1}$) (†)	200	≈ 2	2.5
Zero- dispersion wavelength (μm)	–	1.6	1.3
dn/dT ($10^{-5}\ K^{-1}$)	10	-1.5	1.2
Verdet constant ($deg\ T^{-1}m^{-1}$) (†)	836	–	75.5
Mechanical			
Density ($kg\ m^{-3}$)	4100	4300	2200
Thermal expansion coefficient ($10^{-6}\ K^{-1}$)	10.6	17.2	0.55
Young's modulus (GPa)	59	58.3	73.1
Knoop hardness ($10^4\ kg\ m^{-2}$)	200	225	600
Thermal			
Glass Transition Temperature ($°C$)	559	265	1175
Melting Temperature ($°C$)	840	692	> 2200
Specific heat ($J\ kg^{-1}K^{-1}$)	540	427	743
Thermal conductivity ($W\ m^{-1}K^{-1}$)	0.62	0.63	1.38
(†) Value @$1.5\mu m$	Ref. (12)	Ref. (13)	Ref. (14)

of the light inducing such modifications, either reversible or irreversible phenomena can occur. These photoinduced phenomena constitute a very useful tool to investigate the microstructure of the chalcogenide glasses.

As infrared transmitting materials, chalcogenide glasses have been known and investigated for several decades. Originally the interest was for use as passive optical elements. The fabrication of an optical fibre in chalcogenide glass (As_2S_3) was first reported by Kapany and co-workers in 1965 (15). Since then, chalcogenide glasses and fibres have maintained an important role in infrared technology for applications such as thermal imaging, chemical sensing and IR laser power delivery (16; 17; 18). Following the success in low-loss silica fibre fabrication in the '70s, theoretical studies suggested that infrared glasses, such as fluorides and chalcogenides, had a potential for ultra-low loss optical fibre (19), which started a period of renewed interest and intensive research during the 80s. The traditional method for estimating the transparency limit of glasses considered only three 'intrinsic' mechanisms, namely the electronic 'UV' absorption, Rayleigh scattering and the multiphonon 'IR' absorption, to calculate the so-called 'v-curve' of

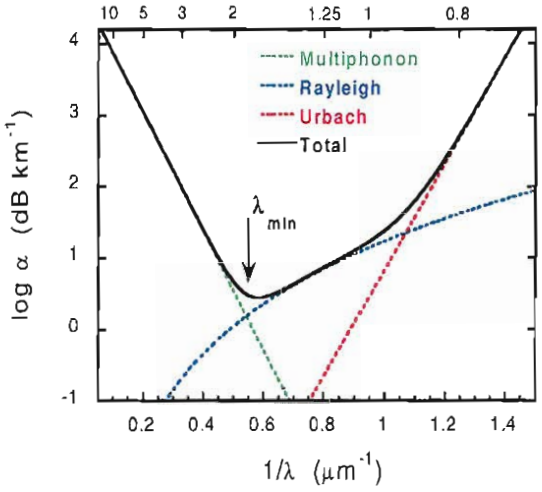

FIGURE 1.2: Theoretical prediction of lowest attenuation by the v-curve method.

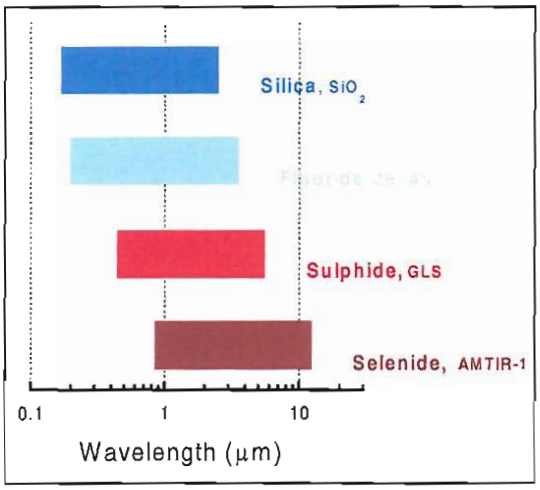

FIGURE 1.3: Transmission of chalcogenide, fluoride and oxide glasses.

spectral attenuation (fig. 1.2). It assumed that the transparency limit was determined by the scattering from small fluctuations of density and refractive index, with the typical $\propto \lambda^{-4}$ dependence on the wavelength. The lowest optical attenuation would then be found as the intersection between the λ^{-4} scattering curve and the IR edge. According to this model, the minimum loss in fluoride and chalcogenide glasses, having their multiphonon edge well into the mid-IR, was expected to be consistently lower than that of silica, with its multiphonon edge falling below 2 μm. Shibata et al. (20) predicted the transparency limit of chalcogenide GeS_3 to be as low as 10^{-2} $dBkm^{-1}$ at 4.5 μm. However, these predictions proved incorrect when it was later pointed out that other loss mechanisms, such as non-Rayleigh scattering from small phase defects (crystals and inclusions) or waveguide imperfections, and, especially in the case of chalcogenide glasses, defect-related intra-gap absorption, had to be taken into account. Consequently, the *practical* loss is three to four orders of magnitude higher than originally estimated by Shibata and other authors by the v-curve method; the lowest attenuation achieved to date in a chalcogenide material is 23 $dBkm^{-1}$ at 2.4 μm in a multimode As_2S_3 fibre (21). Since the mid 90s it was generally accepted that IR fibres could not compete with silica in term of transparency, strength and durability for long distance data transmission. Passive applications of chalcogenide fibres are at present almost exclusively limited to IR applications.

More recently, chalcogenide glasses and fibres have been proposed for active devices, such as rare earth-doped fibre lasers and nonlinear devices (see ref. (22) and (23) for a review). The low phonon energy reduces the non-radiative quenching of electronic levels with small energy separation to the next-lower levels. Radiative transition rates are higher than in oxides and fluorides due to the high refractive index. Thus, optical transitions are available in rare-earth doped chalcogenide glasses that are commonly not

observed in the conventional oxide glass hosts, enabling new and potentially efficient schemes for fibre lasers and optical amplifiers, both in the near and in the mid-IR. Furthermore, the high refractive index of chalcogenides also correlates with a high third order nonlinearity, which can be exploited for photonic applications such as all-optical switching and Raman amplification. Magneto-optical and acousto-optical effects have also been investigated for optical circulators and modulators (8; 9), and for applications in optical sensing.

Most practical devices, however, require a waveguide or, more frequently, an optical fibre geometry, where light signals are subject to tight modal confinement. Monomodal operation in a high quality waveguiding structure with low overall attenuation is essential to ensure good device efficiency. Producing this type of structure in chalcogenide glasses is a very challenging task. It requires, in the first instance, the achievement of very high purity and transparency in the base glass, despite the fact that raw materials are often difficult to obtain with the necessary degree of purity and the preparation of the glass involves long processing under a strictly controlled atmosphere. Also, the glass must be stable enough to withstand the subsequent processing to form single mode fibres, which involves a number of thermo-mechanical steps of shaping; fibre drawing is often complicated because all these steps must be carried out within very tight temperature limits in order not to compromise the glass transparency. Fabrication techniques require a great deal of effort and process refining and a precise knowledge of the material's fundamental properties is paramount.

1.3 Gallium Lanthanum Sulphide (GLS) glasses.

GLS glasses are relatively 'new' among chalcogenide glass systems. The glass forming ability of gallium and lanthanum sulphides was discovered in 1976 by Loireau-Lozac'h and co-workers (24); gallium sulphide is a conditional glass former, that is it cannot form glass by itself but only when mixed with some other sulphides or oxides. GLS glasses have a wide region of glass formation centered about the $70Ga_2S_3 : 30La_2S_3$ composition and can also be modified by the addition of lanthanum or gallium oxides (25; 26; 27; 28); they have high refractive index (≈ 2.4), low maximum phonon energy ($\approx 425\ cm^{-1}$), and good transparency from about 0.53 to 5 μm (29). Early investigators also studied the thermal stability (24), and the microstructure of GLS (30; 31) by Raman spectroscopy and EXAFS.

The original interest in GLS glasses was motivated by the quest for new active materials for solid state lasers. Fluorescent lanthanide ions can be introduced in GLS by partial substitution of the lanthanum sulphide component. Rare-earth solubility is very high in GLS, as opposed to several other chalcogenides, such as $As{:}S$ and $Ge{:}S$ glasses. Reisfeld and co-workers first characterised the spectroscopic properties of Ho^{3+} (32), Nd^{3+} (33)

and Er^{3+}-doped GLS (34), and reported higher radiative quantum efficiencies as compared to oxide glasses, leading to low threshold for laser operation (35). Unfortunately, GLS glasses also have high dn/dT and low thermal conductivity, causing strong thermal lensing, thus they are not suitable for bulk lasers (36).

The invention of the erbium-doped optical amplifier triggered new interest in GLS for fibre applications (37; 38). The fibre geometry suffers to a lesser extent from the thermal lensing, because it allows a more efficient dissipation of heat, and also because light guiding enables a more efficient energy transfer from the pump light to the active ions. In addition to the rare-earth solubility and fluorescent properties, GLS has: good transparency in the region 0.5-1.1 μm where most of the pump wavelengths of active ions lie; a high glass transition temperature, which makes them more resistant to thermal damage; good chemical durability; finally, the glass components are non-toxic, which allows more ease in the glass preparation. The combination of all these characteristics is not found in any other chalcogenide system and motivated strong interest from many research groups worldwide; research programs started in early '90s at AT&T Bell Labs (39), Corning Incorporated (40) and, especially, at the Optoelectronics Research Centre at the University of Southampton. The main open question was whether the glass was stable enough to allow the fabrication of good-quality optical fibres; this question, as will be discussed later, is substantially still open.

Work at the ORC was aimed at the development of a 1.3 μm optical fibre amplifier for operation in the O band. Initially Pr^{3+} was evaluated as the active ion, finding a quantum efficiency of $\approx$ 70% for the $^1G_4 \rightarrow {}^3H_4$ transition at 1.34 μm, which compares with only 4% for the same transition in fluorozirconate glass (41). Also Dy^{3+} has an optical transition in the 1.3 μm region ($^6H_{9/2} \rightarrow {}^6H_{15/2}$), which is non-radiatively quenched in non-chalcogenide hosts with higher phonon energy. In the GLS host, however, this transition is active with a quantum efficiency of $\approx$ 30% (42); a new scheme for a dysprosium-doped 1.3 μm chalcogenide fibre amplifier was then proposed (43). The first ever multimode GLS optical fibre was produced in 1996 (44) by the rod-in-tube technique; purified raw materials were supplied by Merck Ltd. at this stage. Laser action was demonstrated, for the first time in a chalcogenide, in Nd^{3+}-doped bulk GLS glass (45) and fibre (46). Acousto-optical properties of GLS were also characterised (9) and the first demonstration was given of thin film of GLS grown by Pulsed Laser Deposition (PLD) (47). Compositional modification through addition of sulphides, oxides and halides and its effect on the glass formation and thermal stability, the visible transparency and RE quantum efficiency were also extensively investigated. Perhaps the most significant achievement of these more fundamental studies was a correct understanding of the role of the oxide component in the glass formation, which the earlier studies by Loireau-Lozac'h failed to recognise. In fact, while Ga_2S_3-La_2O_3 is a true binary glass forming system, the same is not true for the system Ga_2S_3-La_2S_3; a small percentage of lanthanum oxide ($\geq$ 2 $mol\%$) must be added to the 'pure sulphide' compo-

sition (either intentionally or as an impurity) to enable glass formation over the region previously described. However, while adding oxides results in glass with improved thermal properties, it also has a strong impact on the fluorescence properties. Oxide bonds in the glass matrix provide high phonon energy channels for non-radiative de-excitation of rare earth ions; the quantum efficiency of Pr^{3+} and Dy^{3+} are strongly reduced with increasing oxide content. Thus, a trade-off is necessary, where some oxide is added to ensure the glass stability, but must be kept sufficiently low not to compromise the optical properties. Seddon and co-workers produced a detailed study on crystallisation of GLS (see (48) for a review), and first reported the application of the extrusion technique to prepare core/clad preforms from bulk glass ingots (49), which was subsequently also developed at the ORC.

Research at the ORC during the past five years has maintained the focus on spectroscopy and fabrication. Schweizer (50) performed a spectroscopic study of rare-earth doped and co-doped GLS , achieving a very exhaustive mapping and characterisation of the optical transitions in the near and mid-IR. On the fabrication side, the major achievements were obtained in the synthesis and purification of the glass components (gallium and lanthanum sulphide) and in the fabrication of preforms with small ($\approx 1/15$) core/clad ratios (51). Despite a lot of effort, however, it has not been possible, to date, to achieve a good quality, low loss single mode optical fibre. One problem mentioned earlier in this section is the limited thermal stability, especially of the low-oxide GLS; these glasses have a small separation between the onset of crystallisation and the temperature for fibre drawing, and devitrify upon prolonged or repeated heating above the glass transition temperature T_g, which also poses a tight constraint on the number of heating steps that are practically possible in order to fabricate preforms from bulk glass ingots.

The nonlinear properties of GLS were first investigated by Zhou et al. (52); it was found that the third-order nonlinear coefficient of this material is around 100 times that of silica. This result was in line with that observed in other chalcogenide glasses, where n_2 can be up to three orders higher than in silicate glass, and was confirmed by other measurements in the region 0.6-1.25 μm (53) and at 1.5 μm (54). Work at the ORC achieved two important results. Firstly, it was found that GLS and GLSO glasses have very low nonlinear absorption. Both high n_2 and low β_2 contribute to a high nonlinear figure of merit (see section 2.3), which is an expression of how suitable a glass is for nonlinear applications. The other important finding is that oxide addition to the glass, while making the fibre drawing easier, does not critically alter the nonlinear properties of the glass. GLSO is therefore a promising candidate for nonlinear applications.

An interesting recent development is the fabrication of microstructured 'holey' fibres in GLS glass (55). In these fibres, modes are confined in the core and guided due to an effective index difference between the solid core and an holey cladding. As holey fibres can be fabricated with very small mode areas, a high effective nonlinearity can be achieved even in materials with low bulk nonlinearity (56). The possibility of further

enhancing the high material nonlinearity of GLS glass in a holey structure would then open up the possibility of very efficient and short devices (55).

1.4 Scope of the thesis

The present project is focused on the feasibility of GLS based glasses for telecom devices and was originally started in the framework of a collaboration between the Optoelectronics Research Centre and Pirelli Cavi e Sistemi SpA. Low-oxide GLS glass ($Ga{:}La{:}S$) is a candidate for the 1.3 μm praseodymium-doped fibre amplifier (PDFA). High and low oxide GLS have potential for nonlinear applications and in particular all-optical switches.

Considerable effort has been devoted in recent years to searching for new solutions for broadband amplification and all-optical switching, as these are regarded as key areas for further development of the present technology. Although a variety of materials and device concepts have been investigated, chalcogenide glasses such as GLS and other systems ($Ga{:}Na{:}S$, $As{:}S$, $Ge{:}Ga{:}S$ etc.) are still considered viable by several research groups worldwide. The question of which material and which device scheme affords the best chance of providing efficient and cost-effective devices is still unanswered. This thesis will assess the feasibility of GLS for efficient fibre devices.

Practical applications have been impeded until now due to the impossibility of achieving single mode fibres with low attenuation. It is therefore necessary to identify what are the possible solutions for improving the fabrication of GLS optical fibres. As the limited thermal stability of these materials might unavoidably introduce a certain amount of loss, it is also very important to investigate the transparency limit and the loss mechanisms, especially in the near-IR. The target for most RE-doped and nonlinear applications is $\leq 0.5\ dB\ m^{-1}$ attenuation in a single mode fibre; in order to determine if this target can be met in GLS and GLSO glasses, it is crucial to investigate the presence of the weak absorption tail, which limits intrinsically the transparency of other sulphide glasses.

Another issue of great practical relevance is the behavior of GLS based glasses under heavy irradiation at near-IR wavelengths. High signal and pump intensities are generally required for fibre devices, especially in presence of a measurable background attenuation. The response of GLS to high pump powers has not yet been studied in detail, but from studies of related glass systems it is well known that both permanent damage and photorefractive effects can occur. It is therefore necessary to investigate the occurrence of these effects in GLS based glass and to determine possible thresholds for both types of photoinduced damage.

Besides the present introduction, this thesis is structured in six chapters plus the conclusions.

- Chapter 2 discusses the application of GLS based glass for the 1.3 μm PDFA and for the all-optical switch. The aim for this chapter is to identify the principal issues related to the application of sulphide fibres and to set out practical targets for the fabrication.

- Chapter 3 is dedicated to the fabrication and characterisation of GLS glasses and fibres. Although a lot of effort had been devoted to the fabrication process prior to this work, considerable improvements are still required for practical devices. Here, directions of activity are identified and results are presented, especially in the area of fibre characterisation. The fibre properties measured in this work are summarised in Appendix A.

- Chapter 4 describes the application of laser absorption calorimetry for precise measurements of the near-IR absorption of bulk GLS and GLSO samples. The free-electron laser source at the Thomas Jefferson National Accelerator Facility (Newport News, USA) was employed to access the region around 1.5 μm. Also presented is the project and commissioning of the calorimeter utilised in the measurement. The use of a FEL for laser calorimetry is novel and a quantification of the optical absorption of GLS and GLSO at telecom wavelengths had never been achieved before.

- Chapter 5 presents a very exhaustive theoretical description of laser absorption calorimetry. Although the technique is well established, it was found that the theoretical description presented to date was not completely adequate, hence a novel and more general model was formulated and is presented here. The model is well adapted to measurements of glasses with low thermal conductivity (such as GLS) and includes the use of a sample holder in the description. A novel procedure for the solution of the boundary value problem of heat diffusion in thin, 2-d, composite multilayers is presented in section 5.5 and the results are also summarised in Appendix C.

- Chapter 6 investigates the transmission loss of GLS based glass, with particular emphasis on the near-IR region. The chapter is divided into two parts. In the first the loss mechanisms are analysed, the absorption/scattering components are quantified, and the presence of a weak tail is studied. In the second part it is demonstrated that the transmission loss of GLS can be significantly affected by temperature and, especially, by bandgap illumination. The photodarkening effect of GLS and GLSO fibres is thoroughly investigated. The results presented in this chapter provide novel and valuable information on this optical process in GLS and GLSO.

- Chapter 7 presents a study of the response of GLS and GLSO fibres under high-intensity irradiation at 1.06μm. This issue is of great practical relevance for the 1.3 μm PDFA. The occurrence of photorefractive effects and damage thresholds

will be investigated. The results presented here are entirely novel and have indicated a fruitful area of future research.

- Finally, chapter 8 draws the conclusions and identifies the topics that might provide the basis for further studies.

Chapter 2

Near-IR Photonic Applications of GLS-based Glasses

2.1 Introduction

Broadly speaking, the practical applications of chalcogenide glasses and fibres can be classified into passive and active applications (17). The passive applications utilise an optical fibre as a light conveyor which does not induce any modifications, other than attenuation, wavelength dispersion and end-face reflection losses. Examples of passive applications are laser power delivery, remote chemical sensing and IR thermal vision. The main advantage of chalcogenide glasses for passive applications is their mid-IR transmission beyond the 2 μm limit where silica and most of the oxides become opaque; using chalcogenide glasses then allows accessing to regions of crucial importance for industrial, medical, sensing and military applications, such as the output wavelength of high- power IR lasers (CO at 5.4 μm, CO_2 at 10.6 μm), the atmospheric transparency window (3-5 μm), and the MIR vibrational bands of most gases and hydrocarbons. The active applications include all the devices in which the light originally coupled into a fibre or waveguide is modified by some property of the constituent glass; examples in the latter class include fibre lasers and amplifiers, gratings, optical switches, modulators and so forth. Here the advantage of chalcogenides lies in their low phonon energy, their high refractive index and high third order nonlinearity.

The focus of the present chapter is on active applications of GLS-based glasses and, in particular, on the 1.3 μm Pr^{3+}-doped optical amplifier and on nonlinear devices. Here the basic device concepts will be reviewed and the parameters of operation will be presented and discussed in detail, aimed at defining precise targets for the fabrication and at identifying the main issues related to the application of GLS glasses.

2.2 Rare Earth-doped Ga:La:S glasses for Optical Amplifiers

2.2.1 Principles of Operation

The operation of optical fibre amplifiers is similar to that of the laser, but with some important distinctions. As in the laser, it is based on an active optical medium with a gain transition between two of its energy levels. In the present case, the active medium consists of trivalent rare earth ions, which are embedded in the glass host. A pump signal is used to create and maintain the population inversion between the two levels. Under this condition, signal photons traveling in the system with wavelength close to the gain transition induce the stimulated emission of other in-phase photons leading to optical amplification. As opposed to lasers, optical amplifiers have no optical cavity, which implies that the amplification process takes place in a single pass, and also that it can occur over a wide interval of wavelengths. Photons from the gain transition can also be emitted spontaneously; in this case, however, they are not phase-related to the signal and constitute noise. Spontaneously emitted photons can induce the emission of other photons and thus be amplified, producing the Amplified Spontaneous Emission (ASE).

A general representation of the process is shown in figure 2.1: ions from the ground state G are pumped at λ_p into the metastable excited level E; they decay quickly to the third level A, which must have a long lifetime. The gain transition is between the level A and B, and subsequently the ions decay back to the ground state, and become available to be pumped back to E starting the cycle once again. Such an amplification scheme, where the gain transition happens between two intermediate metastable states, is commonly indicated as a four-level system. The case of the 1.3 μm praseodymium doped amplifier is slightly different, as also shown in figure 2.1, since the levels A and E in fact coincide with the same energy level ($^1G_4$) of the Pr^{3+} ion. Although just three levels are involved

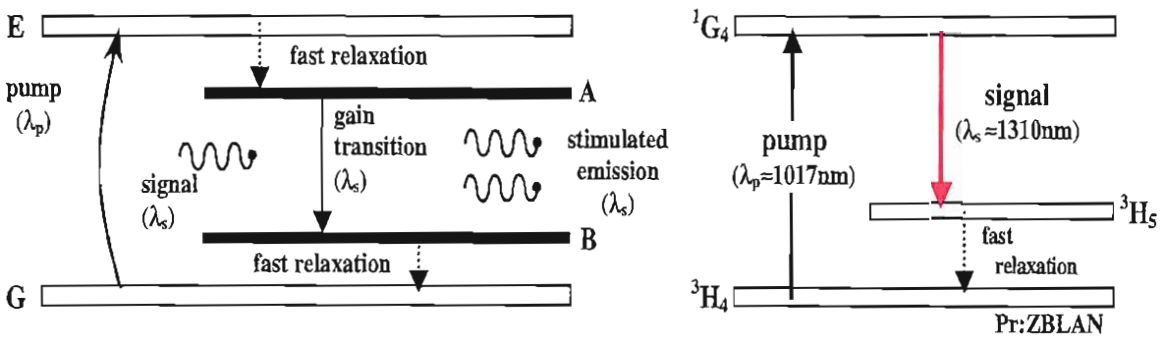

FIGURE 2.1: Diagram of a generic four-level optical amplifier and of the Pr^{3+} energy levels in the 1.3 μm optical amplifier.

in the process, the Pr^{3+} scheme is still indicated as a four level system. In a three level system, the level B is not metastable and coincides with the ground state, which leads to substantially different equations for the gain (57).

The energy difference between the two levels involved in the gain transition determines the wavelength of operation of the amplifier. Amplification schemes based on rare-earth doped materials exploit transitions between $4f$ electronic levels of the triply-ionised rare-earth ions. Each $4f$ level has a fine structure of energy states with small energy separation due to the Stark splitting caused by the local electric field around the ion site. Rare-earth ions can occupy different inequivalent sites in the glass network, where the local variation of symmetry or electric charge around the ion results in a statistical distribution of Stark splittings. The amplitude of this inhomogeneous broadening of energy separations depends on the host, but in glassy materials is comparable to the magnitude of the Stark splitting itself; consequently, the sublevels are not resolved and the optical transitions appear as a single broad band, typically several tens of nm wide. This also implies that optical amplifiers based on rare-earth doped glass can operate over wide wavelength intervals.

From the simplified diagram in figure 2.1, it is clear that the success of any amplification scheme depends to a large extent on the metastable level A ($^1G_4$ in the case of praseodymium) having a long emission lifetime; this condition is necessary to allow for the population inversion. The lifetime of a particular energy state is determined by the various ways in which the excited ion can give up energy. The decay process can either be radiative, i.e. the excitation energy is converted into a photon, or non-radiative. A very meaningful way to express the efficiency of a transition is through the ratio between the radiative transition rate and the total transition rate, which is commonly called the radiative quantum efficiency (RQE). If τ is the total lifetime of the excited state and τ_r is the radiative lifetime, the radiative quantum efficiency $\mathbb{Q}$ is expressed by:

$$\mathbb{Q} = \frac{1/\tau_r}{1/\tau} = \frac{\tau_r}{\tau} \tag{2.1}$$

High RQE of a metastable level, such as the one depicted in fig. 2.1, implies that it decays preferentially through the gain transition rather than in any other possible way; in a purely radiative transition $\mathbb{Q}$ is obviously 100%. When several radiative transitions can originate from the same metastable level, each transition is characterised by a branching ratio $\beta^{\overline{\lambda}}$, i.e. the ratio of radiative transition rate at a certain wavelength to the total radiative transition rate:

$$\beta^{\overline{\lambda}} = \frac{1/\tau_r^{\overline{\lambda}}}{1/\tau_r} = \frac{\tau_r}{\tau_r^{\overline{\lambda}}} \tag{2.2}$$

($\tau_r^{\overline{\lambda}}$ is the radiative lifetime of the transition at the wavelength $\overline{\lambda}$).

The quantity:

$$\mathbb{Q} \times \beta^{\overline{\lambda}} \tag{2.3}$$

is indicated as the radiative quantum efficiency of the transition at wavelength $\overline{\lambda}$. The RQE of an electronic level is usually less than 100% due to the presence of non-radiative decay mechanisms, where the excitation is lost as a result of energy transfer from an ion to the host or to other ions, without the emission of any photons; the RQE of an optical transition is further reduced by the other competing transitions. Non-radiative decay mechanisms include the multiphonon relaxation and quenching of the excited state due to ion-ion interactions such as concentration quenching and impurity quenching and will be discussed in more detail for the case of Pr^{3+} in the next section. Also excited state absorption (ESA) can effectively reduce the RQE of a level; with reference to fig. 2.1, in ESA ions from the excited state E can be promoted, by the absorption of pump or signal photons, to a higher energy level, from which they can decay through different channels; the process then depletes the level E without any signal photon being emitted.

The gain of an optical amplifier is usually quoted in dB and defined as:

$$G = 10 \cdot log\left(\frac{P_s(L)}{P_s(0)}\right) \tag{2.4}$$

where $P_s(0)$ and $P_s(L)$ are the power of the incoming and amplified signals respectively. In log units, the output power is then simply given by:

$$P_s^{out}[dBm] = P_s^{in}[dBm] + G[dB] \tag{2.5}$$

(where $P[dBm] \equiv 10 \cdot log(P[mW])$). The gain of an optical amplifier depends on several variables, firstly on the properties of the active ion and on the amplification scheme, which generally involves transitions between numerous energy levels and is strongly influenced by the glass host. The design and length of the optical waveguide, its background attenuation and the pumping scheme are also very relevant. For a fixed amplification scheme, the gain is dependent on the wavelength, on the input signal intensity and on the pump intensity. It can be proved that, in the limit of small input signals, the gain is approximately proportional to the amount of absorbed power, which allows the definition of an overall efficiency factor F:

$$G(\nu; P_s; P_p) \overset{P_s \to 0}{\approx} F \cdot [P_p(0) - P_p(L)] \equiv F \cdot P_{abs} \tag{2.6}$$

$$F\,[dB/mW] \equiv \lim_{P_s \to 0} \frac{\partial G}{\partial P_{abs}} \tag{2.7}$$

The small signal figure of merit, or efficiency factor, F is usually quoted in dB per milliwatt of absorbed power and is a function of the wavelength (within the bandwidth of the amplifier). For larger signal intensities, the gain is not proportional to the absorbed power and gain saturation occurs.

The key requirements in order to achieve optical amplification with high gain characteristics can be summarised as follows:

- High radiative quantum efficiency of the gain transition.
- High stimulated emission rates of signal photons.
- Efficient pumping scheme.
- Low background loss of the active medium.

The first condition is determined by the properties and concentration of the rare-earth ion, and by the properties of the host glass. Furthermore, since both the rate of stimulated emission of signal photons and the pump absorption rate are proportional to the optical intensity (58), an effective strategy for meeting conditions two and three is by spatially confining both signal and pump in a small active volume, such as the core of a single mode optical fibre or waveguide. Doping levels in the core and the length of the device should be optimised to ensure an efficient transfer of the pump power to the active ions, without compromising the quantum efficiency due to ion-ion interactions. The use of optical fibres allows longer interaction lengths, gives more flexibility in the doping levels and leads to higher gains than waveguides, provided that the overall attenuation of the fibre can be kept low.

Figure 2.2 shows the basic configuration of a rare earth-doped optical fibre amplifier. The active medium is the core of a segment of fibre, with optimised length and concentration of active ions in the core. In EDFAs the active fibre is still a silica fibre and can be fusion spliced in line to the system to minimise the insertion loss. The pump power, provided by a laser diode, is injected through a wavelength-sensitive fibre coupler. Travelling light signals are amplified through an all-optical process. One or more optical isolators are generally inserted to prevent undesired back-reflections and possible laser oscillations and optical bandpass filters suppress the ASE at wavelengths different from the signal.

Optical fibre amplifiers play a crucial role in todays telecom systems. In long-haul terrestrial and submarine communication links, amplifiers are employed to compensate for the fibre loss. In-line amplifiers are placed at regular equivalent intervals of about 10 to 20 dB, with the actual length spacing depending on the fibre attenuation (typically

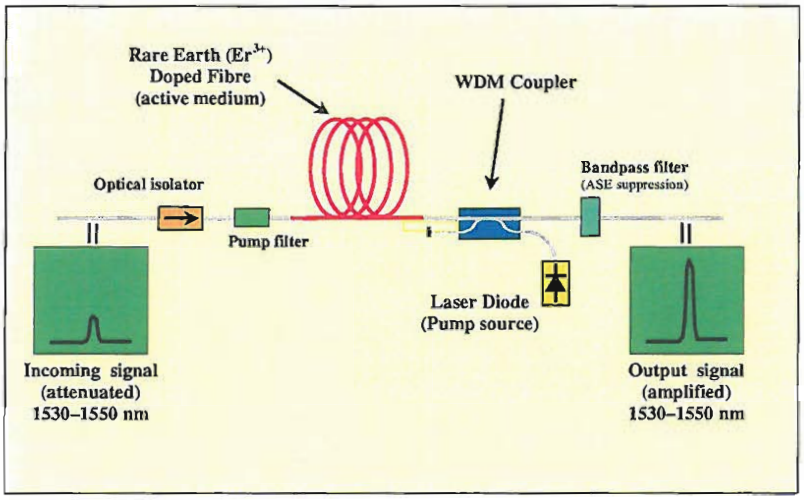

FIGURE 2.2: Rare-earth doped optical fibre amplifier.

spacing is several tens of km to two hundred km). Optical amplifiers are also used in a range of other applications, including lossless splitters, post-amplifiers or 'boosters' (placed after a transmitter to increase its output power) and pre-amplifiers (placed before a detector to increase its sensitivity).

A very useful characteristic of amplifiers is broadband operation; a broad, wavelength independent gain spectrum is highly desirable as it enables operation at several different wavelengths with the same device. This is the basis for wavelength division multiplexing (WDM), where multiple channels of information are carried by the same fibre, each using an individual wavelength. Modern dense-WDM (DWDM) systems are based on EDFAs operating in the C band (1530-1565 nm) and in some cases also on gain-shifted EDFAs operating in the L band (1565-1625 nm); channels are allocated at fixed wavelength intervals. Interference or 'crosstalk' can only occur due to weak nonlinear effects, thus the spacing between channels can be kept as small as a few nm.

2.2.2 1.3 μm Pr^{3+}-doped fibre amplifier (PDFA)

The energy level diagram of the praseodymium ion (Pr^{3+}) is shown in figure 2.3. The Pr^{3+} ion has a transition at about 1.3 μm between the levels $^1G_4$ and the $^3H_5$; this transition is dominant over the other two radiative transitions ($^1G_4 \rightarrow ^3F_2$ and $^1G_4 \rightarrow ^3H_4$), having a branching ratio of 52% to 65% depending on the glass host. Optical pumping around 1.02 μm accesses the $^1G_4$ metastable level directly, providing a four-level-like system.

One important problem concerning the amplification process in Pr^{3+} is represented by the non-radiative decay of the $^1G_4$ level. The energy separation ΔE between $^1G_4$ and the next-lower lying level $^3F_4$ is relatively small (about 2900 cm^{-1}). De-excitation of the

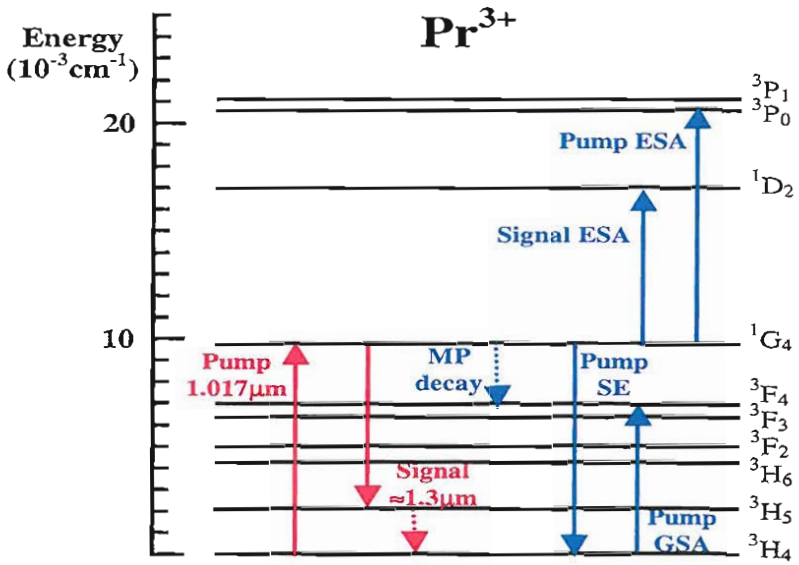

FIGURE 2.3: Diagram of energy levels of Pr^{3+} in GLS glass showing the transitions relevant to the 1.3 μm amplification process.

$^1G_4$ can also take place through the creation of vibrational quanta (phonons). Energy is transferred from the ion to the host glass network without the emission of photons. This process, called multiphonon relaxation, is particularly effective in hosts with high phonon energy. In fact, high-order multiphonon decay processes occur predominantly through the excitation of phonons from the highest-frequency vibrational bands of the glass host, ω^{max}, and a crucial parameter in determining the multiphonon decay rate is the minimum number, p, of high energy phonons required to bridge the energy gap ΔE between the two levels involved (59; 60). This rate can be expressed as:

$$w_{mp} = B\left[N(\omega)+1\right]^p e^{-\alpha\frac{\Delta E}{\hbar\omega}} \tag{2.8}$$

where B is a material parameter dependent on the glass host, $\omega \approx \omega^{max}$, $N(\omega)$ is the phonon occupation number expressed by the Bose-Einstein distribution and the quantity between brackets expresses the temperature dependence of the process, and α is directly related to the electron-phonon coupling constant γ ($\gamma = \exp(-\alpha)$). As $\omega \approx \omega^{max}$, and $\Delta E/\hbar\omega$ equals the phonon number p, equation 2.8 shows that a small value of p leads to high rates w_{mp}. Assuming that multiphonon relaxation is the only non-radiative decay mechanism, the total lifetime and radiative quantum efficiency of the $^1G_4$ of Pr^{3+} can be expressed respectively as:

$$\tau = \left(\frac{1}{\tau_r}+\frac{1}{\tau_{nr}}\right)^{-1} = \frac{\tau_r}{1+w_{mp}\tau_r} \tag{2.9}$$

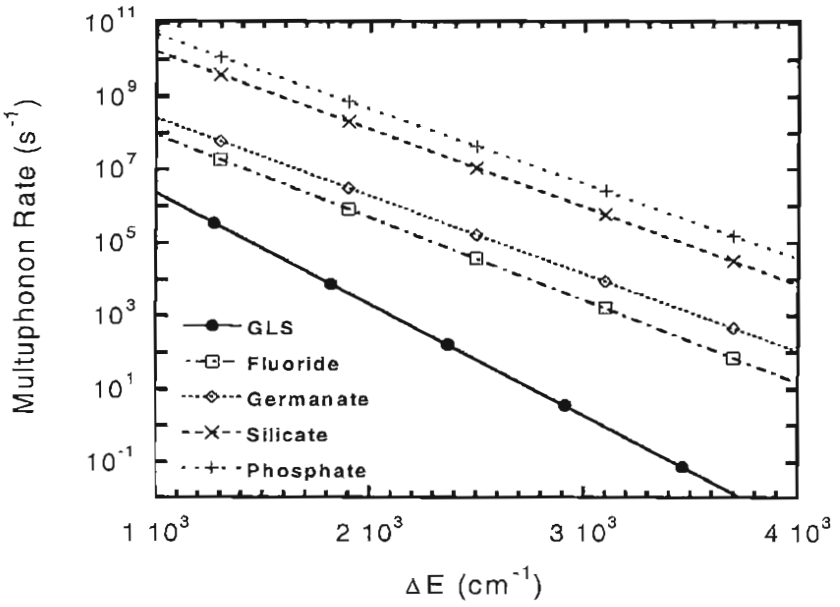

FIGURE 2.4: Multiphonon decay rates as a function of energy separation (from ref. (66; 67; 50)).

$$Q = \frac{\tau}{\tau_r} = \frac{1}{1 + w_{mp}\tau_r} \tag{2.10}$$

The equation 2.10 shows that, due to the small energy separation ΔE between the $^1G_4$ and $^3F_4$ levels, the choice of a glass host with low phonon energy is essential in order to have a high RQE of the $^1G_4$. The dependence of the multiphonon decay rate for various glass hosts is reported in fig. 2.4. Silica has the highest-energy phonon band peaked at about 1100 cm^{-1}; the multiphonon decay of the $^1G_4$ level is accomplished through the emission of only a few phonons and is favoured over the radiative transition to $^3H_5$, which is not observed in Pr^{3+}-doped silica. In fluorozirconate (ZBLAN) or fluorogallate glass (InF_3:GaF_3), with a maximum phonon energy of about 600 and 500 cm^{-1} respectively, the multiphonon decay rate of $^1G_4$ is over two orders of magnitude smaller than in silica, leading to a RQE of 3 to 5% (61). Pr^{3+}-doped fibre amplifiers based on fluorozirconate glass were first reported in 1991 (62) and extensively investigated and developed in the successive years. Exploiting the well-established fabrication technologies of ZBLAN optical fibres (13), gains as high as 38 dB, with output power of 18 dBm have been achieved in device prototypes pumped at 1.017 μm using a Ti-sapphire laser (63); however, due to the low quantum efficiency, a large pump power in excess of 300 mW was required to obtain this sort of gain. The typical efficiency factor in optimised devices is 0.24 dB/mW (0.4 dB/mW with dual pumping scheme) (64), which compares unfavorably to the 11 dB/mW best value reported for an EDFA (65).

An obvious way to increase the RQE of the $^1G_4$ level is to choose a glass host with even lower phonon energy than fluorozirconate glass. Heavy metal halides such as Cd-

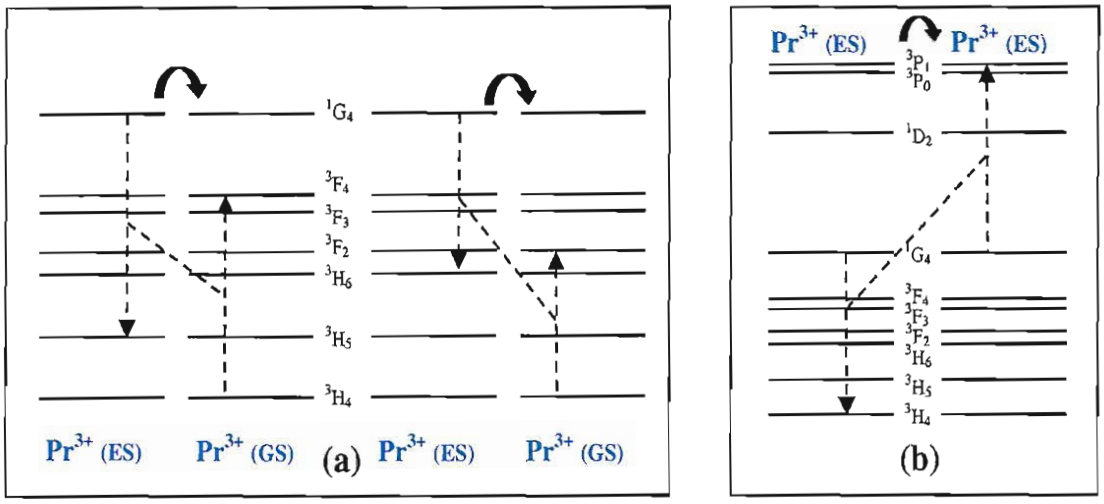

FIGURE 2.5: Representation of non-radiative ion-ion energy transfer processes in Pr^{3+}: cross relaxation (a) and cooperative upconversion (b).

mixed halide glasses (68; 69) and chlorosulphide glasses (70) meet this requirement, but they are very hygroscopic, which hinders any practical application even for the glass compositions that are stable enough to be drawn into fibres. Chalcogenide glasses, on the other hand, have in general better durability and stability and also show very low phonon energy (350-400 cm^{-1}); consequently, the multiphonon relaxation rates of $^1G_4$ are reduced, as shown in figure 2.4, leading to increased lifetimes, of about 300 μs, and RQEs of 50-70% (see table 2.2).

Despite the high RQE, the application of a chalcogenide glass host for a PDFA must also address other difficulties. The pump ground state absorption (GSA) cross section of Pr^{3+} at 1.017 μm is in fact low; efficient power transfer to the active ions then requires long interaction lengths or very high doping concentrations. This second option is impractical because the level $^1G_4$ suffers from concentration quenching due to ion-ion interactions. In these non-radiative phenomena (see fig. 2.5) energy is transferred between neighboring ions through a phonon-assisted process. In particular, cross relaxation occurs when energy is partly transferred from one ion in the excited state to another ion in the ground state, leaving both ions in an intermediate state. Two possible channels for cross relaxation are represented in figure 2.5. When the transfer involves two excited ions, the energy transfer is termed cooperative upconversion (also shown in fig. 2.5). Upconversion, which is observed at high pump powers, results in one of the two ions being promoted to an upper level, and the second being de-excited to a lower. Both cross-relaxation and upconversion have the net effect of depleting the $^1G_4$ level and thus lower its quantum efficiency.

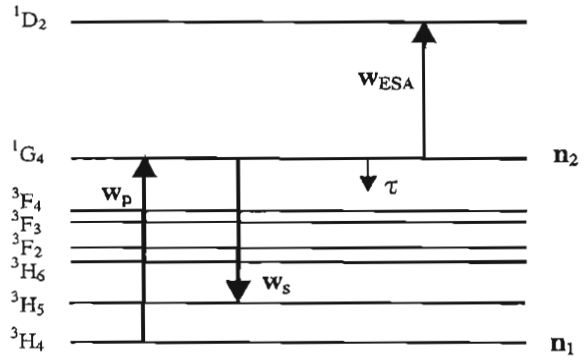

FIGURE 2.6: Simplified amplification scheme for the PDFA.

2.2.3 Efficiency of the PDFA

Numerous radiative and non-radiative transitions contribute to the 1.3 μm amplification process in PDFAs. The prediction of the amplifier performance and the optimisation of its design require a theoretical description that takes into account, apart from the transitions directly responsible for the amplification process, the other mechanisms shown in fig. 2.3 such as signal ASE, signal GSA, pump and signal ESA and cooperative upconversion. General models have been presented by Ohishi (64) for the fluoride PDFA and Van Osch (71) for both fluoride and sulphide PDFAs, the latter based on *Ge:Ga:S* glass. The standard approach to this problem involves as a first step writing the rate equations for the ion population densities of the energy levels, and finding the steady-state solutions of these equations; then, the steady-state populations must be substituted in the differential equations describing the propagation for the pump and the signal powers along the fibre; the resulting equations also depend on the amplifier configuration, including fibre parameters, pumping scheme and the like. Although the procedure as outlined above is straightforward, the result is a system of coupled differential equations for $P_S(z)$ and $P_P(z)$ that in general can only be handled numerically.

On the other hand, by selecting a limited set of transitions, the analysis can be considerably simplified and closed expressions are obtained for the small signal figure of merit and the gain saturation characteristics, which provide good physical insight into the amplification process and a simple way to compare the characteristics of PDFAs in different glass hosts. Simplified models have been presented by several authors, involving different degrees of approximation (72; 73; 74). Here we apply to the Pr^{3+} four-level scheme a modified version of the method presented in reference (75) for the Neodymium-doped fibre amplifier (NDFA).

The set of transitions considered in this model is shown in figure 2.6. The four-level system is pumped at 1.02 μm ($^3H_4 \rightarrow {}^1G_4$), the gain transition is at about 1.3 μm ($^1G_4 \rightarrow {}^3H_5$), and the $^3H_5$ relaxes to the ground state by fast decay. Among the gain-

limiting effects, only the signal ESA ($^1G_4 \rightarrow {}^1D_2$) is taken into account in this model. Other transitions, such as signal GSA and pump ESA are supposed to be negligible at the wavelengths involved, and ion-ion interaction effects are also supposed to be negligible. Furthermore, the spontaneous emission at the signal wavelength (and at any other wavelength) is not amplified, that is, the model assumes that no ASE can occur. The level $^1D_2$, populated by the signal ESA transition, relaxes preferentially through decay to the $^3F_3$:$^3F_4$ doublet and hence to the ground level; therefore, we assume that after signal ESA the excitation is completely lost through fast decay to the ground state. Under these simplified hypotheses, only the $^1G_4$ and the $^3H_4$ levels are populated, and the rate equations for these populations are:

$$\begin{cases} \frac{dn_2}{dt} = w_p n_1 - (w_s + w_{ESA} + 1/\tau)\, n_2 \\ \frac{dn_1}{dt} = -\frac{dn_2}{dt} \end{cases} \tag{2.11}$$

where n_1 and n_2 are the population densities of $^3H_4$ and the $^1G_4$ respectively, while w_p, w_s and w_{ESA} are the stimulated transition rates relative to the pump, signal and ESA transitions. The stimulated rates are proportional to the photon intensities, which in general vary from point to point within the fibre; thus, the above equations are local or microscopic and $n_i = n_i(r, \theta, z)$. The steady-state solutions are:

$$\begin{cases} \overline{n}_2 = \frac{w_p}{w_p + w_s + w_{ESA} + 1/\tau} \cdot n \\ \overline{n}_1 = \frac{w_s + w_{ESA} + 1/\tau}{w_p + w_s + w_{ESA} + 1/\tau} \cdot n \end{cases} \tag{2.12}$$

where n is the total dopant concentration (in ions$\cdot cm^{-3}$). The equations expressing the local variation of pump and signal photon intensities along the fibre are:

$$\begin{cases} \frac{dI_p}{dz}(r, \theta, z) = -\sigma_p \overline{n}_1 (r, \theta, z)\, I_p (r, \theta, z) \\ \frac{dI_s}{dz}(r, \theta, z) = (\sigma_s - \sigma_{ESA})\, \overline{n}_2 (r, \theta, z)\, I_s (r, \theta, z) \end{cases} \tag{2.13}$$

where σ_p, σ_s and σ_{ESA} are the cross sections for the stimulated pump, signal and ESA transitions respectively. It is important to note that no background attenuation of signal and pump intensities is taken into account in the above equation. In order to obtain the total pump and signal power in the fibre as a function of the longitudinal coordinate z, it is necessary to integrate the two differential equations term by term over the transverse coordinates. To perform the integration, some assumptions concerning the dopant density and the propagation of the pump and signal light must be made. Here we assume that the Pr^{3+} ion density has a 'top hat' distribution with uniform density in the fibre core. This hypothesis fits well the case of most compound glass fibres, while in the case of MCVD-deposited silica the doping profile in the core can also be varied radially. Furthermore, it is convenient to assume that the fibre is monomode at the signal wavelength, while the pump propagates with several modes and its power intensity

distribution can be approximated by a uniform distribution. Under these conditions, the transverse integration of the equations 2.13 can be performed analytically and yields the following result (75):

$$\begin{cases} \frac{dP_p}{dz}(z) = -\sigma_p \overline{n}_1(z) P_p(z) \\ \frac{dP_s}{dz}(z) = \sigma_s (1-\varepsilon) \overline{n}_2(z) \frac{A}{A_{eff}} P_s(z) \end{cases} \tag{2.14}$$

where we have introduced the ratio ε between the ESA and signal scattering cross sections (at the signal frequency ν_s):

$$\varepsilon = \frac{\sigma_{ESA}(\nu_s)}{\sigma_s(\nu_s)} \tag{2.15}$$

Also, A is the area of the core ($A = \pi a^2$, where a is the core radius) and A_{eff} is the effective area of the signal mode; assuming a gaussian envelope approximation for the latter (76), with mode field radius ω_s, it follows that:

$$A_{eff} = \frac{A}{1 - \exp\left[-2\left(a/\omega_s\right)^2\right]} \tag{2.16}$$

The quantities $\overline{n}_1(z)$ and $\overline{n}_2(z)$ are defined as in equation 2.12, where however the 'local' stimulated transition rates ($w(r,\theta,z)$) are substituted with the following 'integral' transition rates:

$$\begin{cases} w_p(z) = \frac{\sigma_p(\nu_p)}{A h\nu_p} P_p(z) \\ w_s(z) = \frac{\sigma_s(\nu_s)}{A_{eff} h\nu_s} P_s(z) \\ w_{ESA}(z) = \frac{\sigma_{ESA}(\nu_s)}{A_{eff} h\nu_s} P_s(z) \end{cases} \tag{2.17}$$

The two coupled equations 2.14 can be combined into one single equation, yielding:

$$\frac{1-\varepsilon}{1+\varepsilon} \cdot \frac{\nu_s}{\nu_p} \cdot \frac{dP_p}{dz}(z) = -\left[1 + \frac{B^{sat}}{P_s(z)/h\nu_s}\right] \frac{dP_s}{dz}(z) \tag{2.18}$$

where B^{sat} is the saturation parameter:

$$B^{sat} = \frac{A_{eff}}{\sigma_s \tau (1-\varepsilon)} \tag{2.19}$$

By integrating equation 2.18 between $z = 0$ and $z = L$, the following equation is

obtained:

$$\frac{1-\varepsilon}{1+\varepsilon}\cdot\frac{\nu_s}{\nu_p}\cdot P_{abs}=[P_s(L)-P_s(0)]+h\nu_s B^{sat}\cdot\ln\left[\frac{P_s(L)}{P_s(0)}\right] \tag{2.20}$$

In the latter relationship it was defined that: $P_{abs}=P_p(0)-P_p(L)$. Before analysing and discussing the result, it is worth summarizing all the assumptions made in this model:

- Among the gain-limiting effects, only the signal ESA is taken into account; signal GSA and pump ESA are neglected, as well as ion-ion interaction effects.
- ASE is neglected, i.e. spontaneous emission of signal photons is not amplified.
- The fibre is monomode to the signal and multimode to the pump, which is approximated with a uniform power distribution.
- The concentration of Pr^{3+} ions in the fibre has a 'top hat' distribution and is uniform in the core.
- The fibre is assumed perfectly transparent to both the pump and the signal wavelengths, i.e. no background loss is considered.
- The pump is assumed to be co-directional with the signal.

Equation 2.20 can be solved by any standard technique for transcendental equations, providing the output signal power and hence the gain over a length L of fibre (eqn. 2.4) as a function of the absorbed power P_{abs} and of the input signal power $P_{in}=P_s(0)$. However, both in the small-signal regime ($P_s(z)\ll 1/h\nu_s B^{sat}$) and in the large-signal regime ($P_s(z)\gg 1/h\nu_s B^{sat}$), eqn. 2.18 can be simplified, by neglecting respectively the first and the second term between square brackets. This leads to explicit expressions for the output powers and the small signal and large signal gains can be expressed respectively as:

$$\begin{cases} G=\frac{10}{\ln(10)}\frac{1-\varepsilon}{h\nu_p}\frac{\tau\sigma_s}{A_{eff}}\cdot P_{abs} & \text{small signal} \\ G=10\log\left[1+\frac{1-\varepsilon}{1-\varepsilon}\frac{\nu_s}{\nu_p}\frac{P_{abs}}{P_{in}}\right] & \text{large signal} \end{cases} \tag{2.21}$$

The first relationship in eqn. 2.21 states that the small signal gain is, as expected from eqn. 2.6, proportional to the absorbed power, and also provides an expression for the figure of merit of the amplifier (eqn. 2.7):

$$F=\frac{10}{\ln(10)}\frac{1-\varepsilon}{h\nu_p}\frac{\tau\sigma_s}{A_{eff}} \tag{2.22}$$

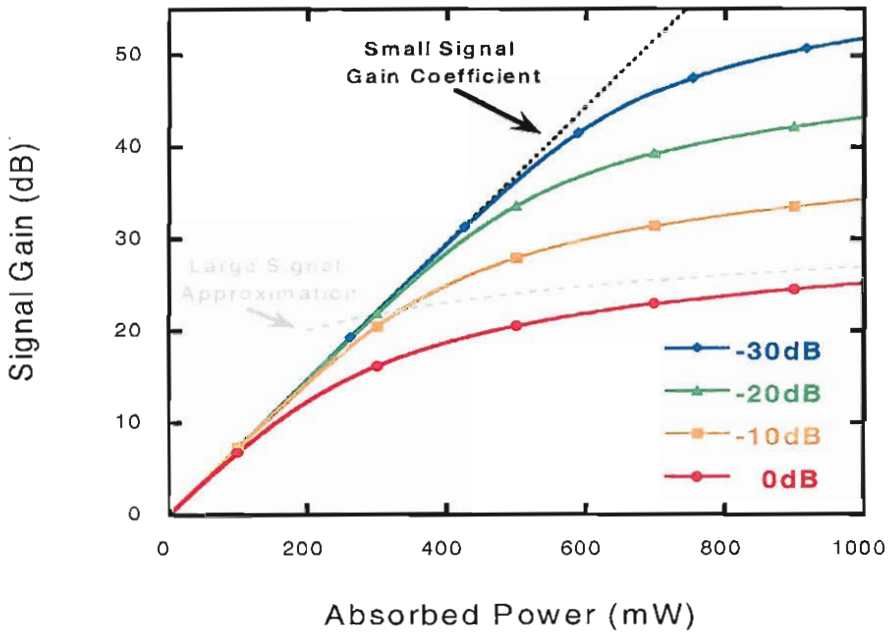

FIGURE 2.7: Theoretical gain curves of a fluoride PDFA for different input powers (material & fibre parameters as in Table 2.1).

TABLE 2.1: Input parameters for the calculation of the theoretical gain curves.

		Pr^{3+}:ZBLAN	Pr^{3+}:GLS
σ_s	$(10^{-25}\ m^2)$	3.5	10.5
σ_{ESA}	$(10^{-25}\ m^2)$	0.7	1.3
τ	(μs)	110	300
ν_s	$(10^{14}\ Hz)$	2.288	2.254
ν_p	$(10^{14}\ Hz)$	2.948	2.948
a	(μm)	1.5	1.5
NA		0.3	0.3
ω_s	(μm)	1.767	1.781
A_{eff}	(μm^2)	9.26	9.32

This expression shows that, for fixed fibre parameters (determining A_{eff}), the efficiency of the Pr^{3+}-doped amplifier is determined by the product between the lifetime of the excited state $^1G_4$ and the radiative scattering cross section of the gain transition, $\tau\sigma_s$; since the latter is largely determined by the host, relationship 2.22 gives a simple criterion to compare different glasses. As expected, the ESA always reduces the amplifier efficiency. The above relationship also states that, for a fixed value of $\tau\sigma_s$, the small signal gain over an assigned length of fibre can be increased by choosing a small core dimension and large NA for the fibre, both of which reduce A_{eff}; this is of course valid only as long as the fibre loss is not considered. In practice, for very small core radii and high NA the optical loss becomes unacceptably high and some trade-off is necessary.

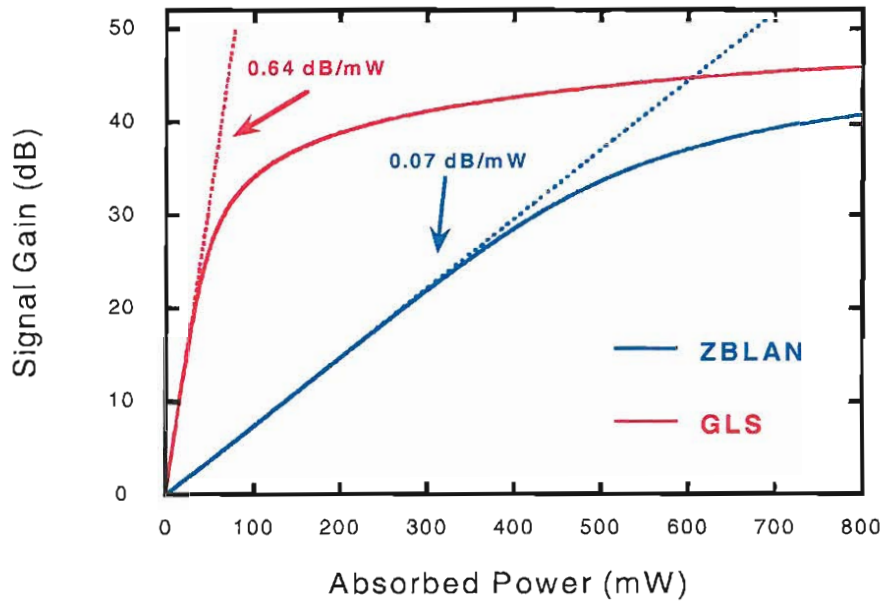

FIGURE 2.8: Comparison between theoretical gain of the fluoride (ZBLAN) and sulphide (GLS) PDFA (input power: -20 dBm, other parameters as in Table 2.1).

Figure 2.7 shows the theoretical gain curves, calculated using eqn. 2.20 and the typical parameters of a fluoride (ZBLAN) PDFA reported in table 2.1. Also shown in the figure are the approximations for small and large signals (eqn. 2.21); the latter curve is calculated for 0 dBm signal input power. A comparison between the theoretical gains of sulphide and fluoride PDFAs are shown in figure 2.8; the input power is fixed at -20 dBm (small signal regime), and the other relevant parameters are as shown in table 2.1. According to the present model, the small-signal theoretical gain of the sulphide PDFA exceeds that of the fluoride PDFA by approximately a factor of ten.

2.2.4 Sulphide vs. fluoride PDFA

The 1.3 μm PDFA requires a low-phonon energy host, such as fluoride glass or sulphide glass. Other chalcogenides, such as selenide and telluride glasses, are not suitable, with very few exceptions, due to their poor transparency in the near-IR and especially at the pump wavelength. A comparison of the key properties of several glass hosts is presented in table 2.2. While the fabrication technologies of fluoride optical fibres are more developed, sulphide glasses have potential for more efficient devices. Their phonon energy is lower than fluorides, leading to longer radiative lifetimes and higher RQEs. Sulphide glasses also have very high refractive index (2.2-2.45), which gives stronger local electric fields around the rare-earth ions and leads to larger cross sections for stimulated emission. The advantage of the sulphide over the fluoride host is evident through the large values of the product $\sigma_s \tau$ shown in table 2.2.

TABLE 2.2: Spectroscopic parameters of the $^1G_4 \rightarrow {}^3F_5$ transition of Pr^{3+} in various glass hosts.

Host	λ^{peak} $[nm]$	τ $[\mu s]$	$\mathbb{Q}$ [%]	β_s	$\mathbb{Q} \times \beta_s$ [%]	σ_s $[10^{-25}\ m^2]$	$\sigma_s \tau_s$ $[10^{-29}\ m^2 s]$	Ref.
Halides								
ZBLAN	1322	110	3.4	0.64	2.2	3.48	3.83	(64)
InF:GaF	1320	186	8.6	0.64	5.5	4.40	8.18	(78)
Cd:Halide	1310	327	11.5			4.15	13.6	(69; 79)
Chalcogenides								
GLS	1334	300	60	0.60	36	10.8	32.4	(41)
Ge:Ga:S	1344	360	70	0.58	41	13.3	47.9	(80)
Ga:Na:S	1332	370	56	0.57	32	10.8	40.0	(81; 82)
As:S:Ga	1336	250	–	–	–	–	–	(83)
Chalcohalides								
Cs:Ga:S:Cl	1312	2460	24	0.42	10	1.98	48.71	(70)
Ge:S:I	1340	368	–	–	–	–	–	(84)

However, the increase in the lifetime of levels with small energy separation plays an adverse rather than a positive role on the level $^3H_5$, i.e. the terminal level of the gain transition. In ZBLAN the lifetime of $^3H_5$ is short, hence its population plays a very minor role in the amplification process. In the low phonon sulphide hosts, however, the increased lifetime of $^3H_5$ can cause a bottlenecking effect and reduce the available gain. The problem has been studied in detail by Quimby et al. (77) and can be alleviated by co-doping or dual pumping schemes.

Another drawback of the sulphide host is the shift to longer wavelength of the fluorescence bands due to the nephelauxetic effect (33). The fluorescence of the $^1G_4 \rightarrow {}^3F_4$ transition peaks at about 1.34 μm (as compared to 1.32 μm for fluorides), leading to a poor overlap between the gain bandwidth of the sulphide PDFA and the O-band; the application for devices operating at wavelengths close to that of zero chromatic dispersion of telecom networks (1.31 μm), apart from the reduced efficiency, must also address a severe issue of gain flatness.

Sulphide hosts have similar values of refractive index and phonon energy; with only small differences in the position of the fluorescence peak λ^{peak}, and close values of the product $\sigma_s \tau$ (see table 2.2), they are substantially equivalent from the spectroscopic point of view. Fibre fabrication then becomes the crucial point, and the possibility to achieve a high purity glass and to draw it into single mode fibres are decisive in order to establish the best sulphide host.

Among the most extensively investigated sulphide glass systems are *As:S* and *Ge:S*. These glasses are thermally stable, and fibre fabrication is well established (5). *As:S*

TABLE 2.3: Glass systems for 1.3 μm PDFAs.

Host	λ_S^{peak} $[nm]$	Pros	Cons	SM fibre fabricated	Device demonstrated	F $[dB\ mW^{-1}]$	Ref.
ZBLAN	1300	Fab developed	Low ℚ, durability	Yes	Yes	0.24	(64)
$InF{:}GaF$	1300	Betters ZBLAN	Low Q, durability	Yes	Yes	0.29	(78)
GLS	1340	High Q	Thermal stability	short lengths	No	–	(12)
$Ge{:}Ga{:}S$	1340	High Q	Thermal stability	No	No	–	(80)
$Ga{:}Na{:}S$	1340	High Q	Durability	Yes	Yes	0.81	(82)
$As{:}S{:}Ga$	1340	High Q	RE solubility	Yes	No	–	(87)
$Cs{:}Ga{:}S{:}Cl$	1310	Good Q	V. hygroscopic	No	No	–	(70)

single mode fibres have been achieved with 0.6 $dB \cdot m^{-1}$ loss around 1.5 μm (23). Unfortunately, they both suffer from poor rare-earth solubility: the solubility limits of Pr^{3+} are about 500 *ppm* in $As{:}S$ (85) and 400 *ppm* in $Ge{:}S$ (86) and in both systems ion clustering occurs for Pr concentrations of a few tens of *ppm*. They are therefore unsuitable as hosts, unless their composition is modified by the addition of other sulphide or halide compounds. While these sulphide glass systems with good thermal stability are hindered by low RE solubility, the systems with higher solubility tend to be less stable and thus more difficult to draw into fibres. This is the case for glass systems based on gallium sulphide, such as GLS, $Ga{:}Na{:}S$ and $Ge{:}Ga{:}S$. RE solubility is excellent in these materials, especially in GLS, where, due to the presence of lanthanum in the glass network, up to 1-2% of Pr^{3+} can be incorporated. The fabrication of single mode fibres suitable for amplifiers requires, on the other hand, many thermal steps, which increases the chance of devitrification and thus the formation of defects that compromise the ability of the fibre to transmit light. To date, among gallium sulphide-based glasses, only $Ga{:}Na{:}S$ have been fabricated in single mode fibres with low loss comparable to the most stable sulphide glasses (82).

The issue of optical attenuation is paramount for the realisation of both fluoride and sulphide PDFAs. In fact, as pointed out previously, the 1.3 μm amplification scheme with Pr^{3+} has its weakest point in the low pumping efficiency of the gain transition. A fibre geometry with long device lengths (10-20 m) is then required for practical devices. In fluoride PDFAs, due to the low intrinsic quantum efficiency, the effective mode area must be small (see eqn. 2.22) in order to achieve a reasonable gain. Small effective areas are obtained by reducing the core diameter (<2 μm) and increasing the numerical aperture; however, by doing that, the scattering from defects in the core and at the core/clad interface also increases, leading to an higher overall attenuation of the fibre. For instance, although large mode area ZBLAN fibres can achieve a minimum loss of a few $dB \cdot km^{-1}$ (at 2.4 μm), the typical loss for small area fibres at 1.3 μm goes up to about 100 $dB \cdot km^{-1}$, owing to the increased scattering.

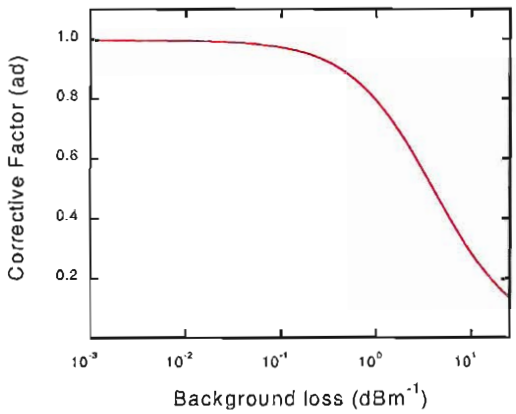

FIGURE 2.9: Corrective factor of the PDFA small signal efficiency as a function of the background loss.

In sulphide PDFAs loss reduction is even more important. Its quantum efficiency is higher, but, as will be discussed more into detail in the next chapters, the sulphide hosts are intrinsically less transparent than the fluorides at near-IR wavelengths. In most sulphide glasses the transparency limit is believed to be $\approx 0.5\ dB \cdot m^{-1}$ (5). Also, ion-ion interactions are stronger, due to the higher refractive index. In Pr^{3+} doped GLS, for instance, concentration quenching starts to become effective at doping concentrations as low as 100 ppm, and poses a limit to the maximum concentration of below 1000 ppm (50). This constraint cancels out the positive effect of the higher cross section of the pump transition (also due to the high refractive index), and implies that sulphide PDFAs too have to rely on fibre geometry and long (5-10 m) device lengths.

The amplifier model which was formulated in the previous section assumed a loss-less fibre. The effect of the background attenuation on the small signal figure of merit (eqn. 2.7) can be estimated by multiplying the factor F (eqn. 2.22) by a correction factor (88):

$$F' = F \cdot \frac{\alpha_i}{\alpha_i + \alpha} \tag{2.23}$$

where α is the background attenuation and α_i is the ionic absorption of Pr^{3+} ions at the pump wavelength. We measured $\alpha_i = 4\ dB \cdot m^{-1}$ in an unclad GLS fibre doped with 1000 *ppm* of Pr^{3+}. The value of the corrective factor (2.23) is shown in figure 2.9 as a function of the fibre attenuation; it is evident that, in order to retain the advantage of the better spectroscopic properties, a sulphide PDFA requires the fibre loss to be below $1\ dB \cdot m^{-1}$

A point worthy of particular attention, and to date not extensively investigated, is that concerning nonlinear and photoinduced effects. Sulphide glasses have a third order nonlinearity a few hundred times stronger than ZBLAN (table 2.6); they also show pho-

toinduced effects, which are not observed in fluorides. Both these phenomena increase with increasing power intensity in the core, i.e., again, with decreasing the effective mode area of the fibre, and deteriorate the amplification process in diverse ways. Nonlinear effects cause interference between signals at different wavelengths (the 'channels' in DWDM systems); photoinduced effects affect the transparency of the host glass and are equally to be avoided in amplifiers. Thus, apart from the loss issue, maximisation of the gain through reduction of the mode area in sulphide PDFAs must also avoid the onset of these effects.

To summarise the results of this section: sulphide glasses, especially a few systems based on gallium sulphide (such as GLS) have potential for more efficient PDFA devices, as compared to the commercially available fluoride PDFAs, provided that:

- It is possible to achieve a thermally stable and durable glass composition with transparency close to the intrinsic limit ($\leq 0.5\ dB \cdot m^{-1}$).
- The thermal stability is sufficient to allow drawing of single-mode fibres with small core radii ($<2\ \mu m$) and high NA, without compromising the transparency of the base glass.
- Fabrication-induced fibre attenuation, nonlinear effects and photoinduced effects can be minimised.

2.2.5 Pr^{3+}:GLS glass for optical amplification around 1.3 μm

The spectroscopic properties of Pr^{3+}:GLS are shown in table 2.2 and place it among the most suitable glass systems for the sulphide PDFA. The lifetime of the $^1G_4$ level is 300 μs, leading to high RQE, and the product $\sigma_s\tau$ is almost one order larger than in ZBLAN; however, the fluorescence peaks at 1.34 μm, well off the center of the O band.

Since the early work by Becker et al. (38) it was recognised that the most serious issue for this material is the thermal stability. GLS has a strong tendency towards crystallisation at temperatures above the glass transition T_g as will be discussed in Chapter 3. The separation between the temperature for fibre drawing and the temperature for which the crystallisation rate is maximum amounts to only a few tens of degrees. GLS glass cannot be subjected to repeated heat treatments above T_g without compromising its transmission properties. This inability to process GLS by a series of thermo-mechanical steps automatically excludes some of the standard techniques for fibre drawing from preforms, such as the rod-in-tube technique used for the fabrication of single mode fluoride fibres. The rod-in tube technique was employed in early trials to prove in principle the 'fiberisability' of GLS and and produced only multimode fibres (44), with large core/clad ratios and, unfortunately, with very high loss.

The problem of glass stability can, at least in principle, be tackled in two different ways. Firstly, modifying the glass composition can improve the stability and alleviate the problem. Secondly, the fabrication process can be adapted in order to reduce the number of steps utilised for preform fabrication and fibre drawing. Apart from these more practical aspects, since in a glass with limited thermal stability the fibre fabrication is always likely to introduce an amount of extra loss, it is also important to establish what is the intrinsic transparency limit of the material. This is a difficult and much debated issue not just for GLS but for chalcogenide glasses in general, as these materials show attenuation mechanisms that are not common to other glasses (such as oxide and fluoride glasses). In GLS the question of what is the transparency limit in the near-IR is still substantially open. Brady et al. (89) applied the V-curve model originally proposed by Shibata et al. (20); they determined the electronic and multiphonon absorption edges by transmission measurements, and assumed theoretical expressions for the Rayleigh scattering from small-scale density and refractive index fluctuations. A minimum loss of 0.51 $dB\ km^{-1}$ at 3.5 μm resulted resulted from this model; the loss in the near-IR was about 0.05 $dB\ m^{-1}$ and was due to scattering. These estimates, however, did not take into account the weak absorption tail (WAT) (90), which has been observed in many chalcogenide glass systems, including $As{:}S$ and $Ge{:}S$. The total attenuation of GLS is also determined by fabrication-related loss mechanisms, such as the impurity from transition metal impurities and the scattering from crystals, defects and inclusions; consequently, it is very difficult to separate the various contributions, hence to investigate the presence and magnitude of the weak tail.

Stabilisation of GLS through compositional modification has been extensively investigated (see section 3.2.2 for a more detailed discussion). Addition of other sulphide compounds does not result in a noticeable improvement of thermal properties. Modification through halides lead to some improvements, particularly with group-I metal halides (91); however, these materials are very hygroscopic, which negatively affects the glass purity and durability. Oxide addition leads to a marked improvement of the thermal properties of GLS, providing wider glass forming regions, reduced critical cooling rates and better stability upon reheating above T_g. The role of oxide was first investigated and reported in the early studies by the group of Flahaut (25). The addition of oxide is not only beneficial, but essential to glass formation of GLS, and this was only pointed out much later by Hewak (92) and Li et al. (48). Compositions with less than 1-2 $wt\%$ of oxygen, either contained as an impurity of other components, or added intentionally as La_2O_3 or Ga_2O_3, produce on quenching a mixture of crystalline and glassy phases.

On the other hand, oxide addition also induces strong modification of the optical and spectroscopic properties. The position of the UV-Visible electronic edge is blue-shifted with increasing oxide fraction; in GLSO glass, where all the lanthanum sulphide component is replaced by lanthanum oxide, the shift is up to about 50 nm. Spectroscopic

properties are radically modified. Oxide bonds act like high-phonon energy channels for non-radiative de-excitation of RE ions. Consequently, the RQEs are progressively reduced with increasing amount of oxygen introduced in the glass network (93). As lanthanide ions have a very large average coordination number ($\approx$ 8), and oxygen-lanthanide bonds are favored over sulphur-lanthanide bonds due to the larger difference of electronegativity, even a small amount of oxide of a few percent produces a noticeable effect. Oxide sites are energetically inequivalent to sulphide sites, the spectroscopic properties of rare earths becomes markedly wavelength-dependent (94), i.e. pumping at slightly different wavelengths inside the GSA bands accesses different groups of ions and hence results in a different fluorescent response.

Although the reduction in the RQEs caused by the oxide has generally been considered a disadvantage for devices, work carried out at the ORC (95) has shown that this is not necessarily the case for GLS. Oxide addition has advantages as well as drawbacks. The disadvantages are the reduction of the RQE and the increase of the signal GSA due to the progressive shift of the $^3H_4 \rightarrow {}^3F_4$ transition with increasing oxide content (reduced nephelauxetic effect). The advantage are better thermal stability, a broadening of the emission at 1.3 μm, the wider range of pump wavelengths and a potential for efficient high-power amplification through the reduced lifetime of lower-lying levels ($^3H_5$, $^3H_6$) causing bottlenecking. All these pros and cons must therefore be carefully considered, as oxide addition in limited amounts may prove beneficial, at least for certain applications.

2.2.6 Alternative candidates for the 1.3 μm optical amplifier

2.2.6.1 Pr^{3+} amplifiers based on other glass systems

Amplification at 1.3 μm was first demonstrated in Pr- doped fluoride glass (ZBLAN) (96; 62; 97). The fluoride PDFA was successively developed particularly by scientists at the BT Labs (UK) (98) and NTT (Japan) (64). Most efforts were devoted towards increasing the gain through waveguide optimisation (63) and towards improving the pumping efficiency. The best efficiency reported in Pr: ZBLAN is 0.24 and 0.4 $dB\ mW^{-1}$ for a single and dual pass pumping scheme respectively. The efficiency is slightly better in InF_3-based devices. The gain bandwidth of the fluoride PDFA, with its center at 1.31 μm is perfectly matched to the O band. However, due to its low intrinsic efficiency, the fluoride PDFA requires a high pump intensity: a 30 dB gain requires over 300 mW of power at 1.02 μm. Compact, cheap and reliable sources are not readily available at this wavelength and level of power. Device prototypes were originally demonstrated using Ti-sapphire or neodymium lasers as the pump source, which however are not suitable for practical devices. Diode pump modules were later developed, based on $InGaAs$ strained quantum well laser diodes (99). PDFA commercial modules, based either on ZBLAN and InF_3- fluoride, and pumped with a compact, diode-pumped Nd:YLF, are

currently available from NTT Electronic Corporation (100). The insertion of fluoride PDFA modules into the standard networks poses further challenges; due to the huge difference of melting points, fluoride fibres cannot be fusion spliced, and must therefore be butt-coupled, to silica fibres; the difference of refractive index and mode mismatch at the interface produces extra loss and unwanted reflections. The problem of connections of fluoride PDFAs to conventional fibres is addressed in ref. (101). Despite the continued improvements, the fluoride PDFA has only had limited technological applications as an optical power amplifier rather than signal amplifier for telecom networks.

Amplification around 1.3 μm has also been demonstrated in Pr^{3+}-doped $Ga{:}Na{:}S$ by Toratani and co-workers at Hoya Corporation (Japan) (82). These authors have successfully fabricated single mode fibres with small core radius (2-2.5 μm), high NA (0.31) and low loss (1.2 $dB\ m^{-1}$) at 1.31 μm, and their result is the best reported so far for a PDFAs based on a sulphide host. They used extrusion to fabricate the preforms from which optical fibers were subsequently drawn. Extrusion allows mechanical processing of glass at lower temperatures than most other techniques, which proves particularly useful in the case of glasses with limited thermal stability. The $Ga{:}Na{:}S$, originally reported by Palazzi (102), has the longest lifetime ever reported for the level $^1G_4$ of Pr^{3+}, and also the shortest emission wavelength (1.332 μm) among the sulphide glasses (see table 2.2); one drawback is caused by the sodium sulphide being very hygroscopic (103). Using a bidirectional pumping configuration, the group at Hoya achieved a low signal gain coefficient of 0.81 $dB\ mW^{-1}$ at 1.34 μm in a 6 m long device (82), which more than doubles the efficiency of the best fluoride PDFA; this prototype delivered 30 dB net gain with less than 100 mW input power. The efficiency was some 40% lower (0.51 $dB\ mW^{-1}$) at the preferred wavelength of 1.31 μm.

Table 2.3 reviews the state-of-the-art of the glass systems relevant to 1.3 μm PDFAs; the first two columns summarise the main advantages and drawbacks of each system, the second two show respectively for which system single mode fibres suitable for practical devices and device prototypes were achieved, and the fifth reports their efficiency.

2.2.6.2 RE-doped amplifiers based on other rare earth ions

Neodymium was first proposed as the active ion for a 1.3 μm fibre optical amplifier (NDFA) (104). A diagram of the main energy levels is shown in figure 2.10; neodymium constitutes a four-level system, where the gain transition $^4F_{3/2} \rightarrow {}^4I_{13/2}$ is purely radiative (i.e., the RQE is almost one). The pump wavelength of 800 nm conveniently falls within the output range of commercially available $AlGaAs$ laser diodes; furthermore, the radiative cross section of the pump transition, unlike in the Pr^{3+}, is large, opening the possibility of high pump efficiency and shorter device lengths. The 1.3 μm amplification scheme in Nd^{3+} has however a fatal drawback caused by signal ESA. Indeed, the gain transition is almost resonant with the $^4F_{3/2} \rightarrow {}^4G_{7/2}$, which is centered at slightly

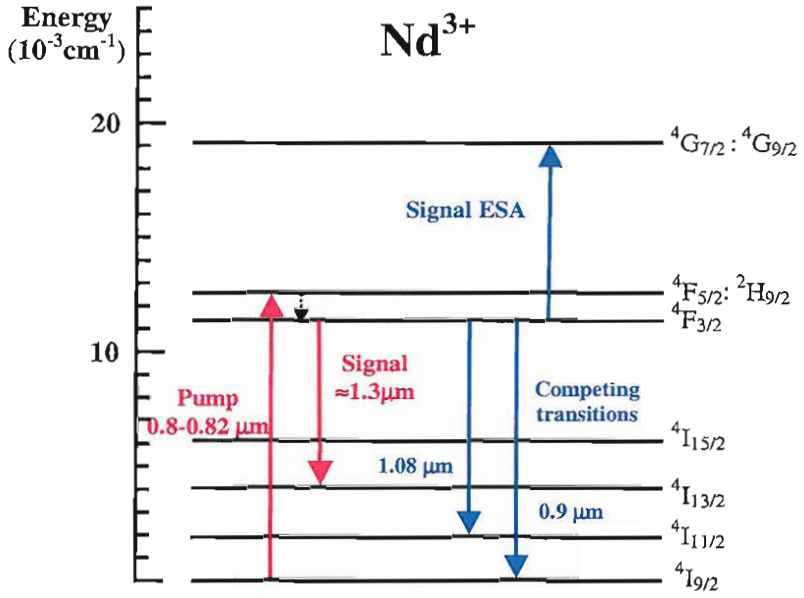

FIGURE 2.10: Diagram of the energy levels of Nd^{3+} relevant to 1.3 μm amplification.

higher energies. ESA depopulates the lasing level, and generally leads to loss, rather than gain, around 1.3 μm, and the gain peaks at longer wavelengths, resulting in a poor overlap with the O band (105). In Nd^{3+}-doped silica, for instance, ESA prohibits gain below 1.36 μm. Choosing a fluoride or fluorophosphate host causes only a slight improvement, with the fluorescence emission peaking at 1.34 μm. The glass host for which the best overlap with the O band results is fluoroaluminate, where the emission peaks at 1.317 μm (106); however, fluoroaluminate glass is far less stable than fluorozirconate and fibre fabrication is difficult (107). Another problem of the neodymium amplification scheme is the existence of other spontaneous transitions from the $^4F_{3/2}$ level, at 0.88 μm ($^4F_{3/2} \rightarrow {}^4I_{9/2}$) and 1.06 μm ($^4F_{3/2} \rightarrow {}^4I_{11/2}$), actively competing with the gain transition; as their branching ratio is higher, they equally contribute to depleting the lasing level through strong ASE, hence they reduce the available signal gain at 1.3 μm, unless they are filtered out. Optical amplification has been demonstrated in a Nd^{3+}-doped fluorozirconate fibre, though with a maximum net gain of 10 dB at 1.33 μm (108). Positive net gain at 1.317 μm has also been recently demonstrated in an Al:F_3-based Nd^{3+}-amplifier employing a waveguide geometry (109). The limitations imposed by ESA and ASE remain unaffected if a chalcogenide is chosen as host; on the contrary, the nephelauxetic effect shifts the $^4F_{3/2} \rightarrow {}^4I_{13/2}$ fluorescence further away from the center of the O band. In Nd^{3+}-:GLS, for instance, the fluorescence peaks at 1.36 μm (50). Lasing in Nd^{3+}: GLS (both bulk and fibre) has been observed only at 1.08 μm (45; 46). It is also important to note that the attenuation at the pump wavelength is higher in the chalcogenides than in fluorides, due to the proximity to the electronic absorption edge and the presence of the weak tail, which reduces the pumping efficiency at 0.8 μm. Optical amplification at 1.08 μm has only been reported for one multicom-

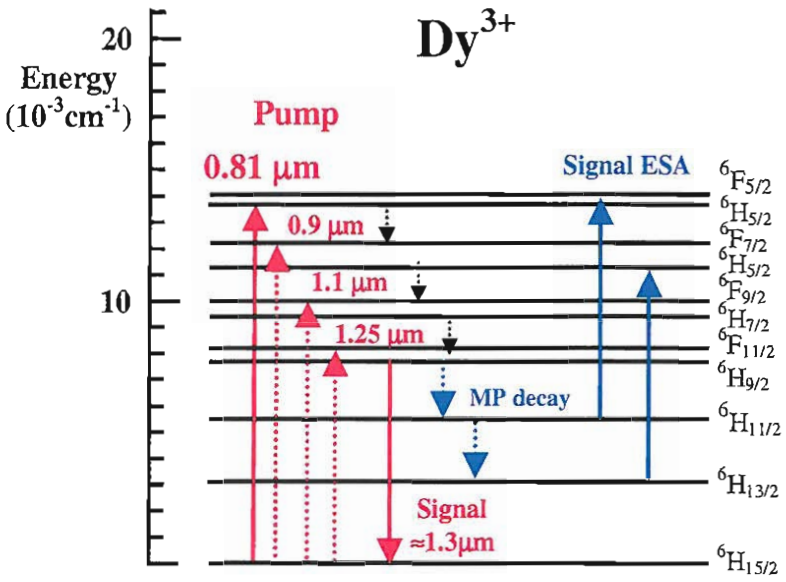

FIGURE 2.11: Diagram of the energy levels of Dy^{3+} relevant to 1.3 μm amplification.

ponent chalcogenide system (Ge:As:Ga:Sb:S) (110) but, due to the high attenuation, no net gain could be observed.

Another candidate for O-band amplification is dysprosium. The transition of interest (see fig. 2.11) is from the doublet $^6H_{9/2}$:$^6F_{11/2}$ to the ground state $^6H_{15/2}$ (111). Due to the very small energy separation ($\approx$ 1800 cm^{-1}) between the $^6F_{11/2}$ and the next-lower lying level, this transition is subject to strong non-radiative quenching from multiphonon decay, and is not observed in oxide or even in fluoride glasses. Thus, the Dy-doped amplifier requires a chalcogenide as the host. In Dy^{3+}-doped GLS the 1.3 μm transition has slightly less than 30% RQE (111), which is suitable for optical amplification. Unlike the PDFA, the metastable level $^6H_{9/2}$:$^6F_{11/2}$ can be accessed by several different pumping schemes; a number of bands are available, all characterised by high GSA: at 0.81, 0.9, 1.1 and 1.25 μm. The shorter wavelength bands (0.81, 0.9 μm) provide a three-level scheme and are conveniently matched to the output of commercial laser diodes. The in-band pumping scheme at 1.25 μm, due to the larger absorption cross section, opens the possibility of short devices (42).

The biggest drawback of the dysprosium amplifier is the presence of two intermediate levels ($^3H_{11/2}$ and $^3H_{15/2}$) with longer lifetimes ($\approx$ ms) as compared to $^6H_{9/2}$:$^6F_{11/2}$ (59 μs for GLS). Significant ion populations are trapped in these intermediate levels ('bottlenecking'), which limits the available gain and further reduces the efficiency through ESA to the higher levels $^3H_{5/2}$ and $^6F_{5/2}$ (see fig. 2.11). Samson et al. (42) have investigated a codoping scheme with high concentrations of Tb (42; 115); this scheme relies on ion-ion energy transfer from Dy^{3+} to Tb^{3+} to deplete the intermediate levels and alleviate the bottlenecking problem. In GLS, however, the presence of oxide, necessary in small quan-

TABLE 2.4: Comparison of spectroscopic parameters of the 1.3 μm transitions of Pr^{3+} and Dy^{3+}.

Host	λ^{peak} $[nm]$	τ $[\mu s]$	$\mathbb{Q}$ [%]	β_s	$\mathbb{Q} \times \beta_s$ [%]	σ_s $[10^{-25}\ m^2]$	$\sigma_s \tau_s$ $[10^{-29}\ m^2 s]$	Ref.
Pr^{3+}:ZBLAN	1322	110	3.4	0.64	2.2	3.48	3.83	(64)
Pr^{3+}:GLS	1334	300	60	0.60	36	10.8	32.4	(41)
Dy^{3+}:GLS	1320	59	29	0.93	27	38.0	22.4	(111)
Dy^{3+}:Ge:Ga:S	1340	17	38	0.90	34	43.5	16.5	(112)
Dy^{3+}:Ge:As:Ga:Se	1340	300	94	0.90	85	27.0	81.0	(113)
Dy^{3+}:Ge:Ga:S:Cs:Br	1310	1580	93	–	–	–	–	(114)

tities in order to form glass and to draw fibres, imposes a further complication, as was pointed out only recently by Schweizer et al. (116). The 1.3 μm transition of dysprosium is an 'hypersensitive' transition, where the cross section is highly sensitive to the local structure and bonding environment surrounding the Dy^{3+} ions (117). When hosted in GLS, Dy^{3+} ions distribute themselves over two groups of sites with markedly different spectroscopic properties, which Schweizer et al. name the 'sulphide site' and the 'oxide site'. Dy^{3+} ions in the oxide site experience a high phonon-energy environment which quenches non-radiatively the 1.3 μm transition, hence they only play a detrimental role in the amplification through pump GSA and signal ESA. Due to the chemical affinity between oxygen and RE metals, a considerable fraction of Dy^{3+} ions occupies oxide sites even for low ($\leq 5\ wt\%$) oxide levels.

As compared to GLS, selenide glasses in the system *Ge:As:Ga:S* (113) and alkali halide-modified *Ge:Ga:S* glasses (114), appear more promising for Dy^{3+}-doped devices. The high values of radiative lifetimes and RQEs, which in these hosts approaches 100%, indicated very low non-radiative quenching of the level $^6H_{9/2}$:$^6F_{11/2}$ (see table 2.4). Consequently, the bottlenecking effect is expected to play a far less critical role in the amplification process at 1.3 μm than in GLS. Although selenide glass has been fabricated into single mode fibres with less than 5 $dB \cdot m^{-1}$ attenuation, no demonstration of a practical amplifier has been reported to date.

2.2.6.3 Raman amplifiers

The idea and first demonstration of Raman Optical amplifiers (RAs), based on the stimulated Raman scattering, dates back to the 70s (118; 119); however, it was only in recent years that the progress achieved in high power pump LDs and cladding-pumped fibre lasers has made this type of device feasible. Raman amplification is attractive because it exploits conventional silica fibre as the amplifying medium; by turning the passive transmission line into a distributed gain medium, it provides an effective way to

TABLE 2.5: Characteristics of technologies for 1.3 μm amplification.

Device	Technology	Materials	Efficiency	Advantages	Disadvantages
RE-doped amplifiers	Optical fiber (non-oxide)	*Pr*-fluoride	0.4 dB/mW	•High power conv. efficiency	•Cost of materials
			38 dB max	•Low noise figure	•Durability
		Pr-sulphide	0.8 dB/mW	•High gain and satur. power (potentially)	•Insertion loss
			$>$ 30 dB max		•Reliable devices achieved in low efficiency fluoride
		Dy-chalcogenide	–	•Good overlap with O band	
Raman amplifiers	Optical fiber (silica)	Silicate glass	$\approx$ 38 dBmax	•'All silica solution' •Wide bandwidth • •Good coupling to standard fibres •Distributed amplification	•High pump power •Expensive pump sources Long device length
SOAs	Planar (semi-conductors)	$InGaAsP/InP$, $AlInGaAs/InP$ MQWs	$\approx$ 38 dBmax	•Possibility of integration •Possibility of hybrid devices (electronic+optical) •Possiblity of production in large numbers	•High insertion loss •Wavelength crosstalk •Polarisation sensitivity

compensate for the fibre attenuation within the fibre itself (repeaterless transmission). RAs can upgrade existing transmission links with little modification. Besides, Raman gain is non-resonant and can in principle be achieved at any wavelength, provided a suitable pump source is available; this opens the possibility for devices spanning the entire window of low attenuation of silica. RAs can operate either as distributed or as discrete or 'lumped' devices. Distributed amplification is less sensitive to degradation of the signal-to-noise ratio and to nonlinear distortions, which is very desirable in DWDM systems with closely spaced channels; hence, distributed RAs are used to improve the performance of conventional, EDFA-based systems operating in the C and L bands. Discrete RAs, on the other hand, can be used to open up new operation bands and increase the system capacity (120).

Since however stimulated Raman scattering is a weak nonlinear effect, amplification is inefficient leading to the requirement for high pump power. Powers of several hundred mW are required in order to obtain a $\approx$ 25 dB gain; as far as pumping efficiency at low signal powers is concerned, a RA is inferior even to a fluoride PDFA. The high operation power poses a problem of availability and reliability of suitable pump devices. At wavelengths where laser diodes are available (e.g. for operation in the C and L bands), several modules are generally necessary to deliver the required pump power reliably. Concerning amplification around 1.3 μm, since in silica the Raman shift is $\approx$ 450 cm^{-1}, the pump wavelength for operation in the O-band is $\approx$ 1.24 μm . This wavelength falls outside the output of laser diodes, hence cascaded Raman fibre lasers, pumped with Yb-doped fibre lasers, have been used as pump source for 1.3 μm RA device prototypes (121). The second penalty of RAs is that they require long device lengths; although a disadvantage for lumped devices, it can be counterbalanced by combining gain and dispersion compensation. Despite these difficulties, RAs for operation in several bands

have been developed at an impressive speed over the past few years; at present, devices operating in the C and L bands are already in use in long-haul transmission systems, and modules for the S band are also quickly becoming available.

2.2.6.4 Semiconductor optical amplifiers

Semiconductor optical amplifiers (SOAs) have been investigated for several years as an alternative to RE doped fibre devices (122). These devices are based on Group III-V compound semiconductor heterostructures, which offer considerable flexibility in tailoring the operating wavelength. The other strong points of SOA devices lie in their compactness, opening the possibility of monolithical integration of multiple devices, in the low power consumption and in the possibility of large scale production. Historically, the application of SOAs has been hindered by serious limitations such as their high insertion loss, leading to poor signal-to-noise ratio and fibre-to-fibre gain, nonlinear distortions and wavelength crosstalk. In spite of the overwhelming success of the EDFA, progress in the field of heterostructured semiconductors has now provided solutions for many of these problems. SOA operating both in the 1.55 and 1.3 μm bands are currently available on the market, and are viable as in-line amplifiers for telecom systems in the O band, where fibre devices have not provided, as yet, a device performance comparable to that of EDFA (123). SOAs operating at 1.55 μm can also be used in integrated optical circuits for other WDM operations such as all-optical switching and wavelength conversion (123).

2.3 Ga:La:S and Ga:La:S:O glasses for nonlinear applications

2.3.1 All-Optical Switching: principles and materials

Modern optical fibre telecommunications systems require components capable of high-speed manipulation of optical pulses. Several operations can be achieved through the use of nonlinear optical materials, where the propagation of a signal beam is controlled by means of another beam in an all-optical process. All-optical signal processing can achieve much faster rates than electronic-mediated signal processing, hence a variety of nonlinear materials and device schemes has been investigated; applications include all-optical modulators, wavelength converters, demultiplexers and, especially, all-optical switches (AOSs).

The refractive index of a nonlinear material is composed of a linear and an intensity-

dependent part, as in the following relationship:

$$n(I) = n_0 + n_2 I \tag{2.24}$$

where I is the optical power intensity ($W \cdot m^{-2}$), n_0 is the linear refractive index and n_2 is the nonlinear refractive index ($m^2 \cdot W^{-1}$). Optical nonlinearities are observed, for instance, in crystalline semiconductors, inorganic glasses and in some polymers. As nonlinearity can arise due to a variety of effects, it is important to establish appropriate figures of merit to enable a comparison between different materials. An useful criterion is to consider the ratio of the maximum nonlinear index change to the thermally induced index change, through the following quantity (124):

$$\mathcal{F}_{NL} = \frac{n_2}{\tau\alpha}\left[\frac{\rho\, C_p}{dn/dT}\right] \tag{2.25}$$

where $\rho \cdot C_p$ is the heat capacity, dn/dT is the temperature coefficient of the (linear) refractive index, τ is the response time of the nonlinearity and α is the total absorption coefficient, which includes both linear and nonlinear (i.e., two-photon) absorption:

$$\alpha(I) = \alpha_0 + \beta_2 I \tag{2.26}$$

It is obvious from equation 2.25 that a nonlinear optical material should ideally have a large nonlinear refractive index, fast response and low absorption at the wavelength of interest. Semiconductors have large nonlinear coefficients at near-IR wavelengths; however, such nonlinearity is associated with the excitation of electron-holes pairs, hence with high absorption and slow relaxation times. Glasses are also good candidates for nonlinear devices, due to their high transparency, durability, high threshold to damage and ability to be fabricated into optical fibres and waveguides; a waveguide structure is essential to achieve high power densities with low operation powers. The nonlinearity of glasses arises from the third order susceptibility, i.e. it has very fast response (sub-*ps*), but also the penalty of being orders of magnitude smaller than in semiconductors. For instance, silica glass has very low absorption in the near-IR, but the nonlinear refractive index is also very small ($n_2 = 2\text{-}3 \cdot 10^{-20}\ m^2W^{-1}$). Consequently, extremely high optical powers are necessary for short AOS devices (125) or, alternatively, very long lengths are required in order to keep the operation power sufficiently low (126). Long device lengths are only acceptable for applications that can tolerate long delays and are also undesirable due to birefringence and dispersion effects.

A possible solution to this problem is to use glasses with higher nonlinearity (127). For instance, heavy metal oxide glasses, such as lead oxide and tellurite glasses, have nonlinear refractive indexes n_2 up to 50 times greater than silica (see table 2.6). More

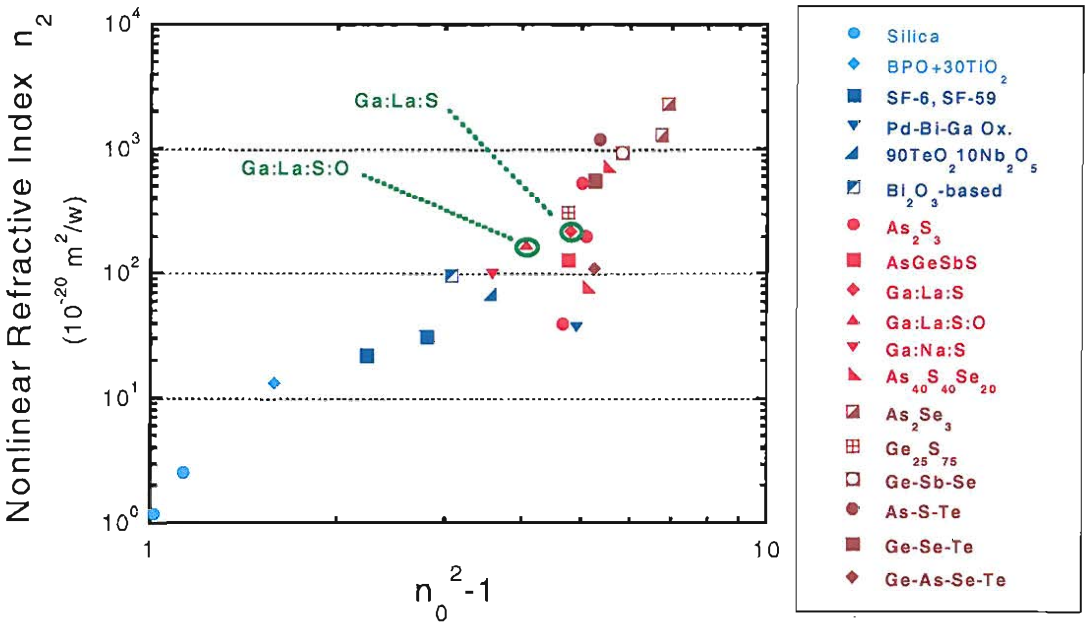

FIGURE 2.12: Correlation between linear and nonlinear optical properties (at 1.5 μm) for various glass systems.

generally, it was observed (128) that a correlation exists in optical glasses between a high linear refractive index and a high third-order nonlinearity at near-IR wavelengths. Several empirical relationships have been proposed in order to predict the dependence between the linear and nonlinear properties (129; 128); the following power dependence (130):

$$n_2 \propto (n_0^2 + 2)^3 (n_0^2 - 1) \tag{2.27}$$

was found to describe the dependence for several families of oxides and chalcogenide glasses. The correlation between n_0 and n_2 (at 1.5 μm) is clearly shown in figure 2.12 for several glass systems. Chalcogenide glasses have very high refractive index ($n_0 \geq 2.3$) and the highest nonlinearity among optical glasses; it can also be seen from figure 2.12 that the n_2 of chalcogenides is in general higher than oxides with approximately the same n_0. This is believed to be a consequence of the large polarizability of the chalcogen ions (131). Among the chalcogenide glasses, the nonlinearity generally increases with increasing atomic number of the chalcogen (fig. 2.12); thus, the n_2 of some selenide and telluride glasses is $\approx$ 1000 times larger than silica (132). This, however, does not automatically mean that selenides and tellurides are the best nonlinear glasses, as nonlinear absorption increases too with the Z of the chalcogen.

In comparing nonlinear materials for all-optical switching, as seen from eqn. 2.25, it is necessary to take into account both n_2 and the material's absorption. Even neglecting the linear absorption, two-photon absorption can still significantly reduce the device

efficiency. It is therefore convenient to refer to the following nonlinear figure of merit:

$$FOM = \frac{n_2}{\beta_2 \lambda} \tag{2.28}$$

where λ is the wavelength of operation and n_2 and β_2 are measured at λ. The design of an efficient AOS requires the above FOM to be large; more specifically, the following criterion should be verified (133):

$$FOM \geq c_{sw} \tag{2.29}$$

where c_{sw} is a numerical constant of the order of unity, and the value of which is determined by the specific design of the switch (e.g. $c_{sw} = 2$ for a nonlinear coupled waveguide switch, $c_{sw} = 0.1$ for a nonlinear Fabry-Perot filter and $c_{sw} = 5$ for a nonlinear Mach-Zenhder interferometer (134)). In semiconductors, the wavelength dispersion of n_2 and β_2 is characterised by a resonant enhancement at frequencies close to half the bandgap. Hence, both quantities increase for $\lambda \approx \lambda_{gap}/2$, but, since β_2 increases more rapidly than n_2, the FOM (2.28) decreases. As $\lambda_{gap} \approx$ 0.7-0.8 μm in most Se- and Te-based chalcogenides, their FOM at $\lambda = 1.5$ μm is low (see table 2.6) and sulphide glasses are in general better candidates for nonlinear applications.

2.3.2 Feasibility of GLS-based glasses for AOS devices

The nonlinear optical properties of optical glasses in the 1.5 μm region have been reported by Canioni, et al. (135), Cerqua-Richardon, et al. (139), Requejo et al. (54), Jha et al. (3), Harboldt et al. (140; 141) and Quemard, et al. (131); the values of n_o, n_2, β_2 and the FOMs (2.28), taken from these references, are presented in table 2.6. It must be noted that large variations exist in the nonlinear properties reported by different authors for certain material (e.g. As_2S_3); these variations can probably be attributed to differences in the glass composition and preparation, and perhaps also on the different precision/accuracy of the techniques used to measure n_2 and β_2. While the nonlinear refractive index increases passing from oxides to sulphides, selenides and tellurides, the maximum values of the FOM are found in sulphide glasses and selenides of the group As-S-Se and Ge-As-Se. Both Ga:La:S and Ga:La:S:O have a large nonlinear index ($n_2/n_2^{silica} \approx 100$) and very low two-photon absorption at 1.5 μm (54), leading to a high FOM; in particular, the condition 2.29 is verified, making them suitable for all-optical switches.

Asobe and co-workers reported the fabrication and characterisation of all-optical switches from As:S fibres; these studies are summarised in reference (23), and offer a good insight into the device requirements and the main issues related to AOSs in sulphide

TABLE 2.6: Linear and nonlinear refractive index and nonlinear absorption coefficients of optical glasses measured at 1.5 μm.

Glass	n	n_2 $[10^{-20}m^2W^{-1}]$	β_2 $[10^{-12}mW^{-1}]$	FOM	Reference
Silica (Herasil)	1.42	1.2	–	–	(135)
Silica (Suprasil)	1.46	2.5	–	–	(135)
Borophosphate-30TiO_2	1.61	13.3	–	–	(135)
SF-6 (40PbO-60SiO_2)	1.80	22	–	–	(135)
SF-59 (55PbO-45SiO_2)	1.95	32	–	–	(136)
Pb-Bi-Ga oxide	2.43	37.9(†)	–	–	(53)
TeO_2-based	2.05	38	–	–	(137)
90TeO_2-10Nb_2O_5	2.14	69.3	–	–	(135)
Tl-Bi-Ga oxide	2.47	58.1(†)	–	–	(53)
65TeO_2-35Tl_2O	2.09	89.0	–	–	(135)
Bi_2O_3-B_2O_3-SiO_2	2.02	96.5	–	–	(138)
As_2S_3	2.4	$2 \cdot 10^2$	$6 \cdot 10^{-3}$	200	(23)
	2.38	$0.4 \cdot 10^2$	0.3	1	(139)
	2.45	$5.4 \cdot 10^2$	< 0.3	> 12	(140)
As_2S_3-GeS_2-Sb_2S_3	2.4	$1.8 \cdot 10^2$	–	–	(137)
$Ge_{15.4}As_{30.8}S_{54.8}$	–	$3.2 \cdot 10^2$	< 0.1	> 21	(141)
Ga:Na:S	2.14	$1.0 \cdot 10^2$	< 0.1	> 7	(54)
Ga:La:S:O	2.25	$1.8 \cdot 10^2$	< 0.1	> 12	(54)
Ga:La:S	2.41	$2.2 \cdot 10^2$	< 0.1	> 14	(54)
$As_{40}S_{40}Se_{20}$	2.47	$0.8 \cdot 10^2$	< 0.1	> 5	(139)
	2.55	$7.4 \cdot 10^2$	0.6	8	(140)
$As_{24}S_{38}Se_{38}$	2.32	$1.75 \cdot 10^2$	< 0.5	> 2	(139)
$Ge_{25}Se_{75}$	2.4	$3.1 \cdot 10^2$	1.0	2	(142)
As_2Se_3	2.78	$1.3 \cdot 10^3$	4.3	2	(142)
	–	$1 \cdot 10^3$(*)	0.1	64	(131)
	2.81	$2.3 \cdot 10^3$	1.4	11	(140)
$Ge_{20}As_{40}Se_{40}$	–	$0.85 \cdot 10^3$(*)	0.1	59	(131)
$Ge_{11}As_{22}Se_{75}$	–	$1.3 \cdot 10^3$	0.3	28	(141)
$Ge_{28}Sb_{12}Se_{60}$	2.61	$9.4 \cdot 10^2$	2.1	3	(142)
$As_{25}S_{55}Te_{20}$	2.52	$1.2 \cdot 10^3$	1.5	5	(140)
$Ge_{25}Se_{65}Te_{10}$	2.5	$5.7 \cdot 10^2$	3.7	1	(142)
$Ge_{30}As_{11}Se_{49}Te_{10}$	2.5	$1.1 \cdot 10^2$	1.6	0.5	(139)

(†) measured at 1.25 μm

(*) measured at 1.43 μm

fibres. Firstly, he found that the background attenuation at 1.5 μm is a considerable drawback; in order to keep the switching (peak) power below 1 W in a device length of a few meters (2-4 m), the attenuation had to be reduced to below 0.5 dBm^{-1} in a fibre with $\approx$ 2.5 μm core diameter. Further loss reduction was considered difficult due to the scattering loss of fibres and the intrinsic limitation of the weak absorption tail (WAT). The second problem investigated by Asobe was the very high group velocity dispersion (GVD) of the sulphide fibre at telecom wavelengths. The GVD causes the spectral broadening and walk-off effect of pump and signal pulses, which limits the interaction length. Dispersion compensation requires either the modification of the fibre structure, as is done for silica fibres, or the inscription of gratings in the sulphide fibre, which was also reported by Asobe (23). Finally, the high intensity required to operate the sulphide AOS could induce degradation of the fibre, either as permanent damage or in the form of photorefractive effects; the possibility of photodarkening (PD) was mentioned, i.e. a red-shift of the material's bandgap producing an increase of the near-IR absorption loss. PD can arise in As_2S_3 glass as a consequence of two-photon absorption (143) and was also observed in *As-S-Se* glass (140).

Since GLS and *As-S* glasses have very similar nonlinear properties (see table 2.6), the analysis made by Asobe provides useful information. It is clear that a first requirement for nonlinear applications of GLS glass is the possibility to fabricate low-loss single-mode fibres. As the loss in the best unclad GLS fibres ($\approx 1-2\ dBm^{-1}$) is higher than the target value established by Asobe for single mode fibres, a considerable improvement of GLS fabrication is necessary. Glass stabilisation through high-oxide addition (section 2.2.5) could be viable, as it does not affect the nonlinear properties of GLS (as opposed to the fluorescent properties): as seen in table 2.6, the *Ga:La:S* and *Ga:La:S:O* have similar n_2 and FOM. Besides the fabrication, it is also important to look at the intrinsic properties and to establish the loss mechanisms in GLS and GLSO, in order to ensure that the transparency limit is compatible with the target loss of $\approx$ 0.5 dBm^{-1}.

Another important point concerns the damage thresholds and the occurrence of photorefractive effects. Both these issues have not been investigated in detail in GLS glasses, hence little is known about the behavior of these materials under irradiation with high-intensity optical pulses. Generally speaking, one can observe that GLS based glasses have higher softening points as compared to most other chalcogenides; however, this might not relate directly to a high damage threshold, since damage can arise from defects and inclusions in the glass. In conclusion, the stability of GLS glasses under high intensity irradiation at near-IR wavelengths is of great practical relevance and should be investigated.

TABLE 2.7: Nonlinearity factor γ_{NL}.

Fibre	γ_{NL} $[W^{-1}m^{-1}]$	Loss $[dBkm^{-1}]$	Reference
Silica DSF	2.7	$0.15 \cdot 10^{-3}$	(144)
High-GeO_2 Silica	20	–	(145)
Silica HF	60	–	(146)
Bi_2O_3-based	64	< 0.8	(144)
SF-57 HF	550	3	(147)
As-S	600	3	(148)

2.3.3 Microstructured fibres for nonlinear applications

The microstructured 'holey' fibres (HFs) are a recent development in optical fibre technology (56). In these structures light modes are confined in the core and guided due to an effective index difference between the solid core and an holey cladding. Holey fibres are important for nonlinear applications as they enable a different approach to obtaining high nonlinearity. In fact, the nonlinearity of an optical fibre is commonly described through the γ_{NL} parameter:

$$\gamma_{NL}\ [W^{-1}km^{-1}] = \frac{2\pi n_2}{\lambda A^{eff}} \tag{2.30}$$

where A^{eff} is the effective mode area of the fibre. In holey fibres mode areas as small as a few μm^2 can be achieved, hence the effective nonlinearity is increased due to the tight confinement.

The values of γ_{NL} for different types of fibres are shown in table 2.7; all-silica holey fibres can achieve over 20 times larger nonlinearity than conventional silica fibres, while lead-oxide HFs have the same nonlinearity as the *As:S* fibres studied by Asobe, et al. (148). Recently, the first chalcogenide holey fibre (*Ga:La:S:O*) was reported (55); while much improvement is still needed in the fabrication, the feasibility of microstructured chalcogenide fibres opens up the possibility of very short device lengths ($\approx cm$). A holey structure might also have an advantage over a traditional fibre structure as far as fabrication is concerned. In the latter light guiding is a consequence of the index difference between core and clad glass; thus, a suitable pair of slightly different compositions is required, and this may lead to a difficult trade-off between optical properties on one hand, and thermal stability and expansion coefficient on the other. In contrast, in a holey fibre the same material can be used for both the core and the clad, as it is the size and the position of the holes which causes the index difference. Holey fibre preforms can be obtained by extrusion or stacking, which might prove advantageous in the case of glasses with limited thermal stability, such as GLS-based glasses. Another important

aspect is that dispersion properties of holey fibres are also strongly dependent on the size and arrangement of the holes, which means that the material dispersion can be engineered by modifying the fibre structure, and this might prove crucial in addressing the problem of the large dispersion of sulphide glass at telecom wavelengths.

2.3.4 Sulphide fibres for Raman amplification

Highly nonlinear fibres are also attractive for Raman amplification and the application of sulphide fibres will be briefly discussed here. It was stated in subsection 2.2.6.3 that one main limitation of silica-based Raman amplifiers is the small gain, which leads to both high operation powers and long device lengths. The Raman gain G_R can be expressed as:

$$G_R \propto e^{g \cdot I \cdot L} \tag{2.31}$$

where g is the Raman gain coefficient, I is the pump intensity and L is the length of the amplifier. As the gain coefficient g is proportional to the nonlinear refractive index n_2 (23), much higher Raman gain G_R can be obtained by using glasses with higher nonlinearity, giving the possibility for shorter devices and/or lower pump powers. For instance, the gain coefficient g measured by Asobe (23) in As:S is ≈ 200 times that of silica. To the best of our knowledge, however, no device prototype has been presented to date. Concerning the use of sulphide and, specifically, of GLS glasses for Raman amplification, the comments made in section 2.3.2 are still valid, i.e. loss reduction, transparency limit and response to high pump powers of GLS are the main issues.

2.4 Conclusions

In this chapter the application of GLS-based glasses for the 1.3 μm praseodymium amplifier and for nonlinear devices was discussed. The 1.3 μm amplifier has been actively sought to enable the WDM operation in the window of low chromatic dispersion of standard telecom fibres (O band). None of the devices realised to date has proved as successful as the EDFA for the C band. The pros and cons of RE-doped fibre amplifiers, semiconductor optical amplifiers and Raman amplifiers have been discussed. RE-doped amplifiers still offer the most elegant solution for telecom applications, but the practicable schemes require a low phonon energy host such as fluoride or sulphide glass. This poses the problem of developing new fabrication technologies, similarly to what was done in the '70s for silica, and also the problem of matching the new devices to the existing technology, almost entirely based on silica fibres. The fabrication of fluorozirconate fibres is well developed, but the success of the fluoride PDFA has been limited

due to the intrinsic low efficiency. Sulphide glass has potential for more efficient devices, however fabrication is less mature than in fluoride glass. Gallium sulphide-based glasses are particularly suitable as hosts, but have limited thermal stability. Among these, GLS glasses have high RE solubility, a high glass transition temperature and good durability; however, the crucial question is whether these glasses can be fabricated into low-loss, single mode fibres. To date, this has not been achieved in GLS. The unavailability of suitable fibres has also impeded a proof of the actual effectiveness of the amplification schemes. However, encouraging results have been obtained in recent years for a closely related glass system, i.e. $Ga{:}Na{:}S$ glass, where the first demonstration of a sulphide PDFA has been achieved.

Sulphide glasses, such as GLS, also have potential for all-optical switching due to their high nonlinear refractive index. Although optical switches have been obtained from conventional fibres, these devices are very inefficient due to the small nonlinearity of silica. Heavy metal oxide and chalcogenide glasses have nonlinear refractive indexes 10 to 10^3 times larger than silica. GLS and GLSO have a large nonlinear figure of merit (FOM), that is, a large n_2 and a small β_2, at 1.5 μm, hence they are both suitable for AOSs in the main telecom window.

Although GLS based glasses show promise for these crucial photonic applications, the demonstration of practical devices has been hindered by difficulties in the fabrication and, ultimately, by the unavailability of single mode fibres with low attenuation. The target for practical devices is $\leq 0.5\ dB \cdot m^{-1}$ attenuation in a fibre with core radius 1-2 μm, although previous results in similar glass systems show that losses up to $1\ dB \cdot m^{-1}$ are tolerable for the demonstration of device prototypes. Since such values of attenuation can currently be achieved only in unclad fibres of GLS and GLSO, it is necessary to identify further improvements of the fibre fabrication process to achieve the goal. In addition, since the limited thermal stability of GLS and GLSO is likely to introduce a certain amount of loss in any case, it is also important to investigate the transparency limit of these materials, especially in the near-IR. This requires the study of the presence of the weak absorption tail and quantification of its magnitude. Finally, a very important aspect specified in this chapter is the behavior of GLS based glass under intense irradiation at IR wavelengths. Very little is known about the thresholds for permanent damage and for photorefractive effects of GLS and GLSO, and these properties should be investigated for their practical relevance. Results from other glass systems suggest that a trade-off between fibre attenuation, device length and operational power must be sought to avoid photorefractive effects. The following chapters will investigate the fabrication, intrinsic transparency and the occurrence of photoinduced effects in $Ga{:}La{:}S$ and $Ga{:}La{:}S{:}O$ glasses.

Chapter 3

Fabrication and Characterisation of GLS and GLSO Fibres

3.1 Introduction

The fabrication of optical fibres based on novel compound glasses involves several steps and is in general more complicated than the fabrication of silica fibres. In fact, chemical vapour deposition methods are poorly adapted to compound glass because of the large differences in the vapour pressures of the various glass components. Therefore, compound glasses, such as GLS, are prepared by powder melting and melt-quenching; four, strongly interdependent steps are required in order to obtain an optical fibre:

- The identification of a suitable glass composition with the required optical properties, low intrinsic attenuation and high thermal stability.
- The preparation of high purity glass, which generally involves synthesis and/or purification of the glass components.
- The fabrication of fibre preforms from pieces of bulk glass; this involves the selection of a suitable pair of compositions for the core and the clad glass.
- The drawing of the preform into an optical fibre.

Appropriate technological solutions for these steps were the basis for the development of the fabrication technologies of fluoride fibre. A transfer of technology from ZBLAN fluoride fabrication to GLS fibre fabrication is only possible to a limited extent, as the two materials are markedly different. Novel solutions are therefore required and a lot of effort had been devoted to that prior to this work.

A very exhaustive analysis of the fabrication issues was presented in a previous thesis (51). In his work, Brady addressed the fabrication of high purity glass and presented

an improved method for the preparation of gallium and lanthanum sulphides with low impurity content. The thermal stability as a function of the glass composition was also studied, although a detailed study of the crystallisation process was not achieved. Finally, the fabrication of fibre preforms was also described and extrusion was identified as a very effective technique. This chapter builds on the results of the previous work by Brady and investigates areas of further improvement.

3.2 Gallium lanthanum sulphide and oxy-sulphide glasses.

3.2.1 Glass formation and basic properties

Sulphide glasses are broadly classified into *As*-based, *Ge*-based and *Ga*-based glasses, with GLS obviously belonging to the latter group. In GLS glass, gallium sulphide is the main component and the glass former, i.e. the base units of the glass network are composed of *Ga* and *S* atoms. Gallium sulphide is a conditional glass former, i.e. it cannot form glass by itself, but it is a glass former when a suitable modifier is added to it. GLS glasses were discovered by Loireau-Lozac'h et al. (24), who reported a wide glass forming region in the binary system $Ga_2S_3 - La_2S_3$. Defining n as the *Ga* cationic fraction ($n = [Ga]/([Ga] + [La])$), the region ranged from $n = 0.50$ to $n = 0.85$, when the melt was quenched from 1200 $^\circ C$, and from $n = 0.50$ to $n = 0.75$ when the melt was quenched from 1100 $^\circ C$ at a critical cooling rate of ≈ 5 $^\circ C$. The same group also found that glasses could be formed between gallium sulphide and lanthanum oxide, and identified a ternary system, Ga_2S_3-La_2S_3-La_2O_3, with improved glass formation ability and thermal stability upon reheating (25).

The role of the oxide impurity was however not fully recognised by these early studies. In fact, the La_2S_3 component was obtained from La_2O_3 through a high-temperature sulphurisation process; as it became clear later, this process led to small quantities of oxide being unintentionally added to the glass. Following the progress in the synthesis of glass precursors, it was shown unequivocally (92; 48) that a small amount of La_2O_3, in the region of a few molar percent, must be added in order to obtain a crystal free glass (see figure 3.1). Therefore, while the Ga_2S_3-La_2O_3 (GLSO) is a proper binary glass-forming system, the 'low oxide' GLS belongs to the ternary system Ga_2S_3-La_2S_3-La_2O_3. A further improvement was achieved by Brady (51), who identified the role of two different gallium sulphide phases (i.e., Ga_2S_3 and GaS) in the glass formation and stability.

The microstructure of GLS-based glasses has been studied by Raman and IR absorption spectroscopy (30), and by EXAFS (extended X-ray absorption fine structure) (31), which allowed the formulation of a model for the short-range arrangement of the atomic species.

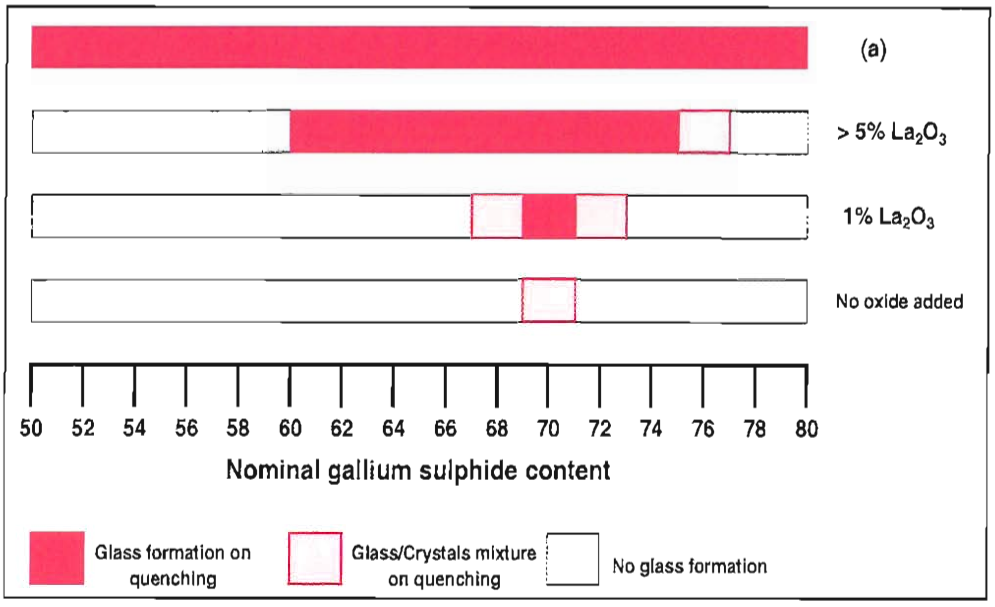

FIGURE 3.1: Regions of glass formation for the 'pure sulphide' GLS; (a) shows the region of glass formation described by ref. (24) (after (92)).

In 'low oxide' GLS glass, gallium atoms are always fourfold coordinated, with average bond lengths very close to those in the crystalline Ga_2S_3 compound. GaS_4 tetrahedra are the glass forming units and the glass network is constituted by GaS_4 tetrahedra linked to each other at the corners. These glass forming units result from the reaction of the Ga_2S_3 phase with extra sulphide ions brought in by the addition of the La_2S_3. Inter-unit interstices in the network provide the sites for the lanthanum cations; these form ionic *La-S* bonds (as opposed to the covalent *Ga-S* bonds) and have a large average coordination number ($\approx$ 8). In this model, the role for the La_2S_3 is then to provide the sulphur atoms necessary in order to complete the glass forming units and to provide charge equilibration. Such a picture is unusual among the chalcogenide glasses, and rather resembles the structure of alkali silicate glasses (31).

The role of lanthanum oxide in GLS and GLSO glasses has not been studied in great detail. Due to the chemical similarity with sulphur, it can be assumed that oxygen substitutes one (or possibly more) sulphur atoms in the glass forming units. The *Ga* surrounding was studied by EXAFS in GLS and GLSO glass (149); it was found that, with increasing La_2O_3 content, oxygen progressively enters in the glass forming units and modifies their shape into distorted octahedra. In this picture, the La_2O_3 acts as a proper network modifier.

Oxide addition has a beneficial effect on the glass formation and stability; however, as discussed in the previous chapter (section 2.2.5), it also has a strong impact on the optical properties of GLS. Oxide bonds increase the maximum phonon energy and decrease the fluorescence quantum efficiency of rare earth ions. Hence, alternative glass modifiers have been sought, which could stabilise the 'low oxide' GLS composition without affecting

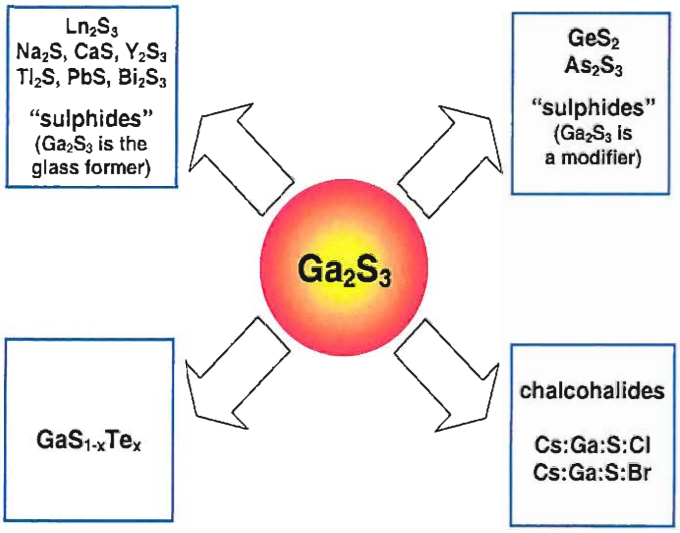

FIGURE 3.2: Classification of the glass forming systems based on Ga_2S_3.

the spectroscopic properties.

3.2.2 Compositional modifications of GLS glasses

Analysis of the other glass forming systems based on gallium sulphide provides a first insight into some compositional modifications of GLS glass. The compounds that are able to form glass with gallium sulphide can be classified into four main groups (see figure 3.2) (26). The first group comprises the rare-earth sulphides, some metal sulphides (CaS, Na_2S, Y_2S_3, AgS_2) and heavy metal sulphides (Tl_2S, SnS_2, PbS, Sb_2S_3, Bi_2S_3). In these glass systems, the Ga_2S_3 is the glass former and a small, but critical, amount of oxide must be added in order to allow glass formation (48; 103). To the second group of compounds belong the semimetal sulphides GeS_2 and As_2S_3. In these systems, the Ga_2S_3 acts as a network modifier, as both GeS_2 and As_2S_3 are themselves glass formers; the properties of Ge:Ga:S (40; 80) and As:Ga:S (150) have been extensively investigated. The third group is composed of $GaS_{1-x}Te_x$, where both the sulphide and and the telluride anions form the glass network. Finally, glass can also be formed by Ga_2S_3-halide systems (such as $CsCl$ and $CsBr$) (70).

The two possible approaches to the compositional modification of GLS glass are shown in figure 3.3. The first option is to replace part of the Ga_2S_3 with a new glass former. Due to their chemical affinity, both Al_2S_3 and In_2S_3 can substitute the Ga_2S_3. Al_2S_3 is an excellent glass former with La_2S_3; however, the Al_2S_3 is a very hygroscopic compound, and this instability is inherited by the glass (151). In:Ga:La:S glasses have been studied in ref. (152); while the addition of In_2S_3 improves the thermal properties of the glass, it also decreases the transmission of the glass in the region 0.7-1 μm where most of the pump wavelengths lie. The same drawback was observed to occur when Ga_2Se_3 was replaced for Ga_2S_3. Ge:Ga:La:S glasses have also been investigated; these glasses have

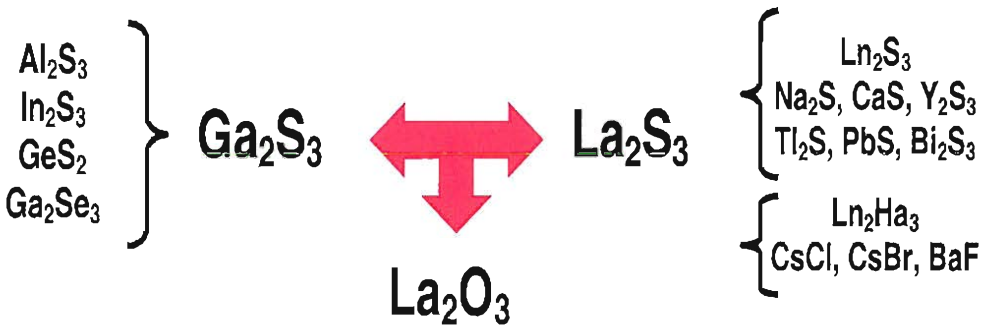

FIGURE 3.3: Ga:La:S:(O) glasses and main compositional modifications.

even higher rare-earth solubility than GLS, but there is no evidence of an improvement of their thermal properties and in fact the fabrication of optical fibres has not been reported (153). Summarising, the compositional modification of GLS through a partial replacement of the gallium sulphide does not achieve an overall improvement of the glass properties for practical applications.

An alternative approach, and potentially with a wider variety of options, is to add a glass modifier (see fig. 3.3). Sulphide modifiers have been identified above (fig. 3.2); the addition of these compounds and its effect on the thermal and optical properties was extensively investigated as a part of two previous ORC research projects on GLS glass (154; 155). A recent study (156) clarified that sulphide additives do not improve the glass stability; a critical amount of oxide is always necessary for glass formation. It was also found that the effect of sulphide addition can be easily overshadowed by their underlying content of oxide impurity, which, in contrast, has a significant impact on the glass formation and stability even at low (0.5-2 $mol\%$) concentration.

The addition of halides has a strong effect on the optical properties of GLS glass; both lanthanum halides (152) and alkali halides (91; 156) were studied as possible modifiers. It was found that halide addition improves the visible transmission of the glass, by progressively shifting the fundamental electronic edge to shorter wavelengths; furthermore, halide-modified GLS retains the low phonon energy and high rare-earth solubility required for RE doped devices. Wang et al. (91) reported an improvement of the fibre drawing properties in GLS doped with 20-30 $mol\%$ $CsCl$, i.e. an increase of the separation between the glass transition and crystallisation temperatures (an indication of the glass stability), and a reduction of the viscosity (which allowed fibre drawing to be performed at lower temperatures than in GLS). Also for this case, however, it was recently clarified (156) that the maximum amount of halide that can be introduced in the glass depends on the oxide concentration. Hence, halide additives per se do not improve the glass stability of GLS, although they can be used to modify its viscosity and refractive index. It must however be remarked that halide addition may raise an issue of durability of glass; indeed, Cs:GLS has poor resistance to moisture attack (157).

Among the lanthanum halides, LaF_3 is less hygroscopic, but it causes a deterioration, rather than an improvement, of the thermal stability of GLS at concentrations 0-10 % (158; 152). The effect of LaF_3 at higher concentrations and of LaF_3-La_2O_3 modification of GLS glass is currently being investigated as a part of another ORC project.

In conclusion, a variety of modifications of GLS glass have been investigated in the past. The aim was to improve the fibre drawing properties and the thermal stability, without however compromising the low phonon energy and hence the fluorescence quantum efficiency of rare earth ions. It showed that no single additive can replace the role of the oxide in the glass formation and stability. A critical amount of oxide is essential for glass formation of GLS and all the sulphide and halide-modified compositions. If sufficient oxide is present, sulphides and halides can be readily incorporated in the glass and can be used to modify its viscosity, refractive index or visible transparency. For applications such as the Pr^{3+}-doped fibre amplifier, it is necessary to find a compromise in the oxide concentration, taking both into account the effects on the glass stability and the effect on the fluorescent properties.

3.3 Synthesis and Purification of Glass Precursors

3.3.1 The conversion of sulphides

GLS-based glasses are prepared by melting batches of the constituent compounds. This is the standard method of preparation of multicomponent glasses, for which chemical vapour deposition (CVD) methods cannot be generally employed. CVD methods are at present not feasible for GLS due to the lack of suitable precursors. As compared to CVD, powder-melting is far more prone to contamination. It is therefore essential to utilise raw materials of very high purity and to maintain the high purity during the glass batching and melting. Impurities can affect both the thermal stability and the optical properties, and the main sources of contamination have been identified in ref. (51). Ions of the $3d$ transition metals (Fe, Cr, Ni, Co, etc.) are well known to have strong and wide absorption bands in the visible and near-IR. Hydrogen containing impurities such the hydroxyl group OH^- and SH^- cause strong absorption in the 2.8-3.2 μm region. Phase impurities such as inclusions cause scattering, which equally reduces the materials' transparency, and can also act as nucleation centres for crystals. In short, impurity levels must be kept as low as possible. A previous study (51) has identified the minimum requirements of purity for a GLS-based glass in order to be useful for practical applications. For transition metal ions, the ideal target is 0.1 part per million weight (ppm) or less.

Unfortunately, the purity grade of commercially available gallium and lanthanum sulphides typically does not exceed 4N, i.e. 99.99 $wt\%$, and thus the impurity levels are

TABLE 3.1: Properties of glass components and raw materials from which they are synthesized.

	Density (kg/m^3)	Melting point °C	Formation Enthalpy (kJ/mole)	Best available purity
Ga_2S_3	3700	1090	516	5N
GaS	3860	965	–	4N
La_2S_3	4900	2110	1222	4N
La_2O_3	6500	2305	1916	5N
Ga	5910	29.8	276	7N
LaF_3	5900	1493	598	4N
$LaCl_3$	3640	859	–	4N
	Data taken from ref. (159)			Commercial grade

two to three orders of magnitude above the target value. In addition, these substances, where available, are very expensive, as they don't have any particular industrial application. The situation is only slightly better as far as lanthanum oxide is concerned; as La_2O_3 is used in the fabrication of high index optical glasses, it is available 'off the shelf' with a higher purity (5N or 99.999 %). In practice, commercial La_2O_3 contains up to $\approx ppm$ of transition metals, hence one order higher than the target. This represents a severe difficulty, also in consideration that neither of these chemical compounds lend themselves to any conventional purification route (51). Therefore, it was necessary to manufacture these compounds in-house, through a dedicated process. In the early ORC projects (154; 155), sulphide materials were provided by Merck Ltd.; subsequently, a novel method of synthesis was conceived and established at the ORC. This method involved both a purification pre-treatment of suitably chosen precursors, where necessary, and their conversion by a sulphurisation process, and is fully described in ref. (51). Here it will be briefly summarised, especially in relation to possible improvements that have been identified in the present work. The physical properties and impurity levels of the GLS precursors is shown in table 3.1.

3.3.2 Synthesis and purification of lanthanum sulphide and oxide

The lanthanum sulphide is obtained through the conversion of lanthanum fluoride under flowing H_2S (51). The conversion is carried out via a multistep process at high temperature ($\approx 1150\ °C$) in a purpose-built reactor, which employs a silica-lined furnace and is operated under tightly controlled atmosphere. Lanthanum fluoride is convenient as a precursor because it is commercially available in an anhydrous state, and because it can be purified by heat treatment, following the same procedure utilised for the precursors of ZBLAN glass (51; 13). The control of the impurity content will be discussed in section 3.4.3.

In addition to impurity control, it is also necessary to ensure that the synthesis process achieves 100% conversion of the LaF_3 precursor into La_2S_3. If any measurable amount of the starting material remained unconverted, it would modify the glass composition with an almost certain impact on the thermal stability of the glass. The utilisation of a flowing system, which is constantly removing the by-products of the chemical reaction and prevents them from taking an active part in it, pushes forward the equilibrium point of the reaction and favours the formation of the final products. This, in principle, should ensure that the precursor is fully converted, provided the process is allowed to run for long enough. In practice, this must be checked for every conversion run by comparing the initial mass with the final (reacted) mass. The conversion reaction of the lanthanum fluoride into lanthanum sulphide is:

$$LaF_3 \quad \xrightarrow{H_2S} \quad \frac{x}{2}\, La_2S_3 \quad + \quad (1-x)\, LaF_3$$

the percent of conversion is calculated as:

$$x \;=\; \frac{\Delta m/m_i}{\Delta M/M_{LaF_3}}$$

where m_i and m_f are the initial and final masses, $\Delta m = m_f - m_i$ is the mass imbalance, M_{LaF_3} and $M_{La_2S_3}$ are the molar weights of lanthanum fluoride and sulphide, and $\Delta M = \frac{1}{2}M_{La_2S_3} - M_{LaF_3}$. This type of analysis allows the calculation of the percent of conversion with a relative precision in the range of 0.1-1 %, depending on the initial mass. It relies on the assumption that both LaF_3 and La_2S_3 do not sublime out of the batch and that only the La_2S_3 phase is produced in the reaction (51).

As far as lanthanum oxide is concerned, its conversion proves more complicated. La_2O_3 is a very stable compound, hence the high value of the enthalpy of formation given in table 3.1. Some attempts at direct conversion by burning the La_2S_3 in an oxygen stream have led to the conclusion that very high temperatures (in excess of 1400 °C) are required in order to obtain the complete oxidation of the intermediate sulphate products. The procedure currently employed involves a high temperature treatment of commercial grade La_2O_3 under flowing oxygen; this procedure has been shown to reduce the amount of absorbed moisture, with some indication of reduction in the content of transition metals.

3.3.3 Synthesis of gallium sulphide

Synthesis of gallium sulphide is based on the direct conversion of ultra-high purity (7N), electronic grade gallium metal. This is also carried out at high temperature ($\approx 1000\ ^\circ C$) under a constant stream of H_2S. The molten gallium is contained in a vitreous carbon

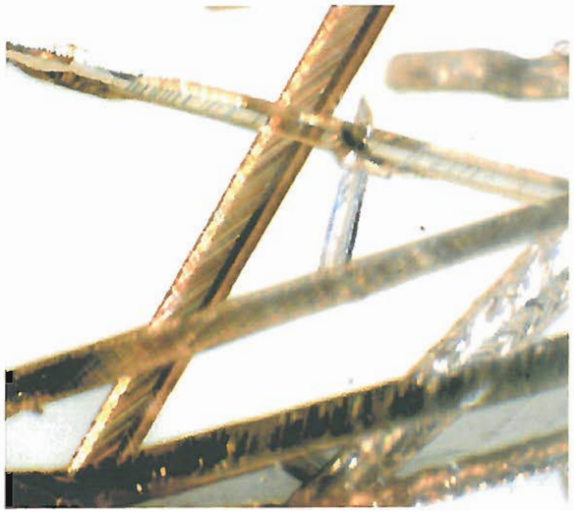

FIGURE 3.4: Ga_2S_3 crystals sublimed off during the synthesis.

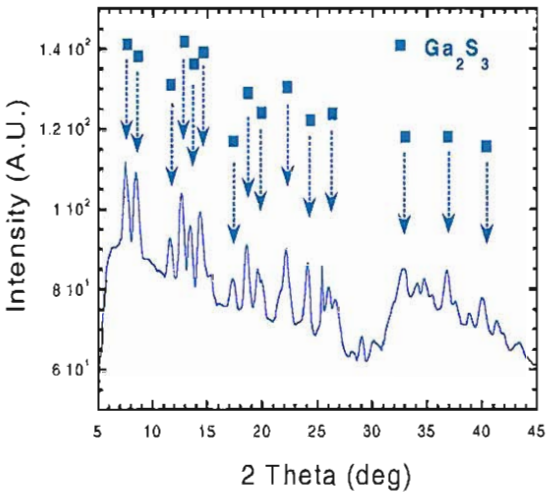

FIGURE 3.5: Single-crystal XRD pattern of the Ga_2S_3 sublimed material.

crucible. In this case, however, the conversion reaction is more complicated than in the previous case, as two gallium sulphide phases can exist at the temperature at which the reaction is carried out, i.e. the reaction is:

$$Ga \quad \xrightarrow{H_2S} \quad \frac{y}{2}\, Ga_2S_3 \quad + \quad (1-y)\, GaS$$

The molar ratio of the two phases, $[Ga_2S_3/2GaS]$, can be controlled, to some extent, by varying the the time or temperature of the conversion process (51). A good degree of control of this parameter is necessary, since the thermal properties of GLS and GLSO glass were found to depend on the $[Ga_2S_3/2GaS]$ ratio. Brady (51) proposed a simple formula to determine $[Ga_2S_3/2GaS]$ from the mass imbalance, that is:

$$\frac{m_f}{m_i} = y \cdot \frac{M_{Ga_2S_3}}{2M_{Ga}} + (1-y) \cdot \frac{M_{GaS}}{M_{Ga}}$$

where m_i is the initial mass of Ga metal and m_f is the final mass and M indicates a molar weight. This relationship, however, contains two approximations. Firstly, it is impossible to establish if the reaction has been brought to completion, i.e. whether some unreacted metallic gallium is left in the batch. Secondly, it assumes that the two gallium sulphide phases produced from the reaction both have negligible vapour pressure at the conversion temperature, so that neither of them escapes from the batch. The second hypothesis is not verified, and some material sublimes and deposits at different points on the silica liner. Part of the sublimed material had the appearance of white elongated crystals (see figure 3.4); XRD analysis revealed that these crystals where in fact Ga_2S_3 (figure 3.5). By collecting the deposits on the silica liner, it was estimated that sublimation can cause a mass loss of $\approx 5\%$ for a process carried out for 24 hrs at $\approx 1000\ ^\circ C$. Clearly, running the conversion at lower temperatures would give less sublimation, but there would be

no easy way to check if the reaction had reached completion.

A more precise characterisation of the gallium sulphide conversion is therefore necessary; we identified X-ray diffraction (XRD) as a viable method to determine the ratio $[Ga_2S_3/2GaS]$. A preliminary analysis of the converted material (see figure 3.6) confirmed that it was composed only of two phases, i.e. the monoclinic Ga_2S_3 and the hexagonal GaS. The characteristic patterns of these two phases, taken from references (160) and (161), are compared in figure 3.7. Although the two patterns have significant overlapping of the stronger peaks (as also seen in figure 3.6), an obvious difference exists in the low angle range, where diffraction peaks with adequate intensity and separation (marked by arrows in fig. 3.7) could be identified. Although XRD is not a quantitative technique, it can be calibrated by measuring a set of standard samples where the two pure phases are mixed in a known proportion (162). Unfortunately, it was not possible, during the course of this project, to get a sufficient quantity of the the Ga_2S_3 and GaS phases to allow for this type of analysis to be carried out. The price of commercially available compounds was prohibitively high, and direct, in-house synthesis was not feasible; we undertook sublimation trials from in-house converted gallium sulphide material, but these failed to produce a sufficient amount of material. Despite these difficulties, we believe that the quantification of the gallium sulphide phases is worth pursuing and XRD is well-adapted to routine characterisation of the conversion products.

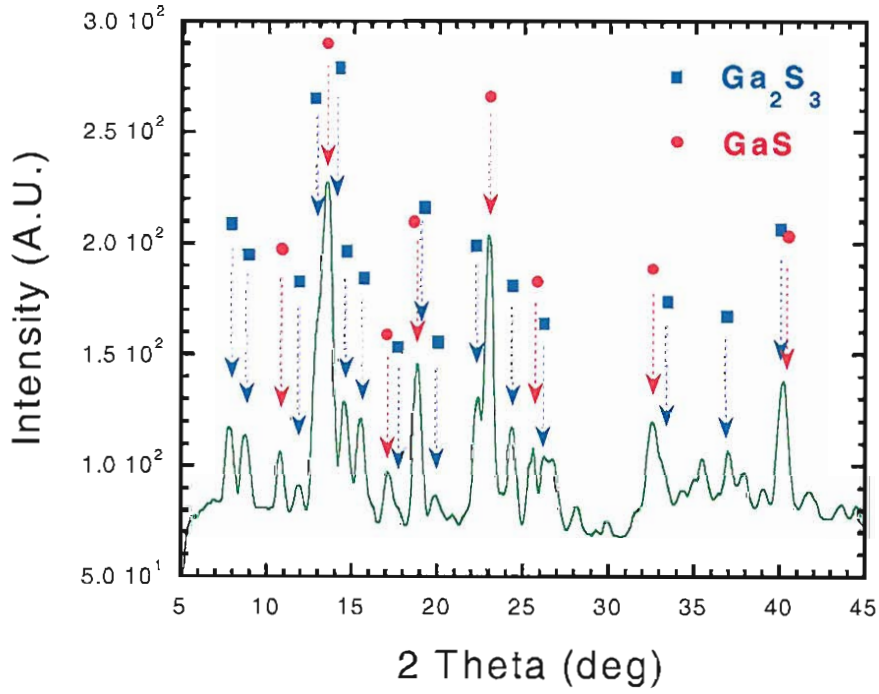

FIGURE 3.6: XRD analysis of the final product of the conversion, showing a mixture of Ga_2S_3 and GaS phases.

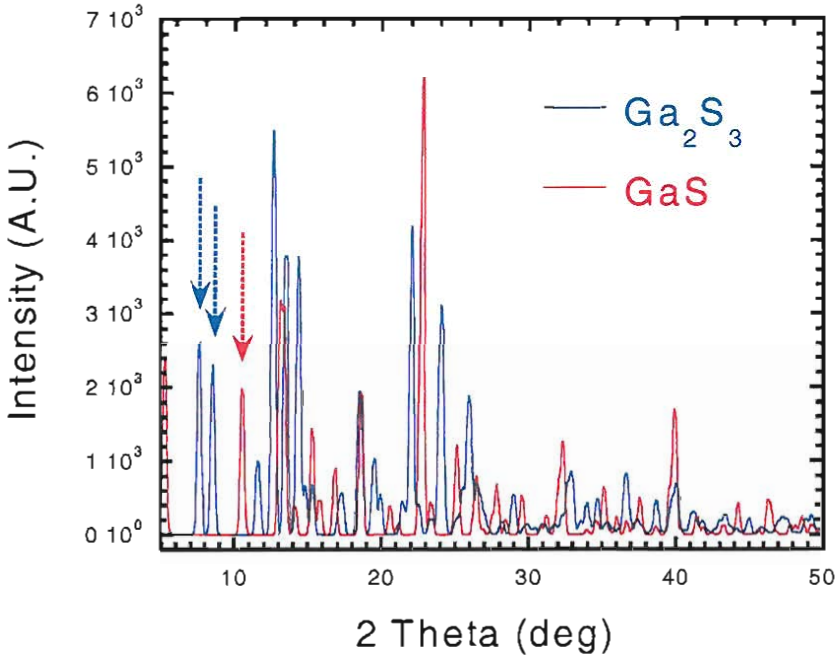

FIGURE 3.7: XRD pattern of the Ga_2S_3 and GaS phases(after (160) and (161)); the arrows point out the lines suitable for quantitative analysis.

3.4 Glass melting and basic characterisation

3.4.1 The melting technique

The preparation of GLS glass requires long melting at relatively high temperatures as compared to other chalcogenide glasses. The melting point of the components are $\approx 1000\ ^\circ C$ for the gallium sulphides and over 2000 $^\circ C$ for the La_2S_3 and La_2O_3 (see table 3.1). According to the phase diagram proposed by Guittard et al. (27), however, a melt can exist at temperatures considerably lower (850-900 $^\circ C$) in the range of composition where the glass forming region is located. Glass melting is carried out at 1150 $^\circ C$; at this temperature, the lanthanum components can be dissolved in the molten gallium sulphides. Long melting time must be allowed in order to ensure homogenisation of the melt (24).

Most chalcogenide glasses have lower melting points and can be compounded and melted at the same time from the constituent elements, using evacuated sealed silica ampoules and rocking furnaces. Sealed ampoule melting is not well adapted to the melting of GLS glass, because GLS tends to slowly react with silica (24). However, the vapour pressure of the glass components is low enough to allow the melting of GLS to be carried out in an open, controlled atmosphere. Batches of powders with the required composition are weighed in a nitrogen-purged glovebox, and then transferred in a silica-lined furnace using a sealed container. Melting must be carried out in vitreous carbon crucibles; using other 'traditional' crucible materials (boron nitride, alumina etc.) invariably ended

with the melt reacting, more or less violently, with the crucible. Vitreous carbon is mechanically very resistant and chemically inert up to over 2000 $°C$ in a non-oxidising atmosphere. The optimum melting schedule was determined by previous studies. The batches are melted at 1150 $°C$ for about 24 hrs under a constant flow of dry argon (500-1000 ml/min); the temperature is lowered to 1050 $°C$ one hour prior to the quenching, which is performed by pushing the crucible out of the furnace and into a silica water jacket. Glass ingots (see figure 3.8) can be remelted into a desired shape, after which they undergo annealing at temperature close to T_g.

In the following, glass composition will be specified (unless otherwise stated) as Ga_2S_3 $[mol\%]$:$La_2O_3[mol\%]$:$La_2S_3[mol\%]$ for the 'low oxide' GLS and as $Ga_2S_3[mol\%]$:La_2O_3 $[mol\%]$ for the GLSO.

3.4.2 Control of glass composition

In the previous subsection it was stated that the GLS components have low vapour pressure at the temperature at which glass melting is carried out. On the other hand, it is also known form the synthesis of these compounds that the gallium sulphide phases

FIGURE 3.8: As-quenched GLS (right) and GLSO (left) ingots.

TABLE 3.2: Composition of glass batches LD1035 (GLS) and LD1034 (GLSO) as measured by Rutherford backscattering spectroscopy (RBS).

Element	Composition (GLSO)		Composition (GLS)	
	nominal	measured	nominal	measured
Ga/La ratio	2.63	2.30 ± 0.04	1.86	1.71 ± 0.04
$[La]$ $at\%$	11.8	13 ± 2	14.9	16 ± 2
$[Ga]$ $at\%$	31.1	31 ± 3	27.7	27 ± 3
$[S]$ $at\%$	39.4	44 ± 4	54.2	57 ± 6
$[O]$ $at\%$	17.7	12 ± 9	3.2	0 ± 10
Glass batch	LD1034		LD1035	
Mass loss	10.2 $wt\%$		6.8 $wt\%$	

are more volatile than the La_2O_3 and La_2S_3 phases, and measurable sublimation can occur in a prolonged treatment at high temperature. In fact, a measurable mass loss is always observed during glass melting. Such mass loss depends on the melting schedule and on the size and shape of the melt (or rather of the crucible); for the 'standard' melting schedule specified in the previous subsection, the mass loss is 5-8 % in GLS and 8-11 % in GLSO. On the other hand, very little or no mass loss is observed if the glass is re-melted, which suggest that the loss happens due to the more volatile species leaving the melt before the glass is fully compounded.

It is clear that such a mass loss can have a significant impact on the glass properties. If the gallium sulphide was preferentially escaping from the melt, the actual Ga/La ratio would be lower than the nominal. The first effect of such a change would be to shift the position of the absorption edge and to modify the refractive index of the glass. Thermal and mechanical properties of the glass would be affected too (see sections 3.3 and 3.4 of ref. (51)). An high degree of control on these properties is especially necessary for defining the ideal matched pair of compositions for core/clad fibre structures. This requires a characterisation of the glass composition to identify which changes occur during the glass melting. This had never been done prior to this work.

We prepared two glass batches with nominal composition 65:2.5:32.5 (GLS) and 72.5:27.5 (GLSO) following the standard procedure and melting schedule described above. The mass loss measured for the two batches was 6.8% for the GLS and 10.2% for the GLSO. The composition of the samples was measured by Rutherford Backscattering Spectroscopy (RBS); the results are presented in figure 3.9 and in table 3.2. RBS measurements were performed by Dr. D. DeSalvador, University of Padova, using the 2 MeV accelerator facility at the 'Laboratori Nazionali di Legnaro', Italy.

RBS is a very powerful technique for compositional measurements of multicomponent samples in the range of few percent (lower detection limits, up to 0.1 $at\%$, can be achieved in particular cases). It involves the scattering of an accelerated beam of light

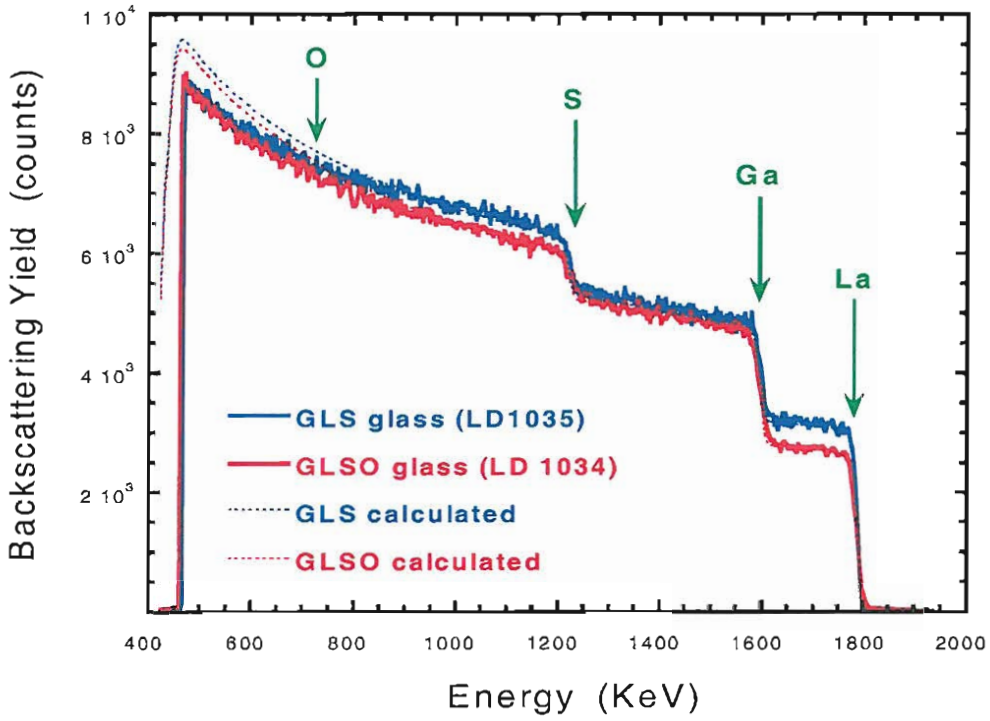

FIGURE 3.9: RBS spectra from samples LD1034 and LD1035.

ions by the nuclei of the atomic species contained in the sample, which is used as a target. In this case, a 2 MeV beam of He^+ ions was employed. The energy analysis of the fraction of ions which is backscattered at a fixed angle allows for the discrimination between different masses; the number of scattered ions, i.e. the signal intensity, is proportional, through the Rutherford scattering cross section, to the concentration of each of the atomic species. With reference to fig. 3.9, the sharp steps represent the signals from the different elements constituting the glass, while their height is related to their concentration in the samples. The sensitivity of RBS is a strongly increasing function of the atomic number of the species detected; in fact, the Rutherford scattering cross section can be expressed as:

$$\sigma_R \propto x_A \cdot Z_A^2 \tag{3.1}$$

where Z_A is the atomic number of the species A and x_A its molar concentration. This is also evident in fig. 3.9, where the signals from heavier La and Ga are much stronger than those of O and S.

Analysis of the experimental spectra was performed by a computer code which calculated the theoretical profiles based on exact formulas (these are also reported in figure 3.9). As can be seen from the reported results, RBS can determine with very good precision the concentration of the heavier elements and particularly the Ga/La atomic ratio. RBS is, on the contrary, much less suited for the quantification of the lighter elements (O

and S), whose weak signals are superimposed onto those from the heavier elements. In particular, RBS is rather inadequate for measuring the oxygen content of the GLS and GLSO samples; as a consequence, the precision of the compositions of the other elements is only about 10 %. In contrast, the Ga/La ratio can be determined more precisely ($\approx$ 2% error), and are significantly lower (8 % for GLS and 12 % for GLSO) than the nominal values for the two batches. Hence, there is clear evidence that the gallium sulphide escapes preferentially during the glass melting and, as a result, the composition is significantly affected. Lanthanum, gallium and sulphur concentrations were found to be uniform throughout the whole sample.

In addition to the the Ga/La ratio, the oxygen content has also a strong impact on glass properties. RBS should therefore be combined with another technique, in order to achieve a more complete characterisation of the composition of GLS and GLSO glasses. RBS can in some cases achieve high sensitivity for lighter elements, by exploiting resonances in the scattering cross section, due to elastic nuclear reactions; this type of technique is also known as resonant backscattering spectroscopy (rBS). Other possible techniques for measuring the oxygen concentration are LECO analysis and EDAX (energy dispersive X-ray analysis).

3.4.3 Control of impurities

Impurity control is paramount in all aspects of the fabrication of glasses for photonic applications. The available techniques for trace impurity analysis are either based on atomic absorption/emission spectroscopy or on mass spectroscopy. Techniques of both types are carried out in ultra-high vacuum chambers, where the ionised atoms are ex-

TABLE 3.3: Trace impurity analysis of raw materials, glass components and GLS glass performed by GDMS (after (51))

Element	Ga	Ga_2S_3	LaF_3	La_2S_3	La_2O_3	GLS
Na	< 0.005	0.04	0.5	0.1	2	1.4
Al	0.004	0.11	1	1	2	0.66
Si	0.002	14	2	7	12	30
Ti	< 0.001	< 0.01	0.1	0.18	0.13	0.18
V	< 0.001	< 0.05	< 0.01	< 0.01	0.04	0.05
Cr	0.001	0.3	0.05	0.1	0.05	0.07
Fe	0.001	0.08	0.07	0.1	0.87	0.08
Co	< 0.001	0.02	< 0.05	< 0.05	0.02	< 0.05
Ni	< 0.001	0.28	0.01	0.1	0.12	0.08
Cu	0.005	< 0.01	0.18	0.15	0.25	0.1
	Impurity concentrations are in *ppm* weight					

tracted out of the sample, usually either by heat thermalisation, by an electric discharge, or by an ion beam. The first group of techniques looks at the characteristic absorption/emission bands of impurity ions, while in the other case a fraction of the ions is collected and analysed by a high resolution mass spectrometer. Both techniques rely on calibrations performed on reference samples, however mass spectroscopy techniques generally offer higher sensitivity and are also more accurate.

Glow discharge mass spectroscopy (GDMS) was identified as the most suitable for the impurity analysis of both GLS glass and its precursors (51). This technique has a detection limit of 0.001-0.05 *ppm* weight, depending on the element and on the material in which it is contained, and an overall certified accuracy and precision of at least 40 %.

Table 3.3 reports some typical results of trace impurity analysis applied to the control of contamination in synthesised raw materials. The data for Ga_2S_3, LaF_3 and La_2S_3 are relative to the best achieved purification/conversion runs (51); the data for Ga and La_2O_3 are relative to the untreated, commercial material; the data for GLS are relative to the as-quenched material. The table shows that the conversion process adopted can give sulphide compounds with the required purity; on the contrary, as already pointed out, the La_2O_3, which is the commercial grade material, does not meet the specifications.

GDMS cannot determine the content of very light elements, such as oxygen, carbon, nitrogen. Trace levels analysis of these elements is also complicated because their concentration can easily be altered by storage, preparation and handling.

3.5 Thermal stability of GLS based glasses

Thermal stability is a well-known issue for GLS based glasses. The crystallisation behaviour upon reheating above the glass transition temperature and slow cooling was first investigated by Loireau Lozac'h, et al. (24). Later on, when these materials were proposed for active applications, it was also recognised that, despite their potential, their limited thermal stability was the most serious obstacle for fibre applications (163; 38). The numerous attempts to stabilise the glass through compositional modification, as seen in subsection 3.2.2, have failed to identify any viable solution, with lanthanum oxide the only exception. Therefore, several fundamental studies were carried out in order to determine which glass composition within the Ga_2S_3-La_2O_3-La_2S_3 system could afford the best chance for making optical fibres.

A basic characterisation of the thermal properties of GLS can be obtained by differential thermal analysis (DTA). DTA detects variations in the specific heat as a small sample of glass is heated up at a constant temperature rate (non-isothermal DTA); this is done by measuring the temperature difference with a reference sample. The glass transition appears as a step in the DTA curve (it corresponds to a 'second order transition'),

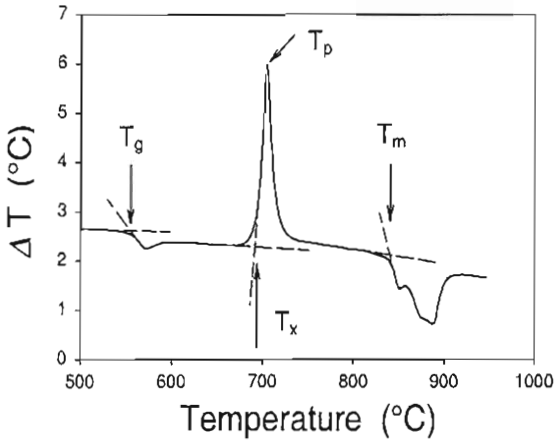

FIGURE 3.10: Typical DTA profile of GLS glass.

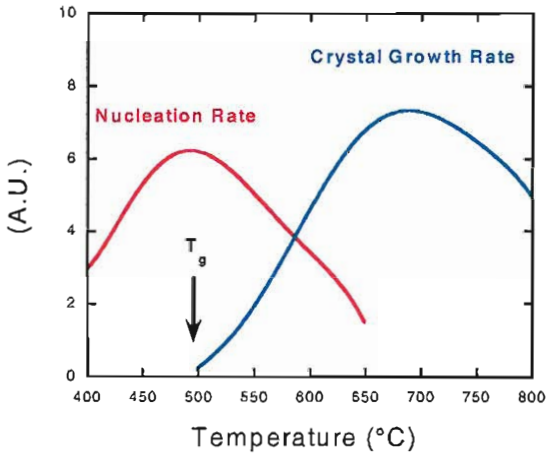

FIGURE 3.11: Temperature dependence of the nucleation and crystal growth rates.

the crystallisation appears as an exothermic peak ($\Delta T > 0$), and the melting as an endothermic peak ($\Delta T < 0$) (see figure 3.10). DTA measures the glass transition temperature, T_g, the onset of crystallisation, T_x, the peak temperature of the crystallisation, T_p, and the onset of melting, T_m; all these parameters depend on the heating rate. DTA measurements are usually complemented by measurements of the viscosity-temperature characteristic curve for the glass, for instance by parallel plate rheometry (164). The glass viscosity, v, decreases exponentially with increasing temperature, according to Fulcher's law:

$$v(T) = v_0 \ \exp\left(\frac{b}{T - T_0}\right) \tag{3.2}$$

where v_0, b and T_0 are constants. Especially for glasses which are prone to devitrification, fibre drawing should ideally be carried out at the highest practical viscosity, in order to reduce the chance of crystallisation; the maximum viscosity for drawing from a preform is approximately $10^{6.5}$-10^7 $Pa \cdot s$ ($10^{5.5}$-10^6 *poise*) (165); the corresponding temperature is indicated as T_η. Based on DTA and viscosity measurements, several criteria are commonly used to gauge the glass stability. For instance, $T_x - T_g$ is widely used to study trends in the glass stability for different glass compositions (see table 3.4); other quantities used include $T_p - T_g$, $T_x - T_\eta$ and the so-called Hruby factor, $(T_x - T_g)/(T_m - T_x)$. While all these are useful to provide qualitative information, they are not quantitatively reliable (166).

For drawing fibre from an unstable glass, the crucial information is to know for how long it can be heated at the temperature T_η before crystallisation occurs, or, in other words, the crystallisation rate at T_η. Crystallisation is a two-step process involving nucleation and successive growth of crystals. Nucleation and crystal growth have different, temperature dependent kinetics (see figure 3.11), and their product determines the

TABLE 3.4: Thermal Properties of GLS and GLSO compared to ZBLAN glass.

	T_g [$°C$]	T_η [$°C$]	$T_x - T_g$ [$°C$]	$T_x - T_\eta$ [$°C$]	$T_p - T_x$ [$°C$]	Reference
GLS (65:3:32)	559	637	136	58	20	(51)
GLSO (72.5:27.5)	567	679	192	80	62	(51)
ZBLAN	265	308	93	50	18	(13)

crystallisation rate. The nucleation rate generally has a maximum (the 'nucleation temperature') close to T_g, while the crystal growth rate peaks at higher temperature ($\approx T_p$). The separation between the two peaks indicates how stable a glass is: the bigger the separation, the more stable the glass; vice-versa, a large overlap of nucleation and crystallisation means that the nuclei formed above T_g can readily grow into crystals, i.e., low thermal stability. Nucleation and crystal growth rates can be determined by combining isothermal and non-isothermal differential scanning calorimetry (DSC), complemented with other techniques such as optical and electron microscopy, and XRD.

Brady (51) carried out an extensive investigation of the thermal properties of GLS and GLSO glasses by DTA and viscosimetry, and studied the trends as a function of the glass composition. By analysing T_x, T_η and T_p, he argued that the compositions $65Ga_2S_3{:}2La_2O_3{:}33La_2S_3$ and $78Ga_2S_3{:}22La_2O_3$ are the most stable for GLS and GLSO, respectively. The DTA parameters relative to these compositions are given in table 3.4. It is useful to remark here that these are nominal compositions, i.e. no correction for the mass loss during glass melting was assumed; the ratio$[Ga_2S_3/2GaS]$ was calculated by eqn. 3.1, and the optimum value as for thermal properties was found to be 0.7. Brady also measured the expansion coefficients and estimated the variation of the refractive index, in order to define matched composition pairs for optical fibres; he worked on a NA value of ≈ 0.2, and identified the compositions: 62:2.5:35.5(core)/65:2:33(clad) for GLS and 72.5:27.5(core)/71:29(clad) for GLSO.

The crystallisation of GLS and GLSO was recently investigated in a series of papers by Seddon and co-workers (156; 167; 168). As it was pointed out in section 3.2, these authors found that the glass stability, the vitrification and devitrification behaviour are strongly influenced by the oxide content. They analysed a set of GLS samples with Ga cationic fraction ranging from $n = 0.62$ to $n = 0.75$ and low (≈ 0.5 $mol\%$) oxide content, and found that the mechanisms of devitrification are very complex. Four different crystal phases were observed to form on re-heating above T_g; the formation and growth rate of each phase was dependent on the Ga fraction, on the oxide content and on the temperature; competition effects between different phases were also observed. Although the nucleation and crystal growth rates were not explicitly calculated, the crystallisation rate was observed to be high in the temperature range for fibre drawing ($620 - 660$ $°C$). This result confirmed the nucleation and crystallisation data of GLS

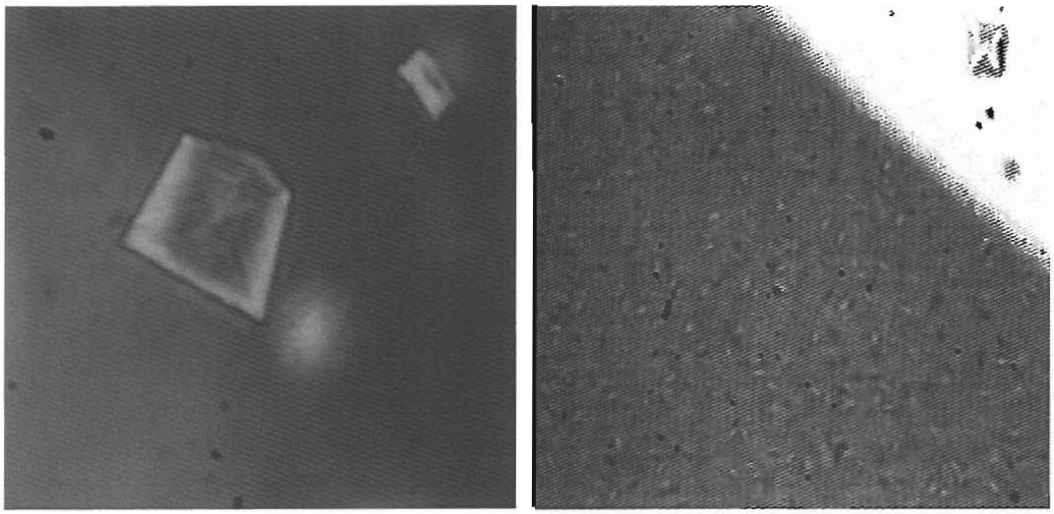

FIGURE 3.12: Transmission optical micrographs of devitrified GLSO glass. Left: barrel-shaped crystals in the core glass ('phase A'). Right: needle-shaped crystals in the cladding glass ('phase B')

samples of composition $70Ga_2S_3{:}30La_2S_3$ (with an unspecified oxide content) measured by Dianov et al. (169). These authors found that the peak nucleation temperature was approximately coinciding with T_g ($\approx 555\ ^\circ C$) and that a large overlap existed between nucleation and crystallisation peaks in GLS.

Takebe et al. (170) used isothermal treatments at different temperatures above T_g and for increasing times, to produce time-temperature-transformation (TTT) curves for GLS and GLSO glasses of composition $70Ga_2S_3{:}30La_2S_3$ and $70Ga_2S_3{:}30La_2O_3$ respectively. In addition, they measured the viscosity curve for these compositions and analysed the behaviour of bulk samples at temperatures close to the fibre drawing temperature. When heated at T_η, GLS crystallised in approximately 10 min, a relatively short time. GLSO glass was found to be more stable, as crystallisation at T_η was found to occur after $\approx 30\ min$. In this study, however, no pre-heating step was performed to simulate the effect of preform fabrication (see section 3.6); therefore, the crystal growth rates in actual fibre preforms are likely to be even higher than those measured by Takebe.

While most of the interest has been catalised by the 'low oxide' GLS compositions, the devitrification of GLSO glasses has not yet been fully characterised. However, we verified that the mechanisms of devitrification are quite complex also for GLSO. This is shown in figures 3.12 and 3.14; a core/clad preform was heated twice at $\approx 630\ ^\circ C$ for $\approx 2\ hrs$ in an extrusion process, and subsequently heated up to the drawing temperature ($\approx 690\ ^\circ C$) for $\approx 30\ min$. The compositions of the core and cladding were the 'optimum' compositions indicated by Brady (51), i.e. 72.5:27.5 for the core and 71:29 for the cladding, respectively. Despite the small difference in the composition, a totally different crystallisation behaviour was found. Large, barrel-shaped crystals were formed in the core ('phase A'); in contrast, a high density of smaller, needle-shaped crystals ('phase B') were observed in the cladding. The two phases were not identified.

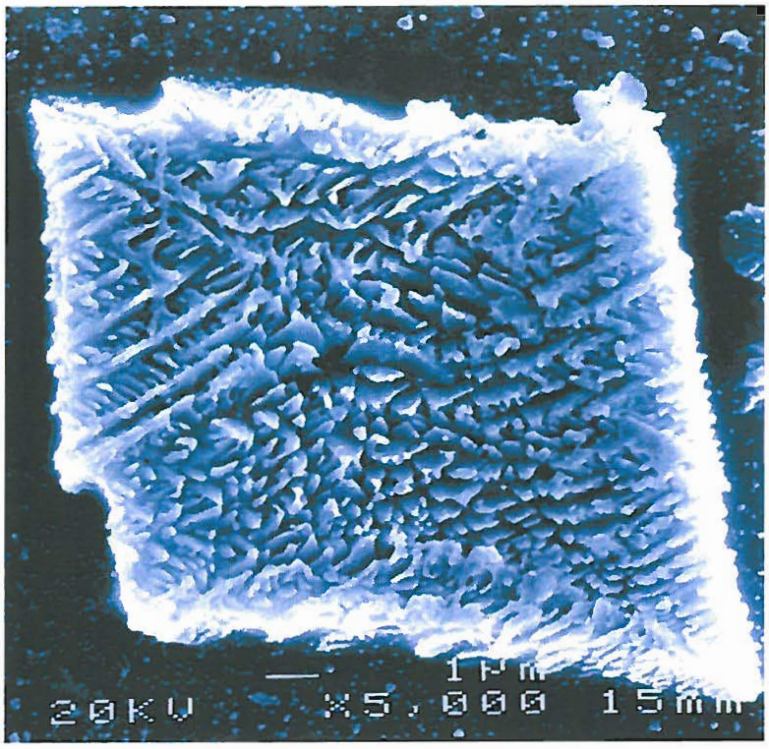

FIGURE 3.13: SEM micrograph of a 'phase A' crystal in devitrified $72.5Ga_2S_3$:$27.5La_2S_3$ glass.

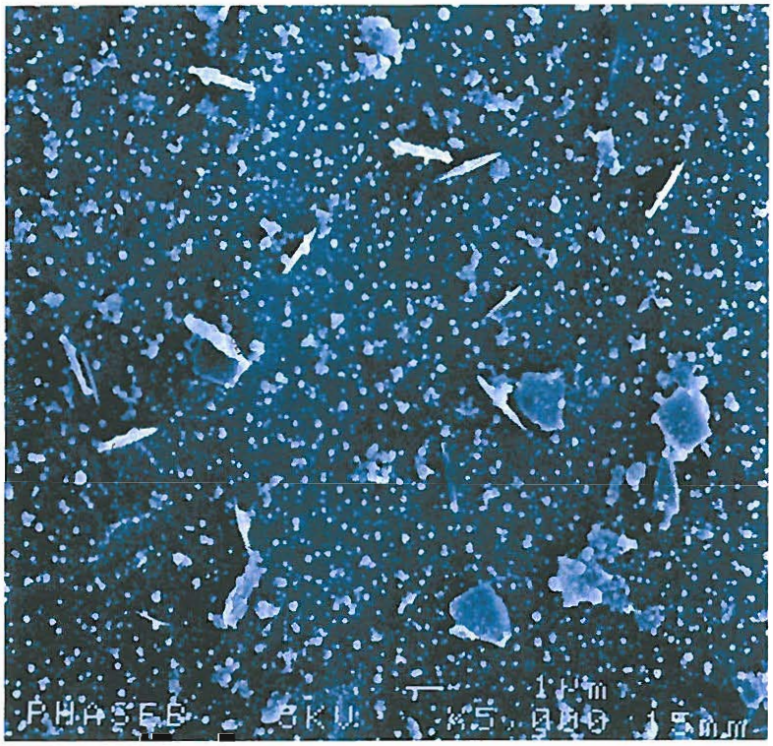

FIGURE 3.14: SEM micrograph of 'phase B' crystals (needle-shaped) in devitrified $71Ga_2S_3$:$29La_2S_3$ glass.

Summarising:

- GLS based glasses have limited thermal stability, which makes the fabrication of optical fibres difficult. Several studied have been carried out, aimed at identifying the most stable compositions.
- The crystallisation of low-oxide compositions is very complicated. Upon reheating above T_g, up to four different crystal phases can form, depending on the glass composition, on the oxide content and on the temperature. Cross-competition of the growth has been observed. The overall nucleation rate largely overlaps with the crystal growth rate, leading to high crystallisation rates at the drawing temperature.
- Repeated thermal treatments above T_g, similar to those employed for preform fabrication and fibre drawing, have been shown to introduce a significant amount of crystallisation in low oxide GLS glass.
- As most of the interest was concentrated on the low oxide composition, believed to be more suitable for rare-earth doped applications, comparatively less information on the crystallisation behavior of GLSO glass is available.
- GLSO glass has better thermal stability than GLS, and can withstand heating to the drawing temperature for $\approx 30\ min$, with no significant devitrification. Hence, the drawing of unclad fibres from glass rods is easier. Whether the thermal properties of GLSO are suitable for the fabrication of single mode fibres, still remains to be verified, and a detailed study of nucleation and crystal growth rates, as already done for GLS, is required.

3.6 Preform fabrication and fibre drawing

A fibre preform is a multilayered rod of glass, with the dimensions of each layer resembling the desired aspect ratio in the final fibre. The composition of each layer is fixed by requirements on optical properties as well as on thermo-mechanical properties. The refractive index of the core must be higher, and the difference between core and clad glass should produce the required numerical aperture. On the other hand, the expansion coefficients should be matched, and the viscosity of the core glass should be slightly higher than the cladding glass ($T_\eta^{core} - T_\eta^{cladding} = 10 - 20\ ^\circ C$) (13).

Silica technology uses a chemical vapour deposition (CVD) method to manufacture fibre preforms, which is made possible by the availability of gas-phase precursors at temperatures close to room temperature. The CVD technique offers several advantages, such as good control over the composition and geometry of the layers, great ease in introducing dopants; especially, it exploits the differences in the boiling points between

the glass precursors and the impurities to achieve a very high purity. As pointed out before, CVD methods are more difficult for compound chalcogenide glasses such as GLS, but could be adopted if appropriate precursors were made available.

For compound glasses, the more common techniques of preform fabrication involve a number of steps of thermomechanical reshaping of pieces of bulk glass. These steps require the ability to process the glass above the glass transition temperature, T_g, without crystallisation taking place, i.e. they require a thermally stable glass. In the case of thermally unstable glasses, such as for instance ZBLAN, the number and the temperature of the heating steps must be adapted in order to prevent devitrification.

'Spin-casting' was employed in the fabrication of preforms in fluoride glass. In this technique, the fabrication of tubes and core/clad preforms is performed by quenching melts of appropriate composition, while spinning them at a very high velocity. Spin-casting achieves high quality interfaces between the core and the clad, but with a relatively large (1/3-1/4) core/clad ratio. A further step is therefore needed, the 'rod-in-tube' technique: the preform obtained by spin-casting is heated up and stretched to a thin cane, and then mechanically inserted in another clad tube; the resulting structure has the correct core/clad aspect ratio and is then drawn into a single mode fibre.

The first GLS and GLSO preforms (44) were fabricated by the rod-in-tube technique. Since a spin-casting technique was not available at that time, tubes were obtained by milling solid rods and at least three thermal steps were necessary to obtain single mode preforms. This led to the crystallisation of the core and of the inner cladding layer, due to the limited stability of the glass and probably initiated by defects at the core/clad interface (51). Spin-casting is difficult for GLS, due to its high melting point and to the reactivity of the melt (as compared to ZBLAN), however it would probably be feasible, if proper technical solutions were identified to address these issues.

As compared to spin-casting and rod-in-tube, extrusion (171) is a far more attractive technique for producing preforms from glasses with limited thermal stability. In fact, while the rod-in-tube technique involves processing the glass at $\approx T_\eta$, extrusion can be carried out at much higher viscosities (10^8-10^9 $Pa \cdot s$), hence at lower temperature. The other advantage is that the extrusion process can be adapted to reduce the number of thermal steps necessary to produce a single mode-proportioned preform. Therefore, although nucleation can still occur during extrusion, the chance of these nuclei growing into actual crystals is lower than in the other techniques, and extrusion affords a better chance to achieve optical fibres. Extrusion was used by Tawarayama, et al. (81) to obtain the single mode $Ga{:}Na{:}S$ fibre that provided the first demonstration of 1.3 μm amplification in a chalcogenide material.

The first report of extrusion of GLS into rods and tubes is given in ref. (49). The technique was subsequently refined and developed (51; 12) and was used to obtain preforms with very small ($\leq$ 1/15) core/clad ratio. Currently, this is the preferred

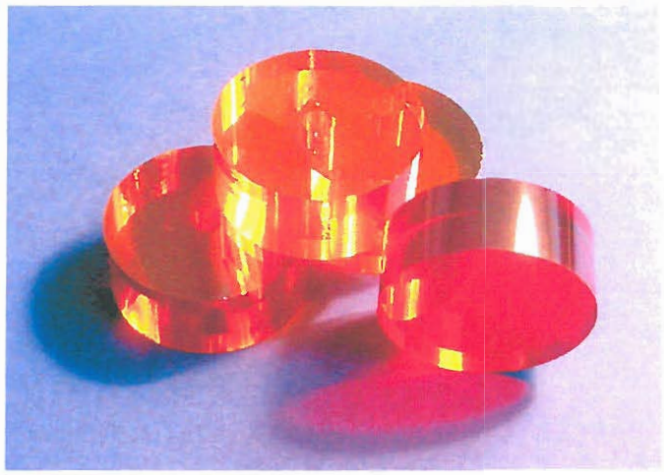

FIGURE 3.15: Polished GLS discs and 'polos' for extrusion

technique for preform fabrication at the ORC. Glass is melted in the shape of disks which subsequently undergo very accurate mechanical polishing of the flat surfaces (see figure 3.15). For the fabrication of preforms with small core/clad ratio, a pair of discs is used, where a bore is made in the upper disk (the 'polo'), and a small cylinder inserted, which can be either a single piece of high purity glass, or a section of small diameter core/clad extruded preform (the 'plug'). The discs are inserted into the extrusion chamber, heated up to the softening temperature; a pressure is applied from above, and the glass is extruded through a carbon die. More details on the preform fabrication and fibre drawing can be found in reference (51). Result until now have been varied. Very short lengths of low oxide GLS fibres with a small core ($\approx$ 2 μm) have been previously reported (51; 12), alas these structures were practically unable to guide light due to the high loss ($\approx$ 100 dBm^{-1}). Fabrication of core/clad structures of GLSO glass have been achieved in longer lengths, but the loss is still high. Determination of the loss in GLS and GLSO fibres is not straightforward due to the high refractive index; a method for loss measurements will be described in section 3.7.2. From the trial performed to date, it seems that the best chance to improve the properties of the fibres would be to obtain a single mode preform in only one extrusion step.

Monomode optical fibres can also be drawn directly from a melt. The technique is referred to as the 'double crucible' technique, and is particularly popular for the fabrication of chalcogenide fibres (5). A crucible, often made of silica or pyrex glass, is held inside a furnace and glass is melted inside it; an inert atmosphere is maintained above the melt and the crucible is pressurised to minimise vaporisation of the melt. At the bottom of the crucible there is a long nozzle, which is kept at lower temperature. When the glass in the crucible has reached the correct viscosity, the nozzle is open and the glass allowed to flow in it. At the nozzle, the glass is still viscous enough, and it is rapidly quenched soon afterwards, and a fibre can therefore be drawn. Core/clad structures are obtained by using two distinct, concentric crucibles for the core and the cladding glass; the core/clad ratio is controlled by varying the respective pressure above the two melts

and adjusting the respective height of the two crucibles. Monomode fibre core sizes can be obtained. The double crucible technique is very suitable for glasses with low melting point (200-400 $°C$), such as, for instance, $As{:}S$, $As{:}S{:}Se$ and $Ge{:}As{:}Se{:}Te$. Since the fibres are obtained directly from the melt, this technique could also have potential for producing fibres from glasses with limited thermal stability. However, there are some difficulties in adapting this technique to GLS and GLSO glass. The most obvious is the very high melting temperature of these material; the reactivity of the melt would require the use of vitreous carbon crucibles for glass melting, hence a more tightly controlled inert atmosphere within the furnace. Finally, the temperature at the nozzle and the quenching rate should be accurately controlled, to prevent crystallisation from occurring on quenching. Although the drawing of GLS by the double crucible technique was previously proposed by Dianov, et al., in the conclusion of their study of the crystallisation of GLS (169), there are to date no reports of this technique being attempted, due to the technical difficulties involved.

3.7 Characterisation of GLS and GLSO fibres

3.7.1 Transmission of unclad fibres

Unclad optical fibres, i.e. fibres drawn from plain, solid glass rods, can be used to measure the material's transmission loss. The intensity of light travelling through an

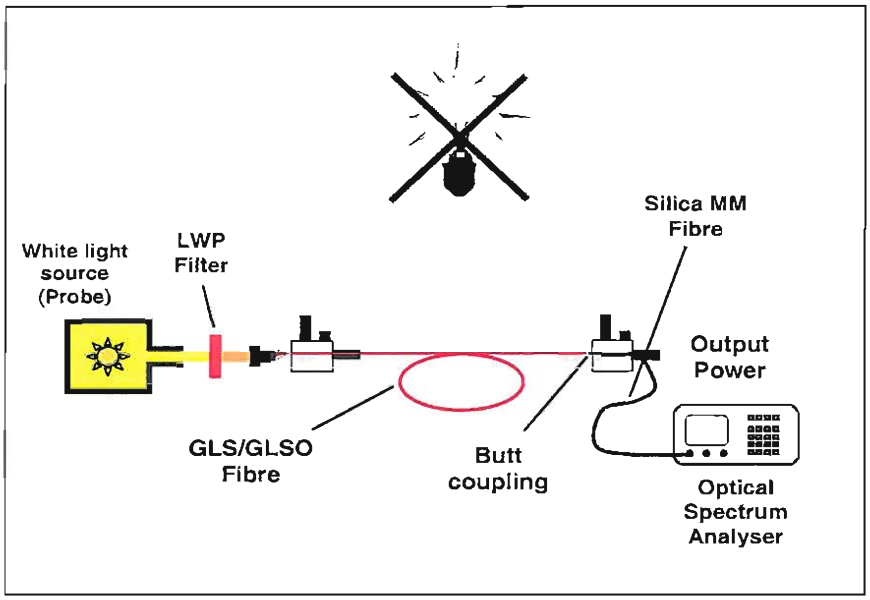

FIGURE 3.16: Setup used for near-IR loss measurements of unclad fibres

optical fibre suffers an exponential decrease described by the Lambert-Beer law:

$$I(L) \;=\; I(L_0)\; e^{-\alpha(L-L_0)} \tag{3.3}$$

where $I(L_0)$, $I(L)$ are the intensity at the lengths L_0, L respectively, and $\alpha(\lambda)$ is the total attenuation coefficient of the fibre. In the case of fibres, α is frequently quoted in dB/km or dB/m, based on the relationship:

$$\alpha_{tot}\left[dB\ m^{-1}\right] \;\equiv\; \frac{10}{L-L_0}\cdot\ \log\frac{I(L)}{I(L_0)} \equiv \frac{\Delta I\,[dB]}{\Delta L} \tag{3.4}$$

The total attenuation coefficient of a fibre is a function of the wavelength and is given by the sum of the contributions due to different loss mechanisms, including absorption and scattering, either intrinsic (i.e. material-related) or extrinsic (i.e., fabrication-related). A more detailed discussion of the loss mechanisms in GLS-based glasses will be given in Chapter 6 (section 6.2).

The measurement of the total attenuation of unclad fibres is straightforward. The most widely used technique is the cutback technique (see figure 3.16) (172). Light is launched into a suitable length of fibre, and the output intensity is collected and recorded. Although this intensity is dependent on the source, output and input coupling losses, etc., these factors are eliminated by performing a differential measurement: the fibre is cut shorter by removing a portion at the terminal end, and the output intensity is measured again. Provided the input and output coupling is not modified in the operation, the difference of the measured intensities only depends on the portion of fibre removed, i.e. the cutback.

The setup used for measuring unclad GLS and GLSO fibres is shown in figure 3.16; it employed a white light source (high-brightness tungsten halogen bulb), suitable launching stage, a butt-coupled, multimode silica fibre for the collection of the output light from the fibre, and an optical spectrum analyser as the detector. A difficulty in the measurements arises from the low mechanical strength of GLS and GLSO fibre, for which the commercial cleavers widely used for silica cannot be used and therefore fibres have to be cleaved by hand. Hand-cleaving introduces a variability of the quality of the end-faces, which also depends on the fibre quality, and must be minimized by choosing an appropriate cutback length. The variability introduced by hand-cleaving was estimated to be 0.5-1 dB for the best quality unclad fibres. The dynamic range of the setup was 25-30 dB, and $\geq$ 20 dB cutbacks were generally employed for the fibre attenuation measurements.

One note of caution necessary when measuring GLS fibres is to ensure that the photodarkening effect does not affect the measurements. GLS and GLSO glasses, when illuminated with a wavelength close to their bandgap (λ = 400-500 nm), experience a

shift in the fundamental electronic absorption towards longer wavelengths. The shift is associated with an increase of the material's loss (photoinduced absorption) in the near-IR region; the loss increase is particularly strong in the region 0.6-1.1 μm. A full characterisation of the Photodarkening of GLS and GLSO fibres will be presented in chapter 6 (section 6.7). Two precautions were adopted to avoid this problem. The first, and more obvious, was to perform the loss measurements in darkness, and also to leave the fibres under no illumination for several hours prior to the measurement. The second was enclose the white light source and to filter out its visible component through a long wavelength-pass filter (RG filters from Schott Glass, 630 nm for GLS and 570 nm for GLSO).

3.7.2 Transmission of core/clad fibres

The measurement of the transmission loss of core/clad GLS and GLSO fibres is not an easy task. These materials have very high refractive index ($n \approx 2.4$ for GLS and $n \approx 2.25$ for GLSO), which means that cladding modes are more efficiently sustained in a GLS fibre as compared, for instance, to silica ($n \approx 1.45$). Furthermore, the conventional coating materials (acrylates), which remove the cladding light in silica fibres, are totally ineffective in the case of GLS and GLSO, and so are the index-matched fluids, which are only available with refractive indexes ≤ 2.0.

A solution sometimes adopted for chalcogenide materials is the selective doping of some

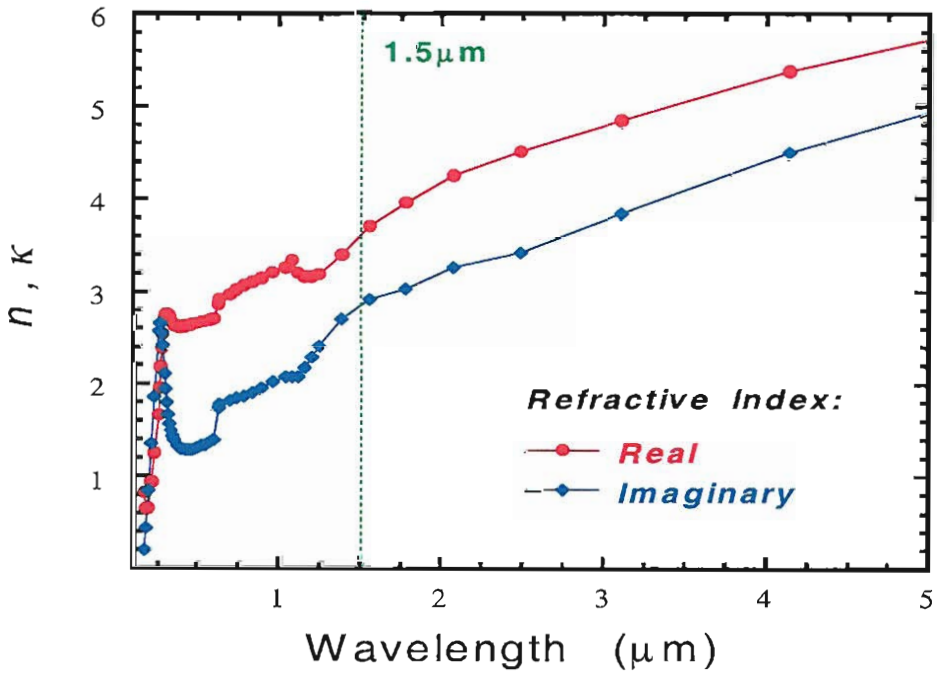

FIGURE 3.17: Real and imaginary refractive index for pyrolytic graphite (data taken from ref. (173))

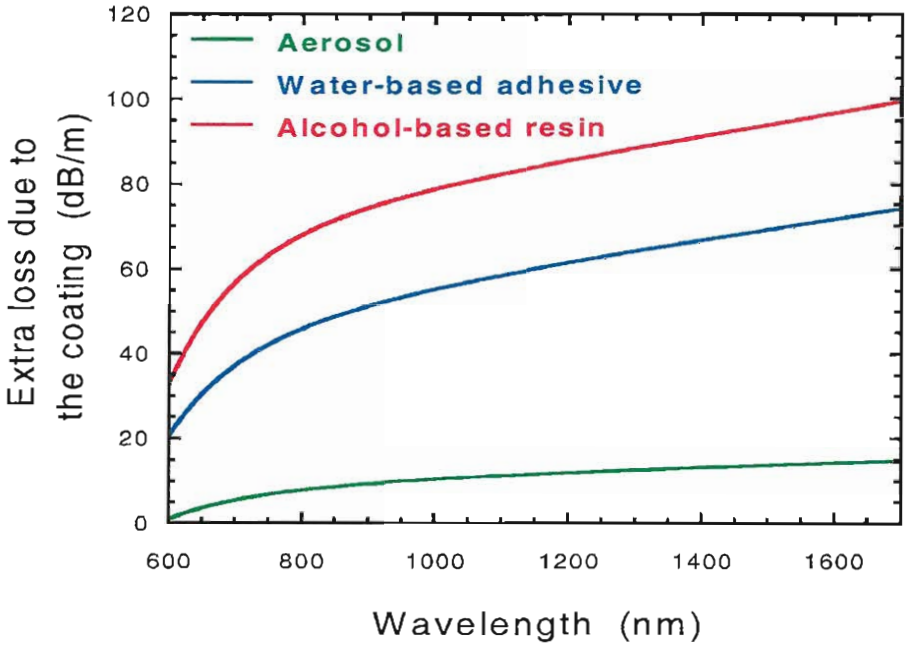

FIGURE 3.18: Extra loss due to the graphite coating in an unclad GLS fibre

or all the cladding layers by means of some active ion. The dopant then removes the cladding modes, but only at particular wavelengths. This technique is also commonly employed, in rare-earth doped fibres or waveguides to suppress any unwanted fluorescence line competing with the lasing transition. Itoh et al. (82) used Dy^{3+} doping for suppressing the cladding light from their $Ga{:}Na{:}S$ fibre and measuring the fibre loss in the region around 1.3 μm. In other cases, including some GLS and GLSO fibres fabricated at the ORC, iron was intentionally doped into the cladding glass; the ion Fe^{2+} has a strong and broad absorption peak in the near-IR from 1 to 4 μm (see section 6.4). The problem in both cases is that light in the core is also inevitably affected by the doping in the cladding, which may lead to an overestimate of the loss in the core.

For our measurements, we investigated the option of a non-conventional coating which could act like a cladding mode stripper. This would offer the advantage of measurements in white light with the setup shown in figure 3.16 even for core/clad fibres. Graphite has very high real and imaginary refractive indexes throughout the visible to mid-IR; in figure 3.17 are reported the wavelength dependence of n and k of polycrystalline pyrolytic graphite. It is obvious that both a high refractice index and a high absorption are useful to suppress the cladding light. In addition, a wide range of graphite-containing preparations are commercially available, including fine powder, aerosols, paints and thixotropic gels. Powder could have been mixed with conventional coating in order to raise their 'effective' refractive index, or paints could have been directly applied onto the fibre.

We tested several materials for their effect on the transmission of GLS and GLSO fibres (see table 3.5). The best result was found using colloidal solutions. These preparations

TABLE 3.5: Graphite-based materials used for coating GLS fibres

	direct fibre coating	mixed with acrylate	mixed with silicon rubber
Aerosol	Yes	not compatible	not compatible
Aqueous colloid	Yes	not compatible	not compatible
Alcohol-based colloid	Yes	$\leq$ 10 $wt\%$	poor curing
Alcohol-based resin	Yes	$\leq$ 20 $wt\%$	poor curing
Graphite/carbon powder	–	$\leq$ 5 $wt\%$	$\leq$ 5 $wt\%$

may be either water or alcohol based, and are thixotropic, i.e. gels that, if shaken, quickly become liquid. They contain typically up to 20 $wt\%$ of graphite (before drying) and some organic binder that improves the consistency of the dried film; the average certified grain size can be as small as a few μm. These preparations have been found to adhere quite strongly to the outer surface of GLS and GLSO fibres. Thicknesses up to 100 μm can be deposited easily in two successive stages. Once dried, the graphite forms a solid coating layer that also improves the mechanical strength of the fibre. The coating obtained from alcohol-based solutions was the most effective and resistant, while the aqueous-based could be easily stripped off even when dried, by dissolving it in water.

Because of the high refractive index, high absorption coefficient and small grain size, the coating was expected to have a very high suppression efficiency when applied to GLS/GLSO fibres. This effect has been quantified by measuring the increase in attenuation of an unclad fibre. The transmission of a short length of fibre was measured,

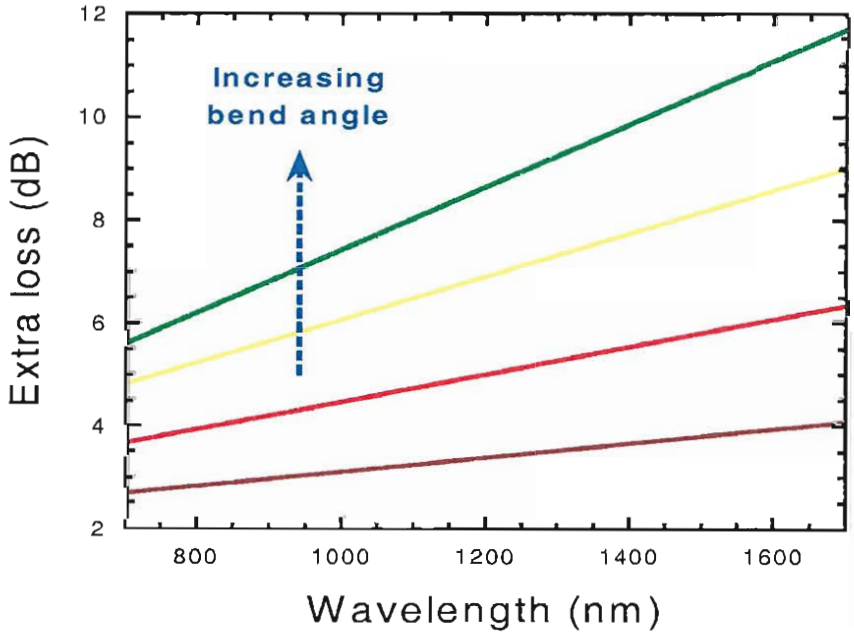

FIGURE 3.19: Bending loss in a GLS unclad fibre coated with graphite

and then a coating was applied onto the fibre by spraying or painting the graphite containing material, and the transmission measured again. The suppression efficiency was measured as an extra loss induced by the coating i.e.:

$$\Delta\alpha_{coating}\,[dB/m] = \frac{I^{uncoated} - I^{coated}}{L} \tag{3.5}$$

where the output intensities are measured in dBm and L is the coated length. The results of the measurements are reported in figure 3.18. An extra loss of up to 100 dBm^{-1} at 1.5 μm was achieved with an alcohol based solution. Figure 3.19 shows that the graphite acts like a high-index coating, and more and more light is suppressed in the fibre by bending it.

The amount of extra loss was clearly dependent on the uniformity of the coating layer and on its adhesion to the fibre; for instance, it was difficult to produce uniform thick layers using aerosols. However, for preparations with similar properties, e.g. thixotropic gels, we observed a direct correlation between the amount of extra loss and the average grain size of the graphite particles contained in the preparation. A smaller average particle size

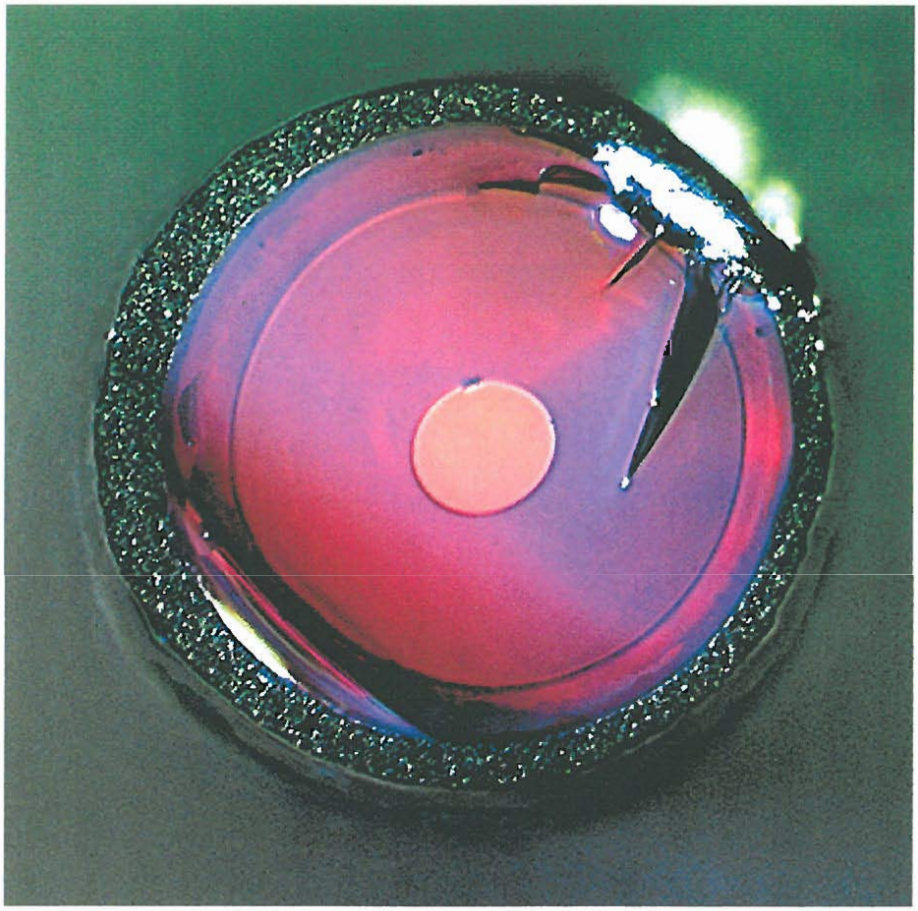

FIGURE 3.20: Optical micrograph of a GLSO fibre coated with graphite; the core size is about 30 μm

always lead to higher extra loss. Besides, as seen in figure 3.18, the loss was increasing with increasing wavelength in the region 0.6-1.7 μm for a coating with 1 μm average particle size; this is an indication that, as the wavelength increases, the granularity of the coating film becomes less relevant, and the film behaves like a homogeneous medium with an effective refractive index probably not too different from that of crystalline graphite (shown in fig. 3.17).

The effect of a graphite-based coating on a core/clad structure is shown in figure 3.20. A layer of about 50 μm was deposited onto a double-clad GLSO fibre; note that the coating layer appears thinner in the figure due to the irregular cleave. The image was collected from a portion of fibre only ≈ 2 cm long, nevertheless the effect of light suppression in the outer layers is very obvious.

Some attempts were also made to obtain graphite-containing materials suitable coating GLS fibres during the drawing. We mixed conventional coating materials, such as acrylate and silicone rubber with graphite powders and other preparations and investigated how this modified their ability to cure. The results for this investigation are presented in table 3.5. Water-based colloids have been found to be incompatible with all the conventional coating materials, as they inhibit the curing. Alcohol-based products and powders give better results; up to 10 $wt\%$ at least of alcohol-based preparations can be mixed with acrylate, and the resulting material still cured, although it was necessary to allow enough time for the alcohol to evaporate off. We also mixed very fine (0.04 μm average particle size) synthetic carbon with acrylate and silicone rubber; trapped air must be completely removed from the mixtures before attempting to cure them. Under correct conditions, good curing and adhesion was observed; an extra loss of 5-10 dB/m at 1.5 μm was measured in coated GLSO fibres.

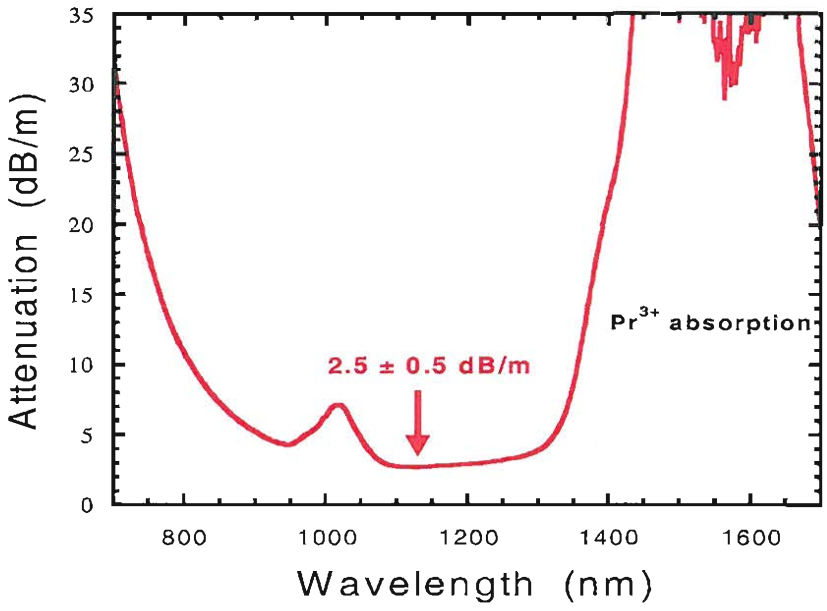

FIGURE 3.21: Near-IR loss of Pr^{3+}-doped GLS fibre LF292.

TABLE 3.6: Attenuation of the best unclad and core/clad GLS and GLSO optical fibres.

Fibre ID	Glass	Composition Core	Composition Clad	Core size [μm]	Loss @1.5 μm [dBm^{-1}]
Unclad fibres					
LF270(♣)	GLS	65:2.5:32.5	–	200	2.5 ± 1
LF276(♣)	GLS	65:2.5:32.5	–	–	2.5 ± 1
LF292(*)	Pr:GLS	65:2.5:32.5	–	130	2.5 ± 1(†)
LF355(*)	GLSO	77.5:22.5	–	170	5.5 ± 1
LF367(*)	GLSO	77.5:22.5	–	160	6 ± 1
Core/clad fibres					
LF282(*)	GLSO	72.5:27.5	71:29	20	30 ± 5
LF284(*)	GLSO	72.5:27.5	71:29	20-30	> 40
LF296(♣)	GLSO	72.5:27.5	70:30	10	≈ 35
LF329(*)	GLSO	72.5:27.5	71:29	100	≈ 40

(*) Fibre measured in this work

(†) Measured @ 1.15 μm

(♣) From reference (51) or prior measurements

3.7.3 Current levels of loss

The complete results of the fibre loss measurements are given in table A.1 in Appendix A. In this section we try to summarise the results and give the values of loss achieved in the best unclad and core/clad fibres. The loss of core/clad GLS and GLSO fibres could only be measured at discrete wavelengths prior to this work, due to the difficulty in removing the cladding modes. By using the graphite coating described in the previous section, we could achieve the first reliable measurements of the attenuation of GLSO fibres in the near-IR range.

The loss of some of the best GLS and GLSO fibres ever produced at the ORC is shown in table 3.6. The attenuation of unclad fibres at important pump and signal wavelengths is in the region of a few $dB \cdot m^{-1}$, with a lowest value of about 2-3 $dB \cdot m^{-1}$ obtained in three GLS fibres (LF276, LF290, LF292). The lowest value for an unclad GLSO fibre is slightly higher, ≈ 5 $dB \cdot m^{-1}$. The attenuation in core/clad structures is much higher(≥ 30 $dB \cdot m^{-1}$), even in crystal free fibres (such as LF329), which probably indicates that core/clad interface defects cause extra loss. Such a high loss clearly made measurements difficult. Reasonably accurate results could only be achieved up to ≈ 40 $dB \cdot m^{-1}$ and at longer wavelengths (1.4-1.6 μm), where the graphite coating was more effective (see fig. 3.18). Losses above 40 $dB \cdot m^{-1}$ could not be measured, because, even with the graphite coating, the loss of the core was comparable to the loss in the cladding, thus the cladding light could not be entirely suppressed. Focussing a laser

beam into the core could have allowed a more precise measurement at fixed wavelengths, but would not have provided a lot more information. Indeed, fibres with such a high loss also showed significant inhomogeneity, and the loss measured over short cutbacks varied from sample to sample. Despite the high loss, all the fibres reported in the table (GLSO) appeared able to guide light. Unfortunately, none of the available core/clad GLS structures was observed to guide light. The fabrication of GLS and GLSO fibres has not been reported to date by any other group worldwide.

In conclusion, the measured attenuation of GLS fibres is relatively high. The loss of unclad fibres is in the range a few $dB \cdot m^{-1}$, with the best fibres approaching a 1 $dB \cdot m^{-1}$ loss in the 1.2-1.5 μm range. This value is about 10 times worse than the lowest loss reported for unclad $As{:}S$ fibres (23). A loss value of 1-2 $dB \cdot m^{-1}$ would be acceptable for the investigation of device prototypes, as attested by the 1.3 μm $Pr^{3+}{:}Ga{:}Na{:}S$ amplifier reported by Tawarayama et al. (81), although lower losses should be achieved for a practical device. Unfortunately, the fabrication of monomode core/clad in GLS and GLSO is very difficult, and the fibre loss in these fibres is a lot higher than in unclad fibres. A considerable improvement in the fabrication is therefore needed and should be matched to fundamental studies of the intrinsic limitation of this material, both in relation to the thermal stability, and in relation to its transparency.

3.8 Conclusions

In this chapter the fabrication of optical fibres in GLS based glasses was discussed. Difficulties arose from two well-known issues. The first is the glass purity; this problem has been largely addressed in previous work at the ORC (154; 155; 51). The second issue is the limited thermal stability, which poses a serious constraint to the reheating of the glass above the glass transition, hence the manufacture of fibre preforms. No glass modifier, alternative to La_2O_3 has been identified, which can increase the stability of GLS glasses. Fundamental studies of the crystallisation kinetics of GLS (156) revealed that the crystallisation rates are high and strongly dependent on the glass composition, oxide content and temperature; hence a very high degree of control of all these parameters is vital. We identified and discussed here how the control of the glass composition could be improved, by determining more reliably the molar ratio of the gallium sulphide phases $[Ga_2S_3/2GaS]$, and by measuring the glass composition directly. It seems, however, that the low thermal stability of GLS poses a problem that cannot be solved by the current technology, therefore alternative fabrication methods should be pursued, i.e. for producing fibre preforms in a single step or for drawing fibres directly from a melt. GLSO glass is more stable than GLS and could afford a better chance to be drawn into monomode fibre, which could have potential for nonlinear devices. To determine whether this is feasible, more studies are required on the crystallisation kinetics of GLSO glasses, as the main focus of previous studies was on low oxide compositions.

While it is obvious that the very high loss of core/clad structures is largely induced by fabrication, the attenuation of GLS and GLSO unclad optical fibres is also relatively high, as compared to other sulphide materials, for instance $As{:}S$. This loss was assumed in the past as mainly due to extrinsic factors, such as impurity absorption or wavelength-independent scattering (51), however a detailed analysis and separate quantification of the loss mechanisms was never performed. It is therefore important to determine the transparency limits of these materials, also in consideration that, due to their limited stability, a certain amount of fabrication-induced loss cannot probably be avoided. The next chapters will be dedicated to these topics and will investigate the mechanisms affecting transmission loss of GLS and GLSO glass.

Chapter 4

Laser Absorption Calorimetry of GLS and GLSO Glasses

4.1 Introduction

The near-IR transparency of sulphide glasses is critical to their application in photonic devices. Several mechanisms can induce optical loss in this region; they will be discussed in more detail in the next chapter. For oxide and fluoride glasses, scattering loss is the prevailing mechanism within the transmission window. In contrast, in chalcogenide glasses a weak absorption tail, due to electronic states within the material's bandgap, persists far from the fundamental absorption edge; consequently absorption, rather than scattering, is believed to determine the ultimate transparency limit in these materials. The total attenuation can be determined easily by measuring unclad fibres; however, in glasses with limited thermal stability fibre drawing itself can induce extra loss, making it difficult to distinguish the extrinsic from the intrinsic contributions. Bulk samples, on the other hand, provide the closest value to the intrinsic limit, but require more sensitive techniques. This chapter describes the use of laser absorption calorimetry to determine the optical absorption of bulk samples of GLS and GLSO glasses; a Free-Electron Laser (FEL) source was employed to obtain values at 1.55 and 1.7 μm. The use of the calorimetric technique allows the discrimination of absorption from scattering and opens up the possibility of identifying the prevailing loss mechanism and determining the transparency limit for these materials.

All the measurements were carried out during a single run with the free-electron laser source at the at the Jefferson Laboratories (USA) in late autumn 2001; the run lasted three days, with one day dedicated to setting up, testing and calibrating the instrumentation and two days entirely dedicated to the measurements.

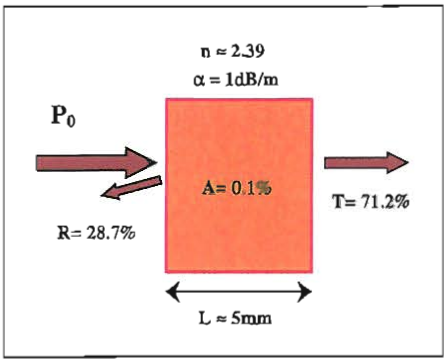

FIGURE 4.1: Schematic of a transmission measurement of a bulk GLS glass sample.

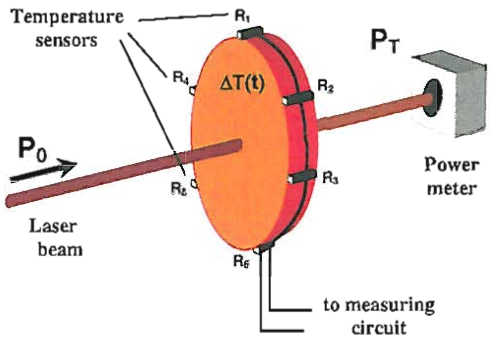

FIGURE 4.2: Schematic of laser absorption calorimetry.

4.2 Laser Absorption Calorimetry

Measuring the residual attenuation of optical glasses in their region of high transparency is best accomplished using optical fibres, where coupling loss can be made small in comparison to transmission loss by evaluating long lengths of fibre. In bulk samples, transmission loss is dominated by the Fresnel reflection loss from air/glass interfaces. This is particularly critical for chalcogenide glasses due to their very high refractive index ($n \approx$ 2.3-2.4); in addition, only small batches of these materials can be prepared having the necessary homogeneity, which limits the thickness of practical samples to $\approx cm$. For instance, a loss of 1 $dB \cdot m^{-1}$ corresponds to just above 0.1% loss in a 5 mm thick sample, which compares to Fresnel losses of approximately 15% per interface (see fig. 4.1). Transmission measurements of low level absorption in bulk samples are notoriously difficult and require samples with excellent surface quality and detection systems with very high signal/noise ratio. The differential transmission can be severely affected by beam deviation and focus shifts, caused by tiny displacement of the samples, and also by interference effects in samples with very flat and parallel surfaces. It is also important to point out that transmission measurements only provide the total attenuation, and are unable to determine if this is due to absorption or scattering. The ability to separate these two is required in order to give a full insight into the mechanisms causing the loss.

Laser absorption calorimetry allows a sensitive, direct measurement of low-level absorption of transparent optical materials (174). The technique is based on the photothermal effect: the absorbed fraction of an optical beam is converted into heat, which is measured as a rise of the sample temperature; this, of course, holds as long as photoluminescence or fluorescence effects are not present. The ability of this technique to detect low level absorption relies on the availability of high power, stable light sources and requires the measured sample to be kept insulated from temperature fluctuations of the environment; sub-*ppm* sensitivity has been demonstrated in optimised conditions (175). Laser calorimetry was first introduced in the early 70s to determine the bulk absorption of

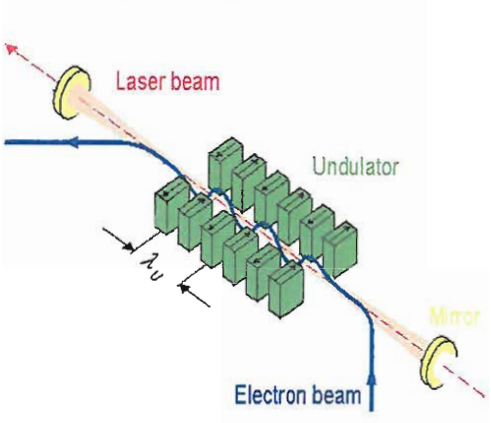

FIGURE 4.3: Schematic of the operation of a Free-electron Laser.

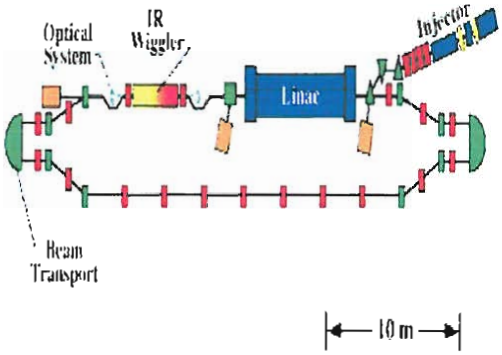

FIGURE 4.4: Layout of the 'IR-demo' free-electron laser at JLABS.

fused silica when fibre fabrication was still in its early stages (176); since then it has become the standard technique for testing the absorptivity of optical components (177). The calorimetric technique has the advantage of being independent of the reflectivity (thus it can be used for measuring high index as well as low index materials) and independent of scattering. Although it cannot distinguish between bulk absorptivity and surface absorptivity (caused by defects and contamination at the interfaces) of a single sample, the two components are readily determined by measuring sets of samples with different thickness. In comparison, other techniques have even higher sensitivity and do not require a high power laser source, but are not as practicable for measurements on high index, bulk optical materials. Cavity Ring-Down spectroscopy (CRD) (178) measures the variation of the ringdown time of laser pulses when an absorbing sample is introduced into a stable, high finesse optical cavity; CRD has been reported for measurement of solids, however it is better suited to low index samples and in particular gases; besides, it can only determine the total attenuation. Photothermal Deflection Spectroscopy (PDS) (179) measures the deflection of a probe beam which is caused by the absorption of a second, confocal beam. PDS is the most flexible and sensitive among the techniques mentioned here, and it also allows spatially resolved measurements; however, it cannot provide absolute absorptivity and is generally calibrated by laser calorimetry.

The main constraint imposed by absorption calorimetry is the need for high power laser sources at the wavelength of interest. For this reason, its application has been restricted in the past to a few 'traditional' wavelengths, such as those provided by CO_2, *Er*-YAG, *Nd*-YAG, *Ar*-ion and, more recently, ArF excimer lasers. Apart from the high power and suitable wavelength, the ideal source for laser calorimetry should have high beam quality in a single mode operation. This is essential in order to allow for optimisation of the power density on the sample, without creation of scattered or diffracted beam components, which might hit the chamber's walls, the sample holder or the temperature sensors and produce a spurious temperature signal.

In the present study, in order to overcome the limitation of conventional sources and to

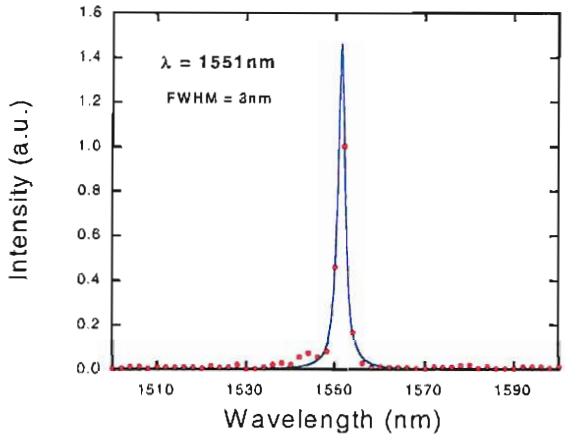

FIGURE 4.5: FEL laser line at 1.55 μm.

Wavelength	2.9-6.5 μm (FHL) 1-2.1 μm (THL)
Average Power	2.1 kW (FHL) 100 W (THL)
Pulse width	$\approx ps$
MPRR	18.75, 37.5, 75 MHz
M^2	≈ 1

TABLE 4.1: Basic characteristics of JL-FEL

measure absorption of GLS and GLSO glasses in the telecom window around 1.5 μm, a Free-Electron Laser (FEL) source was employed. To the best of the author's knowledge, this is the first time that a FEL source is employed for Laser Absorption Calorimetry. FELs are well known sources of tunable, coherent and high power electromagnetic radiation. These sources differ from most conventional lasers in that they exploit a beam of relativistic electrons as the active medium, as opposed to bound atomic or molecular states. Consequently, FELs can be tuned over wide wavelength intervals spanning from the far IR to the deep UV. Spontaneous emission of synchrotron radiation is induced when a bunched electron beam is passed through a periodically alternating magnetic field (the 'undulator' or 'wiggler', see fig. 4.3). The radiation is stored in a high-Q optical cavity, where it is allowed to interact with the electron beam undergoing optical amplification. The operating wavelength can be tuned by varying the energy of the electrons or the strength of the magnetic field in the undulator.

The free electron laser source at the Thomas Jefferson National Accelerator Facility (Newport News, VA, United States), (JLFEL), is very suitable for laser absorption calorimetry. Indeed, it can deliver extremely high powers, having a multi-kilowatt output when tuned in its fundamental lasing frequency region from 3 to 6 μm (first harmonic lasing, FHL); when operated on its third harmonic (THL), JLFEL provides an average power in excess of a hundred watts across the region from 1 to 2.2 μm (see fig. 4.5). The ability to work in the near-IR makes it rather unique among FEL sources. The output is nearly diffraction limited, allowing easy handling of the power density. Another advantage of JLFEL is that the micropulse repetition rate (MPRR) can be varied while keeping the average power constant; this characteristic was very useful, as will be explained in more detail, in order to ensure that damage or nonlinear phenomena were not affecting the result of the calorimetric measurements. Figure 4.4 shows a schematic of the layout of the 'IR-demo' FEL that was used in autumn 2001; JLFEL is currently undergoing a complete reconfiguration, which will extend its range of operation from the UV (250 nm) to the MIR (14 μm) and is also expected to scale up the maximum

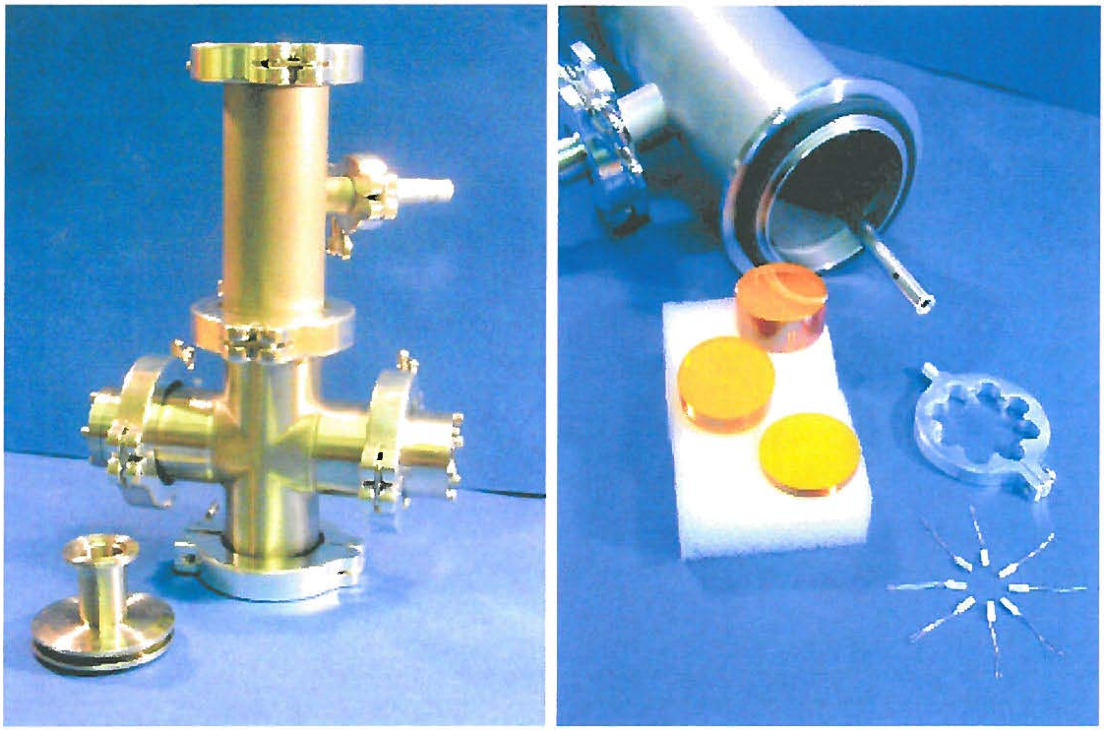

FIGURE 4.6: Details of the calorimeter: vacuum chamber, sample holder and temperature sensors before assembling.

delivered power by at least an order of magnitude.

4.3 Design of the calorimeter

The temperature increase typically measured in laser calorimetry is small. Assuming for instance a sample with 10 cm^3 volume, 500 $Jkg^{-1}K^{-1}$ specific heat and having an optical absorptivity $\mathcal{A}$ of 10^{-3}, which is irradiated for 200 s with a 10 W average power, the maximum temperature increase (disregarding heat losses) amounts to less than one hundredth of a degree. Such a small temperature signal can easily be overwhelmed by thermal noise and drifts of the environment. Therefore, samples must be contained in enclosures to provide adequate shielding.

In addition to the minimisation of thermal noise and drifts, insulating the sample also increases the sensitivity of the laser calorimetry. For small temperature increases, the thermal leakage from the sample to the chamber is proportional to the temperature increase $\vartheta(t) = T_s(t) - T_c$, consequently:

$$\left.\frac{d\vartheta(t)}{dt}\right|_{leak} = -\gamma_{cal} \cdot \vartheta(t) \tag{4.1}$$

where T_s is the sample temperature, T_c is the holder temperature, and γ_{cal}, designated as the heat loss coefficient, is the quantity that expresses how effective the insulation of

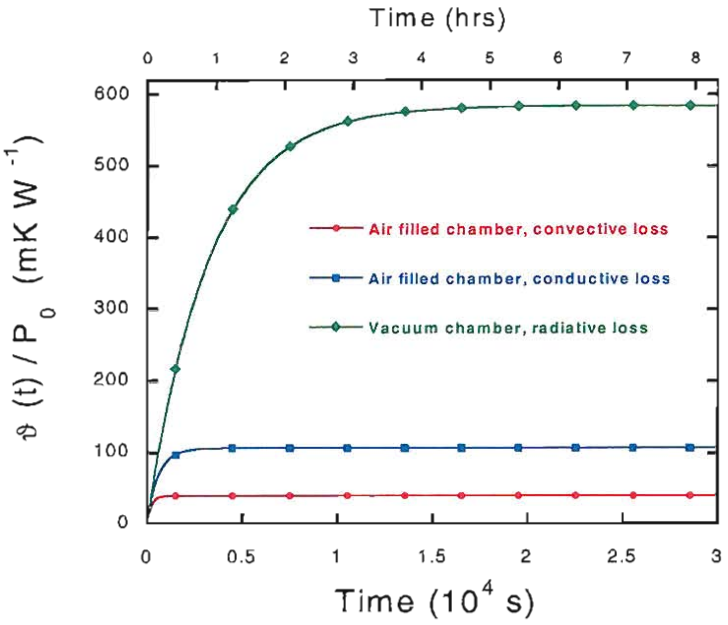

FIGURE 4.7: Sensitivity of a calorimetric measurement performed in a vacuum and air-filled chamber.

the sample is. The sensitivity of the calorimetric measurement is defined as:

$$\begin{aligned} \Sigma_{cal} &= \frac{\text{max. temperature increase [mK]}}{\text{beam power [W]}} \\ &= \frac{10^3 \cdot \mathcal{A}}{mC_p \cdot \gamma_{cal}} \end{aligned} \tag{4.2}$$

where $\mathcal{A}$ is the absorptivity and mC_p the heat capacity of the sample; hence, improving the insulation leads to lower γ_{cal}, and to higher sensitivity Σ_{cal}.

Assuming a cylindrical sample with radius R and thickness L, the time constant γ_{cal} can be expressed through the equation:

$$\gamma_{cal} = \frac{2h_{sc}}{\rho C_p}\left(\frac{1}{R} + \frac{1}{L}\right) \tag{4.3}$$

where ρ is the specific gravity, and h_{sc} is the sample-chamber heat exchange coefficient, which depends on the mechanism of heat transfer. Here we compare the case of a chamber filled with air or other dry gas, such as nitrogen or argon, and a vacuum chamber. For an air-filled chamber, and for temperature increases below $\approx 0.5\ K$, the heat loss mechanism is via conduction of the gas, and h_{sc} can be estimated as:

$$h_{sc}^{cond} \approx \frac{k_{air}}{\ell_{sc}} \tag{4.4}$$

where k_{air} is the thermal conductivity of air and ℓ_{sc} is the average distance between the sample and the chamber's walls. For larger temperature increases ($\vartheta^{max}(t) \approx 0.1 - 1\ K$, depending on the geometry of the sample), free convection may also set in; reference (175) quotes an estimate of $h_{sc}^{conv} \approx 10\ W\ m^{-2}K^{-1}$ for the convective heat exchange coefficient of disc-shaped samples with radius and thickness of $\approx cm$. In the case of a vacuum chamber, heat is lost by radiation from the sample to the calorimeter's inner surface; the radiative heat exchange coefficient can be expressed as:

$$h_{sc}^{irr} \approx \frac{4\sigma_{SB}T_c^3}{\frac{1}{\varepsilon_s} + \frac{A_s}{A_c}\left(\frac{1}{\varepsilon_c} - 1\right)} \equiv 4\sigma_{SB}\varepsilon_s\mathcal{F}T_c^3 \tag{4.5}$$

where σ_{SB} is the Stephan-Boltzmann constant, T_c is the chamber temperature, $A_{s,c}$ are the sample surface and the chamber inner surface respectively, and $\varepsilon_{s,c}$ are the integral emissivities of the sample and the inner surface of the chamber respectively; the quantity $\mathcal{F}$ gives the view factor, and the quantity $\varepsilon_s' \equiv \varepsilon_s \cdot \mathcal{F}$ is defined as the effective sample emissivity. If the enclosure is much bigger than the sample, i.e. $A_s \ll A_c$, thus it results $\mathcal{F} \approx 1$, and h_{sc}^{irr} can be simplified to:

$$h_{sc}^{irr} \approx 4\varepsilon_s\sigma_{SB}T_c^3 \tag{4.6}$$

Figure 4.7 shows a comparison of the sensitivity of calorimetric measurements performed in vacuum and in an air-filled chamber. In calculating the curves, the appropriate parameters for a sample of GLS glass were used (sample E, table 4.2) and an absorptivity of 10^{-4}. It is clear from the graph that the measurement in a vacuum chamber has higher sensitivity, which means that a lower beam power is needed to achieve the same temperature increase; this can be a crucial detail in samples susceptible to damage. On the other hand, a vacuum chamber has the penalty of increased equilibration time; because of that, it becomes impractical to wait for the maximum temperature increase, and a longer time interval has to be allowed between measurements.

The bulk absorption of GLS and GLSO glass had not been measured precisely before this work. The lowest value reported in a chalcogenide glass is $0.2\ dB \cdot m^{-1}$ in As_2S_3 glass, which corresponds to $\approx 5 \cdot 10^{-5}$ absorptivity in a $1\ mm$ thick sample; consequently, a lower detection limit of 10^{-5} was set as a target. Lacking a reliable indication as to the damage threshold of GLS, a vacuum chamber was employed in order to achieve maximum sensitivity.

The chamber (figure 4.6) was composed of thick stainless steel flanges (modular ISO-KF DN50), which had both low thermal conductivity and high heat capacity to minimise the effect of external temperature fluctuations. Additional insulation was placed outside the chamber. The samples were clamped on an aluminum ring holder, onto which the temperature sensors were also permanently attached. The holder was firmly kept in

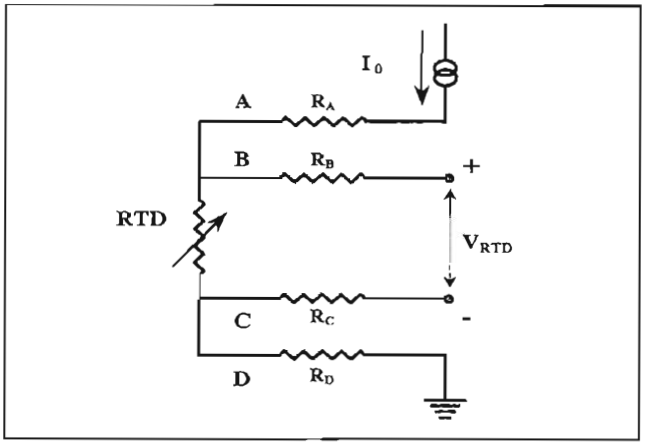

FIGURE 4.8: Four-wires configuration used for the temperature measurement with RTD elements.

place at the center of the chamber by a $\approx 210\ mm$ long piece of stainless steel cryogenic tubing. In the design adopted, the aluminum body contributed to the 'effective heat capacity' during irradiation and provided a very repeatable thermal contact between samples and sensors. Due to the very thin walls (0.16 mm) of the tubing and the low conductivity of stainless steel, both leading to a high thermal resistivity (several small holes were drilled in order to make a vacuum inside the tube). The conduction loss along the support was estimated to be at least 20 times smaller than the radiative heat loss of the sample plus holder. In addition, the tube did not affect the effective heat capacity of the sample holder assembly significantly, since its total thermal mass was at least 20 times smaller (the two above factors coincide accidentally). This ensured that the support was not modifying in any significant way the thermal properties of the heated mass.

Low outgassing materials were used for assembling the sample holder, the sensors and the electrical connections. The adhesive used to glue the sensors onto the holder was thermally conductive, vacuum grade epoxy (EpoTek H74 from Promatech Ltd., with 0% CVCM index). Viton gaskets were used for the vacuum seals, and wires were PTFE insulated. The pump used was also oil-free to prevent contamination. Maintaining a 'clean' vacuum in the chamber is essential in order to prevent surface contamination of the samples, which might induce extra absorption at particular wavelengths and interfere with the result of the calorimetric measurement.

The temperature sensors were eight thin film platinum resistance-temperature detectors (OMEGAFILM RTD Mod. F3107 from Omega Ltd.). Each element had a nominal resistance of 100 Ω at 0 $^{\circ}C$ and a temperature coefficient α_R equal to 3850 $ppm{\cdot}(^{\circ}C)^{-1}$. Their flat shape and miniature size (1.5×4 mm) allowed them to be attached to the ring holder for accurate and repeatable temperature readings with a negligible increase of the thermal mass of the holder. The eight RTDs were connected in series and measured in a four wire configuration (figure 4.8). In this scheme, one pair of wires (A & D) carries the

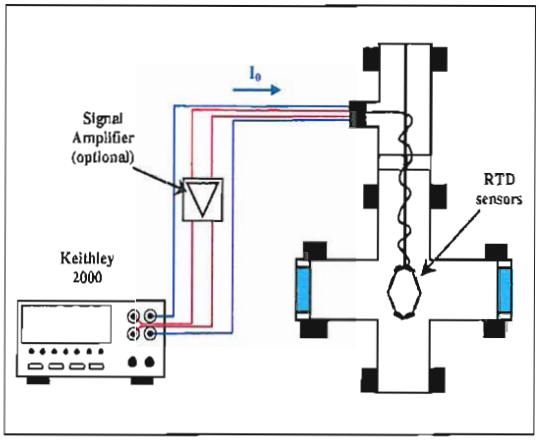

FIGURE 4.9: Schematic of the circuit measuring the sample temperature

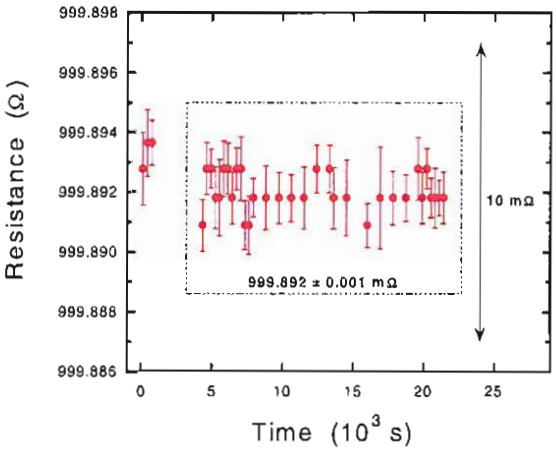

FIGURE 4.10: Resolution of the temperature reading with signal amplifier (10 $m\Omega$ is the resolution without signal amplifier)

current I_0 through the RTD element, while the other pair (B & C) probes the voltage V_{RTD} across the RTD. Since the current flowing through A and D is constant and the current flowing in the sensing wires is negligible, the measurement is unaffected by the resistivity of the leads. However, the sensing circuit is almost inevitably made up of different conductors; thus, an imbalance of thermal EMFs can result as a consequence of slight temperature differences at the junctions. These thermal EMFs, of the order of $\approx$ tens of μV per degree, obviously affect V_{RTD} and hence the result of the temperature reading. This problem was carefully thought through, and appropriate measures were introduced to minimise it. For instance, the same conductor material was used as much as possible for the various sections of the sensing circuit; where this was not possible (e.g. feed-through connectors, soldered points, etc.), the equivalent contact points along the two arms of the sensing circuit were thermally shorted in order to zero the total thermal EMF. As a final verification, both the current I_0 and the polarity between B and C were reversed at the same time during a temperature measurement; a purpose-built device, based on low-thermal EMF relays (Coto Technologies, mod. 3602) was used for this test. Reversing I_0 causes the sign of V_{RTD} to change, which is canceled out by the polarity change; the total thermal EMF, however, is independent of the direction of flow of the current, thus it can be revealed and quantified by this procedure. In our setup, this check produced no measurable difference in the reading of V_{RTD}.

The four-terminal configuration allowed more flexibility in designing the electrical connections. Using thick wires would obviously have compromised the insulation of the sample-holder assembly; on the other hand, reducing the thermal conductivity along the leads inevitably implies an increased electrical resistance too, but this does not affect a four-wire measurement. Thus, tiny copper wires ($\approx$ 75 μm diameter, PTFE insulated wires from Omega Ltd.) were used as the connections; the total thermal conductivity of the four leads was at least a factor of 2 smaller than the cryogenic tube support, i.e.

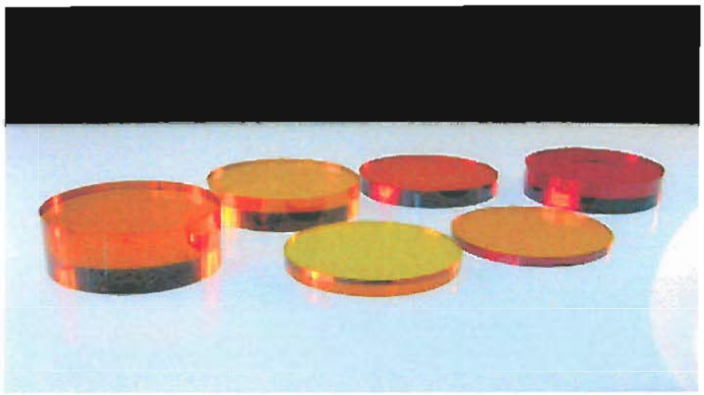

FIGURE 4.11: GLS and GLSO samples used for the calorimetric measurements.

about forty times smaller than the radiative loss; hence, the overall thermal leakage due to conduction along the leads plus the sample support was totally negligible.

A computer-interfaced digital multimeter Keithley 2000 was used for the four-wires measurement of the RTDs. The current flowing in the RTD elements had to be kept as low as possible in order to minimize the Joule heating and prevent interference with the laser heating of the sample. The current provided by the built-in source of the Keithley 2000 was set by the choice of the range: 1 mA for 1 $k\Omega$ range, 100 μA for 10 $k\Omega$ range, and so forth. The total resistance of the RTDs was $\approx$ 871 Ω at room temperature; choosing a current of 100 μA allowed to obtain a 10^{-5} resolution in the absorptivity with as low as 1 W laser power, while 1 mA would have required $\approx$ 100 W to achieve the same resolution, and would have also caused an unacceptable increase of the sample temperature of $\approx$ 5 $mK \cdot min^{-1}$. Consequently, a range of 10 $k\Omega$ was chosen; the resolution of the Keithley 2000 was 10 $m\Omega$, which corresponded to $\approx$3 mK. To further improve the resolution, a simple signal amplifier was designed; the device was based on a chopper-stabilised operational amplifier with very low temperature coefficient of input offset voltage (Maxim ICL-7650) and two low-temperature coefficient metal-film resistors (-0.14 $ppm \cdot (^{\circ}C)^{-1}$), and achieved a very stable $\times$11 gain. The signal amplifier could

TABLE 4.2: Properties of GLS and GLSO samples for laser calorimetry.

Sample	Glass batch	Thickness $[mm]$	T (1.55 μm) [%]	Heat Capacity $[J \cdot K^{-1}]$
A	GLSO [LD1088]	2.00 ± 0.02	74.0 ± 0.1	2.2 ± 0.2
B		3.23 ± 0.02	73.9 ± 0.2	3.6 ± 0.4
C		8.48 ± 0.02	72.9 ± 0.2	9.4 ± 0.9
D		12.80 ± 0.02	72.2 ± 0.5	14.2 ± 1.4
G	GLS [LD1087]	1.96 ± 0.02	71.2 ± 0.1	2.1 ± 0.2
H		3.01 ± 0.02	71.1 ± 0.2	3.2 ± 0.3
E		5.19 ± 0.02	70.9 ± 0.3	5.5 ± 0.6
F		7.62 ± 0.02	70.8 ± 0.3	8.1 ± 0.9

be inserted along the sensing circuit outside the chamber (figure 4.9). The resolution of the temperature measurement using this configuration was determined by measuring a precision resistor (results are shown in figure 4.10); a $\approx 1\ m\Omega$ resolution resulted, which corresponds to $\approx 0.3\ mK$.

4.4 Fabrication and basic characterisation of samples

The nominal compositions chosen for this study were $65Ga_2S_3{:}30La_2S_3{:}5La_2O_3$ for GLS and $78Ga_2S_3{:}22La_2O_3$ for GLSO. Glass batches were prepared by standard melt-quenching; $\approx 250g$ batches were prepared first, which were then crushed and remelted in order to improve the glass homogeneity and to obtain ingots with the desired cylindrical shape. Ingots underwent annealing at 475 $^\circ C$ for several hours, and were subsequently cut into 26 mm diameter discs with thickness ranging from 2 to 13 mm. Small portions were retained for trace impurity analysis and for heat capacity measurements. The samples are shown in figure 4.11 and their basic properties are given in table 4.2.

Trace impurity analysis of the glass batches was obtained by GDMS and the results are reported in table 4.3 (measurements carried out by Shiva Technologies, Ramonville Saint Agne, France). The levels of transition metal impurities are particularly important since they can induce absorption at the measurement wavelengths. The GLS ingot was tested at two points, one close to the periphery and one at the center of the ingot, which corresponded to the measured volume in the actual samples. The results, in table 4.3, confirm a high purity with total content of $3d$ transition metals below 2 $ppm\ wt$; the

TABLE 4.3: Results of trace impurity analysis on the glass batches employed for laser calorimetry.

	GLS LD1087 center [$ppm\ wt$]	GLS LD1087 periphery [$ppm\ wt$]	GLSO LD1088 center [$ppm\ wt$]
Na	1.1 ± 0.1	1.5 ± 0.2	1.0 ± 0.1
Mg	0.16 ± 0.01	0.25 ± 0.04	0.41 ± 0.02
Al	1.0 ± 0.1	0.95 ± 0.03	1.5 ± 0.1
Si	32 ± 1	30 ± 1	31 ± 1
Ca	0.79 ± 0.05	1.4 ± 0.1	20 ± 1
Ti	0.06 ± 0.01	0.10 ± 0.01	0.07 ± 0.02
V	< 0.05	< 0.05	< 0.05
Cr	0.14 ± 0.02	0.11 ± 0.02	0.03 ± 0.01
Mn	< 0.05	< 0.05	< 0.05
Fe	0.83 ± 0.02	1.3 ± 0.1	0.67 ± 0.02
Co	< 0.005	0.02 ± 0.01	< 0.005
Ni	0.07 ± 0.02	0.15 ± 0.03	0.11 ± 0.02
Cu	0.33 ± 0.03	0.28 ± 0.03	0.48 ± 0.03
Zn	< 0.5	< 0.5	< 0.5

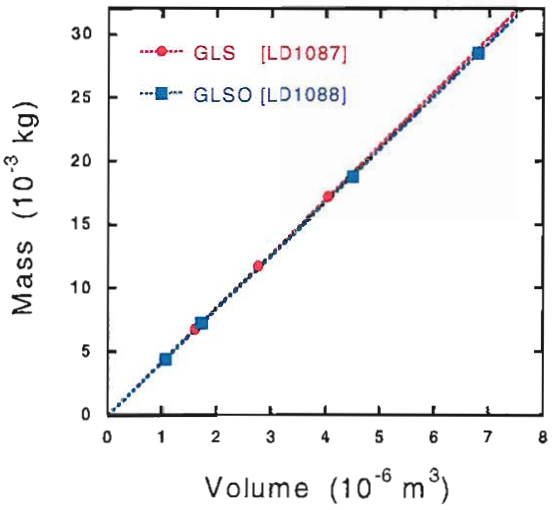

FIGURE 4.12: Density of GLS and GLSO samples.

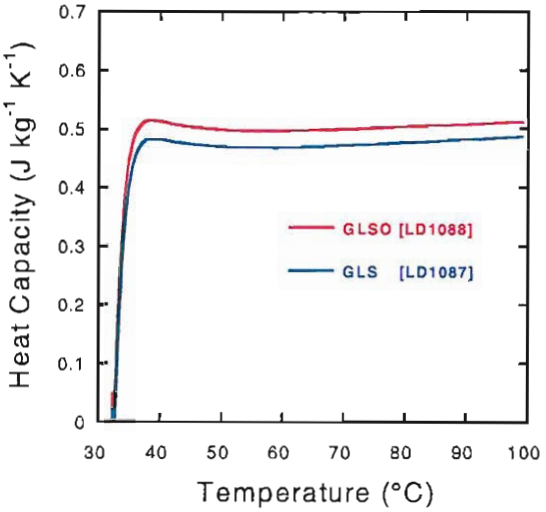

FIGURE 4.13: Specific heat of GLS and GLSO samples by DSC.

main contaminant in the two glass batches was found to be iron.

The disc shaped samples had all faces polished. Because of the big impact of surface defects on calorimetric measurements, the flat faces were polished to the best standard attainable in these relatively soft materials (scratch/dig index 20/10). Samples were also inspected for bulk defects by optical microscopy; a 20 mm diameter central volume resulted, that was defect-free at 100× magnification, while a few small inclusions were present close to the sample border in one GLS sample. These defects were not assumed to affect the measurement since they are located far from the region sampled by the laser beam during the calorimetric measurement, and also because they cause an insignificant modification the thermal properties of the samples due to their very small volume.

The samples were also checked for density inhomogeneity; these defects are sometimes formed upon quenching large glass batches due to the low thermal conductivity of GLS, which makes it difficult to remove heat quickly and uniformly from the melt. The transmission of ≈ 3 mm diameter sections of the samples was measured in several different

TABLE 4.4: Composition and thermal properties of GLS and GLSO samples.

Composition Ga_2S_3:La_2S_3:La_2O_3	Density $[10^3\ kg\ m^{-3}]$	Specific Heat $[10^3\ J\ kg^{-1}K^{-1}]$	Diffusivity $[10^{-7}m^2s^{-1}]$	Conductivity $[Wm^{-1}K^{-1}]$
[GLS] 65:30:5	4.24 ± 0.01	0.47 ± 0.05	3.1 ± 0.3 (*) 2.76 ± 0.09 (†)	0.55 ± 0.06
[GLSO] 78:0:22	4.18 ± 0.01	0.50 ± 0.05	2.78 ± 0.08 (†)	0.58 ± 0.06

(*) By Ångström's bar method
(†) From TL measurements

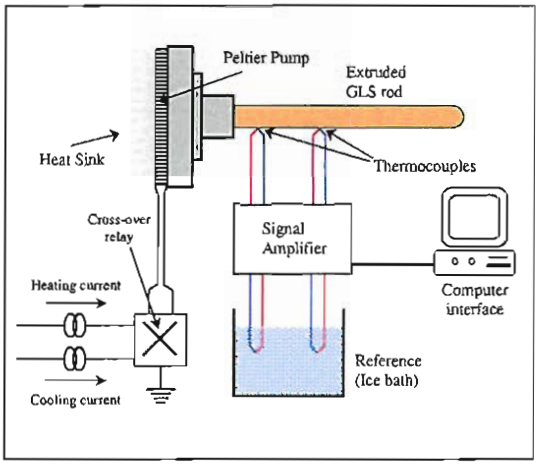

FIGURE 4.14: Scheme of the setup for Ångström's bar measurements of thermal diffusivity.

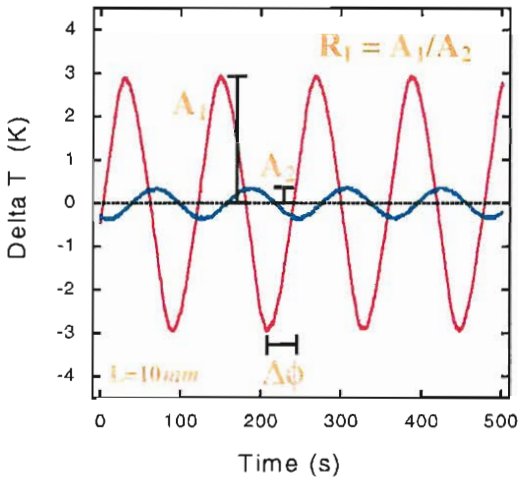

FIGURE 4.15: Propagation of a thermal wave along a GLS rod.

positions and the result was found to be consistent to better than 0.05%, except for the thicker GLSO sample D. This sample had visually discernible density inhomogeneity which caused a significant deflection and scattering of a *He-Ne* laser beam passing through it. Since this was very likely to affect the result of the measurement, via direct heating of the sensors due to scattering, sample D was not used for calorimetric measurements.

The thermal properties, necessary for interpretation of the calorimetric data of the two sets of samples, were also measured. A summary of the results is presented in table 4.4. Density data are shown in figure 4.12. The room temperature heat capacity of the two glass compositions were measured by Differential Scanning Calorimetry (DSC) (fig. 4.13); $\approx 1\ mm^3$ samples were heated up in inert atmosphere from 30 $°C$ to 100 $°C$ at a constant rate of 10 $°C \cdot min^{-1}$, and the specific heat was calculated by calibration against an aluminium oxide standard. The heat capacity of each sample is shown in table 4.2.

The thermal diffusivity of GLS and GLSO samples, which is essential for the heat flow analysis of the calorimetric data, was determined by the Thermal Lens (TL) and Ångström's bar methods. The TL technique measures the time-resolved intensity variation of a probe beam transmitted through a thermal lens, induced in a glass sample by another beam, and is fully described in reference (180). The characteristic formation time of TL in GLS and GLSO was found to be of the order of 1 ms. TL measurements were performed by Dr. S. Lima, University of Sao Paulo, Brasil. In the Ångström's method a sinusoidal thermal wave is made to propagate along a glass rod, and the temporal evolution is evaluated at different lengths (181; 182). The diffusivity is then calculated from the damping factor of the amplitude (R_I) and from the phase difference ($\Delta\phi$) of the thermal wave at two points with separation L (see fig. 4.15), using the

relationship:

$$\kappa = \frac{\pi L^2}{\tau \ \Delta\phi \ \ln(R_I)} \tag{4.7}$$

(where τ is the period of the thermal wave). An 80 mm long, 7 mm diameter extruded GLS rod was used in this second method. The results from the two techniques are shown in table 4.4; the TL technique gave very similar values for GLS and GLSO, and the TL value for GLS is in good agreement with that found by the Ångström's method. Finally, the thermal conductivity k can be obtained from the density ρ, heat capacity C_p and thermal diffusivity κ using the relationship:

$$k \equiv \kappa \rho C_p \tag{4.8}$$

The values of k for GLS and GLSO are given in the last column of the table 4.4.

4.5 Design of the experiment

The experimental setup is detailed in figure 4.18. The FEL was operated in a TEM_{00} mode at 1.55 μm or 1.7 μm, with a sub-ps pulse width and a micropulse repetition rate of 37.4 or 75 MHz. The beam had a diameter of $\approx$14 mm at the exit from the transport line, and was collimated to a diameter of approximately 3 mm using a pair of calcium fluoride lenses. This diameter was sufficiently small to keep the tail of the TEM_{00} mode well separated from the sample holder, and at the same time to maintain a relatively low average power density on the sample ($\leq$0.2 $kW \cdot cm^{-2}$).

A very important aspect in the use of a FEL source was the presence of small amounts of

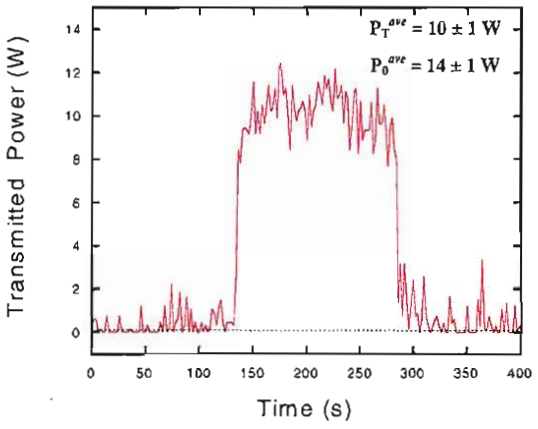

FIGURE 4.16: Transmitted power of a laser pulse.

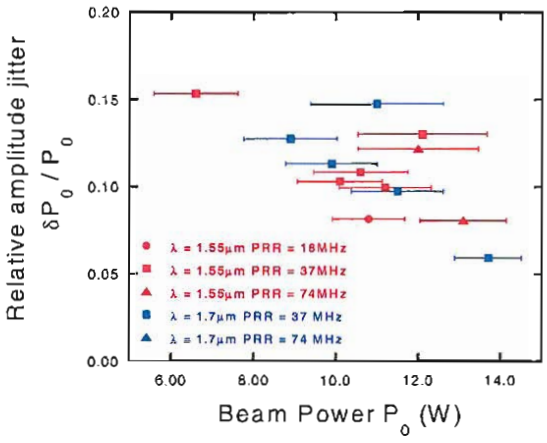

FIGURE 4.17: Power stability of JLFEL source.

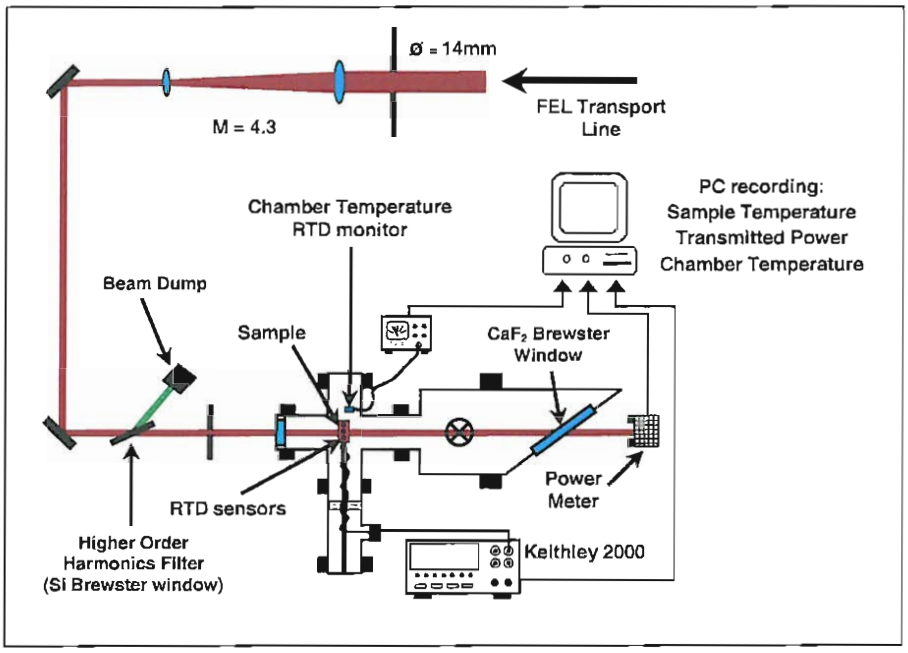

FIGURE 4.18: Layout of the setup for Laser Absorption Calorimetry: beam path, calorimeter and measuring units.

higher order harmonics. In FELS all the odd multiples of the fundamental frequency can undergo optical gain, but in JLFEL the lowest order even multiples are also observed (183). Since the FEL is optimised for operation at the fundamental wavelength, the second and third order harmonics each amount to only 0.1-0.2% of the total power. However, for a fundamental at $\lambda = 1.55\ \mu m$, the third harmonic falls close to the electronic edge, hence in the region of high absorption of GLS. Despite the *absolute* power being low, the amount of *absorbed* power associated with higher order harmonics is still comparable to that due to the 1.55 μm component. In short, the presence of higher order harmonics in the FEL output can affect the calorimetric measurements and must be avoided. A Brewster plate of silicon was used in our setup to filter them out (see fig. 4.18).

The whole calorimeter was mounted on a motorised micropositioner for easy alignment and careful positioning of the optical beam at the center of the sample. The entrance and exit ports of the calorimeter were designed to be as transparent as possible to the laser beam. The entrance port was fitted with a silica window (Spectrosil WF grade, UQG Optics Ltd.). The sample orientation could also be adjusted to ensure that the reflected beam (≈30% of the incident power) was exiting the chamber through the silica window, without disturbing the measurement. The exit port was a calcium fluoride Brewster window, which avoided any backreflections and allowed the full transmitted power out of the chamber. An optical power meter (water cooled Molectron PM5K pyrometric detector), located outside the chamber, measured the transmitted power and also served as beam dump.

FEL sources are generally designed to operate at high powers, and can become unstable when operated at low power levels. Amplitude jitter causes noise and distortion of heating curves, hence it can complicate the analysis of the calorimetric data. We operated JLFEL at 10-25 W, corresponding to an average power on the sample (P_0) of 6-14 W, which produced an excellent signal in our samples. Figure 4.16 shows a time plot of the transmitted power of a 150 s long, $\approx$14 W laser 'heating pulse'; by assuming that the detector noise and the amplitude jitter σ_{P_0} combine quadratically, the latter was estimated as 0.8 W ($\approx 6\%$). The value of σ_{P_0}/P_0 for different values of P_0, wavelength and micropulse repetition rates (MPRRs) is shown in figure 4.17; as expected, the amplitude jitter was increasing with decreasing average power, but was about 10% for $P_0 \geq 10$ W.

The vacuum chamber was operated at about 10^{-3} $mTorr$. In these conditions heat exchange between sample and calorimeter walls was, as seen in section 4.3, irradiation-limited. A dry nitrogen inlet was used to vent the chamber for replacing the samples. Thick polystyrene insulation was placed outside the calorimeter to reduce the amplitude of the temperature fluctuations induced by the external environment. The temperature at the external surface of the chamber was monitored by an RTD element in order to give an indication of slow drifts. Sample temperature data from the Keithley 2000 multimeter, optical power data from the Molectron power meter and chamber temperature data from the external sensor were continuously fed to a computer and remotely monitored from JLFEL's control room.

4.6 Heating curves

Figure 4.19 shows a typical heating curve obtained with the setup described above. The curve refers to sample F (table 4.2), which was irradiated for 210 s with an average power of 12 ± 1 W at 1.7 μm. As the beam was allowed into the transport line and passed

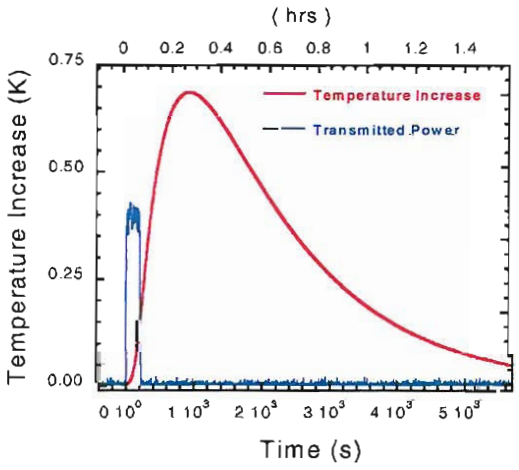

FIGURE 4.19: Laser absorption calorimetry: typical heating curve.

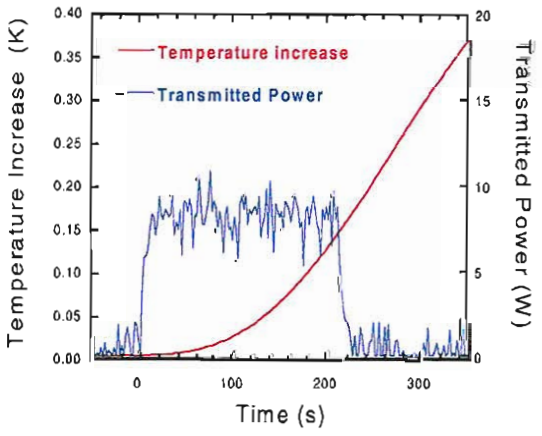

FIGURE 4.20: Initial stage of laser heating

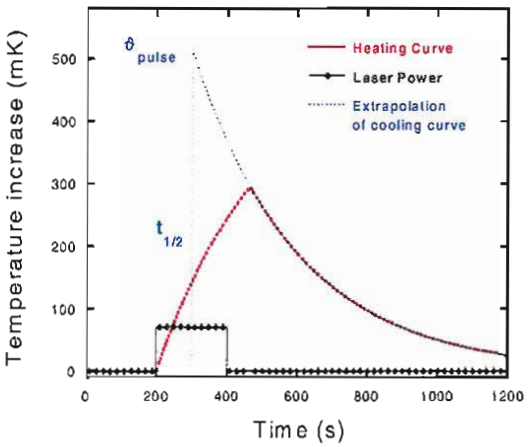

FIGURE 4.21: The pulsed method.

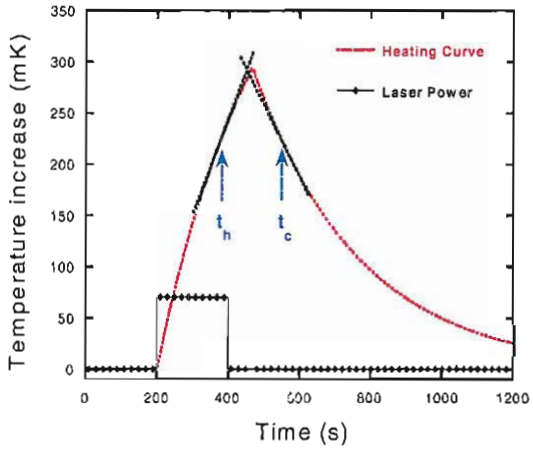

FIGURE 4.22: The gradient method.

through the sample, heating occurred due to absorption. A delay was observed (figure 4.20), which was due to the low thermal conductivity of GLS and GLSO and to contact thermal resistance at the sample/holder and holder/sensors interfaces. The absence of any discontinuity in the heating curves at the instant when the laser beam was turned on/off was also a strong indication that scattering was not affecting the measurement. If a significant amount of light had been scattered by the sample, it would have then caused a direct heating of the sensors, producing a positive and a negative 'kink' at the initial and final time of the heating pulse respectively. A full measurement run, typically 90 minutes long, included recording the background, heating the sample for about 200-300 s and then monitoring the cooling. Three samples were measured for each series in order to determine surface and bulk absorption.

The conventional evaluation methods of calorimetric data are based on the so-called 'homogeneous sample temperature model', which assumes a fast heat equalization within the sample leading to an uniform temperature distribution. According to this model, the time-dependent increase in temperature of the sample, $\vartheta(t) = T_{sample}(t) - T_{chamber}$ is described by a simple differential equation:

$$\frac{d\vartheta(t)}{dt} = \frac{\mathcal{A}P_0}{mC_p} - \gamma_{cal}\vartheta \tag{4.9}$$

where $\mathcal{A}$ is the sample absorptivity, mC_p is the heat capacity of the sample plus the holder, P_0 is the optical power incident on the sample, and γ_{cal} the heat loss coefficient. Assuming a laser pulse of finite duration from $t = t_0$ to $t = t_1$, the solution to equation 4.9 is:

$$\vartheta(t) = \begin{cases} 0 & t < t_0 \\ \frac{\mathcal{A}P_0}{mC_p\gamma}\left(1 - e^{-\gamma(t-t_0)}\right) & t_0 < t < t_1 \\ \frac{\mathcal{A}P_0}{mC_p\gamma}\left(1 - e^{-\gamma(t_1-t_0)}\right)e^{-\gamma(t-t_1)} & t > t_1 \end{cases} \tag{4.10}$$

The ISO standard methods of laser calorimetry (177) are the pulse method (figure 4.21) and the gradient method (figure 4.22). In the former, the cooling curve is extrapolated to a time $t_{1/2\ pulse} = (t_0 + t_1)/2$ and the extrapolated temperature increase, ϑ_{pulse}, is interpreted as the temperature rise equivalent to an amount of heat $Q_{pulse} = P_0 \cdot (t_1 - t_0)$ released instantaneously in the sample at $t_{1/2pulse}$; the absorptivity is then obtained as:

$$\mathcal{A} = \frac{mC_p\vartheta_{pulse}}{Q_{pulse}} \tag{4.11}$$

The gradient method determines the absorptivity from the gradients of the heating and cooling curve, calculated at times t_h and t_c for which $\vartheta(t_h) = \vartheta(t_c)$, according to the following relationship:

$$\mathcal{A} = \frac{mC_p}{P_0} \cdot \left[\frac{d\vartheta(t_h)}{dt} - \frac{d\vartheta(t_c)}{dt}\right] \tag{4.12}$$

These methods give correct results as long as the thermal conductivity of the material under investigation is sufficiently high. This, however, is not the case for glasses, and particularly the chalcogenide glasses, which are as good thermal insulators as, for instance, some common plastic materials. With low thermal conductivity materials, temperature gradients across the samples cannot be ignored; any methods based on the 'homogeneous sample temperature' approximation give a result which is dependent on the position at which the sensors are located and also on the heating time. A correct interpretation of the calorimetric curves then requires the analysis of heat flow within the samples, which will be discussed in the next section.

4.7 Analysis of calorimetric data

As was pointed out in section 4.3, the setup used in the present study differs from the simplified representation of figure 4.2, due to the presence of a sample holder used to hold the sample in place at the center of the vacuum chamber. The holder modifies the thermal properties of the system in two ways: firstly, by increasing its total effective heat capacity; secondly, due to the thermal resistance at the sample/holder interface, by reducing the heat conductivity from the heated volume at the center of the sample towards the points where the temperature is probed by the sensors.

The correct interpretation of the heating curves was achieved by comparing the experimental heating curves with the theoretical predictions of a suitable model. The model describes the unsteady-state heat diffusion within the sample and the holder, taking into account both the finite conductivity of the glass and the interface resistance, and also the radiative losses from all the surfaces. The theoretical heating curves are

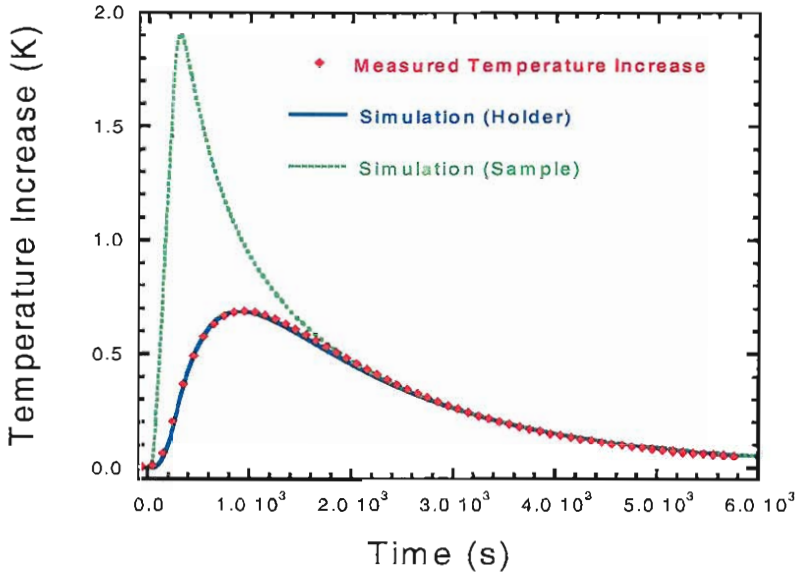

FIGURE 4.23: Comparison between experimental heating curves and theoretical predictions (the curves refer to sample F, measured at 1.7 μm).

TABLE 4.5: Best-fit values of interface and radiation heat exchange coefficients.

Sample	h_c $[Wm^{-2}K^{-1}]$	h_1 $[Wm^{-2}K^{-1}]$	h_2 $[Wm^{-2}K^{-1}]$
G	24 ± 0.5	1.8 ± 0.3	2.1 ± 0.3
E	15 ± 0.5	3.4 ± 0.3	2.4 ± 0.3
F	20 ± 1	4.2 ± 0.3	2.4 ± 0.3
A	27 ± 0.5	1.8 ± 0.3	2.1 ± 0.3
B	20 ± 0.5	2.8 ± 0.3	2.4 ± 0.3
C	10 ± 1	4.8 ± 0.3	2.4 ± 0.3

the time-dependent solutions of a boundary value problem of heat diffusion for a suitable geometry (see figure 5.1). A complete theoretical description of laser absorption calorimetry, including the model used to analyse the data presented in this chapter, is given in Chapter 5.

The calculated theoretical heating curves have then been used to fit the experimental curves. The parameters of the fit are the sample absorptivity, $\mathcal{A}$, the interface conductivity h_C, and the sample-chamber and holder-chamber heat exchange coefficients h_1 and h_2. Figure 4.23 shows a comparison between experimental data and theoretical model, which are in excellent agreement. The dotted curve in the figure is the calculated temperature of the sample in close proximity to the interface; the obvious effect of the contact resistance is to strongly attenuate and delay the thermal wave generated by the laser heating pulse. The best-fit values of the parameters h_C, h_1 and h_2 are given in table 4.5. The dependence of h_1 on the sample thickness are due to geometrical correction

factors required to adapt the model to the actual geometry of the system. The interface conductivity h_c varied slightly from sample to sample, which was probably due to very small out-of-round imperfection of the diameter of the samples affecting the thermal contact with the holder.

The best-fit values of the absorptivity of the samples, $\mathcal{A}$, are given in table 4.8. Measurements were performed at two different wavelengths, 1.55 μm and 1.7 μm, and for different values of the average power and of the micropulse repetition rate, as summarised in table 4.6. The error quoted is the combination of the uncertainty in the average power of the laser beam, and the uncertainty in the subtraction of the baseline temperature. In addition, the uncertainty in the heat capacity of the glass (about 10%, see table 4.4), gives a systematic contribution to the error of $\mathcal{A}$.

TABLE 4.6: Average laser power and duration of the 'heating pulse' used for absorption calorimetry of GLS and GLSO samples.

Sample	**Average power** (P_0^{ave}) and **Pulse duration**			
	MPRR @ $\lambda = 1.55\ \mu m$ $[MHz]$			MPRR @ $\lambda = 1.7\ \mu m$ $[MHz]$
	18.7	37.4	75	37.4
A	$10.8 \pm 1.4W$ for $150s$	-	-	$13.7 \pm 1.3\ W$ for $151\ s$
B	-	$10.1 \pm 1.4W$ for $150s$	$13.1 \pm 1.5W$ for $150s$	-
C	-	$10.6 \pm 1.6W$ for $150s$	-	$8.9 \pm 1.5W$ for $154s$
G	-	$12.1 \pm 2.2W$ for $301s$	-	$9.9 \pm 1.7W$ for $301s$
E	-	$11.2 \pm 1.7W$ for $242s$	$12.0 \pm 2.0W$ for $242s$	$11.0 \pm 2.2W$ for $241s$
F	-	$6.6 \pm 1.9W$ for $601s$	-	$11.5 \pm 1.9W$ for $212s$

4.8 Results and discussion

4.8.1 Damage threshold

The threshold for laser-induced damage (LIDT) of GLS and GLSO glasses is not known. Although time was not available for a systematic investigation, it was necessary, prior to the measurements, to assess if the samples could withstand the optical power levels required to obtain a good temperature signal, without sustaining any damage. This test was performed on two 'dummy' samples, with the same compositions, surface quality

TABLE 4.7: Parameters for successive laser irradiations for LIDT investigation.

P_0^{ave} [W]	Time [s]	MPRR [MHz]	Power density [$kW\ cm^{-2}$]	Peak power density [$MW\ cm^{-2}$]	N. of pulses [10^9]
8 ± 2	180	37.4	0.10	2.6	6.7
15 ± 2	180	37.4	0.18	4.7	6.7
8 ± 2	183	18.7	0.09	4.9	3.3
7 ± 2	180	37.4	0.08	2.1	6.7
7.5 ± 2	792	37.4	0.09	2.4	29.3

and thorough cleaning as the samples used for the measurement. The samples underwent repeated irradiations while operating the laser at different average powers, micropulse repetition rates (MPRRs) and irradiation times, in order to investigate cumulative effects. Table 4.7 shows the list for the GLSO sample. No evidence of damage was observed. The samples were unaltered both visually and when inspected more closely using an optical microscope. Sample transmission did not vary during the irradiation; spectral transmission of all the samples, measured before and after laser calorimetry, also showed no variation. We concluded therefore that GLS and GLSO samples were unaffected, and established a lower limit for the LIDT of these materials around 1.55 μm: $\approx 0.2\ kW \cdot cm^{-2}$ average power density with $\approx 5\ MW \cdot cm^{-2}$ peak power and sub-ps pulses.

4.8.2 Quantification of nonlinear effects

Since GLS and GLSO glasses have strong third order nonlinearity, it was also necessary to ensure that two-phonon absorption (TPA) was not affecting the measurement. The total absorption coefficient of a nonlinear material is:

$$\alpha_{tot} = \alpha + \beta_2 I \tag{4.13}$$

where I is the power intensity and α and β_2 are the linear and nonlinear absorption coefficients respectively. The presence of intensity-dependent absorption can be easily investigated using the flexibility of JLFEL. Figure 4.24 shows the result of this investigation; the first two heating curves refer to the same sample, irradiated for the same time with the same average power. However, the pulse repetition rate was switched from 37.4 to 75 MHz, hence the peak power was approximately halved from the first to the second measurement. If there were a nonlinear component contributing to the total absorption, the reduction of the peak power should have caused a noticeable diminution. As this was not the case in GLS and GLSO samples, we concluded that nonlinear absorption was in fact negligible at the optical power density used. The result is also evident in figure 4.25,

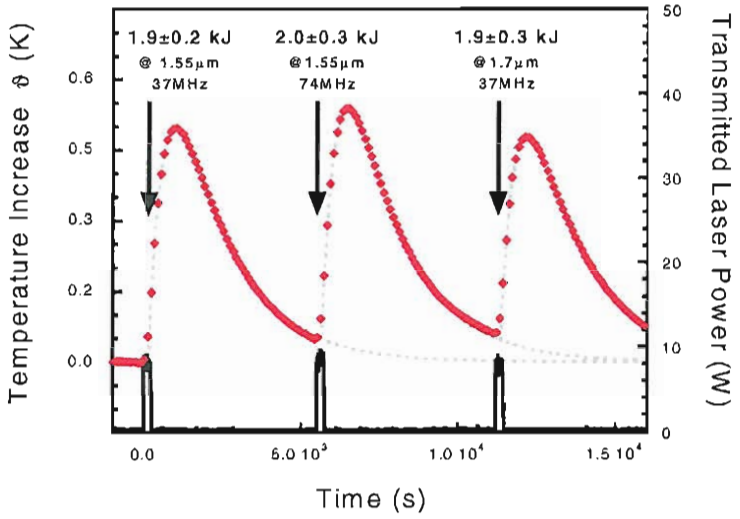

FIGURE 4.24: Heating curves for the same sample irradiated for the same time and at the same average power varying the MPRR and the wavelength.

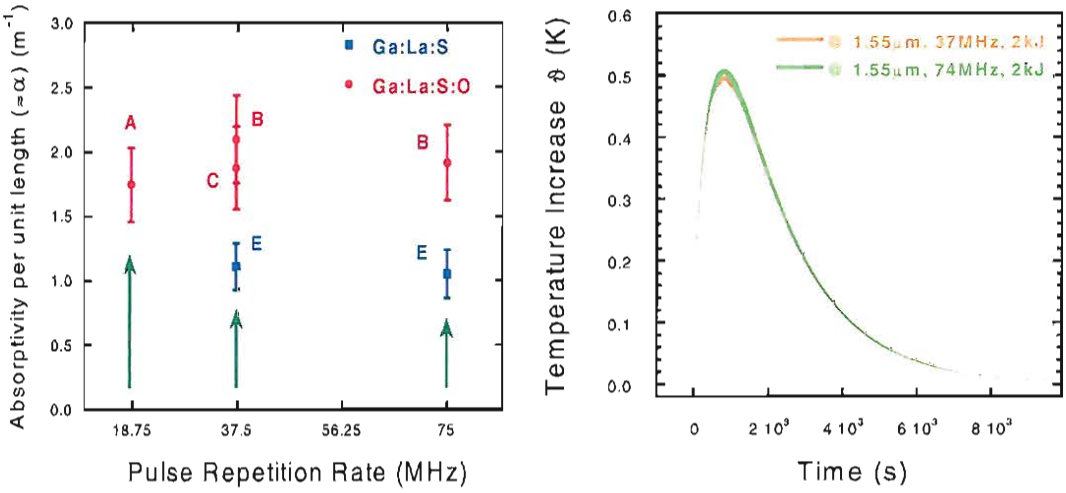

FIGURE 4.25: Measurements of absorptivity at different PRRs for investigation of nonlinear effects. The graph on the right shows the superposition of the heating curves in figure 4.24.

where the absorption coefficients of different samples, measured at different MPRRs, are compared. This result is in agreement with the upper limit of the nonlinear absorption coefficient recently reported by Requejo et al. (54), i.e. $\beta_2 < 0.01\ cm \cdot GW^{-1}$; based on this value of β_2, the nonlinear contribution at the peak power levels of $\approx 5\ MW \cdot cm^{-2}$ used for calorimetry is smaller than $5 \cdot 10^{-5}$.

It is also worth noting that, the repeated measurements for these nonlinear checks showing no difference in the sample's absorption provides further evidence that no damage or permanent changes had occurred in the measured samples.

TABLE 4.8: Results of calorimetric measurements of GLS and GLSO samples.

Sample	Absorptivity $\mathcal{A}$, 10^{-3}			
	MPRR @ $\lambda = 1.55\ \mu m$ $[MHz]$			MPRR @ $\lambda = 1.7\ \mu m$ $[MHz]$
	18.7	37.4	75	37.4
GLSO **A**	3.5 ± 0.6	-	-	3.9 ± 0.5
GLSO **B**	-	6.8 ± 1.1	6.2 ± 0.9	-
GLSO **C**	-	15.9 ± 2.7	-	18.2 ± 3.4
GLS **G**	-	1.5 ± 0.3	-	1.5 ± 0.3
GLS **E**	-	5.8 ± 0.9	5.5 ± 1.0	5.5 ± 1.1
GLS **F**	-	7.8 ± 2.2	-	8.4 ± 1.4

4.8.3 Determination of the absorption coefficient at 1.55 μm and 1.7 μm

The measured values of absorptivity $\mathcal{A}$ of the GLS and GLSO samples are shown in table 4.8. Data are available for three different thicknesses for each glass composition. For thin samples and for low absorption, the absorptivity can be assumed to be linearly dependent on the sample thickness L, according to the following relationship (see Appendix B for details):

$$\mathcal{A} \approx 2\sigma + \alpha L \tag{4.14}$$

The relationship 4.14 expresses the fact that the optical absorption can occur both at the surface and in the bulk. The term 2σ takes into account the localised absorption at the air/sample interfaces, which can be caused either by defects and residues from polishing, or by contamination. The quantity σ is the surface absorptivity, i.e. the fraction of the total optical power that is absorbed at each interface. The other term is the usual bulk absorption described through the Lambert-Beer's law, and α is the absorption coefficient.

From the data obtained for the two sets of samples, both σ and α can now be determined. Figures 4.26 and 4.27 show a plot of the absorptivity, $\mathcal{A}$, as a function of the sample

TABLE 4.9: Surface absorptivity and bulk absorption coefficients of GLS and GLSO samples.

	$\lambda = 1.55\ \mu m$		$\lambda = 1.7\ \mu m$	
	$\sigma\ [10^{-3}]$	$\alpha\ [m^{-1}]$	$\sigma\ [10^{-3}]$	$\alpha\ [m^{-1}]$
GLS	$0^{+0.7}_{-0}$	1.0 ± 0.1	$0^{+0.9}_{-0}$	1.1 ± 0.2
GLSO	$0.2^{+0.5}_{-0.2}$	1.9 ± 0.15	$0^{+0.3}_{-0}$	2.1 ± 0.2

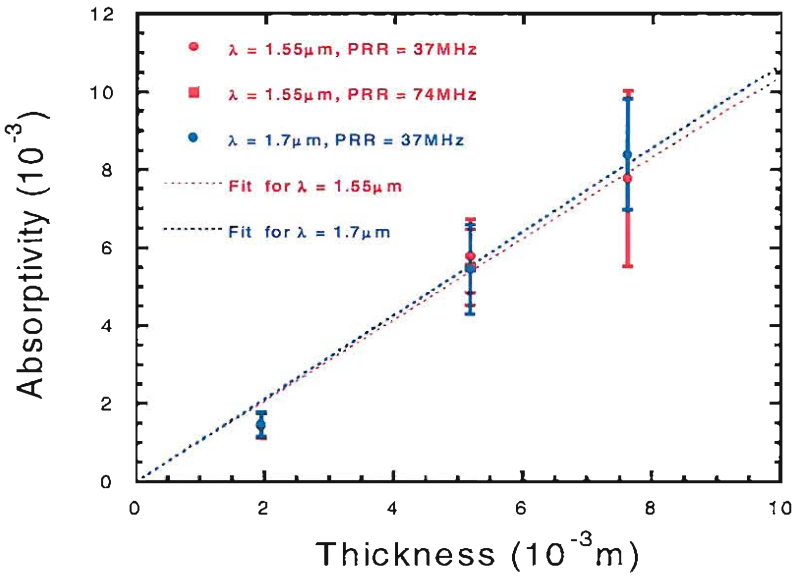

FIGURE 4.26: Plot of the absorptivity as a function of the sample thickness for GLS samples G, E, F.

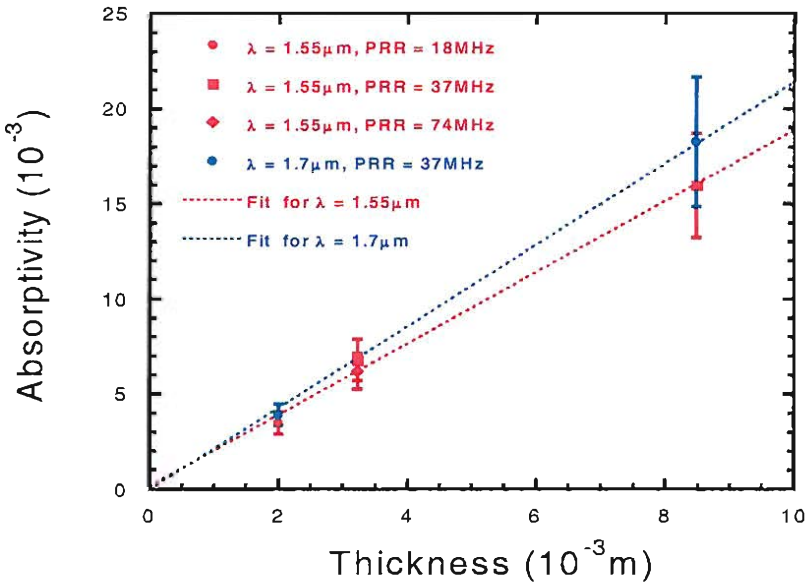

FIGURE 4.27: Plot of the absorptivity as a function of the sample thickness for GLSO samples A, B, C.

thickness for GLS and GLSO respectively. Both data at 1.55 μm and 1.7 μm are given in the graphs. The experimental data are in excellent agreement with the linear law 4.14, and clearly show that surface absorption has a minor contribution in our samples. Data were fitted by the least-squares method, using a linear law and assuming the constraint $\sigma \geq 0$. Since it was verified that the micropulse repetition rate did not affect the measurement, all the data points collected at the same wavelength could be fitted with the same linear law. The resulting values of the absorption coefficient α, and the surface absorptivity σ are summarised in table 4.9.

The original aim of the experiment was to measure the absorption at other wavelengths in the range covered by JL-FEL. Unfortunately, time was not available to perform measurements at 2 and 3 μm, so these measurements had to be rescheduled and will be performed after the upgrade of JL-FEL is completed. The two data points at 1.55 and 1.7 μm, however, provide some information. The dependence of the absorption on the wavelength is flat for both GLS and GLSO; this is not unexpected, since absorption in this region can either be caused by the weak tail, or by extrinsic absorption from transition metal impurities, which have very broad absorption bands in the near-IR. Absorption of GLSO is higher than low oxide GLS, and also increases from 1.55 μm to 1.7 μm; since the fundamental edge of GLSO falls $\approx$ 70 nm shorter wavelength than GLSO, this result suggests that the higher absorption in GLSO is caused by impurities. However, a clear interpretation of the mechanisms causing absorption was not possible with so few data points. This will be the subject of a more detailed discussion in Chapter 6, where the optical absorption induced by transition metal impurities will be investigated.

4.9 Conclusions

In this chapter the results of a calorimetric measurement of the absorption of a set of GLS and GLSO samples was presented. Bulk absorption had not been measured previously in these glasses. The calorimetric method was used in conjunction with a FEL source to achieve measurements at 1.55 and 1.7 μm; a free-electron laser had never been used before for laser absorption calorimetry. The FEL at the Jefferson Laboratories is very suitable due to its high average power, high beam quality, tunability and to the ability to work from 1 to 6 μm. A calorimeter was designed and assembled, based on a vacuum chamber with resistive temperature sensors and an ultimate resolution of better than a mK. Two sets of GLS and GLSO samples were prepared, cut from the same batch of high purity glass and then polished to a high standard; the samples had different thickness allowing separation of the bulk absorption component from any surface absorption. The density, thermal diffusivity and heat capacity of the GLS and GLSO samples were measured by various techniques. A detailed analysis was performed, prior to the calorimetric measurements, in order to rule out laser-induced damage and nonlinear effects. The heating curves were analysed, performing the complete heat flow analysis of the system. The measured absorptivity is in good agreement with a linear dependence on the sample thickness, showing that the samples had no significant surface absorption. The absorption coefficients at 1.55 μm were 1.0 ± 0.1 and 1.9 ± 0.2 m^{-1} for GLS and GLSO respectively, corresponding to 4.3 ± 0.4 and 8.2 ± 0.9 $dB \cdot m^{-1}$. More measurements at different wavelengths could provide conclusive evidence as to what mechanism is causing the absorption loss, whether the 'extrinsic' impurity absorption or the weak absorption tail. However, the measurements presented in this chapter provide

for the first time an important determination of the levels of near-IR optical absorption of GLS and GLSO glasses.

Chapter 5

Modeling Laser Absorption Calorimetry: Heat Flow Analysis

5.1 Introduction

Laser absorption calorimetry is an established technique for measuring low-level optical absorption, such as that of optical components for high-power lasers. The technique has been described in the ISO 11551 (177), which attempted to define a standard for the measurement procedure and data analysis. However, the ISO standard has some important limitations. Firstly, it assumes a 'homogeneous sample temperature' model. Thus, the ISO standard is only suitable for samples with high thermal conductivity, such as metal mirrors and crystal optics. Glasses, on the contrary, have much lower thermal conductivities; that of GLS, 0.55 $Wm^{-1}K^{-1}$, compares, for instance, with 392.9 and 17.8 $Wm^{-1}K^{-1}$ of copper and zinc selenide respectively, which are commonly used in CO_2 optics. Low thermal conductivity leads to inhomogeneous temperature distributions within the samples, and renders the ISO standard method not applicable (184). A second limitation of the ISO 11551 standard concerns the use of a sample holder; although the ISO recommends the use of a holder, it only considers its impact on the total thermal capacity, and ignores the possible effect due to the thermal resistance at the interface between sample and holder. This aspect, on the contrary, is quite important, since the temperature sensors are generally located on the holder. Inhomogeneous sample temperature models, accounting for the finite thermal conductivity of glass samples, have been presented by Bernal (185) and, more recently, by Willamowski, et al. (186), but sample holder effects were not included in those models.

In this chapter an exhaustive model for the heat flow analysis in a laser absorption calorimetry experiment will be presented. The model describes a system composed of sample and holder with arbitrary thermal properties and a cylindrical geometry and, more importantly, it allows for an arbitrary thermal resistance at the sample/holder

interface. By solving the boundary value problem of heat diffusion, analytical solutions are provided for the time-dependent temperature distribution across the sample and the holder. The model extends considerably the theoretical analysis of laser calorimetry presented in the ISO 11551 and in other previous works (185; 186).

The chapter is structured as follows. The general boundary value problem of heat diffusion, describing laser absorption calorimetry, is defined in the next section 5.2. Section 5.3 gives a summary the standard mathematical tool for solving the boundary value problem (Green's functions method). A simplified model of a sample with no holder is presented in section 5.4; results are in agreement with previous work by Bernal (185) and Willamoski, et al. (186). Finally, in section 5.5, a more general, and substantially new model describing sample and holder is presented and analytical solutions are given.

5.2 General formulation of the problem

5.2.1 Boundary value problem of heat diffusion in cylindrical coordinates

The system considered in the present model is shown in figure 5.1. The aim is to model the heat diffusion from the area heated by the laser, at the center of the sample, towards the sample holder, where the sensors are attached. As the laser is turned on only for a finite time interval, a transient, unsteady heat diffusion problem must be formulated. The sample is assumed to be disc-shaped, and the holder is assumed to be annular, with the inner radius matching that of the sample. A TEM_{00} intensity distribution is assumed for the laser beam, producing a gaussian power deposition profile within the sample; the diameter of the beam is much smaller than the diameter of the sample. The sample and holder are thermally insulated inside a vacuum chamber, and can only exchange heat through radiation.

Given the symmetry of the system, the problem is conveniently described by using

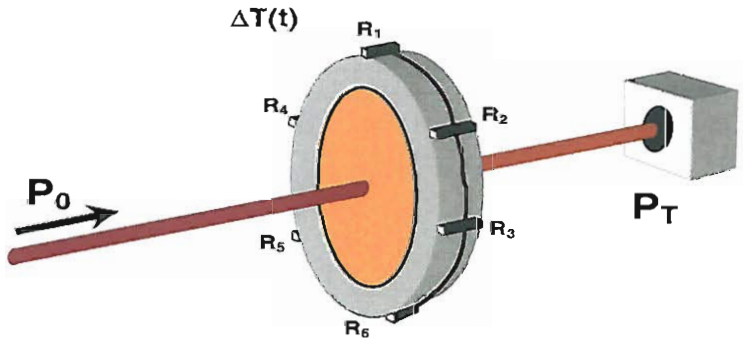

FIGURE 5.1: Schematic of the calorimetric system with sample and holder.

cylindrical coordinates, with the 'z' axis parallel to the direction of propagation of the laser beam. Since the system has rotational symmetry about z ($Q = Q(r, z, t)$), the temperature distribution is independent of the ϑ coordinate, thus the heat diffusion equation is:

$$\left[\partial_r^2 + \frac{1}{r} \cdot \partial_r + \partial_z^2 - \frac{\partial_t}{\kappa}\right] T_s(r, z, t) = -\frac{Q(r, z, t)}{k} \tag{5.1}$$

where κ is the thermal diffusivity and k is the thermal conductivity ($k = \kappa \rho C_p$); T_s is the temperature distribution and Q is the absorbed energy ('heat') per unit time and unit volume. The boundary value problem (BVP) is defined by a set of two equations, like 5.1, for the sample and for the holder, plus a suitable set of boundary conditions and initial values. For instance, the boundary conditions for a disc-shaped sample with radius R, thickness L and radiative loss from all surfaces are:

$$\begin{cases} \partial_r T_s(0, z, t) = 0 & \text{Continuity at } r = 0 \\ -k \cdot \partial_r T_s(R, z, t) = h_{sc} \cdot [T_s(R, z, t) - T_\infty] & \text{Radiative heat flow from side face} \\ k \cdot \partial_z T_s(r, 0, t) = h_{sc} \cdot [T_s(r, 0, t) - T_\infty] & \text{Radiative heat flow from flat face 1} \\ -k \cdot \partial_z T_s(r, L, t) = h_{sc} \cdot [T_s(r, L, t) - T_\infty] & \text{Radiative heat flow from flat face 2} \end{cases} \tag{5.2}$$

In the above equations, T_∞ represents the temperature of the inner surface of the vacuum chamber. Since the temperature increase $T_s(r, z, t) - T_\infty$ is small, the following first-order approximation for the radiative heat flows has been assumed in writing 5.2:

$$\sigma_{SB} \varepsilon_s \mathcal{F} \left[T_s^4(r, z, t) - T_\infty^4\right] \approx 4 \sigma_{SB} \varepsilon_s \mathcal{F} T_\infty^3 \left[T_s(r, z, t) - T_\infty\right] \tag{5.3}$$

where σ_{SB} is the Stefan-Boltzmann constant, ε_s is the sample's emissivity and and $\mathcal{F}$ is a factor approximately equal to 1 (see eqn. 4.5 and 4.6); thus, the heat exchange coefficient in 5.2 results: $h_{sc} \equiv 4 \sigma_{SB} \varepsilon_s \mathcal{F} T_\infty^3$. The boundary conditions 5.2 are non-homogeneous, but it is immediately obvious that they can be modified into a set of homogeneous boundary conditions by defining a *reduced temperature*:

$$T(r, z, t) \equiv T_s(r, z, t) - T_\infty \tag{5.4}$$

5.2.2 Definition of the heat source term $Q(r, z, t)$

In the present model an 'ideal' source, with single mode operation and a TEM_{00} (gaussian) intensity distribution, is considered. The 'uniform heat source approximation' (see

Appendix B for details), was assumed for the absorbed heat distribution; this approximation is correct for low absorption levels, optically thin samples, and for a laser source heating a small portion at the center of the sample (thus preventing the beam from heating the holder). With these assumptions, the heat distribution $Q(r,z)$ of 5.2 can be written:

$$Q(r,z) = \frac{2\mathcal{A}P_0}{\pi d^2 L} \cdot e^{-2\left(\frac{r}{d}\right)^2} \tag{5.5}$$

where: $\mathcal{A} \approx (2\sigma + \alpha L)$ is the total absorptivity, with σ the surface absorptivity and α the absorption coefficient (see Appendix B for definitions); P_0 is the average power of the laser beam, and d is its mode radius ($d \ll R$). The time dependence of Q is defined as:

$$Q(r,z,t) = Q(r,z) \cdot [\phi(t) - \phi(t-t_0)] \tag{5.6}$$

where $\phi(t)$ is the Heaviside 'step' function. Equation 5.6 describes an experiment in which the laser beam is 'on' between $t = 0$ and $t = t_0$. The heat source term is normalised in such a way that:

$$\int_0^\infty dt \int_0^R \varrho d\varrho \int_0^{2\pi} d\vartheta \int_0^L dz \cdot Q(\varrho,z,t) = \mathcal{A}P_0 t_0 = \{\text{absorbed heat}\} \tag{5.7}$$

5.2.3 Approximate description for thin samples

If the sample thickness L is small, the longitudinal dependence of the temperature can be neglected. This is achieved by reducing the '∂_z^2' term in the heat diffusion equation to a constant term through the following approximation, obtained by letting $L \to 0$ and using the last two of the boundary conditions 5.2:

$$\left[\partial_z^2 T(r,z,t)\right]_{L\to 0} \approx k \cdot \frac{\partial_z T(r,L,t) - \partial_z T(r,0,t)}{kL} = -\frac{2h_{sc}}{kL} \cdot T(r,\frac{L}{2},t) \tag{5.8}$$

The BVP 5.1-5.2 is then effectively reduced to a 1-d problem, where the differential equation 5.1 depends only on the radial variable:

$$\left[\partial_r^2 + \frac{1}{r} \cdot \partial_r - \frac{2h_{sc}}{kL} - \frac{\partial_t}{\kappa}\right] T(r,t) = -\frac{Q(r,t)}{k} \tag{5.9}$$

The approximation 5.8 will be proved in section 5.4.5 to be accurate to better than 1% for GLS samples up to 1 *cm* thick. The approximation of 'thermally thin sample' is at

the basis of the procedure of analytical solution of the BVP for the system with sample and holder (section 5.5).

5.3 Solution of boundary value problems by the Green's function method

In this section a method is presented for deriving the solutions of a general boundary value problem of heat diffusion, from the solutions of the associated homogeneous BVP, using the so-called Green's functions method. The approach to the solution of the problem is the same as presented in chapter 6 of reference (187), where the detailed demonstration of the assertions made in this section can be found. In general, linear BVPs are classified as *homogeneous* or *non-homogeneous*. In the first case, both the differential equation and the boundary conditions are homogeneous (if f is a solution, $c \cdot f$ is a solution for every $c \in \mathbf{R}$). The solutions of a homogeneous problem constitute a linear vector space (if f and g are solutions, $\alpha f + \beta g$ is also a solution), which contains at least the trivial solution; the initial conditions then define a unique solution in this vector space.

Let us consider the following non-homogeneous problem of heat diffusion, defined in the most general form by the following:

$$\begin{cases} \nabla^2 T(\mathbf{r},t) - \frac{1}{\kappa}\partial_t T(\mathbf{r},t) = -\frac{1}{k}Q(\mathbf{r},t) & \forall\ \mathbf{r} \in \mathbf{V},\ \ t \geq 0 \\ k_i \frac{\partial T}{\partial n_i}(\mathbf{r},t) + h_i T(\mathbf{r},t) = f_i(\mathbf{r},t) & \text{on the boundary } S_i,\ t \geq 0 \\ T(\mathbf{r},0) = \Theta(\mathbf{r}) & \forall\ \mathbf{r} \in \mathbf{V} \end{cases} \tag{5.10}$$

The problem is defined in a 3-d region $\mathbf{V} \subset \mathbf{R^3}$, bounded by M surfaces $S_1, \ldots, S_M$; the coordinate system can either be rectangular, cylindrical or spherical. The three equations 5.10 are respectively: the heat diffusion equation, a set of boundary conditions for the M boundary surfaces and an arbitrary initial condition for the temperature distribution. In the second equation, the $\frac{\partial}{\partial n_i}$ symbol indicates the differentiation along the outward-drawn normal to the i-th boundary surface, and the thermal conductivity k_i and heat exchange coefficient h_i can also assume an arbitrary value. Thus, it represent a set of arbitrary boundary conditions, that can either be of the first, second or third type, as defined by the following:

$$\begin{cases} k_i = 0, h_i \neq 0 & \Rightarrow & T(\mathbf{r},t) = cost & \Rightarrow & \text{Condition of the 1st kind} \\ h_i = 0, k_i \neq 0 & \Rightarrow & k_i \frac{\partial T}{\partial n_i}(\mathbf{r},t) = cost & \Rightarrow & \text{Condition of the 2nd kind} \\ k_i \neq 0 \neq h_i & \Rightarrow & k_i \frac{\partial T}{\partial n_i}(\mathbf{r},t) + h_i T(\mathbf{r},t) = f_i(\mathbf{r},t) & \Rightarrow & \text{Condition of the 3rd kind} \end{cases} \tag{5.11}$$

The first two boundary conditions defined above correspond respectively to the situation where either the temperature or the heat flux at the i-th boundary is fixed; the third condition describes a case where the heat flux is proportional to the temperature for $f_i = 0$ (that is, the case of radiative loss), or the most general case for $f_i \neq 0$.

It can be verified that the solution of the BVP 5.10 can be expressed as:

$$\begin{aligned} T(\mathbf{r},t) = & \int_{\mathbf{V}} d\mathbf{r}' \left[G(\mathbf{r},t|\mathbf{r}',\tau)\right]_{\tau=0} \Theta(\mathbf{r}') \\ & + \frac{\kappa}{k} \int_0^t d\tau \int_{\mathbf{V}} d\mathbf{r}' \left[G(\mathbf{r},t|\mathbf{r}',\tau) Q(\mathbf{r}',\tau)\right] \\ & + \kappa \int_0^t d\tau \sum_{i=1}^{M} \left\{ \int_{S_i} dS_i' \left[\frac{1}{k_i} f_i(\mathbf{r}',t) G(\mathbf{r},t|\mathbf{r}',\tau)\right]\right\} \end{aligned} \tag{5.12}$$

where $G(\mathbf{r},t|\mathbf{r}',\tau)$ is the *three dimensional Green's function* defined by the following auxiliary BVP:

$$\begin{cases} \nabla^2 G(\mathbf{r},t|\mathbf{r}',\tau) - \frac{1}{\kappa}\partial_t G(\mathbf{r},t|\mathbf{r}',\tau) = -\frac{1}{\kappa}\delta(\mathbf{r}-\mathbf{r}')\delta(\tau-\tau') & \forall\ \mathbf{r} \in \mathbf{V},\ t \geq \tau \\ k_i \frac{\partial G}{\partial n_i}(\mathbf{r},t) + h_i T(\mathbf{r},t) = 0 & \text{on the boundary } S_i,\ t \geq \tau \\ G(\mathbf{r},t|\mathbf{r}',\tau) = 0 & \forall\ \mathbf{r} \in \mathbf{V}, t \leq \tau \end{cases} \tag{5.13}$$

The $G(\mathbf{r},t|\mathbf{r}',\tau)$, gives the temperature solution in the region $\mathbf{V}$, which is initially (at $t = \tau$) at zero temperature and subjected to homogeneous boundary conditions, due to an *impulsive point heat source of strength unity*, located at $\mathbf{r}'$, and releasing heat from time $t = \tau$. In other words: $G(\mathbf{r},t|\mathbf{r}',\tau)$ describes the effect, in $\mathbf{r}'$ at t, of an impulsive point heat source of strength unity turned on at $t = \tau$ in $\mathbf{r}'$.

The Green's function relative to the BVP 5.10 can be calculated directly from the solutions of the homogeneous BVP associated to 5.10, i.e.:

$$\begin{cases} \nabla^2 T(\mathbf{r},t) - \frac{1}{\kappa}\partial_t T(\mathbf{r},t) = 0 & \forall\ \mathbf{r} \in \mathbf{V},\ \ t \geq 0 \\ k_i \frac{\partial T}{\partial n_i}(\mathbf{r},t) + h_i T(\mathbf{r},t) = 0 & \text{on the boundary } S_i,\ t \geq 0 \\ T(\mathbf{r},0) = \Theta(\mathbf{r}) & \forall\ \mathbf{r} \in \mathbf{V} \end{cases} \tag{5.14}$$

The problem 5.14 is solved by standard separation of the variables; this is accomplished by looking for all the solutions of the type: $T(\mathbf{r},t) = \Psi(\mathbf{r})\ \Gamma(t)$, where $\Psi(\mathbf{r}) \equiv \varphi(r_1)\ \chi(r_2)\ \psi(r_3)$. It can be verified that the Green's function $G(\mathbf{r},t|\mathbf{r}',\tau)$ can then be

expressed by means of the eigenfunctions $\Psi(\mathbf{r})$ and $\Gamma(t)$ via the following:

$$G(\mathbf{r},t|\mathbf{r}',\tau)=\sum_{i,j,k}\frac{\Psi_{i,j,k}(\mathbf{r})\Psi_{i,j,k}(\mathbf{r}')}{N_{ijk}\cdot\Gamma_{ijk}(0)}\cdot\Gamma_{ijk}(t-\tau) \tag{5.15}$$

where $N_{ijk}\equiv\|\varphi_i\|^2\|\chi_j\|^2\|\psi_k\|^2$, and $\|f\|^2\equiv\langle f|f\rangle$ is the usual norm in a Hilbert space of functions.

In conclusion, the Green's functions method provides a general method to calculate the analytical solutions of a generic boundary value problem of heat diffusion. Firstly, the homogeneous BVP associated with the original is obtained, by putting the heat sources and possible non-homogeneous terms in the boundary conditions to zero, and its solutions are found. Then, the Green's function is calculated, by using the relationship 5.15. Ultimately, from the Green's function, the solutions of the general problem are found using the relationship 5.12.

5.4 Boundary value problem for a disc-shaped sample

5.4.1 Definition

In this section the simpler problem of the sample with no holder is analysed. As specified in the introduction, this system has already been described in previous works by Bernal (185) and Willamoski, et al. (186), although these authors utilise a different method for the solution of the BVP. The Green's functions method allows a quick and elegant way to solve the BVP, and also can be adapted for the solution of the complete system with sample and holder, which will be presented in section 5.5. This method The system is shown in figure 4.2. The BVP is formulated as follows; the heat diffusion equation for the reduced temperature 5.4 is the eqn. 5.1:

$$\left[\frac{1}{r}\cdot\partial_r\left(r\cdot\partial_r\right)+\partial_z^2-\frac{\partial_t}{\kappa}\right]T(r,z,t)=-\frac{Q(r,t)}{k} \tag{5.16}$$

defined in the region $(r,z)\in[0,R]\times[0,L]\subset\mathbf{R}^2$; the boundary conditions are (see eqn. 5.2):

$$\begin{cases}\partial_r T(0,z,t)=0 & \text{Continuity at } r=0\\ -k\cdot\partial_r T(R,z,t)=h_{sc}\cdot T(R,z,t) & \text{Radiative heat flow from side face}\\ k\cdot\partial_z T(r,0,t)=h_{sc}\cdot T(r,0,t) & \text{Radiative heat flow from flat face 1}\\ -k\cdot\partial_z T(r,L,t)=h_{sc}\cdot T(r,L,t) & \text{Radiative heat flow from flat face 2}\end{cases} \tag{5.17}$$

where k, κ are appropriate material constants for the sample and h_{sc} is defined by eqns. 4.5 and 4.6. The initial value of the reduced temperature distribution is:

$$T(r,z,0) = 0 \quad \forall\ (r,z) \in [0,R] \times [0,L]. \tag{5.18}$$

The $Q(r,t)$ is the heat distribution generated by the absorption of a laser beam with a gaussian intensity distribution of semi-aperture ('radius') d and average power P_0, which, in the limit of the 'uniform heat source' approximation, can be written as in the eqns. 5.6-5.7:

$$Q(r,t) = \frac{2AP_0}{\pi d^2 L} \cdot e^{-2\cdot\left(\frac{r}{d}\right)^2} \cdot [\phi(t) - \phi(t-t_0)] \tag{5.19}$$

5.4.2 Solution of the homogeneous problem ($Q = 0$)

Equation 5.16 is solved by separation of variables. As a first step, the time variable is separated from the other space variables by assuming a solution in the form $T(r,z,t) = \Psi(r,z) \cdot \Gamma(t)$ and obtaining:

$$\frac{1}{\Psi(r,z)}\left[\frac{1}{r}\cdot\partial_r\left(r\cdot\partial_r\right) + \partial_z^2\right]\Psi(r,z) = \frac{1}{\kappa\Gamma(t)}\frac{d\Gamma(t)}{dt} \tag{5.20}$$

In order for the last equation to be true for all the values of the space and time variables, each term must equal the same separation constant. Let us define this constant as $-\lambda^2$ ($\lambda \in \mathbf{R}$); two separated equations are then obtained:

$$\begin{cases} \frac{d\Gamma(t)}{dt} + \kappa\lambda^2\Gamma(t) = 0 \\ \frac{1}{\Psi(r,z)}\left[\frac{1}{r}\cdot\partial_r\left(r\cdot\partial_r\right) + \partial_z^2\right]\Psi(r,z) = -\lambda^2 \end{cases} \tag{5.21}$$

The solutions of these equations must satisfy the boundary conditions, and must also be consistent with the physical constraint; hence, the separation constant λ must be a negative number, otherwise the time-variable equation would allow diverging solutions for $t \to \infty$. Assuming further separation of the space variables, $\Psi(r,z) = F(r)H(z)$, the second equation becomes:

$$\frac{1}{F(r)}\left(F''(r) + \frac{F'(r)}{r}\right) + \frac{H''(z)}{H(z)} = -\lambda^2 \tag{5.22}$$

Again, in order for this equation to be satisfied by all the values of the independent variables r and z, the two ratios in the left-hand side must separately equal a constant,

say $-\beta^2$ and $-\alpha^2$ respectively (and $-\alpha^2 - \beta^2 = -\lambda^2$). Summarising, separation of variables yields the following system of equations:

$$\begin{cases} \Gamma'(t) + \kappa(\alpha^2 + \beta^2)\Gamma(t) = 0 \\ H''(z) + \alpha^2 H(z) = 0 \\ F''(r) + F'(r)/r + \beta^2 F(r) = 0 \end{cases} \tag{5.23}$$

This is clearly an eigenvalue problem for linear differential operators, of which the solutions are determined by the boundary conditions 5.17. The general solutions for the three equations 5.23 are:

$$\begin{cases} \Gamma(t) \propto e^{-\kappa(\alpha^2+\beta^2)t} \\ H(z) \propto B_1 \sin(\alpha z) + B_2 \cos(\alpha z) \\ F(r) \propto C_1 J_0(\beta r) + C_2 Y_0(\beta r) \end{cases} \qquad -\alpha^2 - \beta^2 < 0 \tag{5.24}$$

where the quantities B_1, B_2, C_1 and C_2 are arbitrary constants and $J_0(x)$, $Y_0(x)$ are zero-order Bessel functions. The 'proportional to' symbol is introduced here to stress that, since the equations 5.23 are linear and homogeneous, the solutions are family of functions $\{cf(r,z,t)\}_{c\in\mathbf{R}}$. The first two boundary conditions 5.17 provide conditions on the arbitrary constants, while the second two provide equations for the eigenvalues.

$$(5.17\ i) \rightarrow k\beta \cdot [C_1 J_1(\beta r) + C_2 Y_1(\beta r)]_{r=0} = 0 \quad \Leftrightarrow \quad C_2 = 0 \tag{5.25}$$

$$(5.17\ ii) \rightarrow B_2 = \frac{\alpha}{H} B_1 \tag{5.26}$$

$$(5.17\ iii) \rightarrow \beta J_1(\beta R) = H J_0(\beta R) \qquad \text{with:} \quad H \equiv \frac{h_{sc}}{k} \tag{5.27}$$

$$(5.17\ iv) \rightarrow \tan(\alpha L) = \frac{2\alpha H}{\alpha^2 - H^2} \tag{5.28}$$

Equations 5.27 and 5.28 provide transcendental equations for the determination of the eigenvalues for the space variable eigenfunctions. Note that $\alpha = 0$ is not acceptable as a solution of eqn. 5.28 because it leads to a null eigenvector. The corresponding eigenfunctions are then:

$$\begin{cases} \Gamma(t) \propto e^{-\kappa(\alpha^2+\beta^2)t} \\ H(z) \propto \sin(\alpha z) + \frac{\alpha}{H} \cos(\alpha z) \\ F(r) \propto J_0(\beta r) \end{cases} \qquad \alpha^2 + \beta^2 > 0 \tag{5.29}$$

The only constraint on the eigenvalues is $\alpha^2 + \beta^2 > 0$. However, the problem under examination falls within the category of the '*Sturm-Liouville*' boundary value problems;

thus, the eigenvalues can only assume real, non-negative values (188). It then follows that only the positive roots of the equations 5.27, 5.28 need to be considered.

Once the eigenvalues $\{\alpha_i\}$ and $\{\beta_j\}$ and the corresponding eigenfunctions 5.29 are determined, the general solution for the homogeneous problem is obtained by a linear combination (with arbitrary coefficients $c_{ij} \in \mathbf{R}$) of all the solutions:

$$T(r,z,t) = \sum_{i,j} c_{ij} J_0(\beta_i r) \left[\sin(\alpha_j z) + \frac{\alpha_j}{H}\cos(\alpha_j z)\right] e^{-\kappa(\alpha_j^2+\beta_i^2)t} \qquad H = \frac{h_{sc}}{k} \tag{5.30}$$

5.4.3 Solution of the non-homogeneous problem ($Q \neq 0$)

As seen in section 5.3, once the homogeneous problem with no heat source has been solved, the Green's function method provides a straightforward way to determine the solution of the general BVP of heat diffusion with $Q \neq 0$. The first step is to derive the Green's function by using the expression given in eqn. 5.15:

$$G(\mathbf{r},t|\mathbf{r}',\tau) = \sum_{i,j,k} \frac{\Psi_{i,j,k}(\mathbf{r})\Psi_{i,j,k}(\mathbf{r}')}{N_{ijk}\cdot\Gamma_{ijk}(0)} \cdot \Gamma_{ijk}(t-\tau) \tag{5.31}$$

In the present problem, the following substitutions must be performed in the eqn. 5.31:

$$\Psi_{i,j,k}(\mathbf{r}) \implies F_i(r)H_j(z) = J_0(\beta_i r)\left[\sin(\alpha_j z) + \frac{\alpha_j}{H}\cos(\alpha_j z)\right] \tag{5.32}$$

$$\Gamma_{ijk}(t-\tau) \implies e^{-\kappa(\alpha_j^2+\beta_i^2)(t-\tau)}, \qquad \Gamma_{ijk}(0) \implies 1 \tag{5.33}$$

$$N_{ijk} = \|\Psi_{i,j,k}(\mathbf{r})\|^2 \implies \|F_i(r)\|^2 \|H_j(z)\|^2 \tag{5.34}$$

The two norms appearing in eqn. 5.34 can be expressed as:

$$\|F_i(r)\|^2 = \int_0^R r'|J_0(\beta_i r')|^2 dr' = \frac{R^2}{2}\left[J_0(\beta_i R)\right]^2\left[1+\frac{H^2}{\beta_i^2}\right] \tag{5.35}$$

$$\|H_j(z)\|^2 = \int_0^L \left|\sin(\alpha_j z') + \frac{\alpha_j}{H}\cos(\alpha_j z')\right|^2 dz' = \frac{1}{H} + \frac{L}{2}\left[1+\frac{\alpha_j^2}{H^2}\right] \tag{5.36}$$

where the following identity: $\int u J_0^2(u)du = \frac{u}{2}[J_0^2(u) + J_1^2(u)]$, and the boundary conditions 5.27, 5.28 were used to simplify the expressions. The Green's function 5.31 is then written as:

$$G(r,z,t|r',z',\tau) = \sum_{i,j} \frac{F_i(r)H_j(z)F_i(r')H_j(z')}{N_{ij}} \cdot e^{-\gamma_{ij}(t-\tau)} \tag{5.37}$$

$$\gamma_{ij} = \kappa\left(\alpha_j^2 + \beta_i^2\right)$$

$$N_{ij} = \frac{R^2}{2}\left[J_0(\beta_i R)\right]^2 \left[1 + \frac{H^2}{\beta_i^2}\right]\left\{\frac{1}{H} + \frac{L}{2}\left[1 + \frac{\alpha_j^2}{H^2}\right]\right\}$$

The temperature distribution $T(r,z,t)$ is then obtained by using eqn. 5.12, and the expression of the Green's function just found; in addition, because all the boundary conditions are homogeneous, and the initial condition is $T(r,z,0) = 0$, both the first and the third term in eqn. 5.12 are equal to zero. It follows:

$$\begin{aligned} T(r,z,t) &= \frac{\kappa}{k}\int_0^t d\tau \int_V dv' G(r,z,t|r',z',\tau)Q(r',\tau) \\ &= \frac{\kappa}{k}\sum_{i,j}\frac{F_i(r)H_j(z)}{N_{ij}}\left\{\int_0^t d\tau[\phi(\tau) - \phi(\tau - t_0)]e^{-\gamma_{ij}(t-\tau)}\right\} \\ &\quad \cdot \left\{\int_0^R dr' r' F_i(r')q(r') \cdot \int_0^L dz' H_j(z')\right\} \end{aligned} \tag{5.38}$$

The integrals in eqn. 5.38 can all be simplified to obtain:

$$\int_0^t d\tau[\phi(\tau) - \phi(\tau - t_0)]e^{-\gamma_{ij}(t-\tau)} = \begin{cases} \frac{1}{\gamma_{ij}}[1 - e^{-\gamma_{ij}t}] & \text{for } t < t_0 \\ \frac{1}{\gamma_{ij}}[1 - e^{-\gamma_{ij}t_0}]e^{-\gamma_{ij}(t-t_0)} & \text{for } t \geq t_0 \end{cases} \tag{5.39}$$

$$\int_0^R dr' r' F_i(r')q(r') \approx \frac{\mathcal{A}P_0}{2\pi L} \cdot e^{-\frac{1}{2}\left(\frac{\beta_i d}{2}\right)^2} \tag{5.40}$$

$$\int_0^L dz' H_j(z') = \frac{1}{\alpha_j}\left[1 + \frac{\alpha_j^2 + H^2}{2\alpha_j H}\sin(\alpha_j L)\right] \tag{5.41}$$

In the calculation of eqn. 5.41 the boundary condition 5.28 was used, while eqn. 5.40 was obtained by assuming that $R/d \to \infty$ and the following property of the zero-order Bessel function was used (see ref. (189), formula no. 6.631.4, page 738):

$$\int_0^\infty u e^{-p\cdot u^2} \cdot J_0(au)du = \frac{1}{2p} \cdot e^{-\frac{a^2}{4p}} \qquad a, p \in \mathbf{C} \quad Re(a) > 0 \tag{5.42}$$

The constants κ/k, $\mathcal{A}P_0/2\pi L$ and $2/R^2$ can be extracted from the sum in eqn. 5.38 and their product gives the quantity $\mathcal{A}P_0/mC_p$. Equation 5.38 can be rearranged to give the

following final expression for the time-dependent, reduced temperature distribution as:

$$T(r,z,t) = \frac{\mathcal{A}P_0}{mC_p} \cdot \sum_{i,j} A_{ij} F_i(r) H_j(z) \cdot \begin{cases} \frac{1}{\gamma_{ij}}[1 - e^{-\gamma_{ij} t}] & t < t_0 \\ \frac{1}{\gamma_{ij}}[1 - e^{-\gamma_{ij} t_0}] e^{-\gamma_{ij}(t-t_0)} & t \geq t_0 \end{cases} \tag{5.43}$$

where the symbols in the summation are defined as follows:

$$F_i(r) \equiv J_0(\beta_i r)$$

$$H_j(z) \equiv \sin(\alpha_j z) + \frac{\alpha_j}{H}\cos(\alpha_j z) \qquad H = \frac{h_{sc}}{k}$$

$$A_{ij} \equiv \frac{e^{-\frac{1}{2}\left(\frac{\beta_i d}{2}\right)^2} \cdot \frac{1}{\alpha_j}\left[1 + \frac{\alpha_j^2 + H^2}{2\alpha_j H}\sin(\alpha_j L)\right]}{[J_0(\beta_i R)]^2 \left[1 + \frac{H^2}{\beta_i^2}\right]\left[\frac{1}{H} + \frac{L}{2}\left(1 + \frac{\alpha_j^2}{H^2}\right)\right]}$$

and the eigenvalues β_i and α_j are the positive roots of the two following transcendental equations:

$$\begin{cases} \beta_i J_1(\beta_i R) - H J_0(\beta_i R) = 0 \\ \tan(\alpha_j L) - \frac{2\alpha_j H}{\alpha_j^2 - H^2} = 0 \end{cases} \tag{5.44}$$

5.4.4 Calculation of the heating curves

In order to calculate the solutions 5.43, the first step is to determine an adequate number of eigenvalues β_i and α_j. The graphs of the left-hand side terms of the transcendental equations 5.44 are shown in figure 5.2. When solving the equations numerically, it is useful to put them in an non-dimensional form (by putting $x = \beta R$ and $y = \alpha_j L$).

Once the eigenvalues (and eigenfunctions) have been calculated, it is essential to study the convergence of the series in the solution 5.43, in order to predict the error associated with the truncation. The solution 5.43 was then calculated by considering various subsets of eigenvalues α_j and β_i and relative eigenfunctions. The convergence obtained was very 'fast' for times $t > t_0$, as shown in figure 5.3, where as few as two terms are sufficient to describe the temperature curves (cooling) accurately. By taking the terms with $i = 1, \ldots, 45$ $j = 1, \ldots, 35$ in the calculation, an overall precision of 10^{-10} K was achieved over the entire time range for samples with thickness 2-12.5 mm (such as those analysed in Chapter 4).

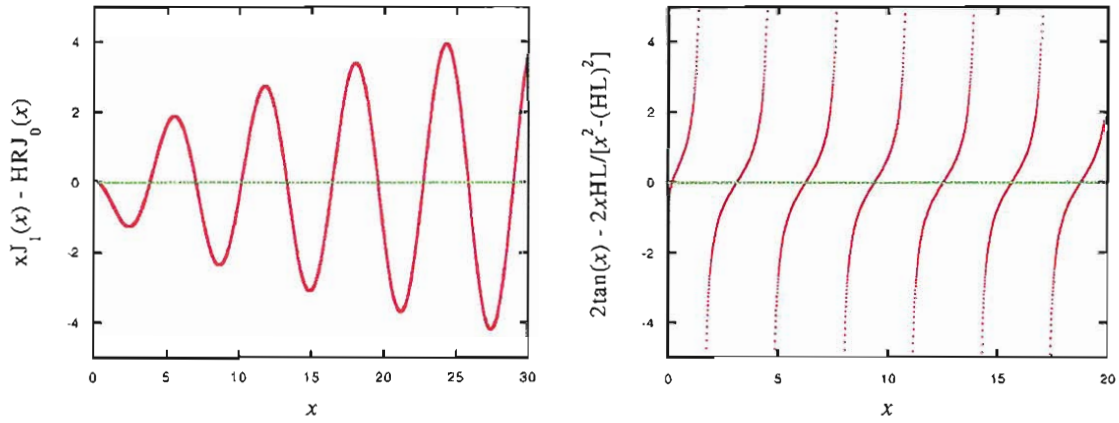

FIGURE 5.2: Graph of the left-hand side terms of the equations 5.44

The effect of the sample thickness, of the thermal conductivity and of the integral emissivity of the sample on the main parameters of the heating curves was studied. The calculated temperature curves can be fitted very accurately with a bi-exponential law ($T(t) \propto [e^{-t/\tau} - e^{-t/\lambda}]$), which provided the rise (λ) and decay (τ) times of the curves. The results are summarized in table 5.1 and shown in figures 5.5, 5.4 and 5.6 respectively. Varying the sample thickness (see fig. 5.5) affects the thermal capacity of the system ($mC_p \propto V_s \propto L$), hence the decay time, while it produces only a small change in the height of the heating curves, since the absorptivity is also proportional to the sample thickness L. A similar effect is observed by varying the sample's emissivity, which affects the sample-calorimeter heat exchange coefficient, hence the decay time (see fig. 5.6). The thermal conductivity of the sample has quite a dramatic impact on the

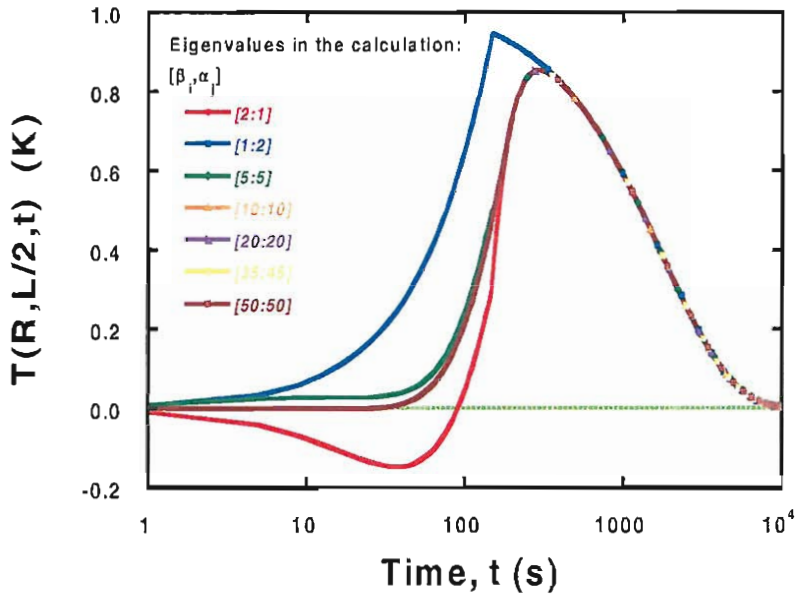

FIGURE 5.3: Heating/cooling curves, calculated for different subsets of eigenvalues and the following parameters: L=5mm, R=13mm, total energy incident on the sample P_0t_0=1 kJ in 150s, and absorptivity $\mathcal{A}$=0.005 (assuming: β=1 m^{-1} and σ=0.)

TABLE 5.1: Parameters of the Heating Curves for the disc-shaped sample, calculated for $P_0\ t_0 = 1\ kJ$ in 150 s, and $\alpha = 1\ m^{-1}$, $\sigma = 0$. Top sector: effect of sample thickness; middle : effect of thermal conductivity of glass; lower: effect of glass emissivity.

L (mm)	k (W/m/K)	h_{sc} ($W/m^2/K$)	κ ($10^{-7} \cdot m^2/s$)	ϵ_s	$\Delta T_z^{MAX,rel}$	λ^{rise} (s)	τ^{decay} (s)
2					0.19%	48.0	868
3					0.28%	48.3	1224
5	0.618	2.28	2.7	0.38	0.48%	48.6	1817
7.6			(= κ_{GLS})		0.7%	48.7	2419
8.5					0.8%	48.8	2594
12.5					1.2%	48.8	3223
	0.006		$2.7 \cdot 10^{-2}$		-	-	-
	0.031		$1.35 \cdot 10^{-1}$		-	740	1903
	0.062		$2.7 \cdot 10^{-1}$		-	406	1870
	0.154		$6.75 \cdot 10^{-1}$		-	172	1840
5	0.309	2.28	1.35	0.38	-	99	1819
	0.927		4.05		-	36	1814
	1.24		5.4		-	33	1812
	3.09		$1.35 \cdot 10^1$		-	30	1808
	6.18		$2.7 \cdot 10^1$		-	28	1806
		0.601		0.10	-	50	6884
		0.902		0.15	-	50	4592
		1.202		0.20	-	50	3446
		1.503		0.25	-	50	2758
5	6.18	1.803	2.7	0.30	-	50	2299
		2.104	(= κ_{GLS})	0.35	-	50	1971
		2.404		0.40	-	50	1724
		2.705		0.45	-	50	1535
		3.006		0.50	-	50	1382

rise time of the heating curves. In figure 5.4 the theoretical heating curves are calculated for increasing values of the thermal diffusivity ($\kappa = k/\rho C_p$), showing that the thermal wave reaches the detectors at the periphery of the sample with increasing delay; as a result, the height of the curves also decreases with decreasing κ. For $\kappa = 2.7\ 10^{-7}\ m^2 s^{-1}$ (a value approximately equal to that of CaF_2) the heating curve resembles the curve obtained assuming the 'homogeneous sample temperature' model (see fig. 4.21); for $\kappa = 2.7\ 10^{-5}\ m^2 s^{-1}$ (i.e. the diffusivity of GLS and GLSO, see table 4.4) however, the delay is evident (the heating curve peaks well after the source was turned off), which implies that the 'homogeneous sample temperature' model is not applicable.

The sixth column of table 5.1 shows the maximum relative temperature difference along the longitudinal ('z') direction of the sample:

$$\Delta T_z^{MAX,\ rel} \equiv \frac{T(R, L/2, t) - T(R, 0, t)}{T(R, L/2, t)} \tag{5.45}$$

The values found are generally smaller than 1%, which proves that the approximation of 'thin sample' (eqn. 5.8 and 5.9) holds for all the samples analysed in Chapter 4. This approximation is discussed in more detail in the next section.

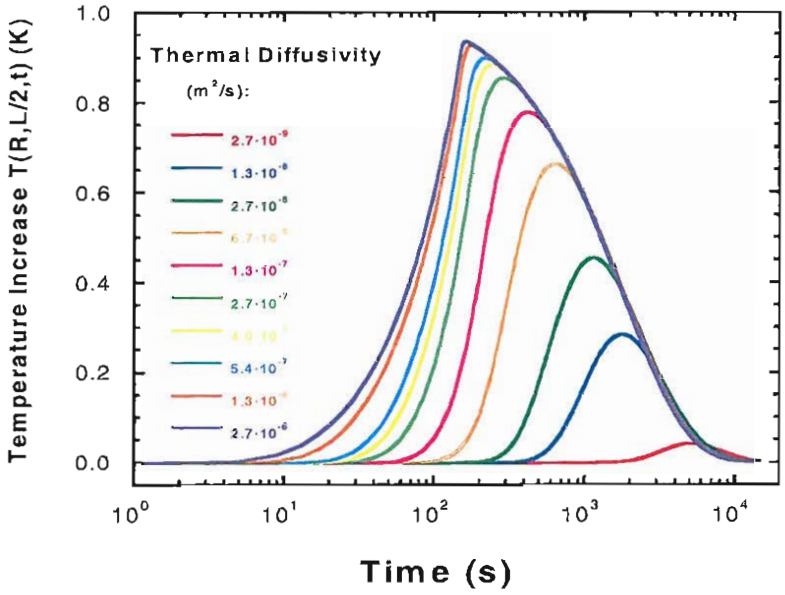

FIGURE 5.4: Heating curves for different values of thermal conductivity of the glass (GLS has $\kappa = 2.7 \cdot 10^{-7}\ m^2 s^{-1}$); refer to table 5.1 for other parameters.

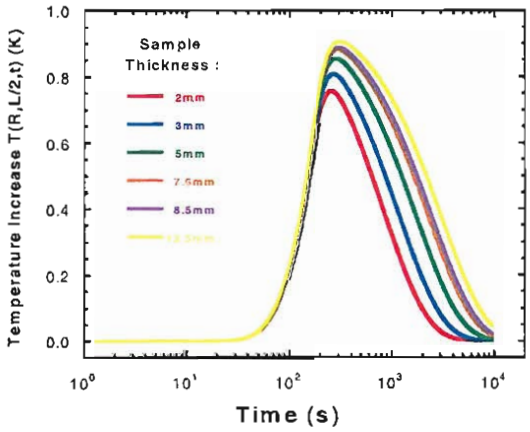

FIGURE 5.5: Heating curves for different values of sample thickness; refer to table 5.1 for details.

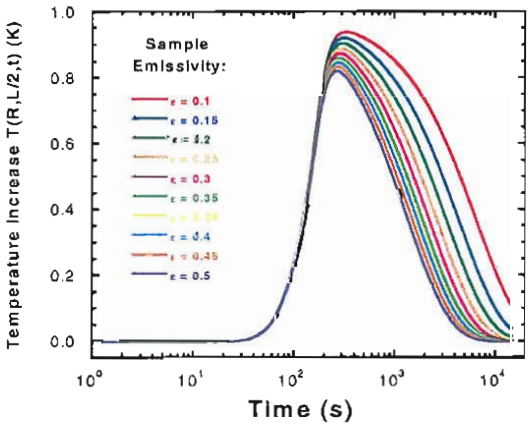

FIGURE 5.6: Heating curves for different values of glass emissivity; refer to table 5.1 for details.

5.4.5 Approximation of 'thermally thin sample': reduction to a 1-d problem

If the 'thin sample' approximation described in section 5.2.3 is assumed, eqn. 5.16 reduces to eqn. 5.9, and any dependence on the longitudinal variable z disappears, effectively reducing the heat diffusion equation to a 1-d equation for the radial variable. The solution for this reduced equation is obtained by following the same formal procedure as in the 2-d case, however with the following modifications:

$$\begin{aligned} H_j(z) &\Longrightarrow 1 \quad \forall j \in \mathbf{N} \\ \alpha_j^2 &\Longrightarrow \frac{2H}{L} \quad \forall j \in \mathbf{N} \\ \gamma_{ij} &\Longrightarrow \gamma_j \equiv \kappa \cdot \left(\frac{2H}{L} + \beta_i^2 \right) \quad \forall j \in \mathbf{N} \end{aligned} \tag{5.46}$$

The solution for the complete heat diffusion equation is then:

$$T(r,t) = \frac{AP_0}{mC_p} \cdot \sum_i A_i F_i(r) \cdot \begin{cases} \frac{1}{\gamma_i}[1 - e^{-\gamma_i t}] & t < t_0 \\ \frac{1}{\gamma_i}[1 - e^{-\gamma_i t_0}]e^{-\gamma_i (t - t_0)} & t \geq t_0 \end{cases} \tag{5.47}$$

$$F_i(r) \equiv J_0(\beta_i r)$$

$$A_i \equiv \frac{e^{-\frac{1}{2}\left(\frac{\beta_i d}{2}\right)^2}}{[J_0(\beta_i R)]^2 \left[1 + \frac{H^2}{\beta_i^2}\right]} \qquad H = \frac{h_{sc}}{k}$$

The figure below shows a comparison between the theoretical heating curve (eqn. 5.43) and the corresponding solution for the 'thin sample'. The relative difference between the exact and the approximate solution is less than 1% max., hence the use of 'thin sample' approximation is justified.

5.5 Boundary value problem for a system with sample and holder

5.5.1 Definition

The system, described in section 5.2.1, is modeled as a composite cylindrical bi-layer (see figure 5.1). The sample constitutes the inner layer, with radius R_1 and thickness L_1. The holder constitutes an annular external region, with inner and outer radii R_1 and R_2 (respectively), and thickness L_2. Sample and holder have different thermal properties; in the following expressions, the subscript i=1 refers to the sample, while i=2 refers to the holder. A gaussian heat source distribution heats up the centre of the sample. Sample and holder exchange heat principally via heat conduction through the interface, where a contact thermal resistance is assumed. Both sample and holder have radiative heat loss from all the other surfaces.

Although relatively simple, the BVP of unsteady heat diffusion in a 2-d, composite

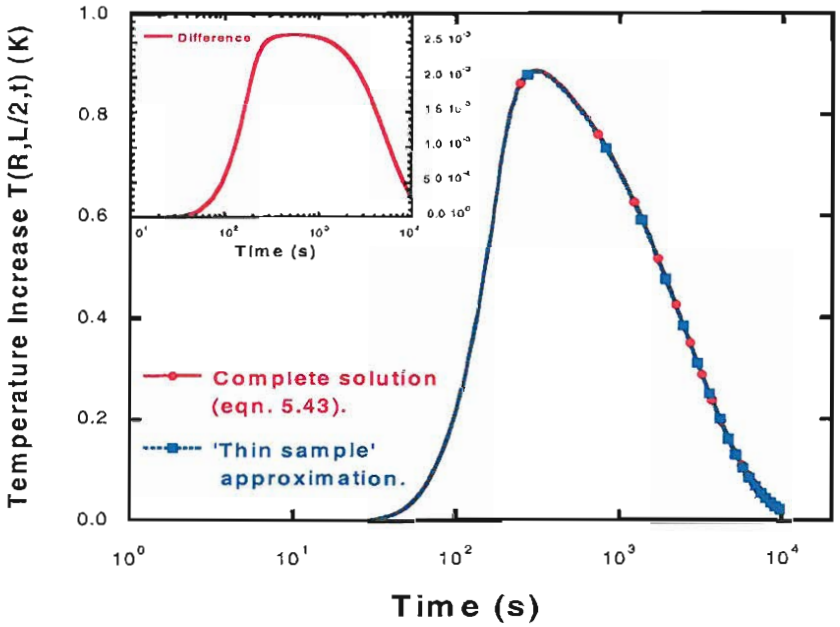

FIGURE 5.7: Comparison between heating curve calculated from the solution (5.43) and using the 'thin sample' approximation (5.47) (L=8.5 mm, P_0 t_0=1 kJ in 150 s, β=1 m^{-1}). The insert shows the difference of the two curves.

double layer with radiative losses at the boundaries cannot be solved analytically (190). However, it will be proved in this section that, since in the system under consideration both the sample and the holder are 'thermally thin' bodies, it is possible to reduce the 2-d problem to a 1-d problem with an exact closed-form solution.

Hence, in writing the heat diffusion equations for the sample and the holder, the 'thin sample' approximation is applied. It was shown in the previous section that this approximation is justified for GLS glass samples up to ≈ 1 cm thick; the same is certainly true for the sample holder, since the thermal conductivity of aluminium is over 200 times greater than GLS. The equations for the sample and holder can then be written in a compact form following the same procedure as in eqn. 5.2:

$$\left[\frac{\kappa_i}{r}\cdot\partial_r\left(r\cdot\partial_r\right)-\frac{2H_i\kappa_i}{L_i}-\partial_t\right]T_i(r,t)=-\frac{\kappa_i}{k_i}\cdot Q_i(r,t)\qquad i=1,2 \tag{5.48}$$

where it is defined that: $H_i=\frac{h_i}{k_i}$, and h_i are the heat exchange coefficients between the sample and the chamber (i=1), and between the holder and the chamber (i=2), defined as in eqn. 5.3. The heat density function $Q_i(r,t)$ is defined as (see eqn. 5.5 and 5.6):

$$Q_i(r,t)=\begin{cases}\dfrac{2\mathcal{A}P_0}{\pi d^2 L}\cdot e^{-2\cdot\left(\frac{r}{d}\right)^2}\cdot\left[\phi(t)-\phi(t-t_0)\right] & \text{for } i\text{=}1\\ \approx 0 & \text{for } i\text{=}2\end{cases} \tag{5.49}$$

The boundary conditions of the 1-*d*-reduced problem are:

$$\begin{cases} \partial_r T_1(0,t) = 0 & \text{Continuity at } r = 0 \\ -k_1 \cdot \partial_r T_1(R_1,t) = h_C \cdot [T_1(R_1,t) - T_2(R_1,t)] & \text{Conduction through interface} \\ k_1 \cdot \partial_r T_1(R_1,t) = k_2 \cdot \partial_r T_2(R_1,t) & \text{Continuity of heat flow at intf.} \\ -k_2 \cdot \partial_r T_2(R_2,t) = h_2 \cdot T_2(R_2,t) & \text{Radiative loss at } r = R_2 \end{cases} \tag{5.50}$$

The initial value is:

$$T_i(r,0) = 0 \quad i = 1,2 \tag{5.51}$$

i.e. sample and holder are in equilibrium with the chamber at T_∞ for $t = 0$. The conduction through the sample/holder interface (eqn. 5.50(ii)) is characterised by a (finite) heat exchange coefficient h_C ($h_C < \infty$ expresses the presence of a contact thermal resistance)

Equations 5.48-5.51 define a linear BVP with non-homogeneous boundary conditions (due to eqn. 5.49(ii)). The problem will be solved following the procedure utilised in the previous section, i.e., by solving the homogeneous problem ($Q = 0$), deriving the Green's function and finally solving the problem in the more general case ($Q \neq 0$).

5.5.2 Solution of the homogeneous problem ($Q = 0$)

If $Q = 0$, the equations 5.48 become:

$$\left[\frac{\kappa_i}{r} \cdot \partial_r \left(r \cdot \partial_r\right) - \frac{2H_i\kappa_i}{L_i}\right] T_i(r,t) = \partial_t T_i(r,t) \tag{5.52}$$

Assuming separation of the variables in the form: $T_i(r,t) = F_i(r) \cdot \Gamma(t)$, it follows:

$$\kappa_i \cdot \frac{F_i'' + F_i'/r}{F_i} - \frac{2H_i\kappa_i}{L_i} = \frac{\Gamma'}{\Gamma} \equiv \lambda \tag{5.53}$$

Since the two ratios depend on different independent variables, they must be equal to a constant λ (arbitrary separation constant). Notice that, in contrast to the previous model (equation 5.20), the thermal diffusivity is retained on the space-variable function side (technically defined as 'Vodicka's approach' (191)). Thus the ratio Γ'/Γ is independent of the index i, and the same λ can be chosen for the two zones of the system. The

following system of separated equations is then obtained:

$$\begin{cases} \Gamma'(t) = \lambda \cdot \Gamma(t) & \text{(time-var. equation)} \\ \kappa_i \cdot \left(F_i''(r) + \frac{F_i'(r)}{r} \right) - \frac{2H_i \kappa_i}{L_i} \cdot F_i(r) = \lambda \cdot F_i(r) & \text{(radial equation)} \end{cases} \tag{5.54}$$

The two equations above are eigenvalue equations for linear differential operators; the first step is to find for which values of the separation constant the two equations have a solution. Note that $\lambda < 0$ is to be assumed, otherwise the equation for the time-variable function would have diverging solutions for $t \to \infty$. Hence, by putting $\lambda = -\gamma^2$, the separated equations can be rewritten as:

$$\begin{cases} \Gamma'(t) + \gamma^2 \cdot \Gamma(t) = 0 & \text{(temporal equation)} \\ F_i''(r) + F_i'(r)/r + \beta_i^2 \cdot F_i(r) = 0 & \text{(radial equation)} \end{cases} \tag{5.55}$$

where:

$$\beta_i^2 \equiv \frac{\gamma^2}{\kappa_i} - \frac{2H_i}{L_i} \tag{5.56}$$

The set of the following two radial equations and relative boundary conditions:

$$F_i''(r) + F_i'(r)/r + \beta_i^2 \cdot F_i(r) = 0 \tag{5.57}$$

$$\begin{cases} \partial_r F_1(0) = 0 & \text{Continuity at } r = 0 \\ -k_1 \cdot \partial_r F_1(R_1) = h_C \cdot [F_1(R_1) - F_2(R_1)] & \text{Heat conduction through interf.} \\ k_1 \cdot \partial_r F_1(R_1) = k_2 \cdot \partial_r F_2(R_1) & \text{Continuity of heat flow at the interf.} \\ -k_2 \cdot \partial_r F_2(R_2) = h_2 \cdot F_2(R_2) & \text{Radiative loss at } r = R_2 \end{cases} \tag{5.58}$$

constitute an eigenvalue problem for the determination of the eigenvalues γ and corresponding eigenfunctions $F_i(r)$. Once the eigenvalues have been found, the solution for the first equation (time-variable function) is easily obtained as : $\Gamma(t) \propto e^{-\gamma^2 \cdot t}$. The general solution for the radial equation 5.57 is a linear combination of zero-order Bessel functions of first and second type:

$$\begin{cases} F_1(r) \propto J_0(\beta_1 \cdot r) & \text{(radial equation - sample)} \\ F_2(r) \propto C_1 \cdot J_0(\beta_2 \cdot r) + C_2 \cdot Y_0(\beta_2 \cdot r) & \text{(radial equation - holder)} \end{cases} \tag{5.59}$$

In the solution for the sample only Bessel functions J_0 appear, because the condition

5.58(i) at $r = 0$ requires the solutions to be bounded. The coefficients C_1, C_2 and the eigenvalues γ are determined from the remaining three boundary conditions:

$$(5.58\ ii) \rightarrow C_1 J_0(\beta_2 R_1) + C_2 Y_0(\beta_2 R_1) + \left[\frac{\beta_1}{H_C} J_1(\beta_1 R_1) - J_0(\beta_1 R_1)\right] = 0 \tag{5.60}$$

$$(5.58\ iii) \rightarrow C_1 \beta_2 J_1(\beta_2 R_1) + C_2 \beta_2 Y_1(\beta_2 R_1) - \frac{k_1}{k_2} \beta_1 J_1(\beta_1 R_1) = 0 \tag{5.61}$$

$$(5.58\ iv) \rightarrow C_1 \left[\frac{\beta_2}{H_2} J_1(\beta_2 R_2) - J_0(\beta_2 R_2)\right] + C_2 \left[\frac{\beta_2}{H_2} Y_1(\beta_2 R_2) - Y_0(\beta_2 R_2)\right] = 0 \tag{5.62}$$

with: $H_C = \frac{h_C}{k_1}$. The boundary conditions give a set of three equations for the three unknowns C_1, C_2 and γ (through the $\beta_i(\gamma)$), that can be written in a more compact matrix form:

$$\mathbf{A}[\gamma] \cdot \begin{pmatrix} C_1 \\ C_2 \\ 1 \end{pmatrix} = \mathbf{0} \tag{5.63}$$

by defining the matrix $\mathbf{A}$:

$$\mathbf{A}[\gamma] \equiv \begin{pmatrix} J_0(\eta_{2,1}) & Y_0(\eta_{2,1}) & \left[\frac{\beta_1}{H_C} J_1(\eta_{1,1}) - J_0(\eta_{1,1})\right] \\ \beta_2 J_1(\eta_{2,1}) & \beta_2 Y_1(\eta_{2,1}) & -\frac{k_1}{k_2} \beta_1 J_1(\eta_{1,1}) \\ \left[\frac{\beta_2}{H_2} J_1(\eta_{2,2}) - J_0(\eta_{2,2})\right] & \left[\frac{\beta_2}{H_2} Y_1(\eta_{2,2}) - Y_0(\eta_{2,2})\right] & 0 \end{pmatrix} \tag{5.64}$$

with: $\eta_{i,j} \equiv \beta_i R_j$ for $i, j = 1, 2$. The solutions for γ are found by requiring the matrix $\mathbf{A}$ to be singular. This condition gives the following transcendental equation in γ:

$$det\,[\mathbf{A}(\gamma)] = 0 \tag{5.65}$$

the solutions of the eqn. 5.65 provide a discrete infinity of eigenvalues $\{\gamma_n\}_{n \in \mathbf{N}}$, from which the $\{\beta_{i,n}\}_{n \in \mathbf{N}}^{i=1,2}$ are calculated via eqns. 5.56. Any two of the equations 5.63 are independent, and can be used to determine the coefficients $C_{1,n}$ and $C_{2,n}$ for each of the γ_n; choosing the first two:

$$\begin{pmatrix} J_0(\eta_{2,1}^{(n)}) & Y_0(\eta_{2,1}^{(n)}) \\ \beta_{2,n} J_1(\eta_{2,1}^{(n)}) & \beta_{2,n} Y_1(\eta_{2,1}^{(n)}) \end{pmatrix} \cdot \begin{pmatrix} C_{1,n} \\ C_{2,n} \end{pmatrix} = - \begin{pmatrix} \left[\frac{\beta_{1,n}}{H_C} J_1(\eta_{1,1}^{(n)}) - J_0(\eta_{1,1}^{(n)})\right] \\ -\frac{k_1}{k_2} \beta_{1,n} J_1(\eta_{1,1}^{(n)}) \end{pmatrix} \tag{5.66}$$

where $\eta_{i,j}^{(n)} \equiv \beta_{i,n} R_j$. The solutions are determined by a standard method and using the following identity (see ref. (189), formula no. 8.477.1 page 738):

$$J_0(x)Y_1(x) - J_1(x)Y_0(x) = -\frac{2}{\pi x} \tag{5.67}$$

from which it follows that:

$$\Delta = \begin{vmatrix} J_0(\eta_{2,1}^{(n)}) & Y_0(\eta_{2,1}^{(n)}) \\ \beta_{2,n} J_1(\eta_{2,1}^{(n)}) & \beta_{2,n} Y_1(\eta_{2,1}^{(n)}) \end{vmatrix} = -\frac{2}{\pi R_1} \tag{5.68}$$

Hence:

$$C_{1,n} = \frac{\pi R_1}{2} \cdot \begin{vmatrix} \frac{\beta_{1,n}}{H_C} J_1(\eta_{1,1}^{(n)}) - J_0(\eta_{1,1}^{(n)}) & Y_0(\eta_{2,1}^{(n)}) \\ -\frac{k_1}{k_2} \beta_{1,n} J_1(\eta_{1,1}^{(n)}) & \beta_{2,n} Y_1(\eta_{2,1}^{(n)}) \end{vmatrix} \tag{5.69}$$

$$C_{2,n} = \frac{\pi R_1}{2} \cdot \begin{vmatrix} J_0(\eta_{2,1}^{(n)}) & \frac{\beta_{1,n}}{H_C} J_1(\eta_{1,1}^{(n)}) - J_0(\eta_{1,1}^{(n)}) \\ \beta_{2,n} J_1(\eta_{2,1}^{(n)}) & -\frac{k_1}{k_2} \beta_{1,n} J_1(\eta_{1,1}^{(n)}) \end{vmatrix} \tag{5.70}$$

Once the eigenvalues $\{\gamma_n\}_{n \in \mathbf{N}}$ and eigenfunctions $F_{i,n}(r)$ of the problem 5.57 have been determined, the general solution of the homogeneous problem eqn. 5.52 is obtained as:

$$T_i(r,t) = \sum_{n \in \mathbf{N}} c_n F_{i,n}(r) e^{-\gamma_n^2 t} \tag{5.71}$$

where the c_n are arbitrary coefficients. This general solution can be expressed in terms of a suitably defined Green's function, which will be utilised to derive the solution of the non-homogeneous problem. Firstly, we notice that the eigenfunctions 5.59 satisfy the following generalized orthogonality relationship (see D.1 for a proof):

$$\sum_{j=1}^{2} \frac{k_j}{\kappa_j} \int_{R_{j-1}}^{R_j} \varrho F_{j,m}(\varrho) F_{j,n}(\varrho) d\varrho = N_m \delta_{mn} \tag{5.72}$$

where $R_0 = 0$ and the norm N_m is defined as:

$$N_m = \sum_{j=1}^{2} \frac{k_j}{\kappa_j} \int_{R_{j-1}}^{R_j} \varrho [F_{j,m}(\varrho)]^2 d\varrho \tag{5.73}$$

If now we assume an arbitrary initial temperature distribution $\Theta_i(r)$, and require the

general solution 5.71 to satisfy the initial condition $T_i(r,0) = \Theta_i(r)$:

$$\sum_{n\in\mathbf{N}} c_n F_{i,n}(r) = \Theta_i(r) \tag{5.74}$$

Then, by operating on both sides with the operator:

$$\mathcal{I}\,[-] \equiv \frac{1}{N_m}\frac{k_i}{\kappa_i}\int_{R_{i-1}}^{R_i} \varrho F_{i,m}(\varrho)[-]d\varrho \tag{5.75}$$

and by summing over the 'zone' index i, we obtain:

$$\sum_{n\in\mathbf{N}} c_n \frac{1}{N_m}\left[\sum_{i=1}^{2}\frac{k_i}{\kappa_i}\int_{R_{i-1}}^{R_i}\varrho F_{i,m}(\varrho)F_{i,n}(\varrho)d\varrho\right] = \frac{1}{N_m}\sum_{i=1}^{2}\frac{k_i}{\kappa_i}\int_{R_{i-1}}^{R_i}\varrho F_{i,m}(\varrho)\Theta_i(\varrho)d\varrho$$

In view of the generalized orthogonality relationship 5.72, the left-hand side term equals c_m. The homogeneous solution is then obtained by substituting the expression for c_n in eqn. 5.71, and it can be written more compactly by introducing a Green's function notation:

$$T_i(r,t) = \sum_{j=1}^{2}\int_{R_{j-1}}^{R_j}\left[G_{ij}(r,t|\varrho,\tau)\right]_{\tau=0}\varrho\Theta_j(\varrho)d\varrho$$

with the G_{ij} defined as:

$$\left[G_{ij}(r,t|r',\tau)\right]_{\tau=0} = \frac{k_j}{\kappa_j}\sum_{n\in\mathbf{N}}\frac{1}{N_n}F_{i,n}(r)F_{j,n}(r')e^{-\gamma_n^2 t} \tag{5.76}$$

G_{ij} is the Green's function for the 1-d reduced BVP for a composite medium. This definition is very similar to the one given in the previous section for the sample only (eqn. 5.37), with the difference in the factor due to the new orthogonality relationship 5.72 satisfied by the eigenfunctions of the homogeneous problem.

5.5.3 Calculation of the eigenvalues and eigenfunctions

Before finding the solutions for the inhomogeneous problem, it is necessary to discuss the calculation of the eigenvalues $\{\gamma_n\}_{n\in\mathbf{N}}$ and corresponding eigenfunctions. The solution of the eigenvalue problem for the 'thin' composite bi-cylindrical medium is not as straightforward as in the case with the sample only. Indeed, the heat diffusion equations

5.48 do not match the 'Sturm-Liouviulle' type, thus the eigenvalues are not necessarily real numbers. This is due to the negative term $2H_i\kappa_i/L_i$, which originates from the operation of 'reduction to 1-*d*' under the 'thin sample approximation'. The physical constraint requires the eigenfunctions to be real functions; thus, all the solutions of the eigenvalue equation 5.65, both real and complex, leading to real eigenfunctions must be considered in solving the problem. It is well documented in the literature (190) that, while heat diffusion problems in unidimensional composite multilayers are 'Sturm-Liouville' and only have real non-negative eigenvalues, multi-dimensional problems also admit imaginary eigenvalues. In the present model, the possibility of imaginary eigenvalues is a consequence of the operation of 'reduction to 1-*d*' under the 'thermally thin sample' approximation, as a reminder of the original bi-dimensionality of the problem.

The case of real eigenvalues is discussed first. Defining:

$$\Phi(\gamma) \equiv det[\mathbf{A}(\gamma)] \tag{5.77}$$

note that $\Phi(\gamma)$ is an even function of γ, restricting the problem to the positive zeros only. $\Phi(\gamma)$ is defined for:

$$\gamma \geq max\left\{\sqrt{\frac{2H_1\kappa_1}{L_1}}, \sqrt{\frac{2H_2\kappa_2}{L_2}}\right\} = \sqrt{\frac{2H_1\kappa_1}{L_1}} \tag{5.78}$$

The above expression is generally satisfied in instances where the inner layer is a glass sample and the outside layer is aluminium. For $\gamma \in \mathbf{R}^+$, $\gamma \geq \sqrt{\frac{2H_1\kappa_1}{L_1}}$, $\Phi(\gamma)$ has the form shown in figure 5.8. The zeros of $\Phi(\gamma)$ define a non-decreasing sequence of real eigenvalues $\{\gamma_n\}_{n\in\mathbf{N}}$, and correspondent eigenvalues $\{\beta_{i,n}\}$ of the spatial equations 5.57 through eqn. 5.56.

The case of the complex eigenvalues is now discussed. The γ eigenvalues must be real numbers ($\gamma^2 < 0$ would otherwise lead to diverging eigenfunctions $\Gamma(t)$ for $t \to \infty$); thus, only real and positive values of γ need to be considered here. Imaginary eigenvalues β_1 and/or β_2 could arise in the following two cases:

$$\sqrt{\frac{2H_2\kappa_2}{L_2}} \leq \gamma \leq \sqrt{\frac{2H_1\kappa_1}{L_1}} \implies \gamma \in \mathbf{R}^+, \quad \beta_2 \in \mathbf{R}^+, \quad \beta_1 \in i\mathbf{R}^+ \tag{5.79}$$

$$0 \leq \gamma \leq \sqrt{\frac{2H_2\kappa_2}{L_2}} \implies \gamma \in \mathbf{R}^+, \quad \beta_2 \in i\mathbf{R}^+, \quad \beta_1 \in i\mathbf{R}^+ \tag{5.80}$$

It is vital to emphasize here the importance of possible eigenvalues in these two regions for the solution of the BVP. Those solutions are expressed as a series of infinite terms (as in the previous section 5.4.3), where the terms corresponding to the lowest-order

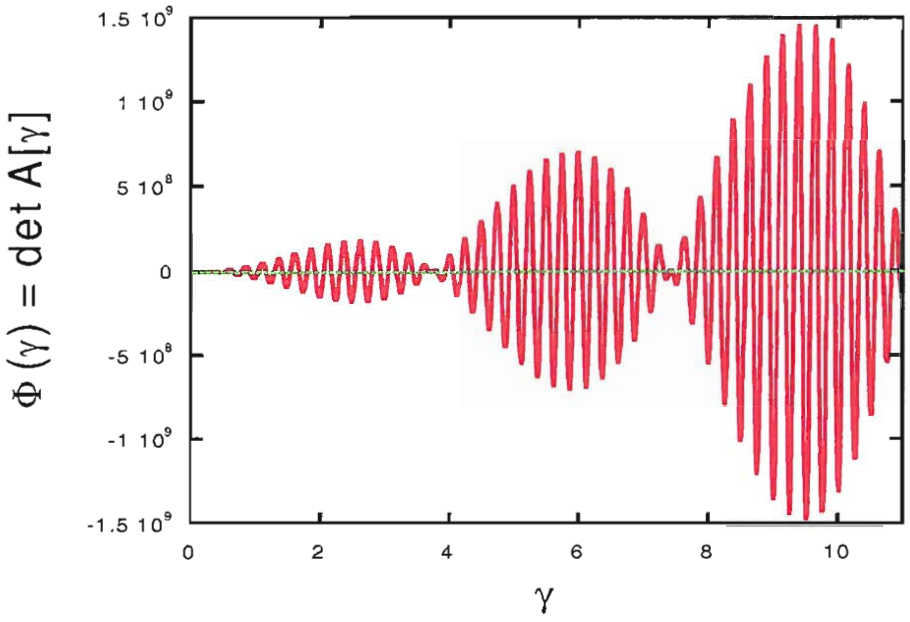

FIGURE 5.8: Function $\Phi(\gamma) \equiv det[\mathbf{A}(\gamma)]$

(i.e., 'smaller') eigenvalues give the bigger contribution, while the terms corresponding to larger eigenvalues give only a smaller contribution to the sum. Hence, eigenvalues γ in the intervals 5.79 and 5.80 are expected to contribute significantly to the solutions of the BVP.

In the first case 5.79, the imaginary eigenvalue β_1 can be written as:

$$\beta_1(\gamma) \equiv ib_1(\gamma), \quad \text{with} \quad b_1 \equiv \sqrt{\frac{-\gamma^2}{\kappa_1} + \frac{2H_1}{L_1}} \quad \text{and} \quad b_1 \geq 0 \tag{5.81}$$

Bearing in mind the following recurrence relationship:

$$J_n(ix) = i^n I_n(x) \qquad \Longrightarrow \qquad \begin{cases} J_0(ix) = I_0(x) \\ J_1(ix) = iI_1(x) \end{cases} \tag{5.82}$$

the matrix $\mathbf{A}$ can be written as:

$$\mathbf{A}'[\gamma] \equiv \begin{pmatrix} J_0(\eta_{2,1}) & Y_0(\eta_{2,1}) & \left[-\frac{b_1}{H_C} I_1(\xi_{1,1}) - I_0(\xi_{1,1})\right] \\ \beta_2 J_1(\eta_{2,1}) & \beta_2 Y_1(\eta_{2,1}) & \frac{k_1}{k_2} b_1 I_1(\xi_{1,1}) \\ \left[\frac{\beta_2}{H_2} J_1(\eta_{2,2}) - J_0(\eta_{2,2})\right] & \left[\frac{\beta_2}{H_2} Y_1(\eta_{2,2}) - Y_0(\eta_{2,2})\right] & 0 \end{pmatrix} \tag{5.83}$$

where $\eta_{i,j} \equiv \beta_i R_j$ $(i, j = 1, 2)$ and $\xi_{1,1} \equiv b_1 R_1$. Thus, for values of γ in the interval 5.79,

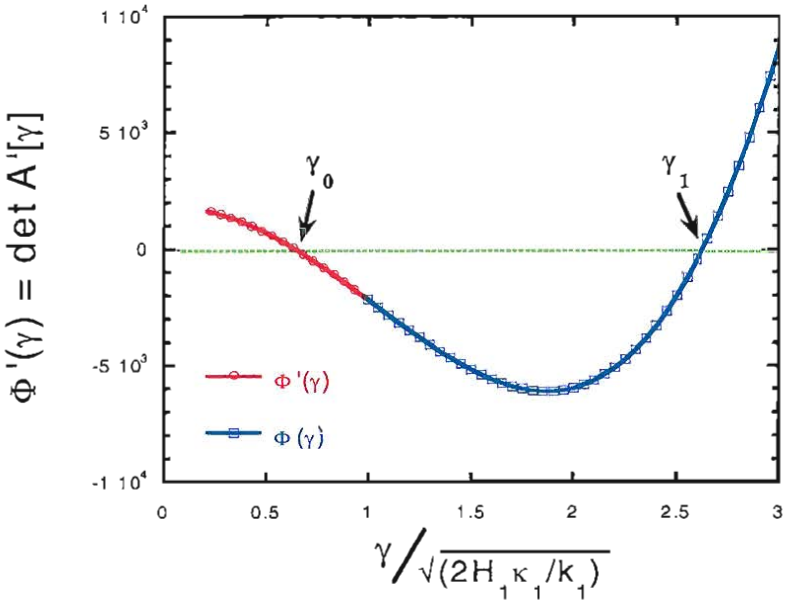

FIGURE 5.9: Plot of the 'determinant functions' $\Phi'(\gamma)$ and $\Phi(\gamma)$ for small γ, showing the two lowest-order eigenvalues.

the matrix $\mathbf{A}'$ is still real-valued and so are the eigenfunctions:

$$\begin{cases} F_1(r) \propto I_0(b_1 \cdot r) & \text{(radial variable - sample)} \\ F_2(r) \propto C_1 \cdot J_0(\beta_2 \cdot r) + C_2 \cdot Y_0(\beta_2 \cdot r) & \text{(radial variable - holder)} \end{cases} \tag{5.84}$$

By studying the quantity $\Phi'[\gamma] \equiv det[\mathbf{A}'(\gamma)]$ in the interval 5.79, it is found that there is at least one zero (see figure 5.9). The $\Phi'[\gamma]$ joins continuously to the $\Phi[\gamma]$ at $\gamma = \sqrt{\frac{2H_1\kappa_1}{L_1}}$.

In the second case 5.80, both the imaginary eigenvalues β_i can be written as:

$$\beta_i(\gamma) \equiv ib_i(\gamma), \quad with \quad b_i \equiv \sqrt{\frac{-\gamma^2}{\kappa_i} + \frac{2H_i}{L_i}} \quad and \quad b_i \geq 0 \tag{5.85}$$

The Bessel functions of the second kind of imaginary argument are related to the modified Bessel functions of first and second type by the following relationship (see ref. (189), formula no. 8.407.1, page 961):

$$Y_n(ix) = \frac{2}{\pi}(-1)^{n+1} i^n K_n(x) + i^{n+1} I_n(x) \quad \Rightarrow \quad \begin{cases} Y_0(ix) = -\frac{2}{\pi} K_0(x) + iI_0(x) \\ Y_1(ix) = -\frac{2}{\pi} iK_1(x) - I_1(x) \end{cases} \tag{5.86}$$

Consequently, the matrix $\mathbf{A}$ can be written in this case as:

$$\mathbf{A}''[\gamma] \equiv \{a_{i,j}[\gamma]\}_{i,j=1,2,3} \tag{5.87}$$

where the elements are defined as follows ($\xi_{i,j} \equiv b_i R_j$):

$$a_{i,j}[\gamma] \equiv \begin{cases} a_{1,1} \equiv I_0(\xi_{2,1}) \\ a_{1,2} \equiv -\frac{2}{\pi} K_0(\xi_{2,1}) + i I_0(\xi_{2,1}) \\ a_{1,3} \equiv -\frac{b_1}{H_C}\, I_1(\xi_{1,1}) - I_0(\xi_{1,1}) \\ a_{2,1} \equiv -\, b_2 I_1(\xi_{2,1}) \\ a_{2,2} \equiv -\, b_2 \left(\frac{2}{\pi} K_1(\xi_{2,1}) + i I_1(\xi_{2,1})\right) \\ a_{2,3} \equiv \frac{k_1}{k_2}\, b_1 I_1(\xi_{1,1}) \\ a_{3,1} \equiv -\frac{b_2}{H_2}\, I_1(\xi_{2,2}) - I_0(\xi_{2,2}) \\ a_{3,2} \equiv -\, \frac{2}{\pi} \left(\frac{b_2}{H_2}\, K_1(\xi_{2,2}) - K_0(\xi_{2,2})\right) - i \left(\frac{b_2}{H_2}\, I_1(\xi_{2,2}) + I_0(\xi_{2,2})\right) \\ a_{3,3} \equiv 0 \end{cases} \tag{5.88}$$

The corresponding eigenfunctions are:

$$\begin{cases} F_1(r) \propto I_0(b_1 \cdot r) & \text{(radial variable - sample)} \\ F_2(r) \propto C_1 \cdot I_0(b_2 \cdot r) + C_2 \cdot \left[-\frac{2}{\pi} K_0(b_2 \cdot r) + i I_0(b_2 \cdot r)\right] & \text{(radial variable - holder)} \end{cases} \tag{5.89}$$

The $F_2(r)$ is real-valued if and only if $C_2 = 0$; this condition implies (see eqn. 5.70) that:

$$\begin{vmatrix} I_0(\xi_{2,1}) & -\frac{b_1}{H_C}\, I_1(\xi_{1,1}) - I_0(\xi_{1,1}) \\ -\, b_2 I_1(\xi_{2,1}) & \frac{k_1}{k_2}\, b_1 I_1(\xi_{1,1}) \end{vmatrix} = 0 \tag{5.90}$$

Summarising, the solutions sought γ_n of the eigenvalue equation:

$$det[\mathbf{A}''(\gamma)] = 0 \qquad \gamma_i \in \left[0, \sqrt{\frac{2H_2\kappa_2}{L_2}}\right] \tag{5.91}$$

must also satisfy the condition 5.90, that is the solutions of the following equation:

$$det[\mathbf{A}''(\gamma)] = -\left[\frac{b_2}{H_2}\, I_1(\xi_{2,2}) + I_0(\xi_{2,2})\right] \cdot \cdot \begin{vmatrix} \left[-\frac{2}{\pi}K_0(\xi_{2,1})+iI_0(\xi_{2,1})\right] & \left[-\frac{b_1}{H_C}\, I_1(\xi_{1,1})-I_0(\xi_{1,1})\right] \\ \left[-b_2\left(\frac{2}{\pi}K_1(\xi_{2,1})+iI_1(\xi_{2,1})\right)\right] & \frac{k_1}{k_2}\, b_1 I_1(\xi_{1,1}) \end{vmatrix} = 0 \tag{5.92}$$

Using the distributive property of the determinant to separate the real from the imaginary part, and taking into account that the first factor in the left-hand side of eqn. 5.92 is always strictly positive, the following system of two equations (in γ) is obtained:

$$\begin{cases} \begin{vmatrix} -\frac{2}{\pi}\, K_0(\xi_{2,1}) & \left[-\frac{b_1}{H_C}\, I_1(\xi_{1,1})-I_0(\xi_{1,1})\right] \\ -\frac{2}{\pi}\, b_2 K_1(\xi_{2,1}) & \frac{k_1}{k_2}\, b_1 I_1(\xi_{1,1}) \end{vmatrix} = 0 \\ \begin{vmatrix} I_0(\xi_{2,1}) & \left[-\frac{b_1}{H_C}\, I_1(\xi_{1,1})-I_0(\xi_{1,1})\right] \\ -\, b_2 I_1(\xi_{2,1}) & \frac{k_1}{k_2}\, b_1 I_1(\xi_{1,1}) \end{vmatrix} = 0 \end{cases} \tag{5.93}$$

A close examination of the two quantities on the left hand side of the above, shows that no further imaginary eigenvalue exists, because the first quantity is always strictly negative. In conclusion, the eigenvalue problem has only one solution, γ_0, leading to an imaginary eigenvalue $\beta_{1,0}$. The radial eigenvalues are:

$$\begin{cases} \beta_{1,0}(\gamma) \equiv ib_{1,0}(\gamma), & \text{with} \quad b_{1,0} \equiv \sqrt{\frac{-\gamma_0^2}{\kappa_1} + \frac{2H_1}{L_1}} \\ \beta_{2,0}(\gamma) \equiv \sqrt{\frac{\gamma_0^2}{\kappa_2} - \frac{2H_2}{L_2}} \end{cases} \tag{5.94}$$

The relative radial eigenfunctions (given by eqn. 5.84) are:

$$\begin{cases} F_{1,0}(r) \propto I_0(b_{1,0} \cdot r) & \text{(radial variable - sample)} \\ F_{2,0}(r) \propto C_{1,0} \cdot J_0(\beta_{2,0} \cdot r) + C_{2,0} \cdot Y_0(\beta_{2,0} \cdot r) & \text{(radial variable - holder)} \end{cases} \tag{5.95}$$

where the coefficients $C_{1,0}$ and $C_{2,0}$ are determined by the system of equations (where $\eta_{2,1}^{(0)} \equiv \beta_{2,0}R_1$ and $\xi_{1,1}^{(0)} \equiv b_{1,0}R_1$):

$$\begin{pmatrix} J_0(\eta_{2,1}^{(0)}) & Y_0(\eta_{2,1}^{(0)}) \\ \beta_{2,0}J_1(\eta_{2,1}^{(0)}) & \beta_{2,0}Y_1(\eta_{2,1}^{(0)}) \end{pmatrix} \cdot \begin{pmatrix} C_{1,0} \\ C_{2,0} \end{pmatrix} = -\begin{pmatrix} \left[-\frac{b_{1,0}}{H_C}\, I_1(\xi_{1,1}^{(0)}) - I_0(\xi_{1,1}^{(0)})\right] \\ \frac{k_1}{k_2}\, b_{1,0} I_1(\xi_{1,1}^{(0)}) \end{pmatrix} \tag{5.96}$$

With solutions:

$$C_{1,0} = \frac{\pi R_1}{2} \cdot \begin{vmatrix} -\frac{b_{1,0}}{H_C} I_1(\xi_{1,1}^{(0)}) - I_0(\xi_{1,1}^{(0)}) & Y_0(\eta_{2,1}^{(0)}) \\ \frac{k_1}{k_2} b_{1,0} I_1(\xi_{1,1}^{(0)}) & \beta_{2,0} Y_1(\eta_{2,1}^{(0)}) \end{vmatrix} \tag{5.97}$$

$$C_{2,0} = \frac{\pi R_1}{2} \cdot \begin{vmatrix} J_0(\eta_{2,1}^{(0)}) & -\frac{b_{1,0}}{H_C} I_1(\xi_{1,1}^{(0)}) - I_0(\xi_{1,1}^{(0)}) \\ \beta_{2,0} J_1(\eta_{2,1}^{(0)}) & \frac{k_1}{k_2} b_{1,0} I_1(\xi_{1,1}^{(0)}) \end{vmatrix} \tag{5.98}$$

5.5.4 Solution of the non-homogeneous problem ($Q \neq 0$)

The Green's function method is now applied to determine the non-homogeneous solutions. The value at $\tau = 0$ was determined in section 5.5.2. It can be proved (see ref. (187), page 318) that, also for the multilayer system, the Green's function at the generic instant t can be obtained from its value at $\tau = 0$, simply by substituting $(t - \tau)$ for t :

$$G_{ij}(r, t|r', \tau) \equiv \sum_{n=1}^{\infty} \frac{1}{N_n} \frac{k_j}{\kappa_j} F_{i,n}(r) F_{j,n}(r') e^{-\gamma_n^2 (t-\tau)} \qquad i, j = 1, 2 \tag{5.99}$$

where the N_n are the normalization coefficients (eqn. 5.74):

$$N_n \equiv \frac{k_1}{\kappa_1} \int_0^{R_1} \varrho \left[F_{1,n}(\varrho)\right]^2 d\varrho + \frac{k_2}{\kappa_2} \int_{R_1}^{R_2} \varrho \left[F_{2,n}(\varrho)\right]^2 d\varrho \qquad n = 0, 1, 2, \ldots \tag{5.100}$$

If $\Theta_i(r)$ is the initial temperature distribution and $Q_i(r, t)$ is the power density function, the general solution of the non-homogeneous problem is found as follows:

$$\begin{aligned} T_i(r, t) = \sum_{j=1,2} \Bigg\{ & \int_{R_{j-1}}^{R_j} \varrho \left[G_{ij}(r, t|\varrho, \tau)\right]_{\tau=0} \Theta_j(\varrho) d\varrho \; + \\ & + \int_0^t d\tau \int_{R_j}^{R_{j+1}} \varrho G_{ij}(r, t|\varrho, \tau) \left[\frac{\kappa_j}{k_j} Q_j(\varrho, \tau)\right] d\varrho \Bigg\} \end{aligned} \tag{5.101}$$

(where $R_0 \equiv 0$ is assumed). In the present BVP, the initial condition is $\Theta_i(r) = 0$ for $i = 1, 2$, and also $Q_2(r, t) \approx 0$ (the laser does not heat the holder), which simplifies eqn. 5.99 considerably (the first term in the summation is zero $\forall\, j$, and also the term corresponding to j=2 in the second is zero), leading to the following expression:

$$T_i(r, t) = \int_0^t d\tau \int_0^{R_1} \varrho \; G_{i1}(r, t|\varrho, \tau) \left[\frac{\kappa_1}{k_1} Q_1(\varrho, \tau)\right] d\varrho \tag{5.102}$$

Substituting the expression 5.99 for the Green's function $G_{i1}(r,t|\varrho,\tau)$:

$$\begin{aligned} T_i(r,t) &= \int_0^t d\tau \int_0^{R_1} \varrho \left[\sum_{n=0}^{\infty} \frac{1}{N_n}\frac{k_1}{\kappa_1} F_{i,n}(r)F_{1,n}(\varrho)e^{-\gamma_n^2(t-\tau)}\right]\left[\frac{\kappa_1}{k_1}Q_1(\varrho,\tau)\right] d\varrho \\ &= \sum_{n=0}^{\infty} \underbrace{\frac{1}{N_n}\left[\int_0^{R_1} \varrho F_{1,n}(\varrho)q_1(\varrho)d\varrho\right]}_{coefficients} \cdot \underbrace{F_{i,n}(r)}_{radial} \cdot \underbrace{\int_0^t e^{-\gamma_n^2(t-\tau)}\cdot[\phi(\tau)-\phi(\tau-t_0)]\,d\tau}_{time\ variable:\ \Omega(t)} \\ &= \sum_{n=0}^{\infty} \frac{\langle F_{1,n}|q_1\rangle}{N_n}\cdot F_{i,n}(r)\cdot\Omega(t) \end{aligned} \tag{5.103}$$

The quantities $\langle F_{1,n}|q_1\rangle$ can easily be calculated as in eqn. 5.40 (replace R with R_1 and β_i with $\beta_{i,n}$), which holds also for the imaginary eigenvalue $\beta_{1,0}$. $\Omega(t)$ has been calculated in eqn. 5.39 (replace γ_{ij} with γ_n^2). The final result is:

$$T_i(r,t) = \mathcal{A}P_0 \cdot \sum_{n=0}^{\infty} A_n F_{i,n}(r)\cdot \begin{cases} \frac{1}{\gamma_n^2}[1-e^{-\gamma_n^2 t}] & t < t_0 \\ \frac{1}{\gamma_n^2}[1-e^{-\gamma_n^2 t_0}]e^{-\gamma_n^2(t-t_0)} & t \geq t_0 \end{cases} \tag{5.104}$$

where:

$$A_n = \frac{e^{-\frac{1}{2}\left(\frac{\beta_{1,n}d}{2}\right)^2}}{2\pi L_1 N_n} \qquad n = 0,1,2,\ldots \tag{5.105}$$

The expression 5.100 for the coefficients N_n can be simplified using the following identities for zero-order Bessel functions (see D.2 for a proof):

$$\int xB_0^2(\alpha x)dx = \begin{cases} \frac{x^2}{2}\left[B_0^2(\alpha x)+B_1^2(\alpha x)\right] & \text{for } B_0(x) = J_0(x), Y_0(x) \\ \frac{x^2}{2}\left[I_0^2(\alpha x)-I_1^2(\alpha x)\right] \end{cases} \tag{5.106}$$

Thus, equation 5.100 can be written as:

$$\begin{cases} N_0 = \frac{k_1}{\kappa_1}\frac{R_1^2}{2}\left[I_0^2(b_{1,0}R_1)-I_1^2(b_{1,0}R_1)\right] + \\ \qquad \frac{k_2}{\kappa_2}\left[\frac{r^2}{2}\left([C_{1,0}J_0(\beta_{2,0}r)+C_{2,n}Y_0(\beta_{2,0}r)]^2-[C_{1,0}J_1(\beta_{2,0}r)+C_{2,0}Y_1(\beta_{2,0}r)]^2\right)\right]_{r=R_1}^{r=R_2} & n=0 \\ N_n = \frac{k_1}{\kappa_1}\frac{R_1^2}{2}\left[J_0^2(\beta_{1,n}R_1)+J_1^2(\beta_{1,n}R_1)\right] + \\ \qquad \frac{k_2}{\kappa_2}\left[\frac{r^2}{2}\left([C_{1,n}J_0(\beta_{2,n}r)+C_{2,n}Y_0(\beta_{2,n}r)]^2+[C_{1,n}J_1(\beta_{2,n}r)+C_{2,n}Y_1(\beta_{2,n}r)]^2\right)\right]_{r=R_1}^{r=R_2} & n\geq 1 \end{cases} \tag{5.107}$$

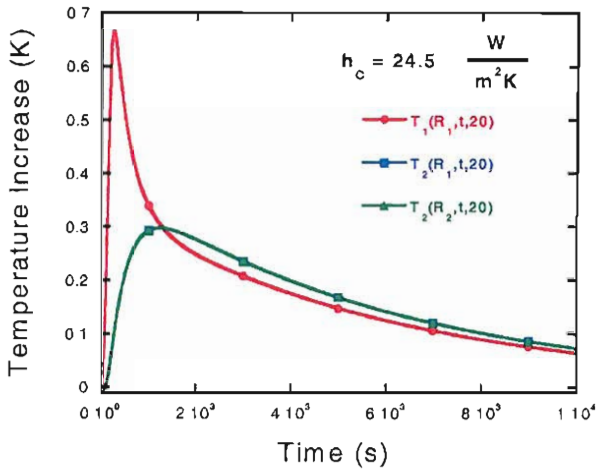

FIGURE 5.10: Temperature solutions at points $r = R_1^-$ (sample), $r = R_1^+$ (holder), $r = R_2$ (sensors).

		Sample	Holder
ρ	$[kg\ m^{-3}]$	4200	2800
C_p	$[Jkg^{-1}K^{-1}]$	540	963
k	$[Wm^{-1}K^{-1}]$	0.618	142
κ	$[10^{-5}\ m^2s^{-1}]$	0.027	5.27
ϵ	$[-]$	0.37	0.02
$\mathcal{A}$	$[-]$	$6\ 10^{-3}$	*n.a.*
radius	$[mm]$	13 (R_1)	19.1 (R_2)
thickness	$[mm]$	5	5
h_c	$[Wm^{-2}K^{-1}]$	24.5	
t_0	$[s]$	150	
Q	$[kJ]$	1	

TABLE 5.2: Parameters used in the calculation of temperature solutions.

5.5.5 Analysis of the solutions

Figure 5.10 shows the solutions, calculated using eqn. 5.104 and the set of parameters shown in table 5.2; the thermal properties of the glass are those given in ref. (192) for a 70:30 GLS glass, while the sample dimensions approximately match those of the samples described in chapter 4. In the graphs, the solutions are referred to as $T(r,t,n)$, where n indicates the number of eigenvalues (and eigenfunctions) considered for the numerical calculation of the solution, in addition to the lowest-order one ($n = 0$). The temperatures at each side of the interface ($r = R_1^-, R_1^+$), and at the sensors ($r = R_2$), are shown in figure 5.10, as a function of time. As expected due to the high thermal conductivity of aluminium, there is very little difference between the curves at the two different points on the holder ($T_1(R_1,t,n) \approx T_2(R_2,t,n)$). This is also very obvious in figure 5.11, where the radial dependence of the temperature at different instants is shown. The discontinuity indicates the interface, which separates the zone with lower conductivity and stronger temperature gradients (sample, $r < R_1$) from the zone with higher conductivity and almost uniform temperature.

A quite dramatic effect is observed in the temperature difference at the interface. The sample heats up more and much faster, as conduction to the holder is slow due to the contact resistance. The temperature of the sample is systematically higher in the initial stages of the heating: for a heating time $t_0 = 150\ s$, the temperature at the sample's border reaches ($r = R_1$) its maximum at $t \approx 200\ s$, while the holder temperature peaks at $t \approx 1500\ s$, and the maximum temperature of the holder is over 50% lower than that of the sample. Eventually, sample and holder reach equilibrium, but, at this point, due to the different emissivities and to the interface resistance, a negative temperature difference builds up. Indeed, the sample has much higher integral emissivity and consequently loses heat much faster than the holder, while temperature equalisation is again impeded by the interface resistance. In the set of graphs 5.13, the holder the

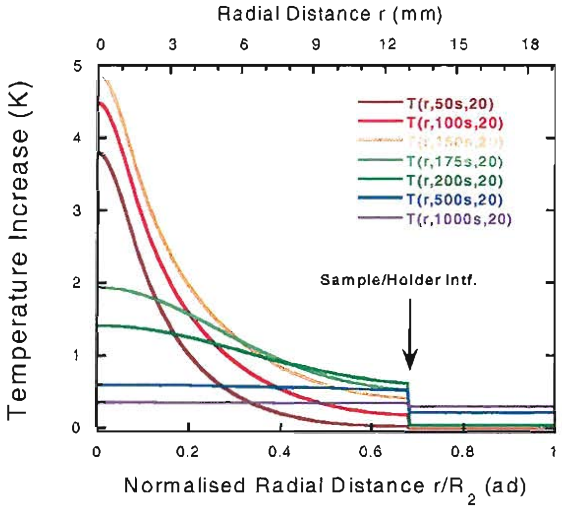

FIGURE 5.11: Radial dependence of temperature at various times. Parameters as in table 5.2.

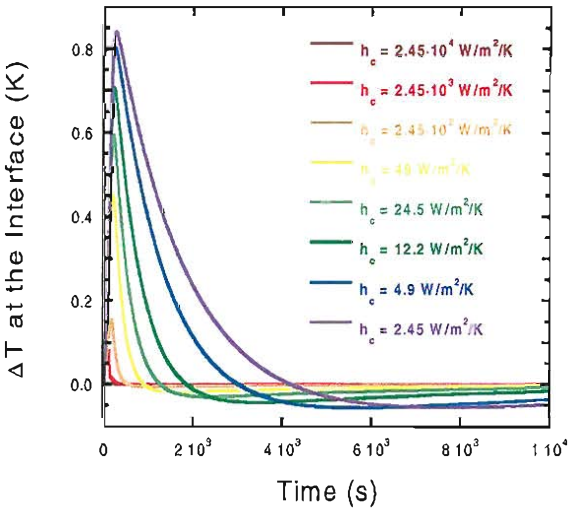

FIGURE 5.12: Time dependence of the temperature difference at the sample/holder interface, for various values of the contact resistance.

holder reaches its maximum temperature when it is in equilibrium with the sample; this is a consequence of the very small value of emissivity assumed for the holder in the calculations (see table 5.2), leading to a negligible radiative loss, and is obviously not true in the general case. Both the sample and the holder temperature, as expected, tend asymptotically to zero for $t \rightarrow \infty$.

Figure 5.13 gives a clear idea of how the solutions vary as a function of the interface thermal resistance. In calculating all the curves, only the parameter h_C was varied, while all the other parameters were kept fixed as in table 5.2. When the contact resistance is low, i.e. h_C is high ($h_C \leq 2.45\ 10^3\ Wm^{-2}K^{-1}$), its effect is negligible, as shown in the first two graphs. With decreasing h_C, the two heating curves become more and more different, with maximum temperature and rise time of the sample increasing, and the maximum temperature and rise time of the holder decreasing. The equilibration time, intended as the instant at which sample and holder reach 'dynamical' equilibrium, becomes longer and longer as the interface resistance is increased. This is also shown very clearly in figure 5.12, where the interface temperature difference is given as a function of time.

The results of a few crucial tests, which have been performed in order to verify the accuracy of the present model and of the procedure of calculation of the solutions, are briefly summarised below.

- **Convergence of the series.** Tests of the convergence of the series 5.104 were performed by considering various subsets of eigenvalues in the numerical calculation. The convergence was found to be reasonably fast for $t > t_0$, where the solutions can be calculated with $n \leq 10$ terms to achieve consistency to $\leq 0.1\%$.

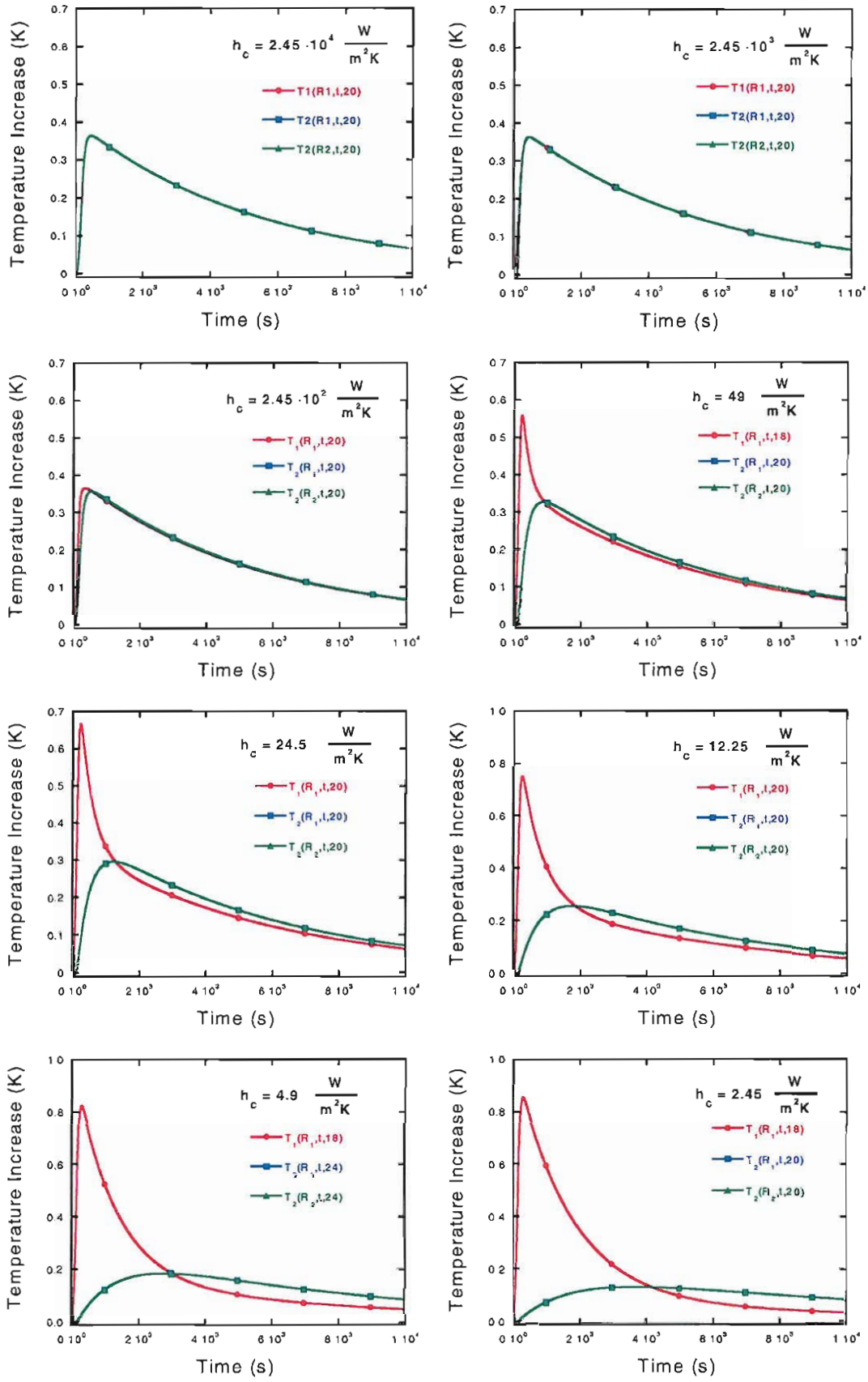

FIGURE 5.13: Effect of the thermal resistance at the sample/holder interface.

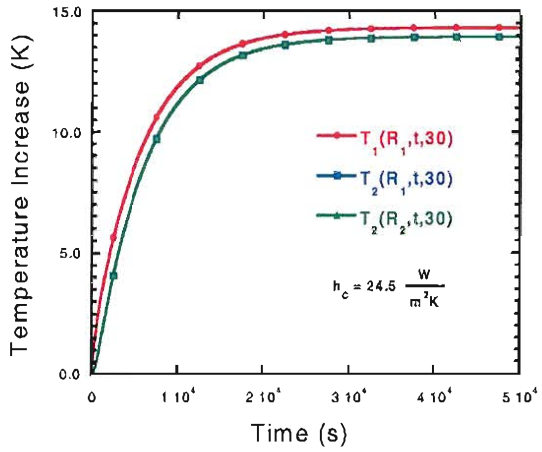

FIGURE 5.14: Asymptotic analysis of the solutions 5.104, allowing $t_0 \rightarrow \infty$.

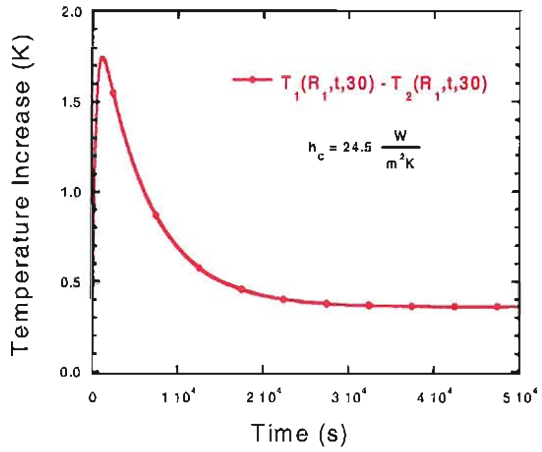

FIGURE 5.15: Asymptotic analysis of the interface temperature difference.

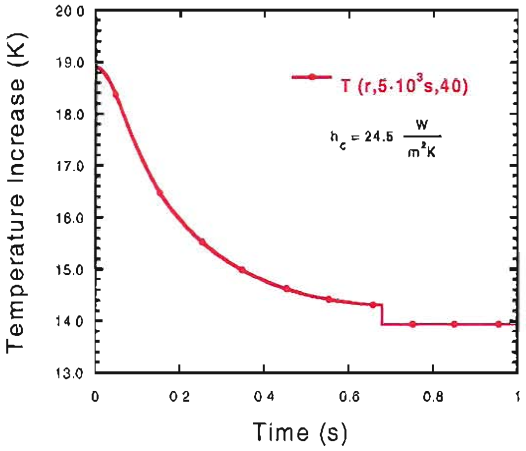

FIGURE 5.16: Steady-state radial temperature distribution ($t_0 \rightarrow \infty$).

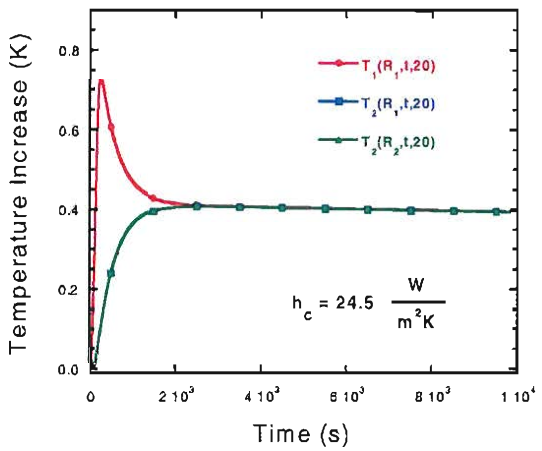

FIGURE 5.17: Temperature distribution in a 1-d composite double layer.

For $t < t_0$, more terms are required, especially at positions near the interface; it was found that, assuming $n \approx 20$ terms, the error associated with the truncation of the series is $\approx 1\%$, reduced to $\approx 0.1\%$ by considering $n \approx 30$ terms. The calculation of the solutions with such a number of terms is reasonably fast using a Pentium III processor and standard mathematical calculation packages.

- **Overall accuracy.** The overall accuracy in reproducing the temperature distribution depends to a large extent on the accuracy of the calculation of the eigenvalues $\{\gamma_n\}$, and can be tested (at $r = R_1, R_2$) by observing the behaviour of the calculated solutions for short times ($t \rightarrow 0$), where it is expected that $T_i(t) \approx 0$. From tests performed for various sets of parameters, it was concluded that the overall accuracy of the curves was better than $\pm 3\ mK$.

- **Asymptotic analysis.** This consists in allowing the irradiation time t_0 to go to infinity. In these conditions, the system heats up indefinitely, eventually reaching

an asymptotic equilibrium condition where the absorbed power equals the total irradiated power, and the temperature distribution becomes stationary, i.e time-independent. The expected result is confirmed by figure 5.14 and 5.15, where the asymptotic behaviour of the T_i and of the temperature difference at the interface is shown; figure 5.16 shows the radial temperature distribution in stationary conditions (the other parameters are as in table 5.2).

- **Case with no interface resistance.** The interface resistance can be put to zero 'mathematically', by eliminating all the terms involving the quantity $1/H_c$ from the matrix **A** defined by eqn. 5.64. It has been verified that, by doing this, the calculated interface temperature difference is zero at all times.

- **Reduction to the 1-d composite double layer.** The description given in section 5.5 can be reduced to that pertinent to the 1-d composite double layer, simply by letting $L_i \rightarrow \infty$ for both the sample and the holder. The results are shown in figure 5.17. In this case, the temperature of the inner layer (the 'sample') is higher at all times, with the interface temperature difference increasing for shorter times, and then tending asymptotically to zero without inversion; consistently, the inner layer now has no radiative loss in this instance (the other parameters are as in table 5.2).

5.6 Conclusions

This chapter presented a very exhaustive theoretical description of laser absorption calorimetry. The 'homogeneous sample temperature model' assumed in the ISO 11551 standard (177) is poorly applicable to measurements of glass samples due to their low thermal conductivity. For these materials, an 'inhomogeneous temperature model' (see section 5.4) is required to reproduce the temperature distribution correctly. Inhomogeneous models have been developed for a simple system, composed of an isolated sample, by several authors but, prior to this study, not for the case of a sample held by a fixed holder, that is practically more relevant. The latter requires us to solve a BVP of heat diffusion in cylicndrical for a bi-dimensional, composite double-layer, allowing for contact thermal resistance at the interface and radiative heat losses from all the surfaces.

A procedure for solving this BVP analytically has not yet been found for the general case. In this study an analytical solution was found for the case of 'thermally thin' samples, which is very pertinent to laser absorption calorimetry; in this case, the bi-dimensional problem can be effectively reduced to one-dimensional, which permits an exact, close-form solution. The method presented in this chapter (section 5.5.4) involves a standard procedure utilizing the Green's function, but both real and imaginary eigenvalues must be considered, as a consequence of the bi-dimensionality of the original problem. The solutions of the BVP are summarised in compact form in Appendix C.

The results obtained under the approximtion of 'thermally thin sample' are accurate for up to ≈ 1 *cm* thick glass samples, a condition which is satisfied in most laser absorption calorimetry experiments. Also, the calculation of the analytical solution can be handled without difficulty by standard calculation packages and state-of-the-art PCs; by comparison, a numerical method would be more complicated and time consuming due to the piece-wise continuous nature of the temperature distribution in a double layer with contact resistance. In conclusion, the present model provides accurate theoretical predictions for the measurement described in the previous chapter and has been used in section 4.7 to analyse the experimental heating curves collected for GLS and GLSO samples.

Chapter 6

Analysis of Near-IR Optical Loss in GLS and GLSO Glasses

6.1 Introduction

The transmission properties of chalcogenide glasses are substantially different from those of their oxide and fluoride counterparts. For instance, in glasses such as arsenic sulfide absorption occurs throughout the entire window of transmission due to the presence of gap states, giving rise to the weak absorption tail of the electronic edge. Furthermore, substantial modifications of the optical transmission of chalcogenides are in general induced by a temperature increase or by exposure to light with a wavelength close to that of the bandgap. These effects are very important in view of the practical applications of chalcogenides.

In practical materials the fundamental loss mechanisms are inevitably added to fabrication-related mechanisms. Inside the transmission window, absorption and scattering from impurities can give rise to loss levels comparable to, or even greater than, those from fundamental loss mechanisms. The presence of several mechanisms of comparable magnitude makes it difficult to investigate the individual contributions as well as to obtain a reliable estimate of the intrinsic transparency limit of GLS and GLSO glasses. As for other chalcogenide systems, the improvement of glass fabrication holds the key to an unequivocal quantification of the different mechanisms.

This chapter is divided in two parts. The fist part (sections 6.2-6.5) will analyse the loss mechanisms in GLS and GLSO glasses, with particular emphasis on the effect of transition metal impurities and on the weak absorption tail, both of which affect the glass transparency in the near-IR region. Original results presented in the first part include: a comparative study of the absorption of transition metals in GLS and GLSO glass and an investigation of the presence of a weak tail in GLS and GLSO, by combining

bulk and fibre transmission measurements and calorimetric measurements presented in chapter 4.

The second part of the chapter (sections 6.5 and 6.6) will present an investigation of the effect of the temperature and illumination (photodarkening) on the transmission loss of GLS and GLSO fibres. Photodarkening (PD) occurs as a shift of the position of the fundamental electronic edge under bandgap illumination. The effect was studied by using unclad fibres and side illumination. This second part will present the results of an entirely novel and complete characterisation of the spectral dependence of the PD, its dependence on the wavelength and intensity of the illumination, its dependence on the temperature, and the characteristic rise and decay times.

6.2 Fundamental limits of transparency of chalcogenide glasses

The range of transmission of optical glasses (the 'optical window') is limited at longer wavelengths by multiphonon absorption, and at shorter wavelengths by electronic absorption, both of which give rise to the sharp edges of the spectral absorption. Chalcogenide glasses have, in general, a smaller optical bandgap than oxide and fluoride glasses; also, due to the large atomic mass of the chalcogen anions and lower force constants of chemical bonds, the main vibrational bands of chalcogenides fall at longer wavelengths. Consequently, their optical window is shifted further into the infrared than their oxide and fluoride counterparts.

The multiphonon absorption occurs due to the interaction of photons with overtones and combinations of the fundamental vibrations of the glass forming units. Consequently, the wavelength dependence of the IR absorption is generally complicated; however, in the region of the so-called 'multiphonon edge', the absorption coefficient can be described via an empirical, single-exponential law (193):

$$\alpha_{MP}(h\nu) \;=\; K_{MP} \cdot \exp\left[-\frac{h\nu}{E_{MP}}\right] \tag{6.1}$$

where $h\nu$ is the photon's energy and K_{MP} and E_{MP} are material parameters. The multiphonon edge of GLS and GLSO glasses have been measured by Brady et al. (89).

Electronic absorption arises from interband transitions between the valence and the conduction bands. In the amorphous semiconductors and chalcogenide glasses the electronic edge consists of three distinct regions (90), (194), as shown in figure 6.1:

- A 'high absorption region' for $\alpha \geq 10^6\ m^{-1}$. In this high-energy region the density of states of the charge carriers can be assumed to be parabolic, which leads to

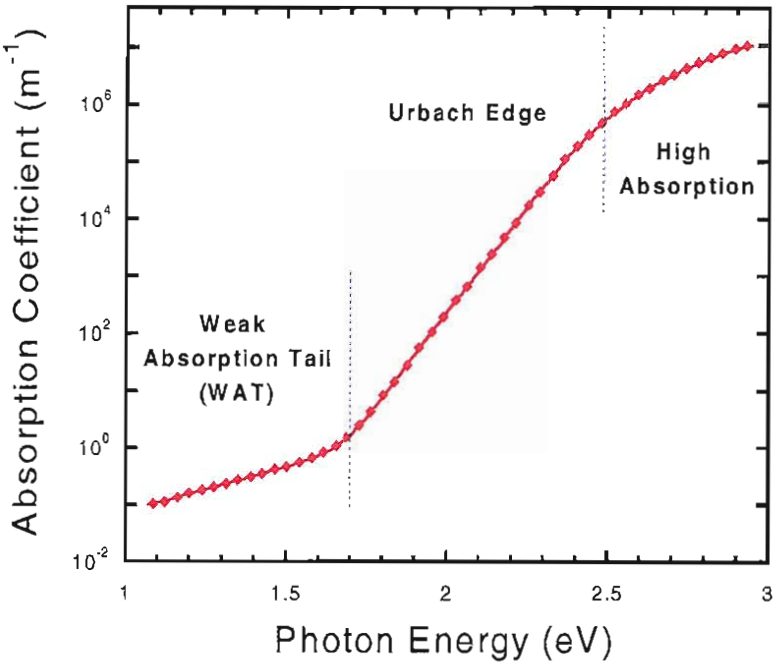

FIGURE 6.1: Electronic absorption edge in arsenic sulphide glass (after (195)).

the following expression for the dependence of the absorption coefficient α and the photon energy/frequency:

$$\alpha_{E,H}(h\nu) = A_0 \cdot \frac{(h\nu - E_g)^2}{h\nu} \qquad \alpha \geq 10^6\ m^{-1} \tag{6.2}$$

where A_0, E_g are frequency-independent material parameters. E_g is defined as the optical bandgap (or 'Tauc bandgap', according to some authors), and is usually determined, from transmission measurements of thin films, as the intercept of the curve $[\alpha(\nu)h\nu]^{1/2}$ versus the photon energy $h\nu$.

- An intermediate region or 'Urbach edge' in the range $10^6 \geq \alpha \geq 10^0 - 10^1\ m^{-1}$, in which the absorption coefficient depends exponentially on the photon energy according to the law:

$$\alpha_{E,U}(h\nu) = A_1 \cdot \exp\left[\frac{h\nu - E_g}{E_1}\right] \qquad 10^0 - 10^1\ m^{-1} \leq \alpha \leq 10^6\ m^{-1} \tag{6.3}$$

where E_g is the optical bandgap and A_1, E_1 are material constants. The slope of the Urbach edge, E_1, takes values between 50 and 80 meV. Optical absorption in this region is attributed to band tails of localised states of the valence and conduction bands.

- A low absorption region or 'weak absorption tail' (WAT) for $\alpha \leq 10^0 - 10^1\ m^{-1}$, in which the absorption coefficient still has an exponential dependence on the photon

energy, but with a much less steep slope as compared to the Urbach edge:

$$\alpha_{WAT}(h\nu) \;\propto\; \exp\left[\frac{h\nu}{E_{WAT}}\right] \qquad \alpha \leq 10^0 - 10^1\ m^{-1} \tag{6.4}$$

The material parameter E_{wt}, or slope of the WAT, is experimentally found to assume values in the range a few hundred meV to one eV. The weak absorption tail is considered to arise from transitions involving localised states deep in the bandgap. Defects such as dangling bonds or 'wrong bonds' are thought to be responsible for these additional gap states, and the magnitude of the WAT is directly related to the total concentration of such states.

Further away from the fundamental edges, light scattering becomes an important loss mechanism. Rayleigh scattering is induced by local fluctuations of the refractive index frozen in the glass network. Such small-scale fluctuations arise as a consequence of glass formation by rapid cooling of a melt. In multicomponent glass, both fluctuations of density and composition may occur. In both cases, the attenuation due to scattering is described by a typical power law:

$$\alpha_{RS}(\lambda) \;=\; R \cdot \lambda^{-4} \tag{6.5}$$

The Rayleigh coefficient R depends on the material and on the cause of index fluctuations. The theory of light scattering in optical media is described in references (196) and (197). It is found that, for the case of thermodynamically driven density fluctuations, the Rayleigh coefficient can be expressed via the following relationship:

$$R_\rho \;=\; \frac{8\pi^3}{3}\,\left(n^8 p^2\right)\left(kT_g\right)\beta_T \tag{6.6}$$

where n is the refractive index of the glass, p its photo-acoustic coefficient, k is the Boltzmann's constant, T_g is the fictive temperature and β_T is the isothermal compressibility at T_g. On the other hand, the concentration scattering can be described via the following expression:

$$R_c \;=\; \frac{32\pi^3}{3}\,\frac{n^2}{N_A}\,\sum_{j=1}^{M}\,\left[\left(\frac{\partial n}{\partial x_j}\right)+\left(\frac{\partial n}{\partial \rho}\right)\left(\frac{\partial \rho}{\partial x_j}\right)\right]^2 M_j\; x_j \tag{6.7}$$

where n is the refractive index, N_A is Avogadro's number, ρ is the density, and M_j and x_j are the molecular weight and the weight fraction, respectively, of the $j-$th glass component. An estimate of the density and composition Rayleigh scattering for GLS and GLSO glass is given in reference (89).

Rayleigh scattering is a weak loss mechanism, which is usually only observed in high purity optical materials. Since scattering can also be induced by defects and impurities, the total attenuation due to scattering can be expressed as (13):

$$\alpha_{SC} = \frac{R_t}{\lambda^4} + \frac{G}{\lambda^2} + I \tag{6.8}$$

where the first term represents the Rayleigh scattering from small-scale index fluctuations (both intrinsic and extrinsic), and the other two terms represent scattering from larger centres, i.e. the Rayleigh-Gans scattering (the '$\propto \lambda^{-2}$' term) and the wavelength-independent scattering (I).

The total attenuation of a chalcogenide glass, allowing for 'extrinsic' absorption due to optically active impurities (α_I), such as OH^-, transition metal ions and rare-earth ions, is then given by the sum of all the absorption and scattering terms:

$$\alpha = \alpha_{MP} + \alpha_E + \alpha_{SC} + \alpha_I \tag{6.9}$$

6.3 The weak absorption tail

The weak absorption tail (WAT) was first reported in the work by Wood and Tauc (90), and has been a much investigated and debated topic ever since, due to the numerous fundamental and practical implications. As far as practical applications of chalcogenides are concerned, the WAT is relevant because it may be the limiting mechanism to their transparency, and also because it may provide additional channels for energy transfer to the glass host through excitation of optically active gap states.

The WAT has been observed in a number of chalcogenide glass systems, as shown in table 6.1. Figure 6.2 shows the transmission of an arsenic sulphide fibre, taken from reference (193), where the presence of a weak tail in the region 0.7-2 μm is very clear; in this material, the WAT extends throughout the entire optical window and determines the minimum transmission loss.

The model proposed by Wood and Tauc states that the WAT arises due to the presence of localised, deep gap states caused either by defects or impurities, and its magnitude is directly related to the concentration of such defects. Weak tails have also been observed in some oxide glasses (but not in silica), however they are several orders of magnitude smaller than in chalcogenides (201). According to Wood and Tauc, this is an indication that the concentration of defects associated with the WAT is large in chalcogenides ($\approx 10^{17}\ cm^{-3}$), and their formation energy is small as compared to oxides. On the other hand, the intensity of the WAT is also known to depend on a number of fabrication-related factors, including the glass purity, its thermal history and preparation, and a

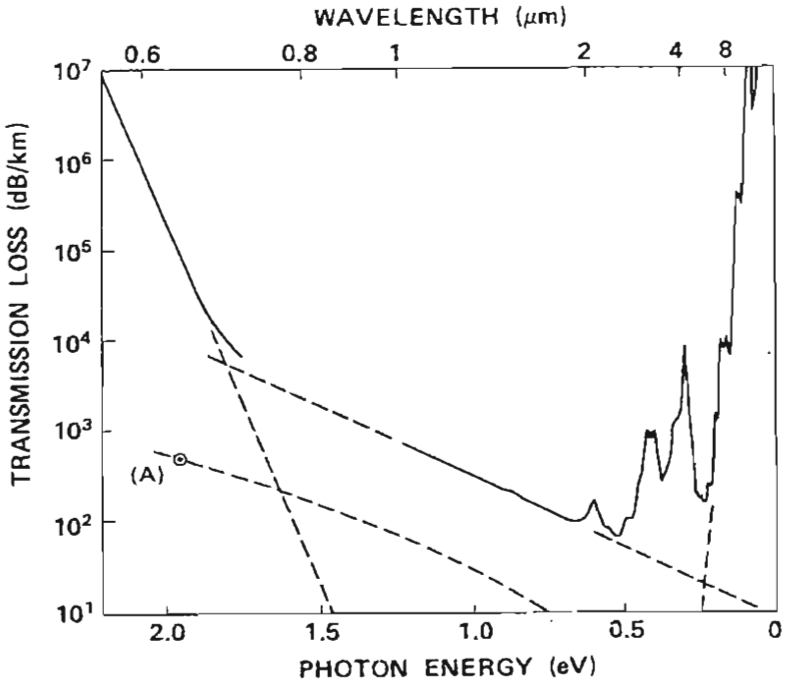

FIGURE 6.2: Transmission loss of a $As_{40}S_{60}$ optical fibre showing the weak absorption tail of the electronic edge; the dashed curve (A) is the measured/calculated scattering loss (after (193)).

Glass system	E_{WT} [eV]	WAT curve [$dB\ km^{-1}$]	Reference
As_2S_3	0.3	-	(90)
As_2S_3	-	8.4 exp(4.4/λ)	(193)
$As_{0.4}S_{0.55}Se_{0.05}$	-	0.8 exp(8/λ)	(198)
$Ge_{0.2}Se_{0.8}$	-	-	(199)
$Ge_{0.4}Se_{0.6}$	-	-	(200)
$Ge_{0.05}As_{0.38}Se_{0.57}$	-	10 exp(6.7/λ)	(193)
$Ge_{0.33}As_{0.12}Se_{0.55}$	0.84	-	(90)
$Ge_{0.28}Sb_{0.12}Se_{0.60}$	1.56	-	(90)

TABLE 6.1: Characteristics of the WAT in chalcogenide glass systems

clear distinction between the intrinsic and extrinsic component to the WAT has not yet been achieved.

From a practical point of view, it is difficult to investigate the presence of the WAT. A number of other loss mechanisms with comparable magnitude are generally active in the same spectral region, including impurity absorption and scattering from heterogeneous inclusions, crystals or waveguide defects. For this reason it has not been possible until now to establish whether a WAT is present in GLS and GLSO glasses. Brady et al. (89) have studied the transmission loss of bulk glass and fibres, but could not determine the origin of the attenuation measured in the near- and mid-IR. Transition metal impurities,

in particular, have broad absorption bands in the near-IR, which can easily screen out the smooth and featureless slope of the WAT. Not unexpectedly, unequivocal evidence of the presence of the WAT was obtained for those glass systems which can be fabricated with very low TM impurity contents; the most notable example is *As-S* glass, where both the components and the glass itself can be purified by distillation.

6.4 Absorption from transition metal impurities

First-row transition metal (TM) ions are well-known active dopants, with optical transitions arising from 3d electrons. The relevance of TM absorption in glasses for optical fibre applications was first established in the work by Schultz (202), who measured the absorptivities of TM ions in fused silica; similar work has also been reported for sodium borosilicate glass (203) and for fluorozirconate glass (204), (13). In TM-doped glass, TM ions give rise to broad absorption and emission bands in the visible and near-IR, the position and intensity of which depend primarily on the oxidation state of the metal ion. TM ions can exist in several oxidation states, and the proportions of the different ionic species depend on both the composition of the host glass and on the preparation method; in particular, the temperature and the atmosphere under which glass melting is carried out can strongly affect the oxidation states present in the final glass (13). The optical properties of each oxidation state also depend on the local geometry of the site where the TM ion sits, which is determined by the host composition and microstructure. Due to the variety of effects and the number of parameters involved, the interpretation of the absorption (and emission) spectra of TM ions is often complicated, and other techniques such as electron paramagnetic resonance are commonly used.

Very few studies have been published on the effects of TM ions in chalcogenide systems. Brady (51) measured the absorptivity of TM ions in 70:30 GLS glass. In chalcogenide glasses most optical transitions in the visible are not observed due to electronic absorption of the host, and the interpretation of the absorption spectra can only rely on the NIR absorption bands. In GLS and GLSO glasses, the presence of both sulphur and oxygen is a further complication, as TM ions may form complexes in several oxidation states. This section presents the results of a comparative study of TM absorption in GLS and GLSO glasses. The aim is to determine the practical absorptivities and to identify, where possible, the oxidation states of 3d transition metals in each glass composition.

Two sets of samples doped with TM ions were prepared following the standard procedure described in Chapter 3. Glass compositions were chosen as $65Ga_2S_3$:$30La_2S_3$:$5La_2O_3$ (GLS) and $78Ga_2S_3$:$22La_2O_3$ (GLSO), to which suitable amounts of TM sulphides were added. The doping level was kept low (approximately 0.05 $wt\%$) in order to ensure that no phase separation occurred in the glass, and also to reproduce the effect of low-level TM impurities more reliably. A detailed list of the doping compounds and corresponding

Compound	Dopant	65:30:5 GLS content [*ppmwt*]	78:22 GLSO content [*ppmwt*]
TiS_2	Ti^{4+}	21 *ppm*	–
V_2S_3	V^{3+}	28 *ppm*	31 *ppm*
Cr_2S_3	Cr^{3+}	31 *ppm*	36 *ppm*
FeS	Fe^{2+}	64 *ppm*	57 *ppm*
Fe_2O_3	Fe^{3+}	59 *ppm*	–
CoS_2	Co^{4+}	36 *ppm*	17 *ppm*
NiS	Ni^{2+}	36 *ppm*	48 *ppm*
CuS	Cu^{2+}	43 *ppm*	40 *ppm*
ZnS	Zn^{2+}	40 *ppm*	–

TABLE 6.2: Nominal content of TM ions in GLS and GLSO samples

nominal content of TM ions is given in table 6.2. All the glass batches weighed 20 g. The amount of dopant added to the batches was measured by a precision balance with a 100 μg resolution; the nominal content of TM ions was estimated to be accurate to within $\pm 15 - 20$ %.

The glass batches were melted for 24 hours to ensure compositional homogenisation. Melting was carried out in a flowing argon atmosphere ($\approx$ 1 $lmin^{-1}$), hence under reducing conditions. However, very little is known about equilibrium oxidation states of TM ions in GLS and GLSO. It is hoped that the long melting time also leads to the equilibration of the redox reactions within the melt. In this study only two glass compositions were considered and a fixed melting schedule was employed, but a more extensive investigation of the effect of glass composition and melting could provide the basis for further study.

Glass ingots were cut into samples with optically polished faces and appropriate thickness. The absorption spectra were measured in the range 0.4-3.2 μm, using a VIS/NIR spectrophotometer (Cary 500) fitted with PM and PbS detectors, and in the range 2-5 μm, using a FTIR spectrometer (Perkin Elmer system 2000), fitted with a triglycine sulphate (TGS) detector. The transmission of an optically thin sample is expressed as:

$$\mathcal{T} = \frac{(1-R)^2}{1-R^2}\, e^{-(\alpha_0+\alpha_{TM})\, L} \tag{6.10}$$

where R is the reflectivity, α_0 is the background attenuation and α_{TM} is the absorption coefficient due to TM ions, L is the sample thickness and the following condition is satisfied in the wavelength range analysed: $(\alpha_0 + \alpha_{TM})L \ll 1$. Since the doping level is very low, the refractive index is not modified by TM ions, and an undoped sample of the same thickness can be used to correct for the background loss and for the interface

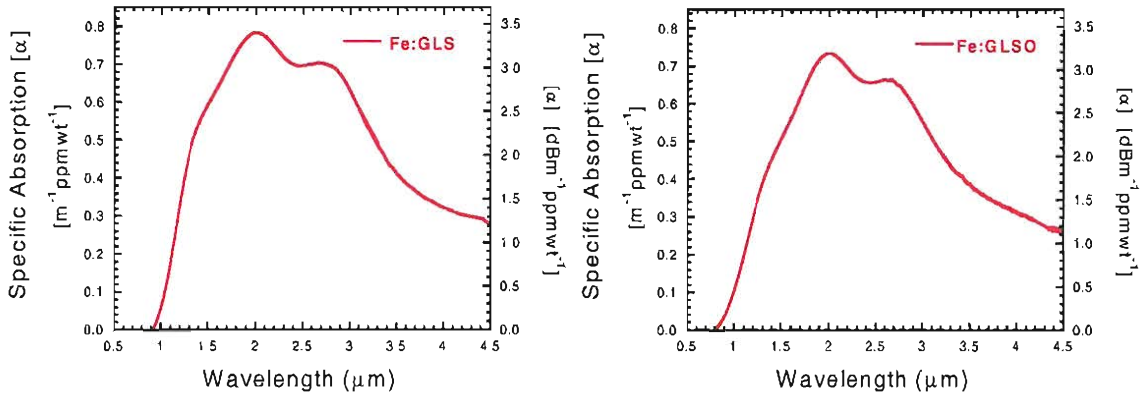

FIGURE 6.3: Absorption of iron (Fe^{+2}) doped GLS and GLSO glass

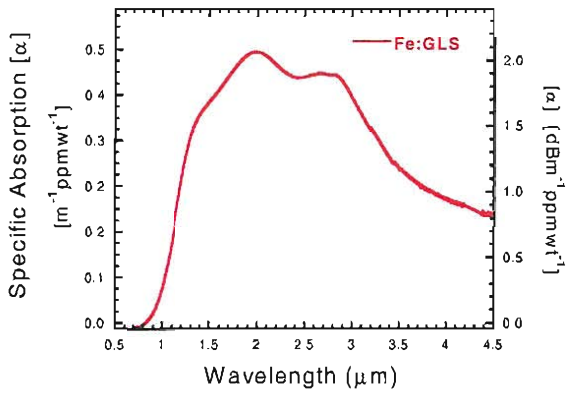

FIGURE 6.4: NIR absorption of iron in GLS doped with Fe_2O_3

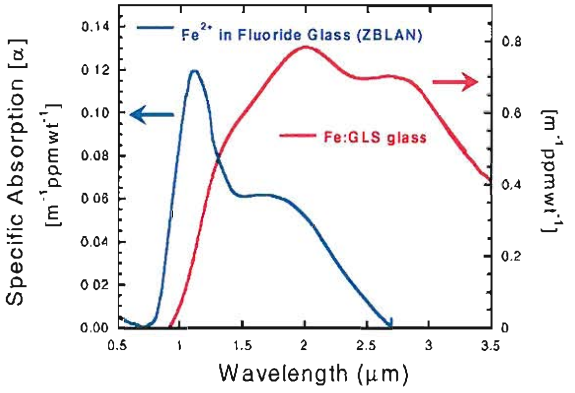

FIGURE 6.5: Absorption spectra of iron in Fe:ZBLAN (after (13)) and Fe:GLS glass

reflection loss; α_{TM} is then determined from the following relationship:

$$\alpha_{TM} = \frac{1}{\log e} \frac{[A_{TM} - A_0]}{L} \tag{6.11}$$

where A_{TM} and A_0 are the absorbances of a doped and an undoped sample respectively. The absorption coefficient 6.11 can be expressed in dBm^{-1} units by multiplying the right-hand side term by $10 \log e$ or 4.3429. A 'practical' specific absorptivity can be obtained by dividing α_{TM} by the total TM-ion content c_{TM} (in *ppm wt*):

$$[\alpha] = \frac{\alpha_{TM}}{c_{TM}} \tag{6.12}$$

While the assumption that α_{TM} is proportional to the concentration of the ion causing the absorption is generally correct in the low concentration range, the relationship 6.12 makes no distinction between different oxidation states and assumes that all the states equally contribute to the total absorption.

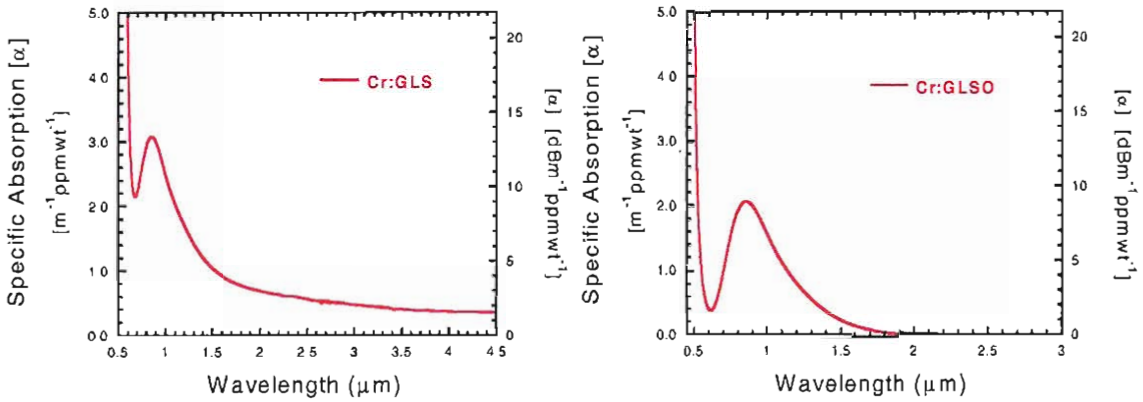

FIGURE 6.6: Absorption of chromium doped GLS and GLSO glass

The absorption spectrum of *iron* in GLS and GLSO (figure 6.3) has a strong and very broad absorption band between 1 and 5 μm. In oxide and fluoride glass, iron can exist in both its oxidation states, i.e. Fe^{2+} and Fe^{3+}. Fe^{3+} causes weak bands in the visible and a sharp edge in the blue-green, which cannot be detected in GLS and GLSO glass. The reduced ion, Fe^{2+}, has absorption bands in the IR. In fluoride glass (204), (13) a band with a double peak structure is observed between 1 and 2.5 μm (see figure 6.5); the same peak structure has also been observed in alkali silicate glass (205), where the two peaks are at 1.1 and 2.0 μm. The fine structure of the absorption has been attributed to Fe^{2+} ions occupying non-equivalent sites with octahedral and tetrahedral symmetry; the octahedral coordination, associated with the peak at ≈ 1.1 μm, is favoured in ZBLAN glass (13). Thus, the broad IR absorption observed in Fe:GLS and Fe:GLSO could equally be due to iron with 2+ valence, although the fine structure of the band is different from oxide and fluoride glass. Three peaks are observed at 1.35, 2.0 and 2.7 μm, with a large tail at longer wavelengths. This suggests the presence of three different sites for the Fe impurity, although the 2.7 μm peak could also be caused by OH^- impurity contained in the doping compound. The position of the three peaks is the same in GLS and GLSO, but the height ratio of the first to the second peak is slightly larger in the GLS host. When iron is introduced as Fe^{3+} (GLS doped with Fe_2O_3, figure 6.4), the IR

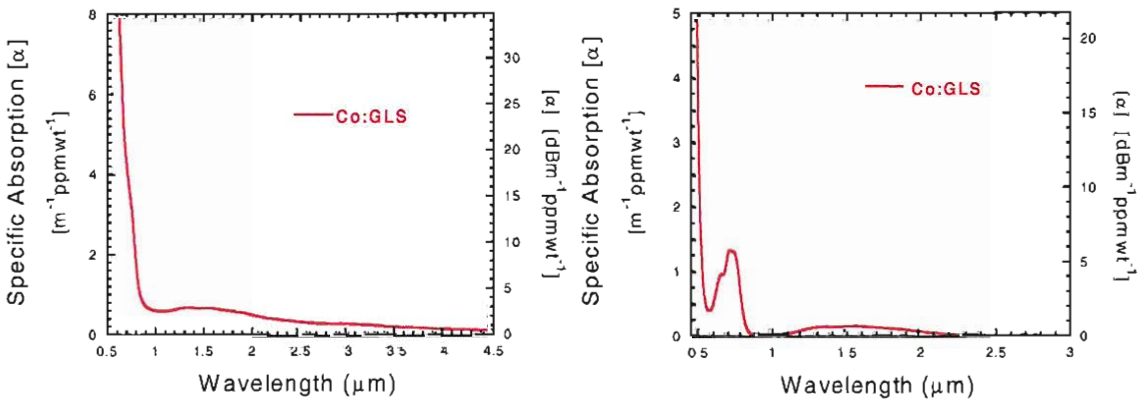

FIGURE 6.7: Absorption of cobalt doped GLS and GLSO glass

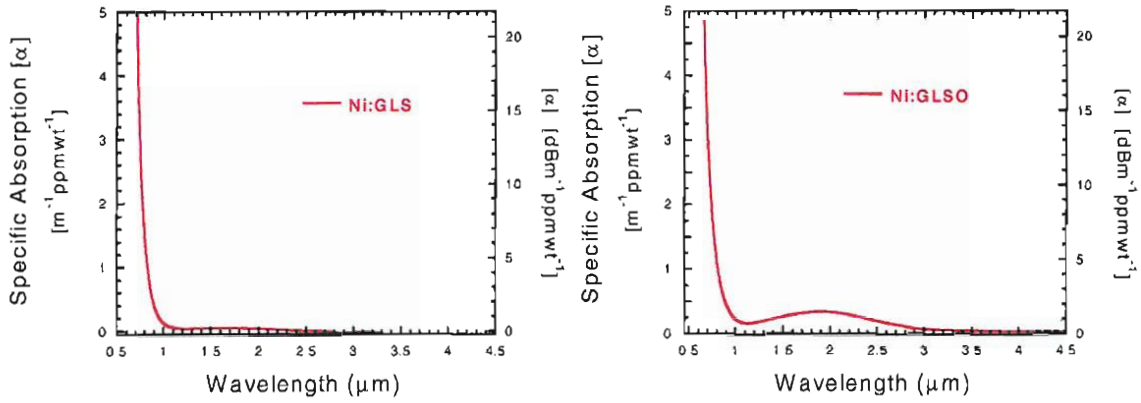

FIGURE 6.8: Absorption of nickel doped GLS and GLSO glass

band is still observed, indicating that part of the Fe^{3+} was reduced to Fe^{2+}; however, the IR band is about $\approx$ 40% lower than in Fe^{2+}:GLS, which suggests that part of the iron is still in the Fe^{3+} state, thus iron in GLS can exist in both oxidation states. The peak at 2.9 μm is also observed and its peak height ratio to the second peak is the same in Fe_2O_3:GLS as the other spectra (figure 6.3, 6.4; this suggests that the peak is genuinely due to Fe absorption, and thus there are three non-equivalent sites for the iron impurity in GLS and GLSO. Further study is required, and in particular fluorescence spectroscopy and EPR could provide additional information leading to a more reliable interpretation for the fine structure of absorption of the Fe^{2+} ion in GLS and GLSO.

Chromium also produces strong absorption in GLS and GLSO (figure 6.6), with a broad peak centered at 0.86 μm; the peak height is higher in the Cr:GLS, in which a shoulder extending into the near-IR is also observed. Chromium can assume several oxidation states in glass: Cr^{2+}, Cr^{3+}, Cr^{4+} and Cr^{6+} (206), (207). The Cr^{6+} ion has no $d-d$ optical transition, and the Cr^{3+} ion has only transitions in the visible range; the red-shift of the electronic edge, observed in Cr:GLS and Cr:GLSO is very likely to be caused by an unresolved peak at 0.66 μm from Cr^{3+}. In contrast, the band around 0.86 μm is probably caused by the $^5E \rightarrow ^5T_2$ transition of Cr^{2+}, which is also observed at 0.84 μm in ZBLAN (206). The long-wavelength tail observed in Cr:GLS could be due to a small fraction of ions existing in the Cr^{4+} state, with an absorption at $\approx$ 1.1 μm, but this point needs further investigation, in particular by emission spectroscopy. The presence of a tail extending in the MIR could hint at scattering caused by reduced metallic Cr^0, however no phase separation was detected in the samples by optical microscopy.

The absorption of *cobalt* is shown in figure 6.7. In Co:GLS, cobalt leads to an almost featureless increase in the absorption in the range 1-5 μm, where a red-shift of the electronic edge and two very broad absorptions are observed at approximately 1.4 and 1.6 μm. In Co:GLSO, two unresolved peaks are also observed in the shorter wavelength region (0.67 and 0.74 μm). All these absorption features can be attributed to divalent cobalt ions, as is also seen in oxide and fluoride glass; in particular, the broad NIR absorption is due to four-fold coordinated Co^{2+} (202), (204). The NIR absorption of

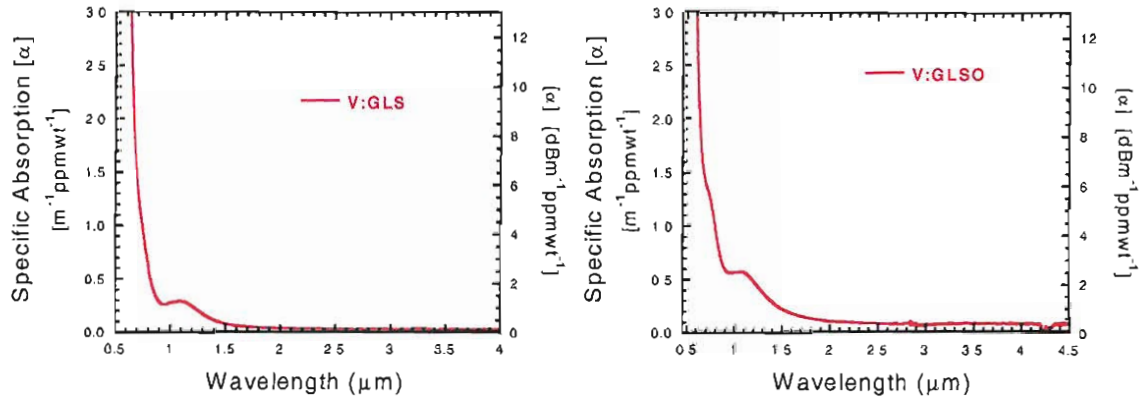

FIGURE 6.9: Absorption of vanadium doped GLS and GLSO glass

Co:GLSO beyond 2 μm is significantly lower than Co:GLS (see table 6.4); this could be due to the presence of metallic cobalt in the glass but also in this case no phase separation was detected, thus the reason for this effect is not fully clear.

The absorption of *nickel* (figure 6.8) is attributed to the divalent ion (208). Ni^{2+} has a very strong absorption in the range 0.45-0.63 μm, which overlaps the electronic edge of GLS and GLSO; hence, it cannot be resolved in our samples and a large red-shift of the edge is observed instead (figure 6.8). Ni^{2+} also produces a weaker absorption band in the NIR; in *Ni*:GLSO the band peaks at 1.9 μm and is almost ten times stronger than in *Ni*:GLS (table 6.4).

Vanadium, like chromium, has been observed in several oxidation states in oxide and fluoride glass (V^{3+}, V^{4+} and V^{5+}). In GLS and GLSO, vanadium produces a shoulder in the absorption edge and a broad peak at about 1.1 μm (figure 6.9). V^{3+} has a strong absorption at about 0.7 μm, which corresponds well to the position of the shoulder observed in *V*:GLSO. The peak at 1.1 μm, indicates that at least a fraction of vanadium ions are in the V^{4+} oxidation state, which is also observed in oxide glasses (202), but not in fluoride ZBLAN (204); the height of the 1.1 μm peak is twice as intense in GLSO

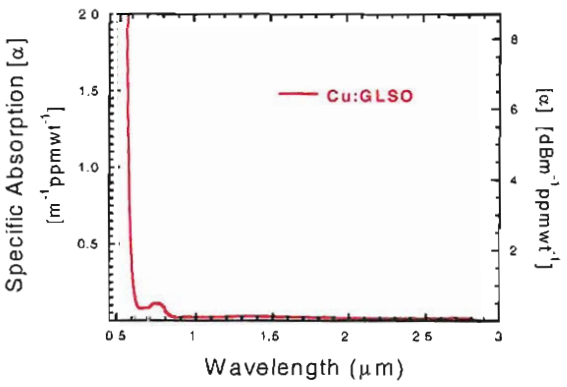

FIGURE 6.10: Absorption of copper doped GLSO glass

Metal	Reduced Ion	Oxidised Ion
Ti	(Ti^{3+})	(Ti^{4+})
V	V^{3+}	V^{4+}
Cr	Cr^{2+}	Cr^{3+} (Cr^{4+})
Fe	Fe^{2+}	(Fe^{3+})
Co	Co^{2+}	Co^{2+}
Ni	Ni^{2+}	Ni^{2+}
Cu	Cu^{+}	Cu^{2+}(*)
Zn	(Zn^{2+})	(Zn^{2+})

(*) observed in GLSO only
(.) not observed or uncertain

TABLE 6.3: Oxidation states of TM ions in GLS and GLSO

TM ion	65:30:5 GLS Wavelength [μm]	65:30:5 GLS Intensity [$m^{-1}ppmwt^{-1}$]	78:22 GLSO Wavelength [μm]	78:22 GLSO Intensity [$m^{-1}ppmwt^{-1}$]	Ref. (51) Intensity (†) [$m^{-1}ppmwt^{-1}$]
Ti^{4+}	–	–	–	–	*tail*
V^{3+}	*n.r.*	*n.r.*	0.72	1.3	1.15
V^{4+}	1.09	0.28	1.06	0.57	0.27
Cr^{2+}	0.86	3.08	0.86	2.08	2.07
Fe^{2+}	1.35	0.52	1.35	0.44	0.48
	2.00	0.78	2.00	0.74	0.80
	2.70	0.70	2.70	066	0.73
Co^{2+}	*n.r.*	*n.r.*	0.67	0.96	–
	n.r.	*n.r.*	0.74	1.33	–
	1.37	0.68	1.38	0.16	0.69
	1.57	0.67	1.58	0.17	0.75
Ni^{2+}	1.75	0.03	1.92	0.38	0.55
Cu^{+}	–	–	0.76	0.11	–
Zn^{2+}	–	–	–	–	–

n.r. = not resolved
(†) refers to an unspecified GLS composition

TABLE 6.4: Position, intensity and attribution of absorption peaks observed in TM-doped GLS and GLSO

as in GLS, indicating that the formation of the oxidised state V^{4+} is favoured in the GLSO host.

Copper is a very strong absorber in the region around 0.8 μm when it is contained in the oxidised state Cu^{2+}. In *Cu*:GLS we could not detect any absorption, which indicates that copper is in the reduced state Cu^{+}. In *Cu*:GLSO a weak band is observed at 0.76 μm, which suggests that a small fraction of Cu^{2+} ions exists in the GLSO host.

Titanium was only studied in GLS glass, where it was not found to produce significant absorption. It can exist in two oxidation states, Ti^{3+} and Ti^{4+}, of which only the Ti^{3+} exhibits an absorption peak around 0.5 μm in oxide and fluoride glass. Finally, *zinc* was also studied in GLS only, and it too was not found to produce any absorption; the ion Zn^{2+} has in fact a $3d^{10}$ configuration and no optical transitions.

In summary, the optical absorption of transition metal ions in GLS and GLSO has been measured; it was confirmed that TM ions can exist in several oxidation states, as was previously found in oxide and fluoride glass. In sulphide glass most transitions in the visible overlap the fundamental electronic absorption, thus making it difficult to identify the oxidation states of TM ions by absorption spectroscopy. The results of the present investigation are summarised in table 6.3, where the observed oxidation states are given, and in table 6.4, where the position and intensity of the absorption peaks are given and their intensities are compared to those given in ref. (51). The 'practical' absorption coefficients of transition metals, estimated using the 6.12, are summarised in figure 6.11 for GLS, and in figure 6.12 for GLSO glass. The stronger absorbers in the NIR are Fe^{2+}, Cr^{2+} and Co^{2+} in GLS, and Fe^{2+}, Cr^{2+}, V^{4+} and Ni^{2+} in GLSO. The values measured for TM ions in GLS are in good agreement with previous results, apart from *Ni*:GLS

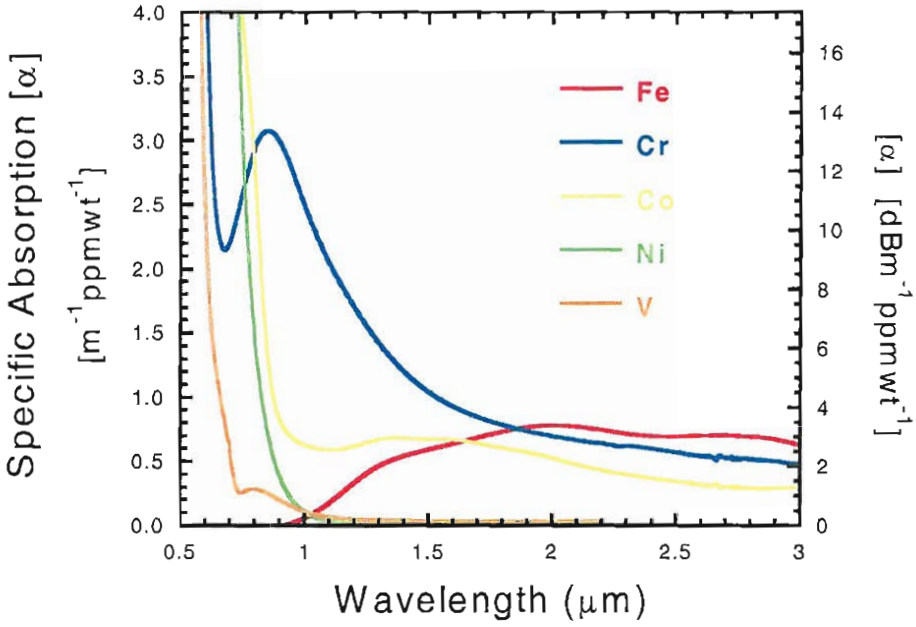

FIGURE 6.11: Absorption coefficient of transition metal ions in GLS glass

and *Co*:GLS, where the absorption measured was significantly lower than previously reported. One possible explanation for the discrepancy is that the samples in ref. (51) had higher doping concentrations, but it is also possible that the glass samples measured in reference (51) were prepared in different conditions and had a slightly different composition. Both the present analysis and the results presented in (51) are approximated in that the nominal TM concentrations were used in the calculations, and it assumes that all the oxidation states equally contribute to the measured absorption. Better informa-

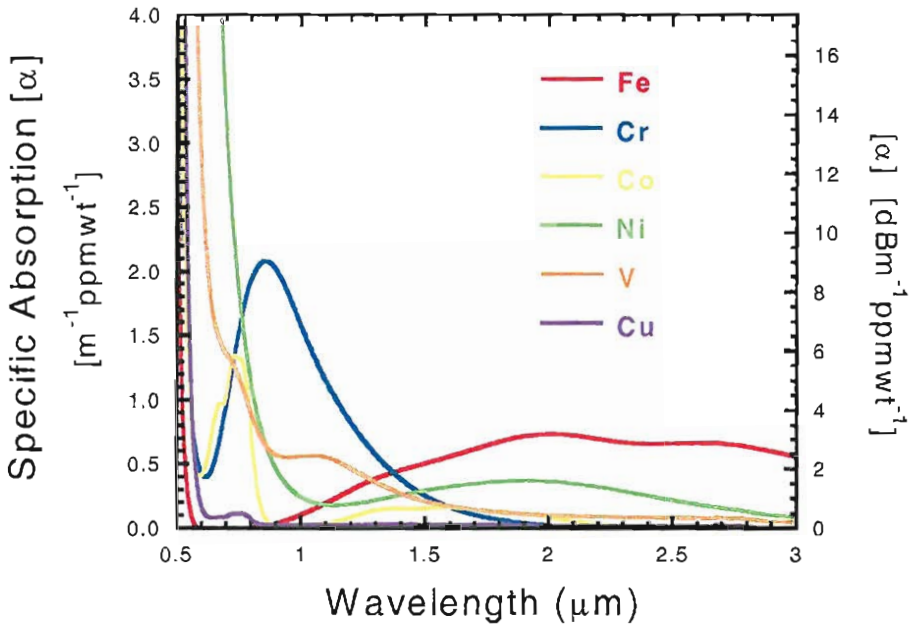

FIGURE 6.12: Absorption coefficient of transition metal ions in GLSO glass

tion on the specific absorptivity of TM ions could be achieved by measuring the actual TM content in the samples (e.g., by GDMS) and utilising emission spectroscopy and magnetic spectroscopy (NMR or EPR) to detect and quantify the different oxidation states.

6.5 Near-IR transmission loss of GLS and GLSO glasses

This section the measurement of the total bulk attenuation of GLS and GLSO will be presented and the results utilised, in conjunction with those from laser calorimetry (Chapter 4), fibre measurements (Chapter 3) and the measurement of TM impurity absorption, to discuss the mechanisms of loss of GLS and GLSO glasses in the near IR range.

In section 3.7.3 measurements of total attenuation of unclad GLS and GLSO fibres were presented. For both materials, the loss in the range 1-2 μm averages about 5 dBm^{-1} for the 'best quality' unclad fibres, with lowest measured values of 2-3 dBm^{-1} for fibres LF276 and LF292 (GLS), and 4 dBm^{-1} for LF367 (GLSO) drawn from polished rods. Fibre loss, however, can be affected by a variety of factors, in addition to the usual intrinsic and extrinsic loss mechanisms of the material. For instance, extra loss can be induced by fibre drawing causing devitrification (e.g. crystals) or other defects. Imperfections or contamination at the fibre surface can also increase the loss of unclad fibres. Furthermore, loss measurements of GLS and GLSO unclad fibres can also be affected by photodarkening, which will be fully described and characterised in the next section 6.7. Low-level side illumination of the fibre with visible light (e.g. from lab illumination and even instrument displays) can induce significant extra loss at shorter wavelength, and, due to the long characteristic time of the photodarkening in GLS and GLSO (see section 6.7.3), this disturbance persists long after the source of illumination is turned off. As a consequence, PD introduces an extra element of uncertainty and makes it difficult to achieve repeatable and precise measurements from unclad fibres.

Bulk glass samples, on the other hand, are more unlikely to contain crystals and are substantially unaffected by photodarkening. Accurate transmission measurements were performed on samples from the same series that were also measured by laser calorimetry. As discussed in section 4.2, the measurement of low-level bulk loss is difficult and several issues must be addressed in order to achieve reliable results. Firstly, the correction of the Fresnel loss relies on measuring the differential transmission of two samples with different thickness, but with exactly the same surface quality and preparation. The samples used for the calorimetric measurements (see table 4.2), as explained in section 4.4, all had excellent surface preparation. Another problem is that $\approx cm$ thick, high index glass slabs can easily deflect the sampling beam off the ideal path, and cause slight shifts of the focal points at the detector; as a result, the detection efficiency is modified, giving

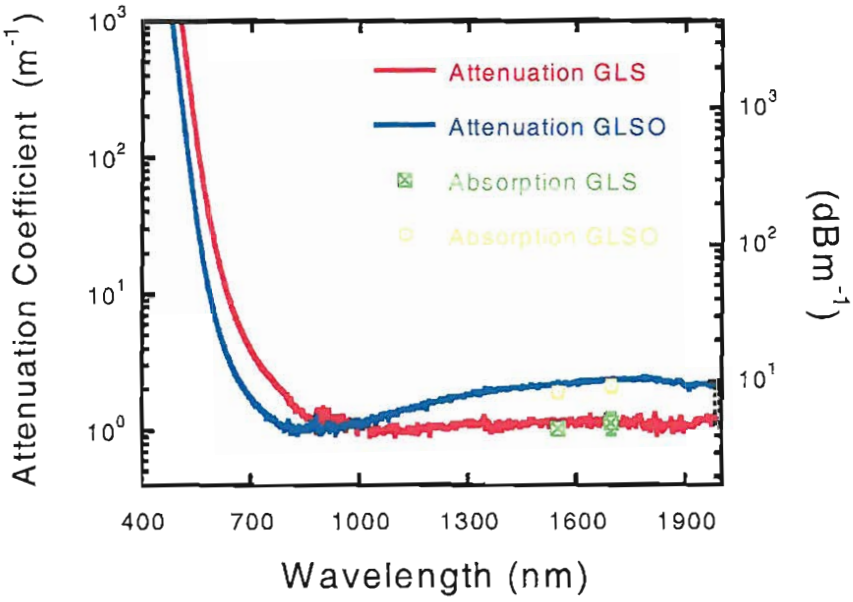

FIGURE 6.13: Total attenuation of GLS and GLSO (by differential transmission) and absorption at 1.55 and 1.7 μm (by laser calorimetry).

a response that is dependent on the sample thickness and positioning; this can lead to large errors especially in the case of small-area detectors (such as MCT detectors) or position-sensitive detectors. In order to eliminate this problem, a detection scheme with an integration sphere was adopted; a standard attachment of a Cary 500 UV/VIS/NIR spectrophotometer was used, with a 15 cm diameter, PTFE coated sphere, which was fitted with a large-area PM tube/PbS detector pair. The accuracy of differential transmission relied on the source and the baseline remaining constant from measurement to measurement. Under normal conditions, the maximum drift of the baseline in the range $0.4 - 2\ \mu m$ was less than 10^{-3} $A.U.$ observed over ≥ 3 hours operation; thus, even in these conditions, the accuracy of the measurement of a sample with $\alpha \approx 1\ m^{-1}$ would have been $\approx 20\%$. In order to further improve the accuracy, a baseline was recorded for each transmission spectrum; this improved the accuracy to better than 10% in the sample specified above. Finally, it is also worth noting that photodarkening does not affect bulk measurements as much as fibre measurements due to the small penetration depth of visible light in GLS and GLSO; anyway, the samples were kept in darkness for ≈ 15 minutes before each measurement to allow any darkening to decay and spectra were always collected by scanning from long to short wavelengths.

In order to obtain the differential transmission, we measured samples F and G for GLS (see table 4.2) and samples C and A for the GLSO composition; the differential thickness in the two cases was 5.66 and 6.48 mm. The transmission was measured through a $10 \times 10\ mm$ area at the center of the samples. The attenuation was obtained from the

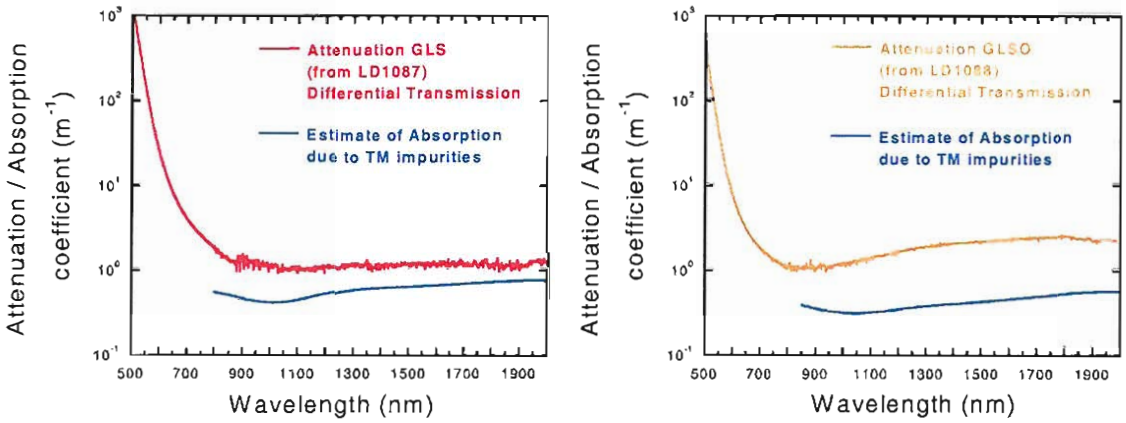

FIGURE 6.14: Total attenuation and estimate of TM impurity absorption is GLS and GLSO.

transmission of the two samples using the following:

$$\alpha = \frac{1}{\Delta L} \ln\left[\frac{T_1}{T_2}\right] \tag{6.13}$$

where $\Delta L \equiv L_1 - L_2$ is the differential thickness and T_1 and T_2 are the samples' transmission. The attenuation spectra of GLS and GLSO glass are shown in figure 6.13. The spectra show the sharp exponential 'Urbach' edge for wavelengths below $\approx 600\ nm$, and then a transition to a much flatter region, where the loss is almost independent of the wavelength, for $\lambda \geq 1000\ nm$. The loss of GLSO appears to be higher and increases slightly in the region 1-2 μm. The noise in the region 800-900 nm of both spectra is due to the lower sensitivity of the PbS detector in that region.

Figure 6.13 also reports the values of absorption measured at 1.55 and 1.7 μm in the same samples by laser calorimetry (see section 4.8.3). It is very clear from the graph that the absorption equals the total attenuation measured by differential transmission for both GLS and GLSO. NIR absorption of GLS and GLSO is caused by TM impurities and, possibly, by the the weak absorption tail; since TM impurities have very broad absorption peaks, and the WAT has a flat dependence on the wavelength, the result obtained suggests that absorption is indeed the main loss mechanism in the NIR for both GLS and GLSO.

In order to interpret the mechanisms producing the measured absorption, an estimate of the absorption due to TM impurities was calculated; we assumed the TM concentrations measured by GDMS trace analysis in the glass batches LD1087 and LD1088 from which the two sets of samples were produced (see table 4.2), and the specific absorption coefficients measured in the previous section 6.5. A comparison between the measured absorption coefficients of GLS and GLSO and the corresponding estimated TM absorption is shown in figures 6.14.

Glass	Wavelength [μm]	Measured Attenuation Coefficient [m^{-1}]	Measured Absorption Coefficient [m^{-1}]	Estimated TM absorption [m^{-1}]
GLS	1.55	1.1 ± 0.1	1.0 ± 0.1	0.6 ± 0.2
	1.7	1.15 ± 0.1	1.1 ± 0.2	0.65 ± 0.2
GLSO	1.55	2.1 ± 0.2	1.9 ± 0.15	0.4 ± 0.1
	1.7	2.2 ± 0.2	2.1 ± 0.2	0.4 ± 0.1

TABLE 6.5: Comparison between measured total attenuation, measured total absorption and estimated absorption due to TM impurities

From the two figures, it appears that the attenuation coefficients of both GLS and GLSO are higher than the calculated total absorption of TM ions. However, a note of caution is necessary when interpreting the available data. The certified precision of the GDMS measurement is $\pm 10\%$ and its absolute accuracy is in the range $\pm 5 - 20\%$ (209). In addition, the impurity content of the GLS batch was measured by GDMS in two samples taken from different points on the ingot, finding an average variation of approximately 30%; this can either be due to the accuracy/precision of the GDMS, or to an actual non-uniformity of the distribution of impurities across the sample. When this is taken into account, the estimated TM impurity absorption at 1.55 μm is $0.6 \pm 0.2\ m^{-1}$ in GLS (which compares to $1.1 \pm 0.1\ m^{-1}$ total (measured) attenuation and $1.0 \pm 0.1\ m^{-1}$ total (measured) absorption), and $0.4 \pm 0.1\ m^{-1}$ in GLSO (which compares to $2.1 \pm 0.2\ m^{-1}$ total (measured) attenuation and $1.9 \pm 0.15\ m^{-1}$ total (measured) absorption). The results at both 1.55 and 1.7 μm are also summarised in table 6.5. We note that the attenuation coefficient in GLSO is higher than in GLS, which would suggest that GLSO has a higher impurity content than GLS; the GDMS analysis, however, indicates that the content of transition metal ions in the two glasses is substantially the same. The GDMS analysis also shows that GLSO has a relatively high content of Ca (20 ppm, as compared to ≈ 1 ppm in GLS); although the effect of Ca doping on the transmission of GLS and GLSO has not been reported yet, it is unlikely that Ca is optically active in this region. From MIR transmission spectra it was also found that the OH^- absorption is higher in the GLSO batch, but the very wide feature seen from 1 to 2 μm in the GLSO spectrum cannot be explained in terms of OH^- absorption. Thus, the disagreement between transmission measurements and GDMS results cannot be explained with the data available.

Summarising, the main result of this section is that the comparison of calorimetric measurements of absorption of GLS and GLSO, with accurate measurements of the total attenuation, by differential transmission, shows that in both glasses the optical loss in the region 1.55-1.7 μm is entirely caused by absorption. Secondly, there is an indication that the total absorption due to TM impurities, estimated from TM concentrations measured by GDMS analysis and from the specific absorption of TM ions measured in section 6.4, does not fully account for the total absorption. This suggests the presence

of an additional mechanism of absorption, which is likely to be the weak asborption tail. Calorimetric measurements at longer wavelengths (2 μm and 3.5-5 μm), could provide a more definitive verification of the presence of a weak tail and the quantification of its magnitude.

6.6 The effect of temperature on the transmission loss

In this section we report measurements of the effect of heating on the optical loss of GLS and GLSO fibres. Temperature is an important parameter affecting the transmission of chalcogenide glasses, for which larger temperature-induced increases of absorption are generally observed, as compared to fluoride and oxide glasses. This effect has been studied in Te and Se containing fibres for IR laser power delivery (210), where it limits the maximum transmitted power by effectively reducing the threshold for thermal damage.

The temperature-induced increase of absorption is due to the combination of two factors. Firstly, the optical bandgap of amorphous semiconductors becomes narrower with increasing temperature (211), which causes a red-shift of the electronic edge. In addition, free-carrier absorption is exponentially dependent on the temperature, as the free-carrier concentration obeys the Fermi statistics. Free-carrier absorption is more important in tellurides and at longer wavelength, and its contribution is much smaller in sulphides (212). The scattering loss is independent of the temperature (212).

Heating GLS and GLSO glasses produces very obvious changes in the optical properties. For instance, the colour of the glass becomes increasingly darker, and for temperatures above $\approx 600\ ^{\circ}C$ both GLS and GLSO are black and totally opaque to visible light. As far as thermal damage is concerned, since GLS and GLSO have relatively high glass transition and melting temperatures, the temperature-induced increase of the loss is a minor concern as compared to other chalcogenides. On the other hand, the shift of the absorption edge impacts the material's transparency in the NIR, thus it is important to achieve a full characterisation of this effect in GLS and GLSO.

In this section a study of the temperature dependence of the loss of unclad GLS and GLSO fibres is reported. The fibres used for the measurements, namely LF294 for GLS and LF344 for GLSO, were pulled from $\approx 9\ mm$ diameter rods, had a diameter of 150 and 170 μm respectively and were both uncoated. The background loss at 1.5 μm, measured by the cutback technique, was $7.5 \pm 1\ dBm^{-1}$ for the GLS fibre and $12.5 \pm 1\ dBm^{-1}$ for the GLSO. A 20 cm portion of fibre was placed on a v-groove and heated by a heater; the v-groove was surrounded by a metal block with large thermal mass in order to maintain a uniform temperature along the fibre and to minimise thermal fluctuations. The temperature was monitored in close proximity to the fibre by two thermocouples. Before each measurement approximately 15-20 minutes were allowed for the system to reach equilibration. The thermocouple readings were consistent to within $\pm 1\ ^{\circ}C$ during

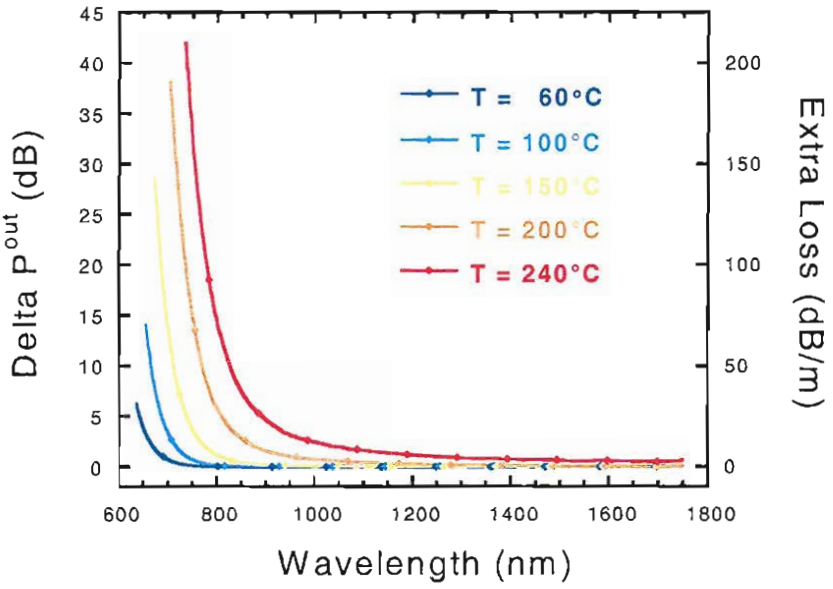

FIGURE 6.15: Extra loss induced by temperature on GLS fibre LF294.

the measurements. The output from a white light source was focussed into the fibre; the visible component was filtered off using a suitable long-wavelength pass filter (RG filters from Schott Glass, 630 nm for GLS and 570 nm for GLSO). Experiments were carried out in darkness in order to avoid photodarkening due to side illumination. The output from the GLS/GLSO fibre was collected via a butt-coupled, multimode silica fibre, and detected by an optical spectrum analyser in the region 500-1750 nm.

The output spectrum of the GLS and GLSO fibres was recorded at room temperature and at fixed temperatures in the range 0-200 $°C$ as the fibre was heated. The temperature-induced fibre loss was calculated using the following relationship:

$$\Delta\alpha_{th}(\lambda, T)\left[dBm^{-1}\right] = \frac{10}{L} \cdot \log\left[\frac{P(\lambda, T)}{P_0(\lambda)}\right] \tag{6.14}$$

where $\Delta\alpha_{th}(\lambda, T)$ is the extra loss, L is the length of the heated portion of the fibre, $P(\lambda, T)$ is the spectral output at temperature T and $P_0(\lambda)$ is the spectral output at room temperature.

The results of the measurements are shown in figures 6.15 and 6.16 for GLS and GLSO respectively. Increasing the temperature results in an obvious shift of the electronic edge. The shift is fully reversible in the range 0-200 $°C$, i.e. the room-temperature background loss measured after a heating cycle remains unaffected. However, when GLS was heated to 240 $°C$ (see figure 6.15), there was evidence of an irreversible increase of the fibre loss; presumably, this increase was caused by some degradation which occurred at the fibre surface.

When plotted on a log scale (see figure 6.16 for the GLSO), the shift of the electronic

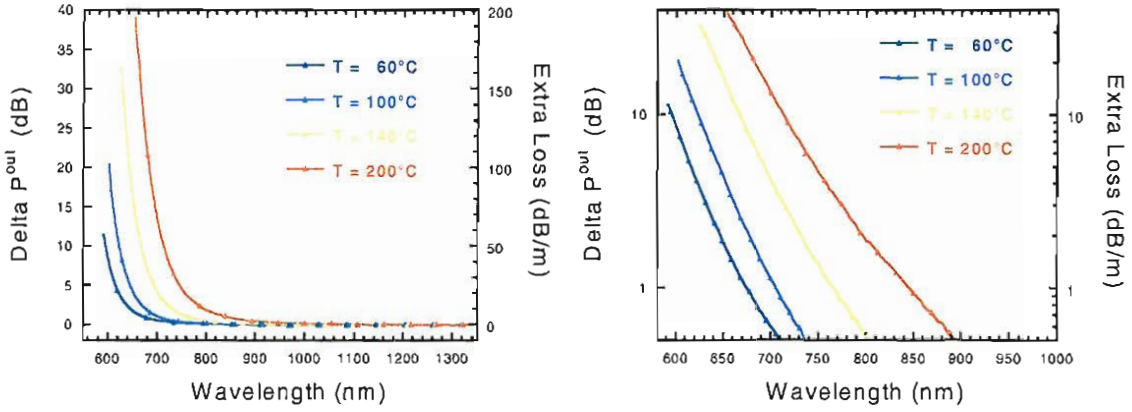

FIGURE 6.16: Linear and logarithmic plots of the extra loss induced by temperature on GLSO fibre LF344.

edge appears approximately parallel, although the temperature-induced absorption is better described by an empirical law:

$$\Delta\alpha_{th}(\lambda, T) = K\exp(C/\lambda) - K_0\exp(C_0/\lambda) \tag{6.15}$$

where the second term on the right-hand side is the usual expression for the Urbach edge (see 6.3), and the first is the absorption at temperature T. With reference to the relationship 6.3, we see that also the 'slope' parameter E_1 depends on the temperature. On the other hand, the temperature dependence of optical bandgap E_g is much stronger; the average variation dE/dT in the range 0-200 $°C$ was calculated by estimating the value of E_g at the absorption $\alpha = 10^5\ m^{-1}$ (213). A value of $(1.7 \pm 0.6)\ 10^{-3}\ eVK^{-1}$ and $(1.9 \pm 0.6)\ 10^{-3}\ eVK^{-1}$ resulted for GLS and GLSO respectively, which compares to 0.91 and 0.99 $10^{-3}\ eVK^{-1}$ measured in AsS and $GeSe$ glass respectively.

6.7 The photodarkening effect in GLS and GLSO

6.7.1 Introduction

Amorphous and glassy chalcogenides show a variety of photoinduced phenomena. These materials are susceptible to modifications of their physico-chemical, mechanical, optical and transport properties by absorption of light with a wavelength close to their optical bandgap (11; 214). For instance photoinduced darkening, bleaching, birefringence, expansion, fluidity and increase of conductivity have been reported (see for instance ref. (11) and references therein). This variety of effects is not matched in any other class of materials, and has attracted scientific as well as technological interest. The type and intensity of the modification observed depends on the material, on the method of preparation (e.g. bulk glass or amorphous film) and on the intensity and wavelength of

the illumination.

Photoinduced phenomena in amorphous and glassy chalcogenides can be classified into irreversible, (temperature) reversible, and metastable phenomena. Irreversible phenomena lead to a permanent modification of the material's properties, such as those observed in as-deposited thin amorphous films. In contrast, in well annealed films modifications can be reversed by heating them up to the glass transition temperature. Metastable modifications are observed in bulk chalcogenide glasses and generally have a smaller intensity as compared to the previous two; they are fully and spontaneously reversible after the illumination is removed. Depending on the material and on the intensity of illumination, both reversible and irreversible effects can occur at the same time. Another important classification of photoinduced phenomena is into scalar and vectorial phenomena (215). Scalar effects are independent of the polarisation of the light inducing them. The vectorial effects, on the contrary, are polarisation-dependent, anisotropic modifications such as photoinduced birefringence.

The photodarkening effect (PD) is a scalar effect. Upon absorption of bandgap light, the position of the fundamental electronic edge shifts towards longer wavelengths; the shift is generally accompanied by a decrease in the slope of the edge and by an increase in the refractive index. Several models have been proposed to explain this effect, although none has proved conclusive for all the materials. The most widely accepted explanation of PD involves the occurrence, upon absorption of bandgap light, of changes in the microstructure, which in turn affect the electronic states and hence the optical properties of the material. The low average coordination of the chalcogen anions (≈ 2) in amorphous and glassy chalcogenides is thought to favour these structural changes.

The absorption coefficient around the optical bandgap is obviously very high ($\alpha \geq 10^5\ m^{-1}$), which leads to a low penetration depth of the light inducing the PD. Consequently, it is difficult to observe PD in bulk samples, where its occurrence is limited to a very small volume below the sample surface. For instance, the transmission of bulk samples is almost unaffected by PD due to the very small interaction length of the transmitted beam with the darkened region. Most studies have been carried out in thin films, with a thickness of a few μm, comparable to the penetration depth of bandgap light. However the photoinduced properties of thin films are generally different from those of the bulk. Thus, a different approach was used to study the PD in GLS and GLSO, employing unclad fibres and side illumination; in this scheme, the interaction length between the light travelling through the fibre and the darkened region at the fibre surface can be made as long as tens of cm, and PD can be easily detected. A more detailed description of the experimental setup will be provided in the following subsections 6.7.2-6.7.4.

The occurrence of PD in GLS and GLSO glasses was first reported by Schweizer et al. (216). Apart from its fundamental interest, PD is also relevant for practical applications.

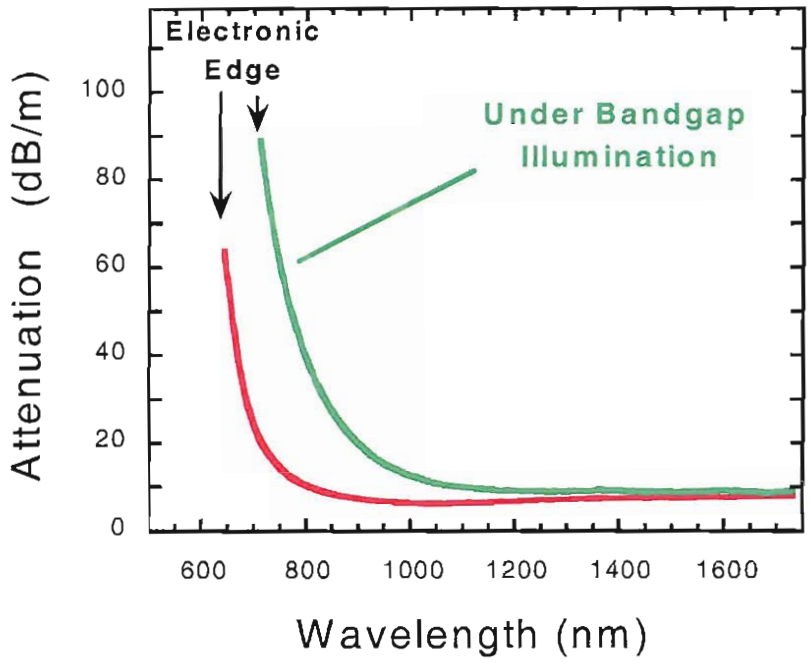

FIGURE 6.17: Transmission of the unclad GLS fibre LF294 in darkness and under side illumination with a white light.

Firstly, PD strongly affects the NIR transmission of GLS and GLSO; it is thus necessary to investigate the impact on practical devices due to all the mechanisms that could induce bandgap absorption in these materials. On the other hand, PD might open up the possibility of modifying the materials properties (e.g. optical loss, refractive index) by an optically-controlled process; furthermore, the photorefractive change associated with photodarkening could be exploited to inscribe erasable structures in the glass.

In this section a full characterisation of the PD in GLS and GLSO glasses will be presented. We investigated the spectral intensity of the effect, its characteristic formation and decay time, its reversibility, its dependence on the wavelength and intensity of the illumination and its dependence on the temperature. Although the detailed mechanisms producing the PD in GLS and GLSO were not investigated here and are still not known, the findings presented in this section provide important information on how PD may affect device applications and also how it could be used to design novel devices.

6.7.2 Room-temperature photodarkening in GLS and GLSO.

The effect of the absorption of bandgap light in GLS is demonstrated clearly in figure 6.17. The transmission of an unclad GLS fibre (LF294) was measured in the dark and under side illumination (SI) from a white light source (tungsten halogen lamp), observing a sizeable shift of the electronic edge to longer wavelengths. The setup used for measuring the transmission is outlined in figure 6.18, and is similar to the setup used for measuring the temperature dependence of the loss (section 6.6). The 'probe'

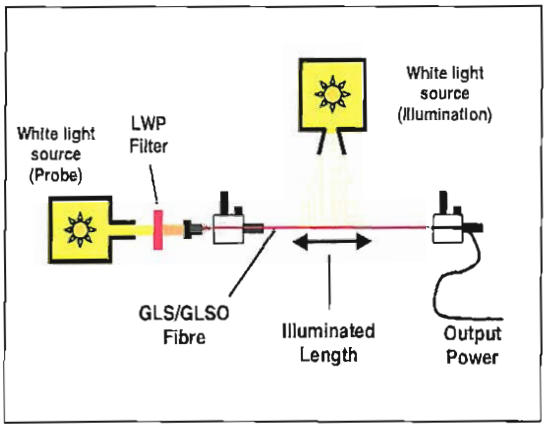

FIGURE 6.18: Scheme of the setup used for detecting the PD in GLS and GLSO unclad fibres.

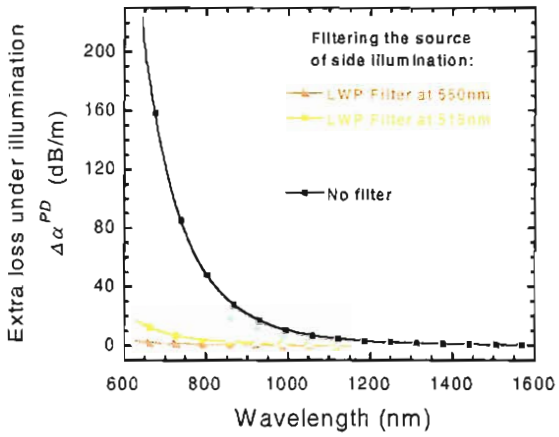

FIGURE 6.19: PD of an unclad GLS fibre under SI by a white light filtered with LWP filters.

light from a second white light source is launched into the GLS fibre to measure its transmission; this source was fully enclosed and its output filtered by a long-wavelength pass filter (Schott Glass, RG filters at 630 nm for GLS and 570 nm for GLSO) to prevent it from causing any PD. The output from the fibre was collected via a silica multimode fibre and detected by an optical spectrum analyser.

From figure 6.17 it is clear that the PD shift causes a substantial increase in the transmission loss of the fibre in the near-IR region below $\approx 1100nm$. The amount of extra loss induced by PD through side illumination (SI) is defined as:

$$\Delta\alpha_{PD}(\lambda, I_\lambda)\left[dBm^{-1}\right] = \frac{10}{L} \cdot \log\left[\frac{P(\lambda, I_\lambda)}{P_0(\lambda)}\right] \tag{6.16}$$

where $\Delta\alpha_{PD}$ is the extra loss, I_λ is the spectral power density of the light inducing the PD, L is the length of the illuminated portion of the fibre, $P(\lambda, I_\lambda)$ is the spectral output from the fibre under SI and $P_0(\lambda)$ is the spectral output of the undarkened fibre. The wavelength dependence of $\Delta\alpha_{PD}$ can be expressed through an empirical relationship (similar to 6.15):

$$\Delta\alpha_{th}(\lambda, T) = K\exp(C/\lambda) - K_0\exp(C_0/\lambda) \tag{6.17}$$

where the first term is the absorption under SI and the second is the absorption under no illumination. The material parameters K and C depend on the intensity and spectral distribution of the SI, I_λ (as will be discussed in subsection 6.7.3), on the exposure time (subsection 6.7.4) and on the temperature (subsection 6.7.5).

Using a simple setup as shown in figure 6.18, some useful basic information on PD can be obtained (216). Firstly, it can be verified that the magnitude of the PD shift, hence

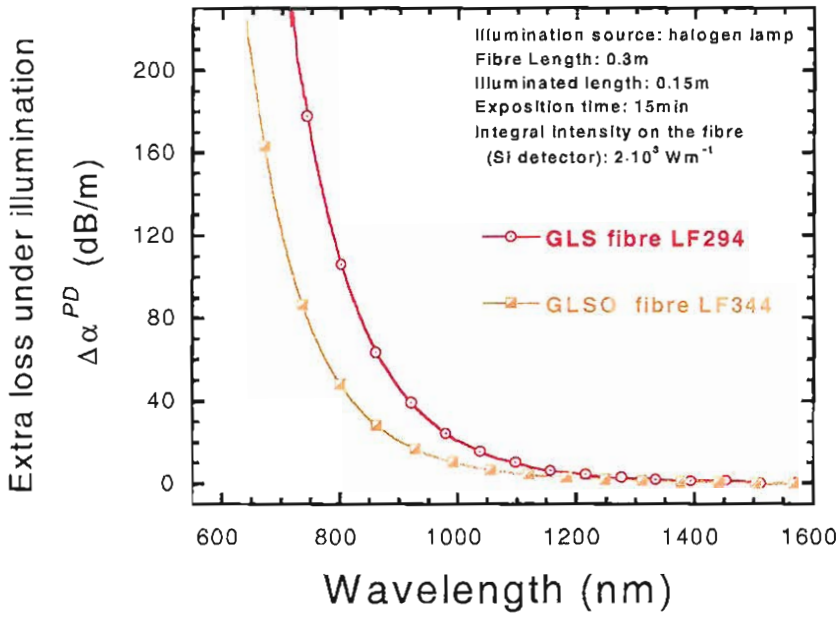

FIGURE 6.20: PD in unclad GLS and GLSO fibres under broadband transverse side illumination (SI) and for equal exposure time.

the extra loss induced by PD, depends on the intensity and on the spectral distribution of the side illumination (SI) on the fibre. By selective filtering of the SI light it is easy to confirm that the shift is caused by bandgap absorption; for instance, using long-wavelength pass (LWP) filters (fig. 6.19), large shifts are observed at shorter wavelengths (435 nm), while almost no shift is observed in GLS at wavelengths above $\approx$ 550 nm. In addition to the magnitude, the dynamics of formation and decay of PD can also be studied; PD in GLS has slow formation ($\approx$ tens of seconds) and decay times ($\approx$ several minutes), and the formation and decay of PD are even slower in GLSO glass. Finally, it is shown that the PD observed in GLS and GLSO fibres is fully reversible upon removal of the SI, i.e., with respect to the classification given in section 6.7.1, it is a *metastable* effect.

Figure 6.20 shows the extra loss due to PD, $\Delta\alpha_{PD}$, measured in two unclad, uncoated GLS and GLSO fibres under the same SI; the two fibres (GLS LF294 and GLSO LF344) were $\approx$ 0.3 m long and in both cases a section of $\approx$ 0.15 m was illuminated by a high power halogen projector lamp. The integral intensity of the SI at the fibre surface was estimated using a silicon detector at about $2 \cdot 10^3$ Wm^{-2}, although the actual intensity of the SI light inducing the PD (bandgap light) was approximately 15% of that measured by the detector. The fibres were kept in dark for several hours before measuring the background transmission; the transmission of the fibre was measured after 15 min illumination. The PD induces a large increase in the transmission loss in the region 0.7-1 μm, where the most important pump wavelengths lie; for instance, up to 110 dBm^{-1} at 0.8 μm (Nd^{3+}, Dy^{3+}), 46 dBm^{-1} at 0.9 μm (Dy^{3+}) and 18 dBm^{-1} at 1.02 μm (Pr^{3+}) were measured in GLS. This result indicates that even the absorption

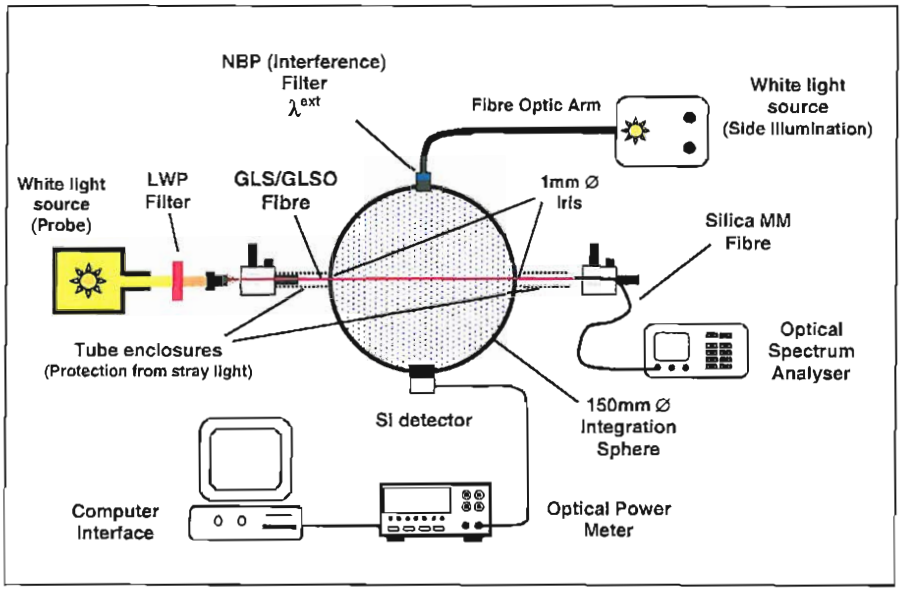

FIGURE 6.21: Setup used for measuring the dependence of PD on the wavelength and intensity of the SI.

of low-level bandgap light can have a major impact on the pumping efficiency of rare earth doped devices. The extra loss in GLS is still measurable in the signal region at 1.3 μm (4 dBm^{-1}) and at 1.55 μm (1 dBm^{-1}).

In order to obtain more precise and repeatable information about the dependence of PD on the excitation wavelength of SI and about the formation and decay times in GLS and GLSO glass, an improved layout of the setup for measuring PD in unclad fibres was devised. The results are presented in the next two sections 6.7.3 and 6.7.4. It is also worth mentioning that, in a preliminary investigation, we also observed PD due to bandgap illumination in unclad fibres of other sulphide glasses , such as $Ga{:}Na{:}S$, $In{:}Ga{:}La{:}S$, $As{:}S$ and LaF_3:GLSO. Thus, the results presented in this thesis for GLS and GLSO glass could be relevant to other sulphide and chalcogenide glass systems.

6.7.3 Dependence of PD on the excitation wavelength

As stated in the previous section, PD is strongly dependent on the intensity and spectral distribution of the SI. One effective way to obtain information about this dependence is to produce a uniform and monochromatic illumination and analyse the PD effect at different wavelengths of the SI.

In order to achieve that, we used the setup described in figure 6.21. Uniform side illumination of the fibre was obtained through the use of a 150 mm, PTFE coated integration sphere (from LabSphere). The output from an enclosed white light source was coupled into the sphere via a fibreoptic arm and a 1/4" port, which was fitted with narrow band pass (NBP) interference filters (IL series from Comar optics, 10 nm bandwidth). The

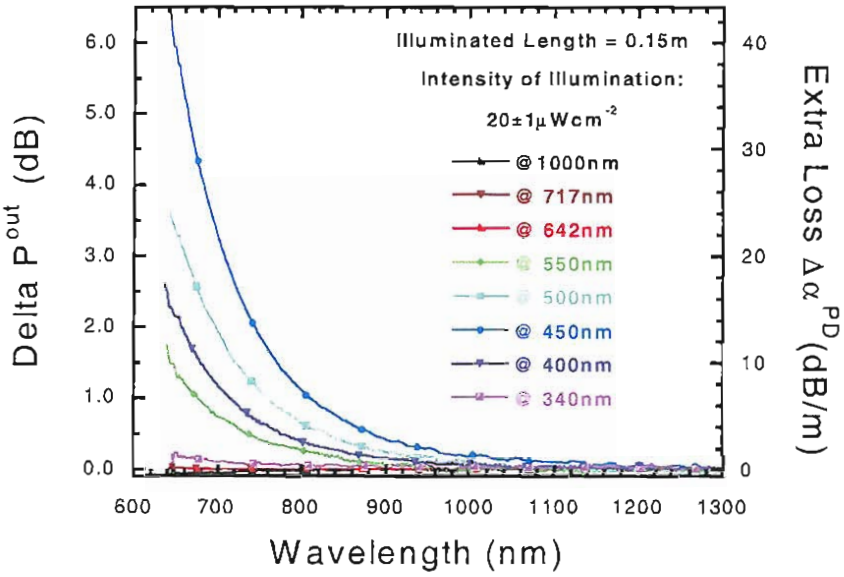

FIGURE 6.22: Increase of transmission loss due to PD, measured at different excitation wavelengths and constant intensity of SI.

white light source had a dual control of the intensity and the colour temperature, which allowed the variation of the power density within the sphere throughout the wavelength range from 1000 to 340 nm. The power density inside the sphere was measured by a silicon detector; repeated measurements revealed that the power density during the measurements was constant to within $\pm 5\%$.

The unclad (and uncoated) GLS/GLSO fibres were passed through the sphere via two diametrically opposed apertures; each of these ports was fitted with a 1 mm diameter iris, in order to prevent any stray light from entering the sphere. The transmission of the fibre was measured in the usual way, i.e. the output from another white light source, filtered of its shorter wavelength component by a LWP filter, was coupled into the fibre and the output collected via a silica multimode fibre and detected by an OSA (see figure 6.21). Although the amount of stray light was minimal (both the illumination and the 'probe' source were enclosed and the experiments were rigorously conducted in darkness), the sections of the fibre outside the sphere were fully enclosed, to ensure that any measured darkening was produced in the portion of fibre inside the sphere.

The first experiment studied the effect of side illumination (SI) at a constant intensity and different wavelengths, λ^{ext}. Measurements were performed using NBP filters at 1000, 719, 642, 550, 500, 450, 400 and 340 nm. The intensity of SI was fixed at 20 $\mu W cm^{-2}$, which was the maximum that the source could provide at all the wavelengths λ^{ext}. Sufficient exposure time was always allowed for the PD effect to reach saturation. We assumed that saturation of PD had occurred when the maximum change in the fibre transmission $\Delta\alpha_{PD}$ measured in 15 minutes was less than the resolution, 0.2 dB. A more detailed discussion of the characteristic times of PD will be presented in the next

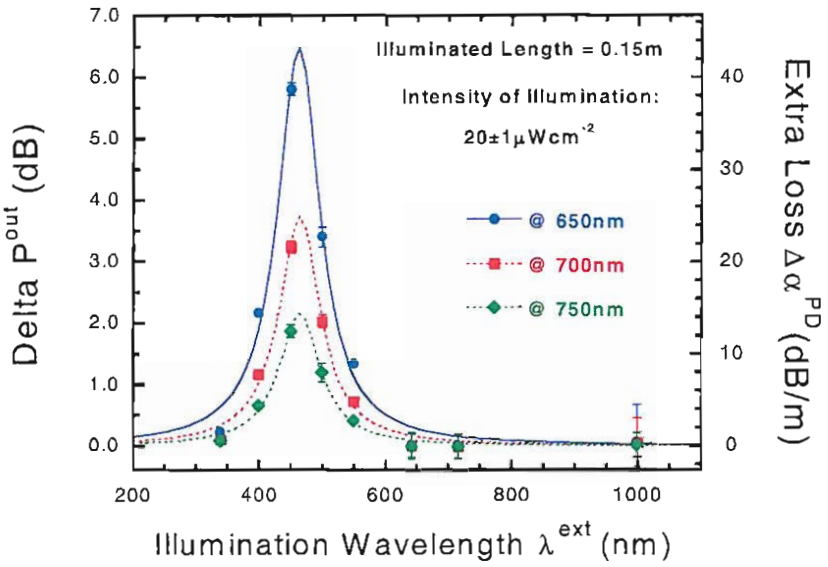

FIGURE 6.23: Extra loss $\Delta\alpha_{PD}$ at fixed wavelengths versus the excitation wavelength of SI, λ_{ext}, in GLS fibre LF294.

subsection.

The increase in the transmission loss, $\Delta\alpha_{PD}$, induced by SI at different wavelengths λ^{ext} in GLS fibre LF294, is shown in figure 6.22 (the colours of line plots are attributed accordingly to the wavelength λ^{ext} for better clarity). SI at longer wavelengths produced very little change in the fibre transmission. Measurements at 719 nm and 1 μm suggest the presence of a very weak photobleaching effect in GLS, i.e. a shift of the edge to shorter wavelengths inducing a loss decrease; however, the change was just comparable to the resolution of the measurement and no definitive proof of this effect could be obtained. In contrast, for wavelengths $\lambda^{ext} \leq 550\ nm$, the occurrence of PD was observed and a maximum $\Delta\alpha_{PD}$ was measured using the NBP filter at 450 nm. By 'sectioning' the curves for $\Delta\alpha_{PD}$ at fixed wavelengths (fig. 6.23), the dependence on the excitation wavelength λ^{ext} becomes clearer. Figure 6.23 provides further, convincing evidence that the measured increase in the fibre loss is associated with the absorption of bandgap light. The graph of $\Delta\alpha_{PD}$ versus λ^{ext} shows a broad maximum at $\lambda_0^{ext} \approx 460\ nm$ (with a FWHM of $\approx 80\ nm$). The same analysis was repeated for a GLSO fibre (LF367), and the results are shown in figure 6.24; the same peak structure is observed for GLSO (in this case it is $\lambda_0^{ext} \approx 430\ nm$ and FWHM $\approx 55\ nm$). It also appears that the increase $\Delta\alpha_{PD}$ is higher than in GLS; however it must be noted that the values of $\Delta\alpha_{PD}$ measured for the two fibres LF294 and LF367 cannot be directly compared because the fibres did not have the same diameter.

As was pointed out in subsection 6.7.1, PD in amorphous and glassy chalcogenides has been explained in terms of photostructural changes (10; 214). According to these models, bandgap absorption causes two types of configurational changes. In an initial step, the photoexcitation of an electron-hole pair causes a 'metal-chalcogen' bond to break, hence

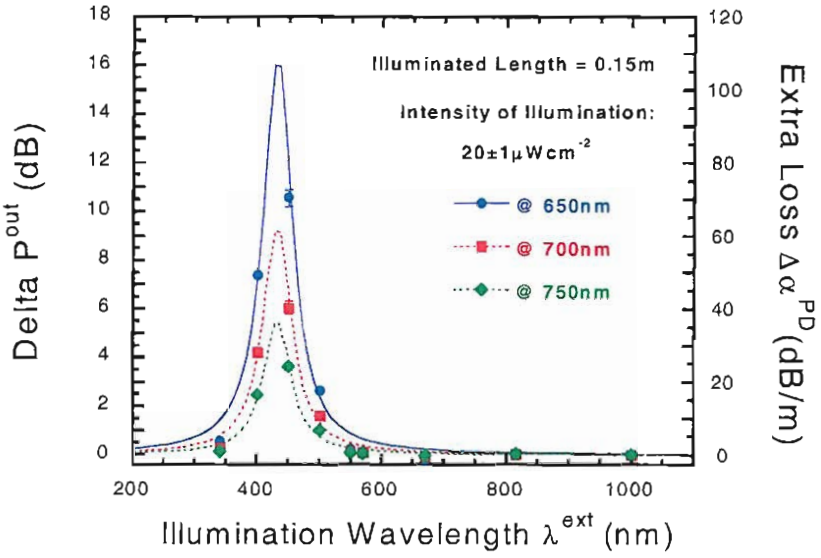

FIGURE 6.24: Extra loss $\Delta\alpha_{PD}$ at fixed wavelengths versus the excitation wavelength of SI, λ_{ext}, in GLSO fibre LF367.

a local rearrangement of bonds and coordinations, and forms a 'coordination defect pair', more properly defined as a 'self-trapped exciton' (STE) state. Such a coordination defect pair can either consist in an under-coordinated metal atom, or by a homopolar 'metal-metal' wrong bond (214); these coordination changes are believed to be responsible for the shift of the edge, hence the photodarkening. Subsequently, the coordination defect pair non-radiatively decays into a 'random pair', where the two original charged defects 'drift away' through bond-switching mechanisms and become widely separated. The random pair defects are metastable at room temperature and will slowly recombine. The configurational potential of these systems is schematised through a three-well structure (217), where the random pairs have an intermediate energy between the coordination pairs and the ground state, and photoexcitation by bandgap illumination results in a transfer of the system to the highest energy state, from which it then decays to the intermediate and back to the ground state, upon the removal of the illumination. The kinetics of these transitions is generally described as 'dispersive' because the promotion and decay rates are time-dependent (217). It must be remarked that these models have been formulated and investigated for 'simple' materials such as stoichometric As_2S_3, and it still remains to be verified whether they can be applied to a system with a far more complex microstructure as GLS.

The analysis of PD presented in this subsection, and the results shown in figures 6.23 and 6.24, could be used to investigate the mechanisms producing PD in GLS (and GLSO) glass. Although it is tempting to assume the validity of the above-mentioned model and to interpret the maxima, observed at wavelengths close to the bandgap energy, as peaks associated with a transition 'causing the PD' (i.e., the formation of the STE), a note of caution is necessary. Indeed, the increase in the fibre loss $\Delta\alpha_{PD}$, measured by the SI

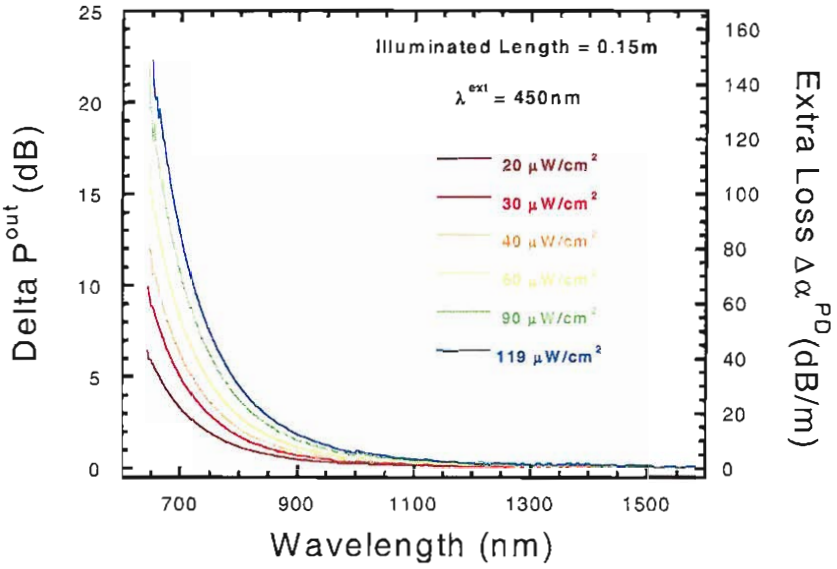

FIGURE 6.25: .

technique also depends on the optical penetration depth δ_{op} at the wavelength λ^{ext}; δ_{op} is unknown, as the absorption coefficient of GLS and GLSO in the 'high absorption region' (with reference to figure 6.1) has not been measured yet. Thus, the sharp decrease of $\Delta\alpha_{PD}$ for wavelengths $\lambda^{ext} < 450\ nm$ may not be an 'intrinsic' property of GLS glass, and could be caused by a δ_{op} decreasing with λ^{ext} instead. Summarising, several factors contribute to the dependence of the quantity $\Delta\alpha_{PD}$ on the excitation wavelength λ^{ext}: firstly, the penetration depth of the SI light depends on λ^{ext}; secondly, assuming the model of the configurational changes for the PD in GLS and GLSO, the probability of the excitation to the upper state (coordination defect pair - STE) is also expected to depend on λ^{ext}, and to have its maximum at wavelengths close to the optical bandgap; finally, it must also be noted that the photon flux at constant power density also increases linearly with λ^{ext}.

Consequently, direct information about the validity of the 'three-level' model of PD in GLS and GLSO cannot be extracted from the data shown in figures 6.23 and 6.24 and the nature of the 'peaks' is still undetermined. However, a more detailed investigation, including analysis at different power densities and, especially, a precise measurement of the absorption coefficient of GLS and GLSO in the range of the optical bandgap, would allow the interpretation of the dependence of $\Delta\alpha_{PD}$ on λ^{ext} and the separation of the 'extrinsic' effect due to the optical penetration depth, from the intrinsic contribution genuinely due to PD of the glass. This will provide the basis for possible 'further work'.

In addition to the dependence on λ^{ext} (at a fixed I), we also investigated the dependence on the power density I at fixed λ^{ext} (450 nm). The power density I was varied from 20 to 118 $\mu W cm^{-2}$. Figure 6.25 shows that $\Delta\alpha_{PD}$ increases with increasing I; from a log plot (fig. 6.26), it appears that the shift of the edge is also accompanied by a small decrease in its slope. The value of $\Delta\alpha_{PD}$ at a fixed wavelength (800 nm), versus the

power density of the SI at $\lambda^{ext} = 450\ nm$ is shown in figure 6.27, which proves that even low levels of bandgap light can induce measurable PD.

6.7.4 Formation and decay times of PD

A slightly modified version of the setup described in the previous subsection was employed to perform time-resolved measurements of the formation and decay of PD. The new setup is illustrated in figure 6.28. In this instance, the unclad fibre was probed with monochromatic light at 810 and 719 nm, which was obtained by filtering the probe light source by means of NBP filters. The output from the unclad GLS/GLSO fibre was measured by a silicon detector, while a second silicon detector measured the power density at λ^{ext} within the sphere. Data were collected by a computer-interfaced optical power meter (Newport mod. 2832C, dual channel). Measurements were carried out with SI at fixed wavelength ($\lambda^{ext} = 450\ nm$).

The time dependence of PD can be studied by measuring the normalised transmission at $\overline{\lambda}$ ($\overline{\lambda} = 810\ nm$ for GLS and $\overline{\lambda} = 719\ nm$ for GLSO):

$$\Theta^{\overline{\lambda}}_{PD}(t) = \frac{P^{out}(I, \lambda^{ext}; \overline{\lambda})}{P^{out}_0(\overline{\lambda})} \tag{6.18}$$

where $P^{out}_0(\overline{\lambda})$ is the output power at $\overline{\lambda}$ under no SI, and $P^{out}(I, \lambda^{ext}; \overline{\lambda})$ is the output power (at $\overline{\lambda}$), measured under SI with power density I at $\lambda^{ext} = 450\ nm$.

The normalised transmission of GLS fibre LF294 is shown in figure 6.29, while that of GLSO fibre LF367 is shown in figure 6.30. The formation time of PD (upper graph) is in the range of tens of seconds, while the decay time (lower graph) is in the range of

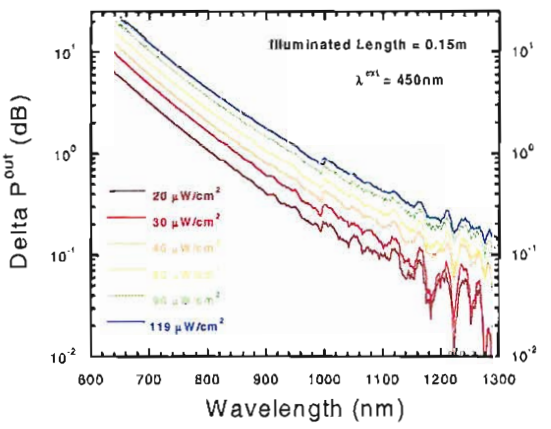

FIGURE 6.26: Log plot of $\Delta\alpha_{PD}$ in GLS fibre LF294, for different power densities of the SI at $\lambda^{ext} = 450\ nm$

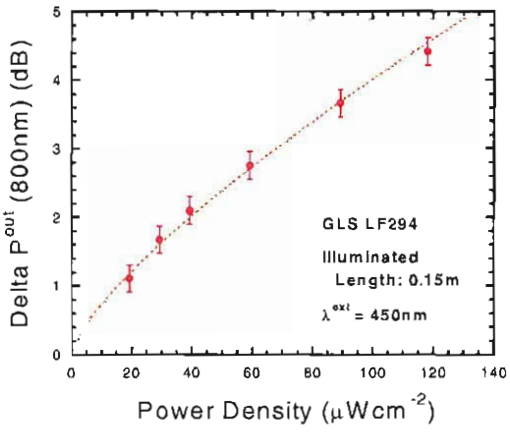

FIGURE 6.27: Plot of $\Delta\alpha_{PD}$ at 800 nm versus the power density of the SI at $\lambda^{ext} = 450\ nm$

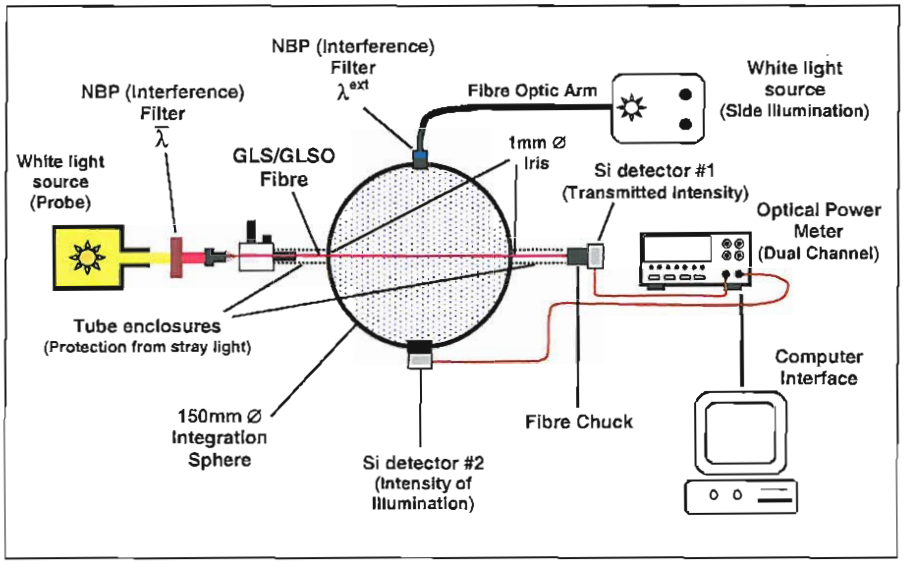

FIGURE 6.28: Setup used for measuring the characteristic formation and decay times of PD in GLS and GLSO.

tens of minutes. The time-dependent normalised transmission during the formation of the PD can be fitted with a stretched exponential function (218):

$$\Theta^{\overline{\lambda}}_{PD,\ rise}(t) = (1 - B_\infty) \exp\left[-\left(\frac{t}{\tau_r}\right)^{\gamma_r}\right] + B_\infty \tag{6.19}$$

where the parameter B_∞ specifies the maximum amplitude of PD (i.e., the minimum transmission), τ_r is the characteristic rise time, and γ_r is a dispersion parameter ($0 < \gamma_r < 1$). The stretched exponential law is generally used to describe time-dispersive transitions (where the transition rate is time-dependent) (217), and it has been used to describe the time evolution of PD in other chalcogenides (219), (220). A similar law can be used to fit the curves for the spontaneous decay of PD (lower graph in figure 6.29):

$$\Theta^{\overline{\lambda}}_{PD,\ decay}(t) = 1 - (1 - B_0) \exp\left[-\left(\frac{t}{\tau_d}\right)^{\gamma_d}\right] \tag{6.20}$$

Intensity, I	**GLS**, $\overline{\lambda} = 810\ nm$					**GLSO**, $\overline{\lambda} = 719\ nm$				
@ 450 nm	B_∞	τ_r [s]	γ_r	τ_d [s]	γ_d	B_∞	τ_r [s]	γ_r	τ_d [s]	γ_d
20	0.43	96	0.76	528	0.56	0.35	682	0.80	3052	0.68
40	0.30	51	0.73	436	0.54	–	–	–	–	–
60	0.23	34	0.71	380	0.55	0.16	259	0.72	3341	0.64
80	0.19	22	0.73	300	0.55	–	–	–	–	–
118	0.16	17	0.73	267	0.53	–	–	–	–	–

TABLE 6.6: 'Stretched exponential' fit parameters for the rise and decay curves of PD 6.29 and 6.30.

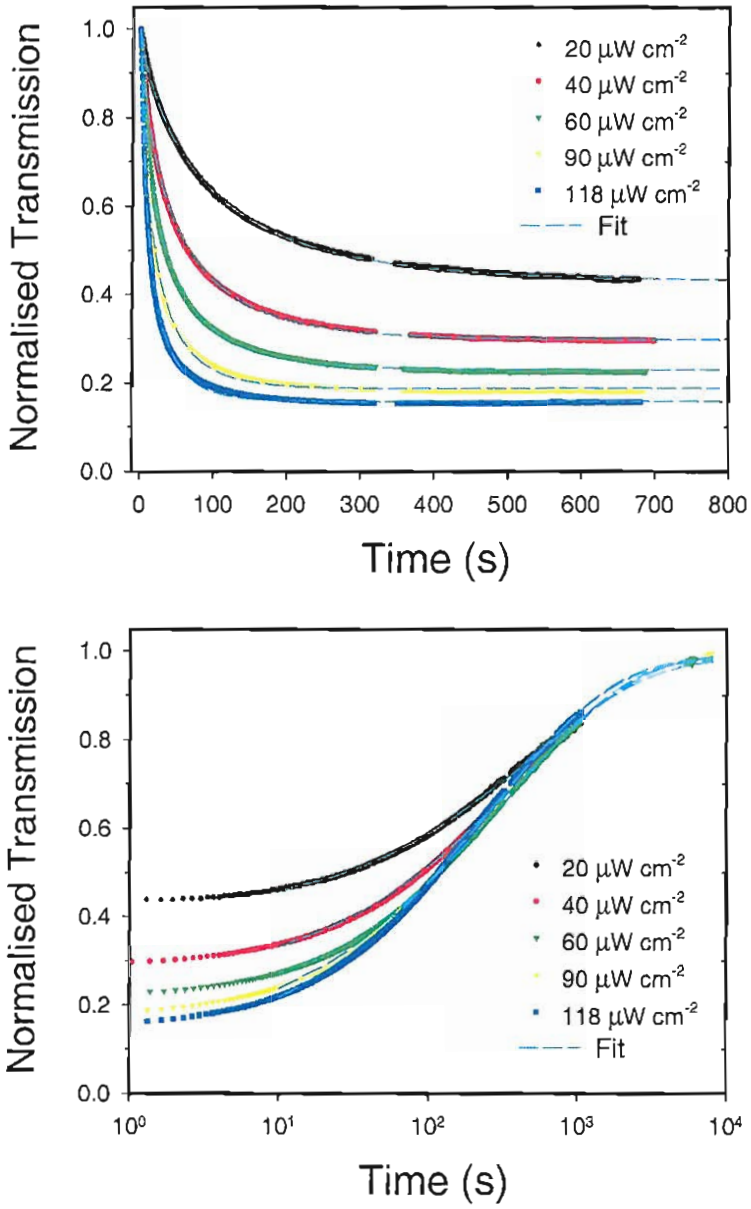

FIGURE 6.29: Formation (upper graph) and decay (lower graph) of PD at 810 nm in GLS LF294 for different power densities of SI at $\lambda^{ext} = 450nm$.

where B_0 is the normalised transmission of the (darkened) fibre at $t = 0$, τ_d and γ_d are the characteristic time and the dispersion parameter relative to the decay. In our analysis we assumed $\gamma_r \neq \gamma_d$, since the detailed mechanism of PD of GLS and GLSO glass is unknown. The results of the fits of the rise and decay curves of $\Theta^{\overline{\lambda}}_{PD}(t)$ are shown in table 6.6. All the curves of each material can be fitted with approximately the same dispersion parameters γ_r and γ_d (for the rise and decay respectively). An interesting point about the decay curves is that, for long times, they all seem to converge to the same curve irrespective of the initial intensity (fig. 6.30). This might correspond to the decay of coordination pairs into random pairs and hence to the 'ground state' in the configurational model proposed above.

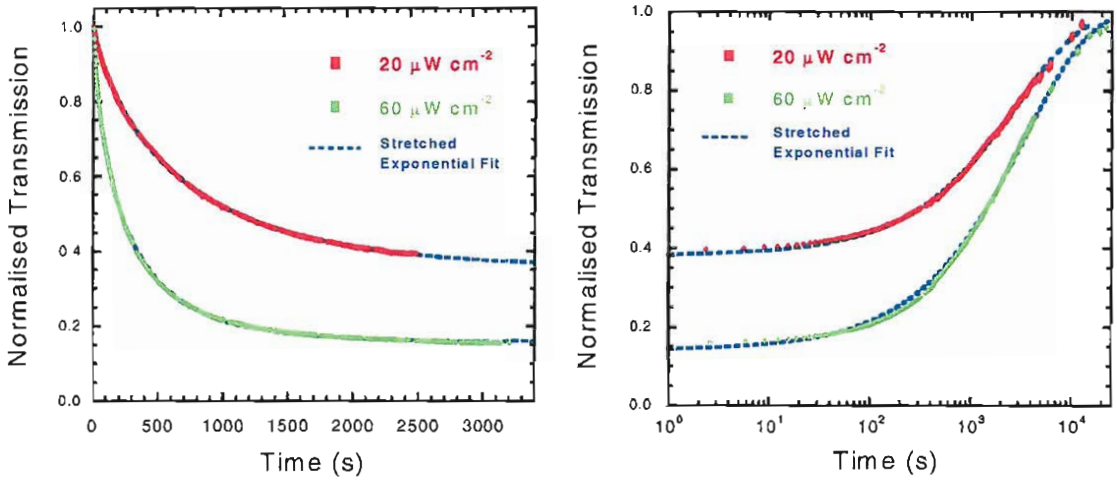

FIGURE 6.30: Formation (left column) and decay (right column) of PD at 810 *nm* in GLS LF367 at different power densities of SI.

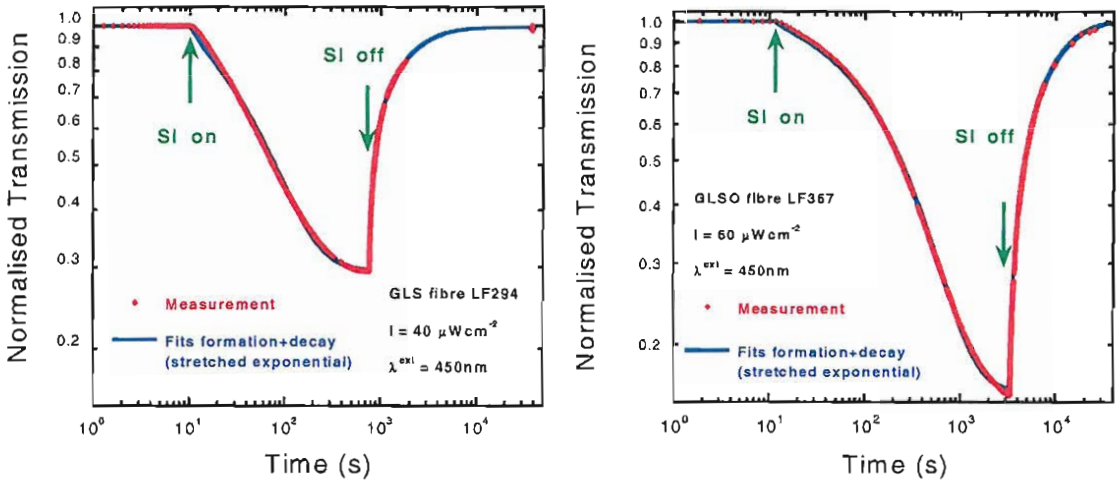

FIGURE 6.31: Reversibility of PD in GLS LF294 (810 nm) and GLS LF367 (719 *nm*).

Figure 6.31 provides an unequivocal proof of the metastable nature of the PD in GLS and GLSO; upon removal of the side illumination, the fibres revert, spontaneously and fully, to their background transmission. By comparing the two graphs, the marked difference in the time scales of the PD in GLS and GLSO is also evident, as can be also seen from the values of the time constants in table 6.30.

6.7.5 Temperature dependence of PD

All the measurements described in the previous sections 6.7.2-6.7.4 were conducted at room temperature (RT). However, it is known from previous studies that temperature is an important factor affecting the PD of chalcogenide materials (214), as larger shifts are generally observed in amorphous films at low temperature. The effect of the temperature is also very relevant to any practical application of PD which exploits the photorefractive effects associated with PD.

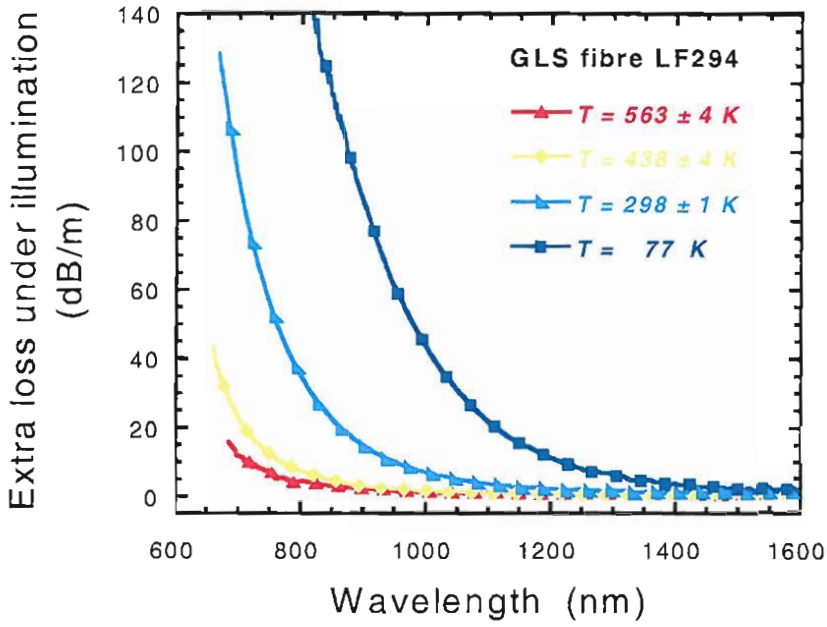

FIGURE 6.32: Photodarkening of a GLS unclad fibre under transverse illumination.

Here we report the measurement of the temperature dependence of PD in GLS fibre LF 294. The extra loss under side illumination (SI), $\Delta\alpha_{PD}$, was first measured at RT, and at temperatures above RT; the setup used for these measurements was similar to that described in section 6.6. In addition, $\Delta\alpha_{PD}$ was measured at 77 K, by dipping the fibre in a liquid nitrogen bath. In both cases, the SI was provided by an unfiltered halogen lamp fitted with a reflector, i.e. the configuration used for the illumination was that shown in figure 6.18; the integral power density on the fibre (measured by means of a silicon detector) was about $2 \cdot 10^3\ Wm^{-2}$. The results are shown in figure 6.32. The magnitude of the PD shift above RT decreases with increasing temperature, and a very large shift is found at low temperature, as compared to that normally observed at room temperature. Summarising, the magnitude of the PD induced in GLS glass by bandgap illumination is strongly dependent on the temperature. A similar behaviour was observed in GLSO fibres.

While both temperature increase 6.6 and bandgap illumination produce a similar shift of the electronic edge and an increase in the transmission loss in GLS and GLSO glass, the simple experiment presented in this subsection provides clear evidence that the two phenomena are substantially different. Further confirmation was obtained by observing that PD and temperature-induced darkening have very different characteristic times. Temperature darkening appears to be limited by heat diffusion, having equal formation and decay times (about 1-2 s in GLS/GLSO fibres). In contrast, PD has a much slower kinetics and, as seen in the previous subsection 6.7.5, widely different formation and decay times.

The setup used in this experiment was very basic (similar to fig. 6.18) and only allowed

a qualitative analyis of the temperature dependence of PD. However, the setup could be improved without difficulty to allow for wavelength-resolved measurements to be carried out at different temperatures. The temperature dependence of the PD magnitude, formation and decay rates might then provide important information on the mechanisms causing the PD.

6.8 Conclusions

The aim for this chapter was to investigate the optical loss of GLS and GLSO glasses in the near-IR region. The background loss of these glasses is determined by several of factors, both intrinsic and fabrication-related, which makes it difficult to quantify them separately and to estimate the transparency limit. Before this work, it was not clear whether the optical loss in the near-IR was due to scattering or absorption. By performing laser absorption calorimetry measurements and accurate transmission measurements, we obtained convincing evidence that the near-IR loss in GLS and GLSO is almost entirely due to absorption. Two mechanisms are known to cause optical absorption in chalcogenide glasses over this range: impurity absorption from transition metal ions and the weak absorption tail, caused by optically active bandgap states. The latter has been observed in several other sulphide and chalcogenide glasses, but its occurrence in GLS and GLSO had never been investigated in detail. In order to separate the contribution of transition metal absorption and the contribution of a possible weak tail, we measured the excess absorption of GLS and GLSO samples doped with known amounts of transition metal ions. The results of this investigation showed that the absorption due to metal impurities only cannot account for the total absorption measured by laser calorimetry. More measurements are needed to obtain definitive evidence for a weak tail, especially calorimetric measurements in the 2-2.5 and 3.5-4 μm range, which will provide the basis for further work. Summarising, based on the results presented in this chapter, it is only possible to state that the data are not incompatible with the presence of a weak absorption tail in GLS and GLSO.

In addition to the mechanisms affecting the background loss, we demonstrated that other parameters can affect the transmission loss of GLS and GLSO, namely temperature and bandgap illumination. Both temperature and bandgap illumination cause a shift of the fundamental electronic edge to longer wavelengths and, consequently, decrease the material's transparency in the near-IR, especially in the short wavelength range below 1 μm. Temperature-induced darkening does not impose practical limitations on the applications of GLS and GLSO, as the effect at 'important' device wavelengths is negligible for temperatures below 100 $^{\circ}C$. In contrast, photodarkening might impose more serious limitations. Bandgap absorption produces a large increase in the transmission loss of GLS glass in the crucial region 0.8-1 μm, where most of the pump wavelengths for rare earth-doped devices lie, and the increase is still measurable at signal wavelengths,

especially at 1.3 μm. Since several linear and nonlinear effects in chalcogenide glasses are known to produce bandgap absorption, it is very important to fully investigate photodarkening in GLS and GLSO. Here we presented, for the first time, a detailed study of the dependence of the PD on the excitation wavelength in unclad GLS and GLSO fibres and a study of the kinetics of its formation, decay and reversibility. Still very little is known about the mechanism producing the PD in GLS and GLSO, but useful information was obtained by the 'side illumination technique'. This work has clearly shown the fundamental and practical relevance of photodarkening in GLS and GLSO and has also identified new directions of investigation.

Chapter 7

Transmission of GLS and GLSO Fibres under High-pump Powers

7.1 Introduction

In section 6.7 of the previous chapter, the photodarkening due to low-intensity illumination in the visible was analysed. It was found that absorption at wavelengths close to the optical bandgap induces an increase of the optical loss of GLS and GLSO glasses at important pump and signal wavelengths in the near-IR. In this chapter we intend to study the effect of intense IR laser irradiation on the transmission loss of these materials.

Photorefractive effects at wavelengths longer than the optical bandgap have been observed in other sulphide glasses; for instance, fibre gratings were written in As-S fibres by exposure to the 0.63 μm light from a He-Ne laser (221), and optical waveguides were produced in bulk As_2S_3 glass at 0.8 μm using the self-writing technique (222). It was found (143) that the photosensitivity of As_2S_3 to sub-bandgap photons is a consequence of the high third-order nonlinearity of this material, i.e. it is caused by two-photon absorption (TPA). Furthermore, high intensity irradiation at 1.064 μm was observed to increase the optical loss of As_2S_3 (143). In GLS glass, photorefractive effects similar to As_2S_3 have been recently reported, and optical waveguides were successfully produced by the self-writing technique at 1.064 μm (223); also in this case, the photosensitivity was attributed to a nonlinear two-photon process.

Photoinduced effects have also been reported in rare earth-doped glasses under intense irradiation with IR wavelengths. For instance, photo-degradation was observed in thulium-doped fluorozirconate (218) and aluminosilicate fibres (224) pumped at 1.064 μm. Such degradation was evident through a permanent increase of the fibre attenuation and was explained as a consequence of visible and UV upconversion fluorescence of rare-earth ions producing defects in the glass. Visible upconversion is also well-known to occur in

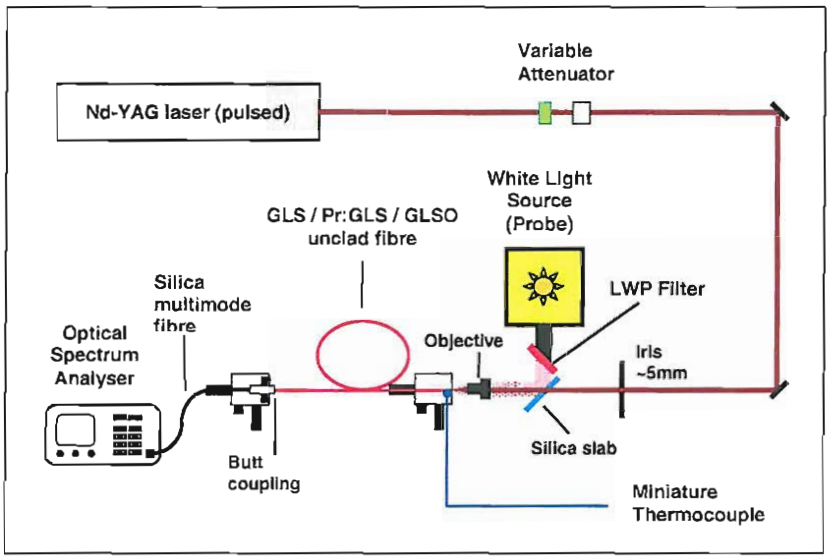

FIGURE 7.1: Setup used for high intensity measurements of Photodarkening

rare-earth doped GLS glass (225), but the occurrence of photoinduced effects associated with it were never investigated in detail.

We analysed the stability of Pr^{3+}-doped GLS, and of undoped GLS and GLSO fibres under intense irradiation at 1.064 μm from a Nd:YAG laser. The Pr^{3+} ion has an upconversion transition in the blue-green ($^3P_0 \rightarrow 3H_4$ at 508 nm (225)), which is almost resonant with the optical bandgap of GLS and also with the 'peak' of photodarkening in figure 6.23. Consequently, the excitation energy of Pr^{3+} ions could be transferred to the host either directly (electronic transfer) or through the emission and re-absorption of a photon; hence, photorefractive changes might occur, in Pr:GLS, both due to an intrinsic factor (i.e. material-related) and due to the dopant. In undoped GLS and GLSO photorefractive changes can obviously only be material-related. The aim for the present analysis is to assess the occurrence of such photo-induced changes, to establish their nature (i.e. whether they are metastable or permanent) and measure their impact on the material transparency.

7.2 Analysis of transmission of GLS/GLSO fibres in the high-peak power regime

7.2.1 Measurement technique

The setup used is illustrated in figure 7.1. The 1.064 μm source was a mode-locked, Q-switched Nd:YAG laser with $\approx$ 1 W maximum average power and $\approx$ 300 ps pulse width; the pulse structure of the laser beam is shown in figure 7.2. In addition to the very high peak intensity (up to 178 kW), this source also enables access to the $^3H_4 \rightarrow {}^1G_4$

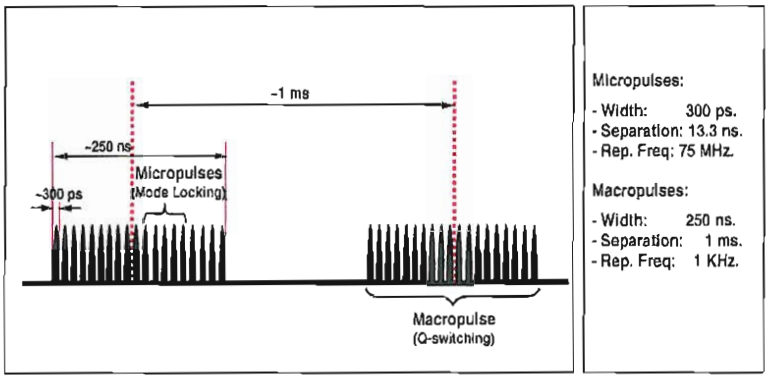

FIGURE 7.2: Peak pulse structure and characteristics of the pulsed Nd:YAG laser

pump transition (1.02 μm) for studying upconversion effects. The beam was passed through a variable attenuator and then focussed into the fibre; the coupled-in power was determined by measuring the transmitted power and correcting for the background loss of the fibre. Since low-loss core/clad GLS and GLSO fibres were not available, we employed unclad, uncoated fibres. The fibres used were LF292 (Pr^{3+}:GLS), LF294 (undoped GLS) and LF367 (GLSO). The loss of the three fibres at the pump wavelength was respectively 5 dBm^{-1} (LF292), 8 dBm^{-1} (LF294) and 9 dBm^{-1} (LF367); the other characteristics of the fibres can be found in table A.1 in Appendix A. Since the fibres were cleaved by hand, the end-faces were inspected using an optical microscope to ensure good quality, before coupling the laser light.

The transmission of the fibres was probed using a broadband source. This was a tungsten halogen lamp, filtered by a suitable LWP filter to eliminate the visible component. The output of the fibre was collected via a multimode silica fibre and detected by an optical spectrum analyser (fig. 7.1). Since the transmission of the unclad fibres could have easily been affected by photodarkening due to side illumination, the white light source was fully enclosed and the measurements were rigorously carried out in dark conditions. In addition, fibres were kept in complete darkness for 15 $hrs+$ prior to the experiments; this ensured the full decay of any previously induced PD of the fibres. Since it was shown in the previous chapter (section 6.6) that temperature darkening can be induced by heating up the fibre to above $\approx 50\ ^{\circ}C$, the temperature of the fibre near the input end was monitored during the measurements. As a preliminary test, samples of the three fibres were analysed for end-face damage (226) and thermal effects using a CW Nd:YAG laser; the power coupled into the fibres was $\approx 85\ mW$. As no change was observed in the transmission of the probe light, we concluded that temperature darkening was not affecting the measurements, and no damage was occurring at the fibre ends. The 1.3 μm fluorescence of Pr^{3+} was observed in fibre LF292, which indicated that the pump light was exciting the $^1G_4$ level of Pr^{3+}.

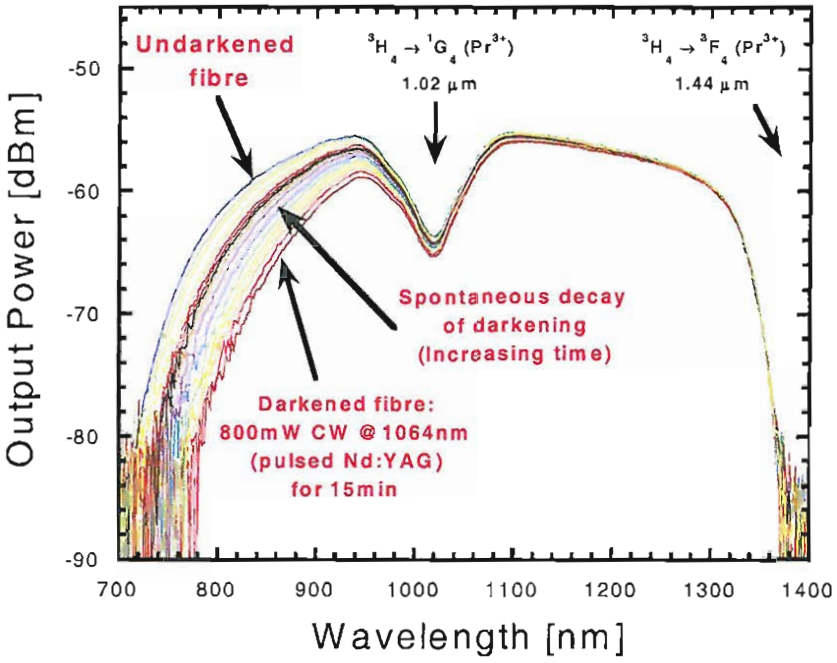

FIGURE 7.3: High-power photoinduced darkening of fibre LF292 (Pr^{3+}:GLS)

7.2.2 Analysis of a Pr^{3+}:GLS fibre

When the pulsed Nd:YAG laser light was coupled into the fibre, it was very obvious that photorefractive effects were occurring in the fibre (see figure 7.3). A shift in the position of the absorption edge, with an increase of the transmission loss, was observed; this shift was very similar to the photodarkening induced by side illumination with bandgap light. In fact, this high-intensity photoinduced darkening (HI-PD) was also observed to be metastable at room temperature, i.e. the fibre reverted back to its background transmission loss upon the removal of the pump. The decay time of HI-PD was in the range of $\approx$ tens of minutes, and the formation time was in the range of $\approx$ minutes, which also correlates well with what was previously observed for the PD.

The magnitude and characteristic time of HI-PD were determined by measuring the photoinduced increase of the transmission loss of the fibre. Firstly, the white-light (WL) transmission of the unexposed fibre was recorded in the range 0.7-1.4 μm; the pump was then coupled into the fibre and 15 minutes were allowed for the darkening to saturate; subsequently, the pump was turned off and the spectral transmission of the darkened fibre was recorded by the optical spectrum analyser. This procedure could be adopted due to the slow decay of HI-PD and ensured that the measurement was not affected by the unabsorbed pump or by the 1.3 μm fluorescence. The extra attenuation due to HI-PD was then calculated as:

$$\Delta\alpha_{HI-PD}(\lambda, I_{pump})[dBm^{-1}] = \frac{10}{L} \cdot \log\left[\frac{P(\lambda, I_{pump})}{P_0(\lambda)}\right] \tag{7.1}$$

where L is the fibre length, $P(\lambda, I_{pump})$ is the WL intensity transmitted by the darkened fibre and $P_0(\lambda)$ is the transmitted intensity of the fibre before exposure to the pump. The spontaneous decay of $\Delta\alpha_{HI-PD}$ was observed by collecting WL transmission spectra for increasing times after the pump was removed; since the decay of the of HI-PD was much slower than the acquisition time for a single scan ($\approx 30\ s$), this analysis provided reliable information on the characteristic decay time.

Figure 7.4 shows the spectral dependence of $\Delta\alpha_{HI-PD}$ for increasing times, measured at an average power of 280 mW. The higher curve was collected soon after removing the pump from the fibre, hence it is the saturated value for this pump intensity. The wavelength dependence of $\Delta\alpha_{HI-PD}$ is virtually identical to the $\Delta\alpha_{PD}$ measured in the previous chapter by side illumination. The log plot on the right-hand side of figure 7.4 clearly shows that the photoinduced loss is due to a shift of the electronic edge. The loss increase decayed spontaneously to zero, which proved that the effect was metastable at room temperature.

Figure 7.5 shows $\Delta\alpha_{HI-PD}$ at 0.8 μm and at the important wavelength of 1.02 μm as a function of time. The decay curve can be fitted by a stretched-exponential function, as previously done for the PD decay. However, as also shown in figure 7.5, decay time of HI-PD is even longer ($\approx 1400\ s$) than the one measured for the PD.

The magnitude of the photoinduced loss versus the pump intensity is shown in figure 7.6. The pump power was varied from 0.35 to 280 mW and in all the cases the photoinduced change was metastable and no permanent damage of the fibre was observed. The maximum temperature increase at the input end of the fibre was less than 3 K, which confirmed that $\Delta\alpha_{HI-PD}$ was in fact due to photorefractive effects and not to the temperature darkening. Plotting $\Delta\alpha_{HI-PD}$ at fixed wavelengths versus the pump power (figure 7.7) shows clearly that the amplitude of the photorefractive change is proportional to the pump power.

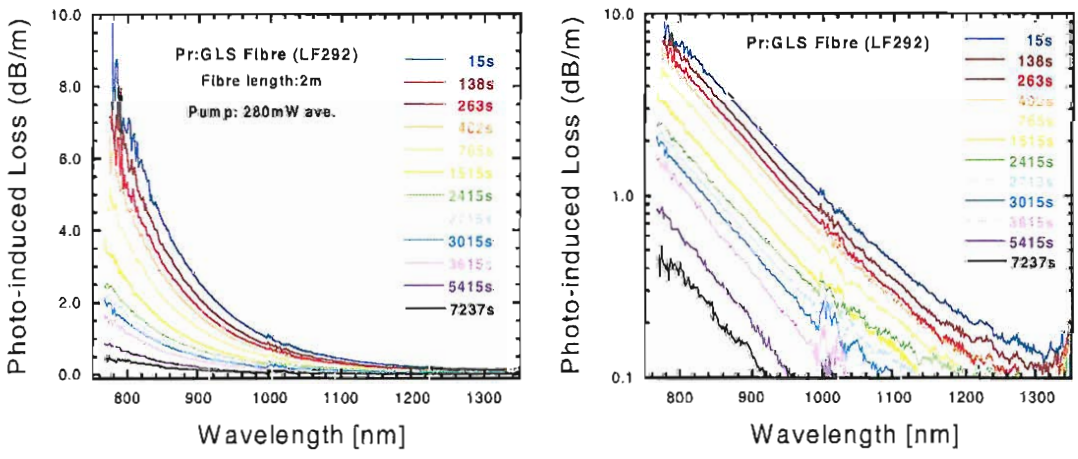

FIGURE 7.4: Photoinduced increase of transmission loss in Pr^{3+}:GLS fibre LF292 and its spontaneous decay (average pump power: 280 mW @1.064 μm)

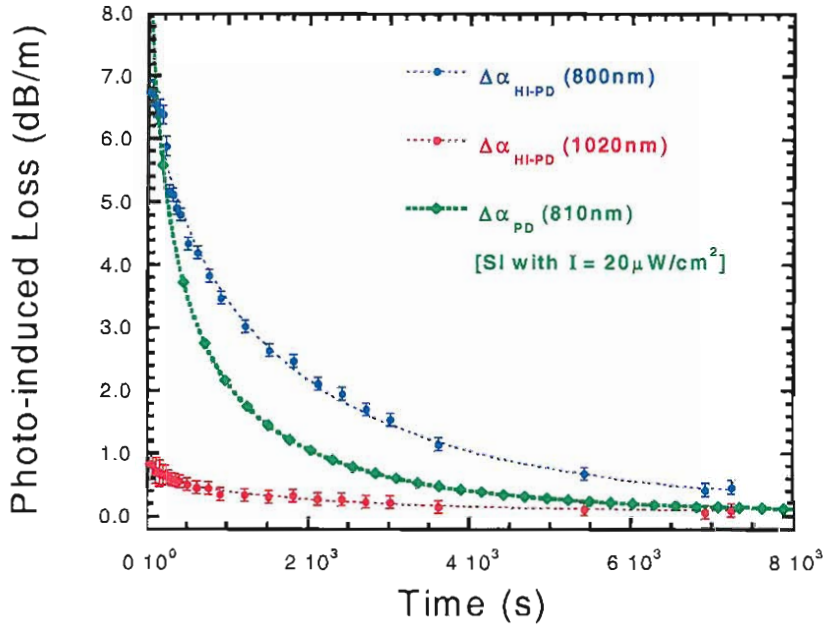

FIGURE 7.5: Analysis of the decay of HI-PD of fibre LF292 at 0.8 and 1.02 μm and comparison with the decay of PD due to bandgap absorption

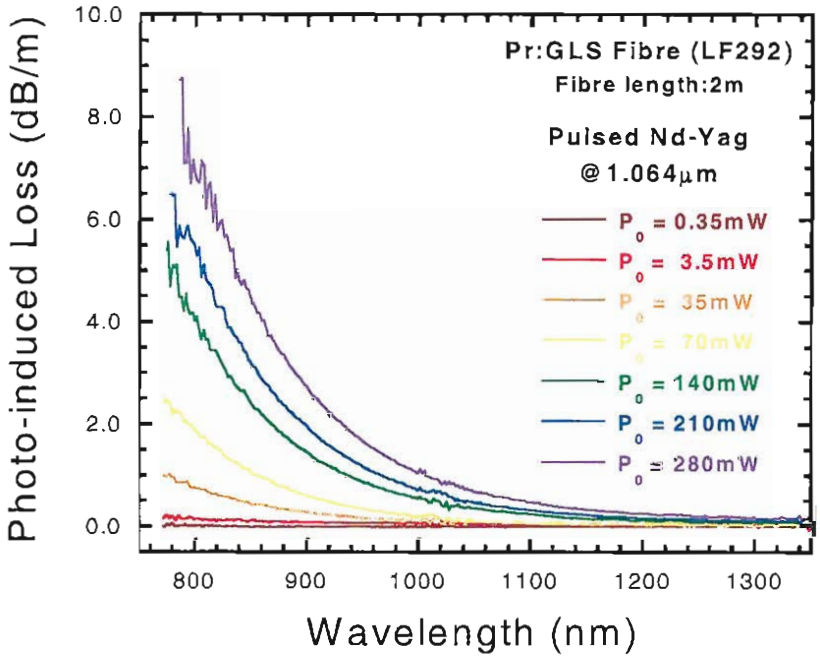

FIGURE 7.6: Photoinduced loss due to HI-PD in Pr^{3+}:GLS (LF292) for different pump powers

7.2.3 Analysis of an undoped GLS and GLSO fibres

In order to better understand the origin of the photoinduced changes measured in the Pr^{3+}:GLS, the same experiment was repeated using an undoped GLS fibre (LF294). Photorefractive effects were observed also in the undoped fibre. Figure 7.8 shows the

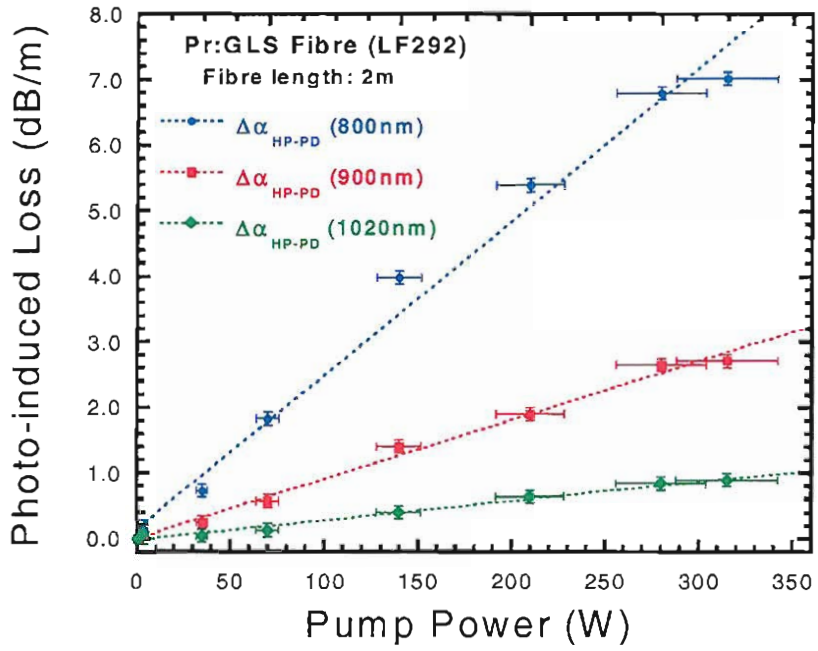

FIGURE 7.7: Photoinduced loss due to HI-PD at fixed wavelengths versus the (average) launched pump power.

photoinduced attenuation $\Delta\alpha_{HI-PD}$ for different pump powers at 1.064 μm. A quick comparison with figure 7.6 reveals that the order of magnitude of the effect in the doped and undoped fibre is comparable. Figure 7.9 shows the loss increase $\Delta\alpha_{HI-PD}$ at 800 nm in the Pr^{3+}-doped and undoped GLS fibres; the $\Delta\alpha_{HI-PD}$ in the undoped fibre is approximately 25% smaller, and it appears to have a threshold at pump power of about 70 mW; the origin of this threshold is not clear.

Samples of GLSO fibre (LF367) were also analysed in the same range of pump powers and no photoinduced effects could be observed.

7.3 High-intensity photodarkening: thresholds and possible practical implications

The results given in the previous section provide convincing evidence that photorefractive effects occur when GLS glass is exposed to a high-intensity pump source at 1.064 μm, as previously reported in ref. (223). In this work we established that such photorefractive changes also induce an increase of the transmission loss of GLS. The effect is qualitatively very similar to the PD induced by low-intensity bandgap absorption described in section 6.7.

The photoinduced attenuation is higher in the Pr^{3+}-doped fibre than in the undoped fibre 7.9; the difference is more obvious at lower pump intensities, as the effect appear

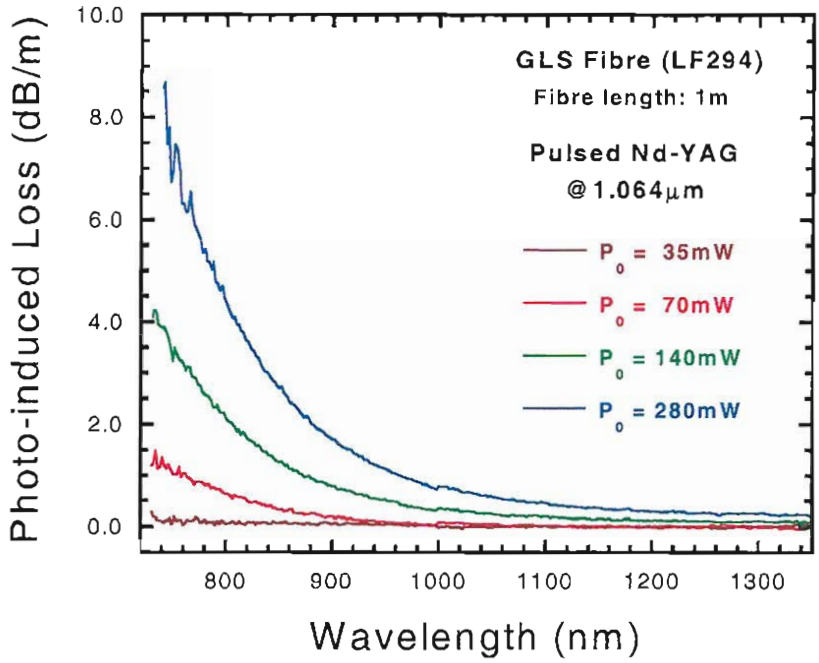

FIGURE 7.8: Photoinduced loss due to HP-PD in a GLS fibre (LF294, undoped) for different values pump power.

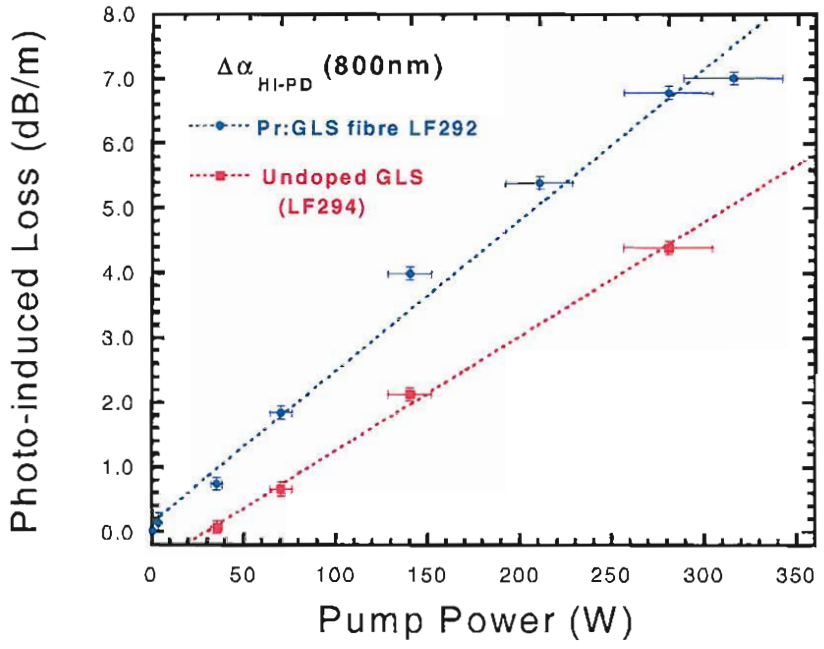

FIGURE 7.9: Comparison of the photoinduced loss at 800 *nm* in Pr^{3+}-doped (LF292) and undoped (LF294) GLS fibres

to have different thresholds for the two fibres. These differences might partly be due to a differences in the preparation of the glass and in the drawing conditions for the two fibres. Consequently, it is difficult to draw a definitive conclusion whether the presence dopant enhances the effect; while the occurrence of high-intensity darkening at this wavelength is certainly intrinsic of GLS, from our measurements a contribution due to

the Pr^{3+} ion cannot be completely ruled out.

The analysis of the dependence of $\Delta\alpha_{HI-PD}$ on the peak intensity of the pump provided an unexpected result. In general, it can be assumed that the magnitude of the photorefractive change is proportional to the absorbed pump intensity, hence the following relationship:

$$\Delta\alpha \propto (I_{pump})^n \tag{7.2}$$

where n is the 'order' of the absorption process, i.e. $n = 2$ for TPA, $n = 1$ for linear absorption and $n > 2$ for higher order processes. Our results show unequivocally that the dependence is linear, hence the true two-photon absorption is to be ruled out as the cause of the high-intensity darkening. This result contradicts what was previously assumed for GLS.

Since one-photon absorption at $\approx 1\ \mu m$ can only be caused by gap state absorption, our results provide a proof of the presence of such states in GLS. What is the nature of these states still remains to be determined, but it is possible that a correlation exists between our findings and the midgap luminescence peak previously observed in GLS by Lima, et al. (227). As to what is causing the photodarkening, Tanaka remarks that carriers excited to gap states could be thermally excited to extended states (228), or also two-step sequential absorption of photons might occur (229; 230). Energy transfer between rare earth ions and gap states is also known to occur in chalcogenide glasses (231; 232), which might provide an explanation for the differences observed in the undoped and Pr^{3+}-doped fibre. The results presented here should be complemented by more measurements at different wavelengths, and this will also provide an explanation for the different behaviour observed in GLSO.

The information on the stability and damage thresholds of GLS and GLSO at 1.064 μm is summarised in table 7.1 Permanent damage was never observed, which provides a lower limit for the damage threshold (LIDT); the corresponding average and peak power densities are given in the first two columns of the table. It is worth noting that the values provided here are over an order of magnitude larger than those measured in section 4.8.1 on bulk samples by a FEL with $\approx ps$ pulses (also shown in the table for comparison), hence they provide a more realistic estimate of the damage threshold in GLS and GLSO. The thresholds for metastable damage (darkening) are given in the third column; these thresholds are correctly defined in terms of peak power density, given the nonlinear nature of the photorefractive effect observed in GLS.

The occurrence of a photoinduced increase of the fibre loss is very important for device applications of GLS. As seen in Chapter 2, devices such as the 1.3 μm PDFA require small core diameters and high pump and signal intensities. Here it was found that high pump intensities around 1 μm can introduce an extra term of attenuation, proportional to the

Glass & sample	Threshold for permanent damage		Threshold for metastable damage	λ	pulse width
	Ave. Intensity	Peak Intensity	Peak Intensity	$[\mu m]$	$[ps]$
Pr^{3+}:GLS fibre LF292	$> 2.4\ kWcm^{-2}$	$> 0.4\ GWcm^{-2}$	$0.5\ MWcm^{-2}$	1.064	≈ 300
GLS fibre LF294	$> 2.1\ kWcm^{-2}$	$> 0.4\ GWcm^{-2}$	$33\ MWcm^{-2}$	1.064	≈ 300
GLSO fibre LF367	$> 2.1\ kWcm^{-2}$	$> 0.4\ GWcm^{-2}$	$> 0.4\ GWcm^{-2}$	1.064	≈ 300
GLS bulk LD1087	$> 0.2\ kWcm^{-2}$	$> 5\ MWcm^{-2}$	$> 5\ MWcm^{-2}$	1.55	≈ 1

TABLE 7.1: Damage thresholds for metastable damage and lower limits for permanent damage of GLS and GLSO.

pump intensity. This term would reduce the transmission of the signal and especially of the pump light, and negatively affect the efficiency of the amplifier. A similar effect was very recently reported in another sulphide glass by Kobelke and co-workers (233). These authors fabricated low loss Pr^{3+}:*As-Ga-S* single mode fibres, and evaluated the amplification performance at 1.3 μm. They found that the efficiency was strongly limited by intensive material degradation induced by the pump at 1.02 μm. The degradation was observed to be metastable and was attributed to photoinduced effects similar to the PD due to bandgap illumination. A decrease of the fibre transmission at both pump and signal wavelengths was already evident with just a few mW pump power. Modeling the effects of the photoinduced loss, they concluded that the maximum attainable gain was limited to $\approx 5dB$, as compared to an expected gain of over 30 dB (see chapter 2).

Further study is necessary to establish the practical implications of high-intensity photoinduced attenuation of GLS. However, this investigation provides an initial insight into this novel effect and shows its relevance. A more quantitative analysis of the effect at different wavelengths should be performed as a next step. Although the observed 'high-intensity darkening' is likely to affect devices requiring pumping around 1 μm (such as the 1.3 μm amplifier), it is possible that devices operating at longer wavelengths are unaffected. No photoinduced effects were observed in GLSO glass, which indicates that glass composition is also very important and varying the composition could be used to reduce the photoinduced effects. Further studies should also be directed to a better understanding of the wavelength dependence and to the role of glass composition.

7.4 Conclusions

In this final chapter we investigated the transmission properties of GLS and GLSO and Pr^{3+}-doped GLS fibres under intense IR pump irradiation. We observed photoinduced attenuation in GLS and Pr^{3+}:GLS. The wavelength dependence, metastable behaviour and decay time was found to be qualitatively and quantitatively similar to the PD induced by bandgap illumination. By comparing the undoped and the Pr^{3+}-doped GLS fibres, we concluded that the photorefractive effect is an intrinsic property of GLS but an enhancement of this effect due to the rare earth dopant cannot be totally ruled out. We also found that the magnitude of the photoinduced attenuation is linearly dependent on the pump intensity, which rules out two-photon absorption as the cause of the darkening and also provides evidence for the existence of gap states in GLS. The nature of these gap states and the mechanism of high intensity darkening still remains to be fully investigated. The possible impact on active fibre devices pumped at approximately 1 μm was briefly discussed. We believe that this effect has practical relevance and should be seriously considered for practical applications of GLS. Photoinduced loss was recently observed to have a very detrimental effect on the amplifier performance of Pr^{3+}-doped *As:Ga:S* fibres. This will be included in the topics for future study.

Chapter 8

Conclusions and Further Work.

Chalcogenide glasses have been known for several decades as infrared transmitting materials. After the invention and development of silica optical fibre technology, these materials attracted a renewed interest for all-optical devices. Sulphide glasses and a few selenide glasses, in particular, were regarded as very promising for several device applications, owing to their low phonon energy, their high third order nonlinearity and their transparency from the red-end of the visible to the mid-IR. Gallium sulphide-based glasses, such as GLS glass, having very high rare-earth solubility, were proposed for optical amplification schemes alternative to the EDFA, such as the 1.3 μm praseodymium amplifier.

Despite the promise, and after over a decade of active research, the success of chalcogenide glasses for fibre devices is still rather limited, with only a few device prototypes demonstrated, such as the Pr^{3+}-doped GNS amplifier at 1.34 μm demonstrated by Tawarayama and co-workers (81) and the all-optical switch in As-S fibres demonstrated by Asobe and co-workers (234). Fabrication of chalcogenide optical fibres is arguably very challenging. In their vast majority, chalcogenides cannot be obtained by chemical deposition, thus they are prepared by melt-quenching; as a result, complicated purification techniques must be employed in order to keep the impurities to an acceptable value. Another problem is glass stability. Glasses like GLS are prone to devitrification upon heating, which makes the fabrication of single mode fibres very difficult.

In addition to the fabrication-related, chalcogenides have also other, more fundamental issues. The intrinsic transparency of these materials is very difficult to predict. In oxide and fluoride glasses, the fundamental transparency limit is determined by the Rayleigh scattering, which can be estimated and measured with good accuracy. In contrast, in chalcogenides glasses absorption may occur throughout the whole transmission window due to the presence of bandgap defects, which give rise to the weak absorption tail. The weak tail has been identified in several glass systems, including As_2S_3, where it causes a much higher loss than the Rayleigh scattering and determines the transparency

limit; this limit, however, is difficult to gauge as the magnitude of the tail depends also on extrinsic factors such as impurities. A precise theoretical model has not yet been achieved for the weak absorption tail, therefore it is still not known whether a weak tail is also to be expected for the other chalcogenide glasses. This is also the case for GLS and GLSO glasses, for which the loss mechanisms and the transparency limit are not yet fully identified.

Another very important point concerns the photoinduced changes. Chalcogenide glasses are susceptible to a variety of light-induced modifications of their optical properties. In particular, absorption of light with a wavelength close to the material's optical bandgap results in a red-shift of the electronic absorption edge, i.e. the photodarkening effect, and causes a large increase of the transmission loss at important wavelengths in the near-IR range. Optical fibre devices require high pump and signal intensities at near-IR wavelengths; the occurrence of linear and nonlinear absorption or upconversion processes in the 'high intensity' regime could then give rise to photoinduced changes similar to direct bandgap absorption and in turn affect the material's transmission of the pump and signal.

As far as GLS and GLSO glasses are concerned, a great deal of effort was devoted in the past towards improving the various aspects of fabrication, from the synthesis of the glass precursors to preform fabrication and fibre drawing. However, the loss mechanisms and the transparency limit for these glasses had not yet been fully identified. Similarly, the occurrence of photoinduced effects and their impact on practical applications of GLS and GLSO glasses had not been previously assessed. To investigate these two very important and novel aspects was the principal aim of the research that inspired this thesis. Suitable analytical techniques were identified and developed to this purpose, such as the innovative use of FEL-based laser calorimetry for measuring bulk absorption and the side illumination technique for characterising the photodarkening effect.

In the following we summarise the main achievements of this work.

- **Glass and fibre fabrication (Chapter 3).** In the area of fabrication of high purity GLS and GLSO glasses, improvements are required in the control of composition of raw materials and also of the glass composition. In this thesis, it has been shown that XRD can be effectively used to quantify the amounts of the gallium sulphide phases and thus to accurately determine the nominal composition of the glass batches. Due to the substantial mass loss during glass melting of GLS and GLSO in an open controlled atmosphere, a compositional characterisation of the as-quenched glass is also required. We showed that Rutherford Backscattering (RBS) can measure very accurately the Ga/La ratio, however a different technique is required to quantify the lighter elements, particularly oxygen. As the optical properties and, especially, the thermal stability of GLS and GLSO are strongly dependent on the oxygen content, this a very relevant point. Glass stability was also

analysed, and some initial work on the devitrification of GLSO was carried out. However, the crystallisation of GLS and GLSO glasses is complex and when the present project was carried out, a suitable setup for thermal analysis (high temperature DSC) was not yet available. Finally, a novel characterisation technique for core/clad fibres was devised. GLS and GLSO have a very high refractive index, which implies that cladding light cannot be suppressed by conventional techniques, i.e. by acrylate coating or index-matched oils. The properties of graphite-based coatings were investigated and the more suitable preparations, among those commercially available, were identified. We demonstrated that graphite coating provides a very effective way to remove the cladding modes and to characterise high index fibres. Unfortunately, the loss of core/clad fibres is still in excess of several tens of dB per meter, thus substantial improvements of fabrication and a better understanding of glass stability are required for GLS and GLSO.

- **Laser Absorption Calorimetry (Chapter 4, 5).** A new concept was proposed and realised in order to overcome one of the main limitations of this technique. While its use has been limited to the very few wavelengths for which high power laser sources were available (typically CO_2 and Nd-YAG lasers), we used a used a tunable free-electron laser source to achieve measurements at different wavelengths. The FEL source at the Jefferson Labs is a unique light source with ideal characteristics such as a very wide tunability range, high average power and high beam quality. The results presented in this thesis included the design and commissioning of a calorimeter and the first measurement of near-IR bulk absorption of GLS and GLSO at 1.55 and 1.7 μm. As a part of this project, a very comprehensive modelling work was produced in order to fill a significant gap in the theoretical heat flow analysis of laser calorimetry; the improved model takes into account the effect of a sample holder with thermal contact resistance at the sample/holder interface, and provides the theoretical heating/cooling curves for a calorimetric measurement with disc-shaped samples. The theoretical description presented in the Chapter 5 of this thesis is, to the best of the author's knowledge, the most exhaustive theoretical description of laser calorimetry produced to date.

- **Interpretation of the optical loss of GLS and GLSO (Chapter 6).** By comparing the bulk absorption, measured by laser calorimetry, and the total attenuation of the same set of samples in the same wavelength range, we obtained clear evidence that the transmission loss of GLS and GLSO is mainly caused by optical absorption in the region 1.55-1.7 μm. This is a novel result, as previous studies failed to identify whether the loss in the region above $\approx$ 1 μm was to be attributed to scattering or absorption. The other important question is what mechanism is actually causing this absorption, as both a weak absorption tail and impurity absorption from transition metal ions could cause optical absorption in the near-IR range. More absorption measurements by laser calorimetry at longer wavelengths (beyond 2 μm) are required to draw a definitive conclusion on this

point. However, we measured the specific absorption of transition metal ions in GLS and GLSO, and the estimated value for the impurity absorption is in both cases lower than the total absorption measured by laser calorimetry; this suggests that impurity absorption cannot fully account for the total absorption and that another mechanism, i.e. the weak tail is present in these materials.

- **Study of photoinduced effects (Chapter 6, 7).** Two different types of effects have been investigated. On one hand, the photodarkening due to bandgap illumination was characterised using unclad fibres and the side illumination technique. Furthermore, the transmission loss of GLS and GLSO fibres under high-intensity optical pumping at 1.064 μm was examined. Photorefractive effects have been studied in several chalcogenide systems, but are a relatively novel topic in GLS and GLSO glasses. In this thesis we presented a detailed study of the dependence of PD on the excitation wavelength in unclad GLS and GLSO fibres and a study of the kinetics of its formation, decay and reversibility. Although the the mechanism producing PD in GLS and GLSO was not investigated in detail, we proposed the use of the side illumination technique to that purpose. In particular, the measurement of the absorption coefficient in the region of the optical bandgap region will enable the determination of the nature of the peaks observed in the spectral dependence on the excitation (see figures 6.23 and 6.24). The high-peak power transmission loss had never been investigated before, to the best of our knowledge, in GLS and GLSO optical fibres. Our results show that high-intensity optical pumping at 1.064 μm causes a significant increase of the transmission loss of undoped and Pr^{3+}-doped GLS. This photoinduced loss can affect the performance of any optical device requiring optical pumping in that region, such as the 1.3 μm GLS optical amplifier. The loss was observed to increase proportionally to the pump intensity, which clearly rules out two-photon absorption as the cause and provides clear evidence of absorption from gap states. Damage thresholds for metastable damage (darkening) and lower limits for permanent damage of GLS and GLSO were also established here for the first time. The results presented in this thesis are novel and very interesting, and could stimulate a more complete study at different wavelengths.

Below are given some topics for further study.

Concerning the critical issue of the glass stability, the crystallisation of GLS and GLSO still appears to be poorly understood. Owing to the initiative of the author, a new high-temperature DSC-TGA (system Q600 from TA Instruments) has now been acquired by the Optoelectronics Research Centre, which provides a very powerful tool. This instrument will enable the quantitative study of stability and phase changes and hence more precise information on the kinetics of the devitrification and its dependence on the atmosphere, on the glass composition, impurities and thermal history.

Concerning the interpretation of the loss mechanisms in GLS and GLSO glasses, more calorimetric measurements in the wavelength regions around 2 μm and in the range 3.5-5 μm, will provide a definitive answer to the question of the presence of a weak tail and, consequently, a quantification of its magnitude and of the transparency limit of these materials. Direct measurements of the scattering loss in bulk samples could provide an independent verification of the results.

Another important direction for further activity is the characterisation of photo-induced effects in GLS and GLSO. Concerning the low-intensity photodarkening due to bandgap absorption, more studies are required to identify the mechanism causing the photodarkening, and in particular to verify the model of the photostructural changes proposed for other materials. To this end, wavelength-resolved measurements at different temperatures should be performed. In addition, the effect of bandgap illumination at higher intensities should also be investigated.

The photo-induced increase of transmission loss of GLS in the high-intensity regime is very relevant to device applications and needs to be fully characterised. The mechanisms producing this effect in GLS should be identified and the reason for the different behaviour of GLSO should also be identified. On a more applied topic, the photo-induced loss increase should be studied at different wavelengths, aimed at quantifying the non-linear 'photoinduced' absorption coefficients, which would then be used to gauge the impact on practical devices. Although this 'high intensity' darkening is likely to negatively affect rare-earth doped devices requiring optical pumping around, or below, 1 μm, it is possible that devices employing pumps at longer wavelengths are unaffected. As shown in this thesis, the glass composition has an important impact, as the photorefractive changes observed at 1.064 μm in GLS, are not observed in GLSO; this point should be investigated too.

Finally, it is also worth mentioning that these photorefractive changes could possibly be used for the design of new devices. In our studies we could only measure metastable changes. These could be exploited for writing erasable structures, such as waveguides and gratings; the results of this thesis show that changes are observed at relatively low intensities, which could be attractive for practical devices. Photodarkening could also be used to obtain an optically-controlled change of the refractive index or the attenuation in GLS and GLSO glass, alas a fast response would not be attainable due to the slow intrinsic time of PD in these materials. The possibility of writing permanent structures through irreversible effects at higher intensities is another point of interest, which could provide an alternative to the more conventional UV writing.

Appendix A

Summary of the Characterisation of GLS and GLSO Optical Fibres.

TABLE A.1: Characteristics and measured loss of unclad GLS and GLSO fibres

Code	Glass	Composition	Diameter	Attenuation		(‡)
			$[\mu m]$	@1.3 μm $[dBm^{-1}]$	@1.55μm $[dBm^{-1}]$	
LF291	(Er,Dy):GLS	65:2.5:32.5 1000*ppm Dy*, 500*ppm Er*	135-160	$35-45$ (†)	–	**P**
LF292	Pr:GLS	65:2.5:32.5 1000 *ppm Pr*	130-140	$2-3$ (*)	–	**P**
LF293	Er:GLS	65:2.5:32.5 1000 *ppm Er*	140	$5-6$	–	**P**
LF294	GLS	65:2.5:32.5	150	$7-8$	$8-9$	**P**
LF316	GLS	65:2.5:32.5	155	20 ± 2	19 ± 2	**E**
LF321	GLS+LaF_3	62.4:3.8:25.3:8.5	180	$5-10$	$5-10$	**E/Et**
LF322	GLS+LaF_3	62.4:3.8:25.3:8.5	190-200	$30-35$	$20-30$	**E/Et**
LF325	GLS	65:31:4	170-180	$15-20$	$15-20$	**P**
LF327	GLSO	72.5:27.5	160-170	20	20	**E**
LF328	GLSO	72.5:27.5	160-180	> 40	≈ 40	**E**
LF340	GLSOF	–	150-160	≈ 20	≈ 20	**P**
LF344	GLSO	72.5:27.5	140-160	13 ± 2	13 ± 2	**P**

(‡) Rods pulled from: **P** = polished rod; **E** = extruded rod; **Etc** = etched

(†) @ 1.4 μm

(*) @ 1.15 μm

TABLE A.2: Table A.1 (continued)

Code	Glass	Composition	Diameter $[\mu m]$	Attenuation @1.3 μm $[dBm^{-1}]$	Attenuation @1.55μm $[dBm^{-1}]$	(‡)
LF345	GLSOF	–	140-160	34 ± 5	34 ± 5	**P**
LF346	GLSO	72.5:27.5	140-150	15 ± 2	15 ± 2	**P/Et**
LF355	GLSO	77.5:22.5	150	$6 - 7$	$5 - 6$	**P**
LF361	GLSO	77.5:22.5	140-150	$13 - 14$	$12 - 13$	**E**
LF365	GLSOF	–	120	3-4	3-4	**P**
LF367	GLSO	77.5:22.5	140-160	7 ± 1	6 ± 1	**E**

(†) Rods pulled from: **P** = polished rod; **E** = extruded rod; **Etc** = etched

TABLE A.3: Characteristics and measured loss of unclad GLS and GLSO fibres

Fibre ID	Glass	Composition Core	Composition Clad	Core size $[\mu m]$	Loss @1.5 μm $[dBm^{-1}]$
LF282	GLSO	72.5:27.5	71:29	20	30 ± 5
LF284	GLSO	72.5:27.5	71:29	20-30	> 40
LF329	GLSO	72.5:27.5	71:29	100	40

Appendix B

Expression of the 'Heat Source' Term in Laser Calorimetry

B.1 General expression of absorbed optical powers from a glass plate

B.1.1 Definitions

A collimated beam incident on a plate-shaped glass sample undergoes reflection and refraction at the air/glass interfaces, absorption at the sample surfaces and attenuation in the bulk. Surface absorption is caused by residual damage from polishing and possible surface contamination. Bulk attenuation occurs due to scattering and absorption. Reflection and refraction are governed by Snell's Law. In this description the beam is assumed to be perfectly collimated and normally incident, which allows the expressions to be simplified (no complicated dependence on the angle of incidence and on the polarisation of the beam). Also, the beam is assumed monochromatic, the optical medium is supposed to have low absorption at the wavelength of interest and nonlinear effects (i.e. intensity-dependent refractive index) are also considered negligible.

The three above mentioned phenomena are described as follows:

Reflection/Refraction: if Π_0 is the optical power of the incident beam and r is the *reflection coefficient* (normal incidence), which, in the limit of low absorption, is expressed as:

$$r = \left(\frac{n-1}{n+1}\right)^2 \tag{B.1}$$

($n = n(\lambda)$ is the refractive index), then the reflected and transmitted powers at every

air/glass interface are:

$$\begin{cases} P_{refl,\ intf.} = r \cdot \Pi_0 \\ P_{transm,\ intf.} = (1-r) \cdot \Pi_0 \end{cases} \tag{B.2}$$

Surface Absorption: The *surface absorptivity* σ $(=\sigma(\lambda))$ is defined as:

$$\sigma = \frac{P_{abs,surf.}}{\Pi_0} \tag{B.3}$$

Thus, the absorbed and transmitted fraction of power are:

$$\begin{cases} P_{abs,\ surf} = \sigma \cdot \Pi_0 \\ P_{transm,\ surf.} = (1-\sigma) \cdot \Pi_0 \end{cases} \tag{B.4}$$

Bulk Attenuation: The power intensity *inside* the glass sample decreases exponentially with increasing traversed thickness, z, according to the Lambert-Beer's Law:

$$P(z) = P(0) \cdot \exp(-\alpha \cdot z) \tag{B.5}$$

The quantity $\alpha = \alpha(\lambda)$ is called the *absorption coefficient* and is the sum of the terms due to different attenuation mechanisms (scattering and absorption), which are material and wavelength dependent. Since laser absorption calorimetry does not measure scattering, it is assumed here to be negligible, thus the bulk attenuation is assumed to be entirely caused by absorption. The absorption in a region of infinitesimal thickness between z and $z + dz$ is:

$$[dP(z)]_{abs} = \alpha P(z) dz \tag{B.6}$$

The total absorbed fraction over a finite thickness L of material is:

$$P_{abs}(L) = 1 - \exp(-\alpha L) \equiv 1 - \tau_i \tag{B.7}$$

where we have defined the quantity $\tau_i = \exp(-\alpha L)$, commonly indicated as the *internal transmission* of a thickness L.

Note: r and σ are non-dimensional, and usually expressed as a percentage; τ_i is also non-dimensional, while $[\alpha] = l^{-1}$ is usually expressed in cm^{-1} or dBm^{-1}. It must be noted that n (thus r), σ and *beta* are all temperature dependent material properties; however, the dependence is relatively weak, and can be neglected for temperature variations of

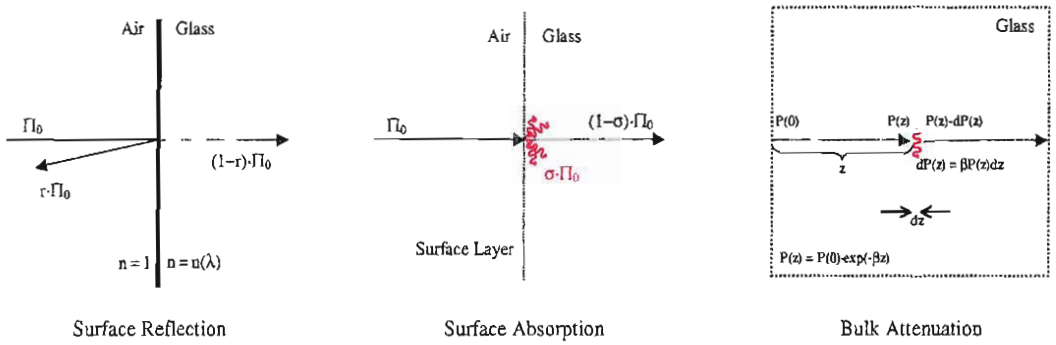

FIGURE B.1: Simplified sketch of reflection, surface absorption and bulk absorption processes.

up to a few degrees. Also note that, in the expressions above, the powers Π_0 and $P(0)$ can have an arbitrary dependence on the transverse coordinates, as long as the beam is collimated.

We also define:

- The **absorptivity**, i.e the total fraction of power absorbed by the sample:

$$\mathcal{A} = \frac{P_{abs,tot}}{\Pi_0} \tag{B.8}$$

- The **reflectivity**, i.e the total fraction of power reflected by the sample:

$$\mathcal{R} = \frac{P_{refl,tot}}{\Pi_0} \tag{B.9}$$

- The **transmissivity**, i.e the total fraction of power transmitted by the sample:

$$\mathcal{T} = \frac{P_{trans,tot}}{\Pi_0} \tag{B.10}$$

In the absence of scattering:

$$\mathcal{A} + \mathcal{R} + \mathcal{T} = 1 \tag{B.11}$$

The total absorptivity $\mathcal{A}$ is the sum of the bulk absorptivity plus the contribution from the surfaces (surface absorptivity). To give the orders of magnitude, in the case of a 1 cm thick GLS glass sample: $\mathcal{R} \approx 32\%$, $\mathcal{T} \approx 67\%$, $\mathcal{A} \approx 1\%$.

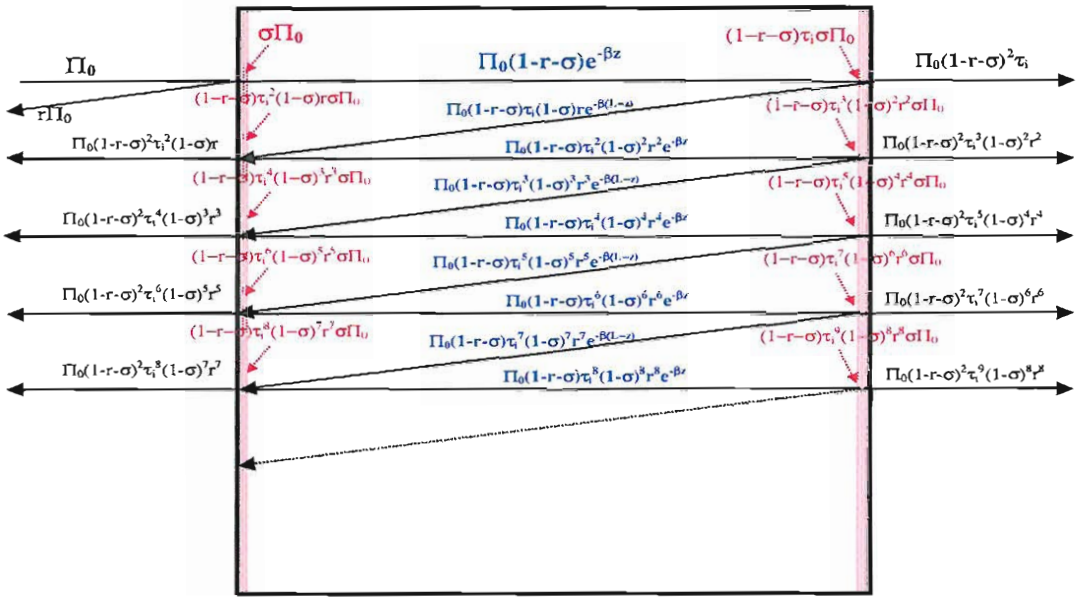

FIGURE B.2: Representation of transmission, reflection and absorption processes in a glass plate.

B.1.2 Exact expressions for $\mathcal{A}$, $\mathcal{R}$, $\mathcal{T}$

As seen above, when the beam traverses an interface, it is split into two components. Thus an infinite number of components is created by the two parallel surfaces of a glass plate, with the multiple bounce situation shown in figure B.2. All the components contribute to the exact expressions for the three quantities $\mathcal{A}$, $\mathcal{R}$, $\mathcal{T}$. The simplest case is when the power components interact incoherently, i.e. they do not produce interference. This approximation works well for thicker samples or for slightly wedged samples. In our case, this assumption is valid because the light source is pulsed, the pulses are ultra-short ($\sim ps$) and the repetition rate is low ($\sim 18 - 74\ MHz$) (see Chapter 4).

The exact expressions for T, R, A_{bulk} and A_{surf} are calculated through the sums of geometrical progressions (see fig. B.2); it follows that:

$$
\begin{aligned}
T &= \sum_{n=0}^{\infty} T_n = \sum_{n=0}^{\infty} P_{T,n}/\Pi_0 \qquad \text{(B.12)} \\
&= (1-r-\sigma)^2\tau_i + (1-r-\sigma)^2\tau_i^3(1-\sigma)^2r^2 + (1-r-\sigma)^2\tau_i^5(1-\sigma)^4r^4 + \ldots \\
&+ (1-r-\sigma)^2\tau_i^{2n+1}(1-\sigma)^{2n}r^{2n} + \ldots = \\
&= (1-r-\sigma)^2\tau_i \cdot \sum_{n=0}^{\infty} [(1-\sigma)r\tau_i]^{2n} \\
&= \frac{(1-r-\sigma)^2\tau_i}{1-(1-\sigma)^2r^2\tau_i^2}
\end{aligned}
$$

$$
\begin{aligned}
R &= \sum_{n=0}^{\infty} R_n = \sum_{n=0}^{\infty} P_{R,n}/\Pi_0 \qquad \text{(B.13)}\\
&= r + r(1-r-\sigma)^2\tau_i^2(1-\sigma) + r(1-r-\sigma)^2\tau_i^4 r^2(1-\sigma)^3 + \ldots \\
&\quad + r(1-r-\sigma)^2\tau_i^6 r^4(1-\sigma)^5 + r(1-r-\sigma)^2\ tau_i^{2n+2} r^{2n}(1-\sigma)^{2n+1} + \ldots = \\
&= r \cdot \left[1 + (1-r-\sigma)^2\tau_i^2(1-\sigma) \cdot \sum_{n=0}^{\infty} [(1-\sigma)r\tau_i]^{2n}\right] \\
&= r \cdot \left[1 + \frac{(1-r-\sigma)^2\tau_i^2(1-\sigma)}{1-(1-\sigma)^2 r^2\tau_i^2}\right]
\end{aligned}
$$

$$
\begin{aligned}
A_{bulk} &= \sum_{n=0}^{\infty} A_{bulk,n} = \sum_{n=0}^{\infty} P_{A_{bulk},n}/\Pi_0 \qquad \text{(B.14)}\\
&= (1-r-\sigma)(1-\tau_i) + (1-r-\sigma)(1-\sigma)r\tau_i(1-\tau_i) + \ldots \\
&\quad + (1-r-\sigma)(1-\sigma)^2 r^2\tau_i^2(1-\tau_i) + (1-r-\sigma)(1-\sigma)^n r^n\tau_i^n(1-\tau_i) + \ldots = \\
&= (1-r-\sigma)(1-\tau_i) \cdot \sum_{n=0}^{\infty} [(1-\sigma)r\tau_i]^n \\
&= \frac{(1-r-\sigma)(1-\tau_i)}{1-(1-\sigma)r\tau_i}
\end{aligned}
$$

$$
\begin{aligned}
A_{surf} &= \sum_{n=0}^{\infty} A_{surf,n} = \sum_{n=0}^{\infty} P_{A_{surf},n}/\Pi_0 \qquad \text{(B.15)}\\
&= \sigma + (1-r-\sigma)\tau_i\sigma + (1-r-\sigma)(1-\sigma)r\tau_i^2\sigma + \ldots \\
&\quad + (1-r-\sigma)(1-\sigma)^2 r^2\tau_i^3\sigma + (1-r-\sigma)(1-\sigma)^n r^n\tau_i^{n+1}\sigma + \ldots = \\
&= \sigma \cdot \left[1 + (1-r-\sigma)\tau_i \cdot \sum_{n=0}^{\infty} [(1-\sigma)r\tau_i]^n\right] \\
&= \sigma \cdot \left[1 + \frac{(1-r-\sigma)\tau_i}{1-(1-\sigma)r\tau_i}\right]
\end{aligned}
$$

A_{surf} is the sum of the contributions contributions from the first and second interface, that are respectively:

$$
[A_{surf}]_1 = \sigma \cdot \left[1 + \frac{(1-r-\sigma)r\tau_i^2(1-\sigma)}{1-(1-\sigma)^2 r^2\tau_i^2}\right] \qquad \text{(B.16)}
$$

$$
[A_{surf}]_2 = \sigma \cdot \left[\frac{(1-r-\sigma)\tau_i}{1-(1-\sigma)^2 r^2\tau_i^2}\right] \qquad \text{(B.17)}
$$

The total absorptivity (bulk plus surface) is then:

$$\begin{aligned} A &= A_{bulk} + A_{surf} \\ &= \sigma + \frac{(1-r-\sigma)(1-\tau_i+\tau_i\sigma)}{1-(1-\sigma)r\tau_i} \end{aligned} \tag{B.18}$$

In the limit of low bulk absorption ($\alpha \ll 1$, $\tau_i \sim 1+\alpha L$) and low surface absorption ($\sigma \ll 1$, $\sigma \ll 1-r$), the above expression can be simplified to:

$$A \approx \sigma + (1-\tau_i) + \sigma\tau_i \approx 2\sigma + \alpha L \tag{B.19}$$

It is also useful for the following discussion to write the expression for the (internal) total optical power within the glass plate:

$$\begin{aligned} P_{i,tot}(z) &= P^+(z) + P^-(z) \\ &= \left[\Pi_0(1-r-\sigma)e^{-\alpha z}\cdot\left(1+(1-\sigma)^2r^2\tau_i^2+\cdots\right)\right] + \\ &\quad + \left[\Pi_0(1-r-\sigma)e^{-\alpha(L-z)}\cdot\left((1-\sigma)r\tau_i+(1-\sigma)^3r^3\tau_i^3+\cdots\right)\right] \\ &= \Pi_0(1-r-\sigma)\cdot\left[e^{-\alpha z}\cdot\sum_{n=0}^{\infty}\left[(1-\sigma)r\tau_i\right]^{2n} + r\tau_i^2(1-\sigma)e^{\alpha z}\cdot\sum_{n=0}^{\infty}\left[(1-\sigma)r\tau_i\right]^{2n}\right] \\ &= \Pi_0\cdot\frac{(1-r-\sigma)}{1-(1-\sigma)^2r^2\tau_i^2}\cdot\left[e^{-\alpha z}+r\tau_i^2(1-\sigma)e^{\alpha z}\right] \end{aligned} \tag{B.20}$$

It can be easily verified that, as expected, it follows:

$$\int_0^L \alpha P_{i,tot}(z)dz = A_{bulk}\Pi_0 \tag{B.21}$$

B.2 Expressions of the heat source term

B.2.1 Exact expression

The above formalism is now applied to the description of laser absorption calorimetry on a disc-shaped sample. A rigorous heat flow analysis of a laser calorimetric experiment should take into account three 'heat source' terms, i.e. a 'volume' term due to bulk absorption, and two surface terms due to absorption at each of the interfaces. Absorption in the bulk produces a 3-d extended heat source in the sample; a general form is assumed

for the incident power distribution:

$$\Pi_0(r,\vartheta,z) = P_0 \cdot I(r,\vartheta) \tag{B.22}$$

where P_0 is the total power of the laser beam and $I(r,\vartheta)$ is an arbitrary normalised intensity distribution. For instance, for a beam with a uniform, 'top-hat' power distribution of diameter d and a gaussian beam of diameter d, it follows respectively:

$$I_{unif}(r,\vartheta) = \frac{1}{\pi}\left(\frac{2}{d}\right)^2 \tag{B.23}$$

$$I_{gauss}(r,\vartheta) = \frac{2}{\pi d^2} e^{-2\left(\frac{r}{d}\right)^2} \tag{B.24}$$

To calculate the absorbed power density, the expression (B.6) must be modified in order to account for the multiple reflected beam components within the plate. The absorbed power in a region between z and $z+dz$ is:

$$dQ(r,\vartheta,z) = \alpha P(r,\vartheta,z)dz \tag{B.25}$$

where $P(r,\vartheta,z)$ is the total power, given by the relationship (B.20), where however the expression (B.22) for Π_0 is substituted; the absorbed power density is then:

$$\begin{aligned} Q(r,\vartheta,z) &= \alpha P_0 I(r,\vartheta) \cdot \frac{(1-r-\sigma)}{1-(1-\sigma)^2 r^2 \tau_i^2} \cdot \left[\, e^{-\alpha z} + r\tau_i^2(1-\sigma)e^{\alpha z} \,\right] \\ &= \alpha P_0 I(r,\vartheta) \cdot \frac{(1-r-\sigma)\tau_i}{1-(1-\sigma)^2 r^2 \tau_i^2} \cdot \left[\, e^{-\alpha(z-L)} + r(1-\sigma)e^{-\alpha(L-z)} \,\right] \end{aligned} \tag{B.26}$$

Note that $Q(r,\vartheta,z)$ can also be expressed by means of the total transmitted power $P_{trans,tot} = T \cdot P_0 I(r,\vartheta)$ (i.e. the power that is actually measured):

$$Q(r,\vartheta,z) = \frac{\alpha P_{trans,tot}}{(1-r-\sigma)} \cdot \left[\, e^{-\alpha(z-L)} + r(1-\sigma)e^{-\alpha(L-z)} \,\right] \tag{B.27}$$

The relationship (B.20) and the definition (B.22) ensure that the above quantity is normalised correctly, i.e. it follows:

$$\begin{aligned}
\int_0^{\infty}\int_0^{2\pi}\int_0^{L} Q(r,\vartheta,z)\,r\,dr\,d\vartheta\,dz &= \int_{R^2} I(r,\vartheta)\,r\,dr\,d\vartheta \cdot \\
&\quad \cdot \int_0^{L} \alpha P_0 \frac{(1-r-\sigma)}{1-(1-\sigma)^2 r^2 \tau_i^2} \cdot \left[e^{-\alpha z} + r\tau_i^2(1-\sigma)e^{\alpha z}\right] dz \\
&= 1 \cdot \frac{(1-r-\sigma)}{1-(1-\sigma)^2 r^2 \tau_i^2} \cdot \left[1-\tau_i + r\tau_i^2(1-\sigma)(\tau_i^{-1}-1)\right] \cdot P_0 \\
&= \frac{(1-r-\sigma)(1-\tau_i)}{1-(1-\sigma)r\tau_i} \cdot P_0 \\
&= A_{bulk} P_0 = P_{abs,tot} \qquad \text{(B.28)}
\end{aligned}$$

On the other hand, the 'surface terms' translate into terms in the boundary conditions for the flat faces of the disc sample. The heat flow at these boundaries is determined by surface absorption (heat flowing in, expressed using the equations B.16, B.17) and by irradiation towards the chamber's walls (heat flowing out). The correct formalism for these terms is not developed here.

The description with three source terms leads to a far more complicated heat diffusion problem than the model described in Chapter 5. The solutions are expected to have a complicated dependence on the two 'unknown' quantities of the problem, α and σ, making it hard or impractical to use the theoretical solutions for interpretation of experimental heating curves.

It is therefore necessary to introduce some degree of approximation; indeed, while the expressions developed in the previous two sections are valid for the general case, in laser calorimetry one is generally measuring small bulk and surface absorption; also, samples are thin discs, i.e. temperature gradients along the longitudinal direction can often be neglected. Bearing this in mind, it is possible to simplify the heat source term.

B.2.2 The 'uniform heat source' approximation

This approximation is based on a few assumptions:

- The bulk absorption of the glass sample is small at the wavelength measured, and the sample is optically thin ($\alpha L \ll 1$); thus, the variation of intensity of the laser beam along the longitudinal coordinate z is negligible. The absorbed heat per unit volume is then independent of the longitudinal coordinate z, i.e. the beam releases heat uniformly in a cylindrical volume (diameter d, height L) at the center of the sample.

- Bulk and surface absorption are low, the sample is thin, the laser beam hits a small area at the center of the sample and the temperature is measured at the edge of the

disc ($R \gg d$, where R and $d/2$ are the disc and the laser beam radius respectively); thus, the surface heat source terms are considered as volume terms, i.e. the heat absorbed by the surfaces is assumed to be 'spread' in the same cylindrical volume.

Under these assumptions, the absorbed heat density in a sample of thickness L is given by (B.19, B.22, B.24):

$$Q(r,\vartheta) = (2\sigma + \alpha L)\ P_0 \cdot \frac{I_{gauss}(r,\vartheta)}{L} \tag{B.29}$$

where the $1/L$ term must be added in order to ensure that a correct 'normalisation' such as in (B.28) is satisfied, i.e.:

$$\int_{R^2}\int_0^L Q(r,\vartheta) r dr d\vartheta dz = (2\sigma + \alpha L)\ P_0 = P_{abs,tot} \tag{B.30}$$

The expression (B.29) provides a very practical way to determine both α and σ. The absorbed power is a linear function of the sample thickness L; hence, by measuring the absorption of a set of samples with different thickness, both α and σ can be determined.

Different approximations can be assumed; one possibility is to relax the approximation of 'uniform heat source' and allow for a single exponential dependence of the absorbed power inside the sample, i.e. to assume a source term:

$$Q(r,\vartheta,z) \propto (2\sigma + \alpha L) \cdot P_0 I_{gauss}(r,\vartheta) \cdot e^{-\alpha z} \tag{B.31}$$

The exponential of the longitudinal coordinate z can be approximated with a linear dependence, obtaining:

$$Q(r,\vartheta,z) = (2\sigma + \alpha L) P_0 \cdot \frac{I_{gauss}(r,\vartheta)}{L\left(1 - \frac{\alpha L}{2}\right)} \cdot (1 - \alpha z) \tag{B.32}$$

This form of absorbed heat density is still relatively 'simple', retains the advantage of eqn. (B.30), and still allows the boundary value problem of heat diffusion for a disc sample to be solved analytically.

Appendix C

Summary of the Solutions of the BVP for the Calorimetric System with Sample and Holder (Composite Double Layer Problem)

The solution of the boundary value problem of heat diffusion in the cylindrical double layer (originally 2-d, reduced to 1-d through the 'approximation of thin sample') is given by eq. 5.104:

$$T_i(r,t) = \mathcal{A}P_0 \cdot \sum_{n=0}^{\infty} A_n F_{i,n}(r) \cdot \begin{cases} \frac{1}{\gamma_n^2}[1 - e^{-\gamma_n^2 t}] & t < t_0 \\ \frac{1}{\gamma_n^2}[1 - e^{-\gamma_n^2 t_0}]e^{-\gamma_n^2(t-t_0)} & t \geq t_0 \end{cases} \tag{C.1}$$

where $i = 1$ indicates the sample, and $i = 2$ indicates the holder. The variable r is defined in the interval $[0, R_2]$, where the interface sample/holder is located at $r = R_1$. In addition, $\mathcal{A}$ is the optical absorptivity of the sample, and P_0 is the average power of the laser beam *on the sample*; the laser is 'on' between $t = 0$ and $t = t_0$. In eqn. C.1, the $\{F_{i,n}(r)\}_{n\in\mathbf{N}}^{i=1,2}$ are the (radial) eigenfunctions, defined as (see eqns. 5.59, 5.84):

$$\begin{cases} \begin{cases} F_{1,0}(r) \propto I_0(b_{1,0} \cdot r) & n = 0 \\ F_{1,n}(r) \propto J_0(\beta_{1,n} \cdot r) & n \geq 1 \end{cases} & \text{(sample)} \\ \begin{cases} F_{2,0}(r) \propto C_{1,0} \cdot J_0(\beta_{2,0} \cdot r) + C_{2,0} \cdot Y_0(\beta_{2,0} \cdot r) & n = 0 \\ F_{2,n}(r) \propto C_{1,n} \cdot J_0(\beta_{2,n} \cdot r) + C_{2,n} \cdot Y_0(\beta_{2,n} \cdot r) & n \geq 1 \end{cases} & \text{(holder)} \end{cases} \tag{C.2}$$

where the coefficients $\{C_{i,n}\}_{n\in\mathbf{N}}^{i=1,2}$ are defined by the expressions (see eqns. 5.69-5.70, 5.97-5.98):

$$\left\{\begin{array}{lll}
\left\{\begin{array}{ll} C_{1,0} = \frac{\pi R_1}{2}\cdot\left|\begin{array}{cc} -\frac{b_{1,0}}{H_C}\,I_1(b_{1,0}R_1) - I_0(b_{1,0}R_1) & Y_0(\beta_{2,0}R_1) \\ \frac{k_1}{k_2}b_{1,0}I_1(b_{1,0}R_1) & \beta_{2,0}Y_1(\beta_{2,0}R_1)\end{array}\right| & n=0 \\ C_{1,n} = \frac{\pi R_1}{2}\cdot\left|\begin{array}{cc} \frac{\beta_{1,n}}{H_C}J_1(\beta_{1,n}R_1) - J_0(\beta_{1,n}R_1) & Y_0(\beta_{2,n}R_1) \\ -\frac{k_1}{k_2}\beta_{1,n}J_1(\beta_{1,n}R_1) & \beta_{2,n}Y_1(\beta_{2,n}R_1)\end{array}\right| & n\geq 1 \end{array}\right. & \text{(sample)} \\
\left\{\begin{array}{ll} C_{2,0} = \frac{\pi R_1}{2}\cdot\left|\begin{array}{cc} J_0(\beta_{2,0}R_1) & -\frac{b_{1,0}}{H_C}\,I_1(b_{1,0}R_1) - I_0(b_{1,0}R_1) \\ \beta_{2,0}J_1(\beta_{2,0}R_1) & \frac{k_1}{k_2}\,b_{1,0}I_1(b_{1,0}R_1)\end{array}\right| & n=0 \\ C_{2,n} = \frac{\pi R_1}{2}\cdot\left|\begin{array}{cc} J_0(\beta_{2,n}R_1) & \frac{\beta_{1,n}}{H_C}J_1(\beta_{1,n}R_1) - J_0(\beta_{1,n}R_1) \\ \beta_{2,n}J_1(\beta_{2,n}R_1) & -\frac{k_1}{k_2}\beta_{1,n}J_1(\beta_{1,n}R_1)\end{array}\right| & n\geq 1 \end{array}\right. & \text{(holder)}
\end{array}\right. \tag{C.3}$$

The $b_{1,0}$ and the $\{\beta_{i,n}\}$ are the (radial) eigenvectors, defined respectively as in eqns. 5.56, 5.94:

$$\left\{\begin{array}{lll}
\left\{\begin{array}{ll} b_{1,0} = \sqrt{-\frac{\gamma_0^2}{\kappa_1} + \frac{2H_1}{L_1}} & n=0 \\ \beta_{1,n} = \sqrt{\frac{\gamma_n^2}{\kappa_1} - \frac{2H_1}{L_1}} & n\geq 1 \end{array}\right. & \text{(sample)} \\
\beta_{2,n} = \sqrt{\frac{\gamma_n^2}{\kappa_2} - \frac{2H_2}{L_2}} \quad n\geq 0 & \text{(holder)}
\end{array}\right. \tag{C.4}$$

The quantities $\{\gamma_n\}_{n\in\mathbf{N}}$, which determine the radial eigenvalues C.4, and also determine the time-variable dependence of the solutions C.1, are defined as the solutions of the following 'eigenvalue equations' (eqns. 5.65, 5.77):

$$\left\{\begin{array}{lll}
\Phi'(\gamma) \equiv det[\mathbf{A}'(\gamma)] = 0 & \gamma\in[\frac{2H_2\kappa_2}{L_2}, \frac{2H_1\kappa_1}{L_1}] & \text{defining: } \gamma_0 \\
\Phi(\gamma) \equiv det[\mathbf{A}(\gamma)] = 0 & \gamma\in[\frac{2H_1\kappa_1}{L_1}, \infty] & \text{defining: } \{\gamma_n\}_{n\geq 1}
\end{array}\right. \tag{C.5}$$

In writing these equations it was assumed the condition $\frac{H_2\kappa_2}{L_2} < \frac{H_1\kappa_1}{L_1}$. The matrices $A'[\gamma]$ and $A[\gamma]$ are defined respectively as (eqns. 5.64, 5.83):

$$\mathbf{A}'[\gamma]\equiv\left(\begin{array}{ccc}
J_0(\beta_2(\gamma)R_1) & Y_0(\beta_2(\gamma)R_1) & \left[-\frac{b_1(\gamma)}{H_C}\,I_1(b_1(\gamma)R_1) - I_0(b_1(\gamma)R_1)\right] \\
\beta_2(\gamma)J_1(\beta_2(\gamma)R_1) & \beta_2(\gamma)Y_1(\beta_2(\gamma)R_1) & \frac{k_1}{k_2}\,b_1(\gamma)I_1(b_1(\gamma)R_1) \\
\left[\frac{\beta_2(\gamma)}{H_2}\,J_1(\beta_2(\gamma)R_2) - J_0(\beta_2(\gamma)R_2)\right] & \left[\frac{\beta_2(\gamma)}{H_2}\,Y_1(\beta_2(\gamma)R_2) - Y_0(\beta_2(\gamma)R_2)\right] & 0
\end{array}\right) \tag{C.6}$$

$$\mathbf{A}[\gamma] \equiv \begin{pmatrix} J_0(\beta_2(\gamma)R_1) & Y_0(\beta_2(\gamma)R_1) & \left[\frac{\beta_1(\gamma)}{H_C}\ J_1(\beta_1(\gamma)R_1) - J_0(\beta_1(\gamma)R_1)\right] \\ \gamma_2(\gamma)J_1(\beta_2(\gamma)R_1) & \beta_2(\gamma)Y_1(\beta_2(\gamma)R_1) & -\frac{k_1}{k_2}\beta_1(\gamma)J_1(\beta_1(\gamma)R_1) \\ \left[\frac{\beta_2(\gamma)}{H_2}\ J_1(\beta_2(\gamma)R_2) - J_0(\beta_2(\gamma)R_2)\right] & \left[\frac{\beta_2(\gamma)}{H_2}\ Y_1(\beta_2(\gamma)R_2) - Y_0(\beta_2(\gamma)R_2)\right] & 0 \end{pmatrix} \tag{C.7}$$

In the above expressions (C.3-C.7), the following material constants also appear: the thermal conductivities k_i (i=1: sample; i=2: holder), the thermal diffusivities κ_i, the thicknesses (i.e., longitudinal dimensions) L_i; $H_i \equiv \frac{h_i}{k_i}$ and $H_C \equiv \frac{h_C}{k_1}$, where h_i are the radiation heat exchange coefficients and h_C is the sample/holder interface heat exchange coefficient.

Finally, the generalised Fourier coefficients A_n are defined by the following expressions (valid in the limit: $R_1/d \longrightarrow \infty$) (see eq. 5.105):

$$\begin{cases} A_0 = \dfrac{e^{\frac{1}{2}\left(\frac{b_{1,0}d}{2}\right)^2}}{2\pi L_1 N_0} & n = 0 \\ A_n = \dfrac{e^{-\frac{1}{2}\left(\frac{\beta_{1,n}d}{2}\right)^2}}{2\pi L_1 N_n} & n \geq 1 \end{cases} \tag{C.8}$$

where d is the radius of the (gaussian) laser beam and the normalisation coefficients N_n are defined as follows (eqn. 5.107):

$$\begin{cases} N_0 = \frac{k_1}{\kappa_1}\frac{R_1^2}{2}\left[I_0^2(b_{1,0}R_1) - I_1^2(b_{1,0}R_1)\right] + \\ \qquad \frac{k_2}{\kappa_2}\left[\frac{r^2}{2}\left(\left[C_{1,0}J_0(\beta_{2,0}r) + C_{2,n}Y_0(\beta_{2,0}r)\right]^2 - \left[C_{1,0}J_1(\beta_{2,0}r) + C_{2,0}Y_1(\beta_{2,0}r)\right]^2\right)\right]_{r=R_1}^{r=R_2} & n = 0 \\ N_n = \frac{k_1}{\kappa_1}\frac{R_1^2}{2}\left[J_0^2(\beta_{1,n}R_1) + J_1^2(\beta_{1,n}R_1)\right] + \\ \qquad \frac{k_2}{\kappa_2}\left[\frac{r^2}{2}\left(\left[C_{1,n}J_0(\beta_{2,n}r) + C_{2,n}Y_0(\beta_{2,n}r)\right]^2 + \left[C_{1,n}J_1(\beta_{2,n}r) + C_{2,n}Y_1(\beta_{2,n}r)\right]^2\right)\right]_{r=R_1}^{r=R_2} & n \geq 1 \end{cases} \tag{C.9}$$

Appendix D

Proof of Additional Relationships (Chapter 5)

D.1 Proof of the generalized orthogonality relationship 5.72

Eigenvalue equations 5.57 for the n-th and m-th eigenfunction:

$$\begin{cases} \frac{1}{r}\frac{d}{dr}\left[r \cdot \frac{dF_{i,n}}{dr}(r)\right] + \beta_{i,n}^2 \cdot F_{i,n}(r) = 0 & \beta_{i,n}^2 = \frac{\gamma_n^2}{\kappa_i} - \frac{2H_i}{L_i} \\ \frac{1}{r}\frac{d}{dr}\left[r \cdot \frac{d}{dr}(r)\right] + \beta_{i,m}^2 \cdot F_{i,m}(r) = 0 & \beta_{i,m}^2 = \frac{\gamma_m^2}{\kappa_i} - \frac{2H_i}{L_i} \end{cases} \tag{D.1}$$

Multiply the first by $F_{i,m}$, the second by $F_{i,n}$ and subtract:

$$\left(\beta_{i,n}^2 - \beta_{i,m}^2\right) F_{i,n}F_{i,m} = \frac{1}{r}\left[F_{i,n}\frac{d}{dr}\left(r \cdot \frac{dF_{i,m}}{dr}\right) - F_{i,m}\frac{d}{dr}\left(r \cdot \frac{dF_{i,n}}{dr}\right)\right] \tag{D.2}$$

Substitute the expression for the βs and reorganize the right-hand side term:

$$\frac{1}{\kappa_i}\left(\gamma_n^2 - \gamma_m^2\right) F_{i,n}F_{i,m} = \frac{1}{r}\frac{d}{dr}\left[rF_{i,n} \cdot \frac{dF_{i,m}}{dr} - rF_{i,m} \cdot \frac{dF_{i,n}}{dr}\right] \tag{D.3}$$

Multiply by r and integrate between r_{i-1} and r_i (over 'zone 1'):

$$\frac{1}{\kappa_i}\left(\gamma_n^2 - \gamma_m^2\right) \cdot \int_{r_{i-1}}^{r_i} rF_{i,n}F_{i,m}dr = \left[r\left(F_{i,n} \cdot \frac{dF_{i,m}}{dr} - F_{i,m} \cdot \frac{dF_{i,n}}{dr}\right)\right]_{r=r_{i-1}}^{r=r_i} \tag{D.4}$$

Multiply by k_i and sum over the 'zone' index i:

$$(\gamma_n^2 - \gamma_m^2) \cdot \sum_{i=1}^{2} \frac{k_i}{\kappa_i} \int_{r_{i-1}}^{r_i} r F_{i,n} F_{i,m} dr = \sum_{i=1}^{2} \left[r \cdot B_{n,m}^i \right]_{r=r_{i-1}}^{r=r_i} \tag{D.5}$$

where:

$$B_{n,m}^i \equiv k_i \left(F_{i,n} \cdot \frac{dF_{i,m}}{dr} - F_{i,m} \cdot \frac{dF_{i,n}}{dr} \right) \tag{D.6}$$

It will be now proved that the right hand side term of eqn. D.5 vanishes (reference (187) gives a more general demonstration for a composite multilayer system):

$$\begin{aligned}
&\textstyle\sum_{i=1}^{2} \left[r \cdot B_{n,m}^i \right]_{r=r_{i-1}}^{r=r_i} = \left[r \cdot B_{n,m}^i \right]_0^{R_1} + \left[r \cdot B_{n,m}^i \right]_{R_1}^{R_2} \\
&= R_1 k_1 \left[F_{1,n} F'_{1,m} - F_{1,m} F'_{1,n} \right]_{R_1} + R_2 k_2 \left[F_{2,n} F'_{2,m} - F_{2,m} F'_{2,n} \right]_{R_2} - R_1 k_2 \left[F_{2,n} F'_{2,m} - F_{2,m} F'_{2,n} \right]_{R_1} \\
&= R_1 k_1 \left[F_{1,n} F'_{1,m} - F_{1,m} F'_{1,n} \right]_{R_1} - R_1 k_1 \left[F_{2,n} F'_{1,m} - F_{2,m} F'_{1,n} \right]_{R_1} + R_2 k_2 [F_{2,n}(-H_2 F_{2,m}) - F_{2,m}(-H_2 F_{2,n})]_{R_2} \\
&= R_1 k_1 [F'_{1,m}(F_{1,n} - F_{2,n}) - F'_{1,n}(F_{1,m} - F_{2,m})]_{R_1} + 0 \\
&= R_1 k_1 [(-H_C)(F_{1,m} - F_{2,m})(F_{1,n} - F_{2,n}) - (-H_C)(F_{1,n} - F_{2,n})(F_{1,m} - F_{2,m})]_{R_1} \\
&= 0
\end{aligned} \tag{D.7}$$

where the boundary conditions at $r = R_1$ and $r = R_2$ were used in the simplification. Thus, equation D.5 reduces to:

$$(\gamma_n^2 - \gamma_m^2) \cdot \sum_{i=1}^{2} \frac{k_i}{\kappa_i} \int_{r_{i-1}}^{r_i} r F_{i,n} F_{i,m} dr = 0 \tag{D.8}$$

from the latter, the generalised orthogonality relation 5.73 is directly obtained.

D.2 Proof of the integral identity 5.106

Given the integral on the left-hand side of eqn. 5.106, and assuming in a first instance the case $B_0(x) = J_0(x), Y_0(x)$, a partial integration is performed:

$$\int x B_0^2(\alpha x) dx = \frac{x^2}{2} B_0^2(\alpha x) - \int x^2 B_0(\alpha x) \cdot [-\alpha B_1(\alpha x)] dx \tag{D.9}$$

Then, the following identity for the Bessel functions $J(x)$, $Y(x)$ is used (see eqn. 17a,

pag 662, ref. (187)):

$$\frac{d}{dx}\left[x \cdot B_1(\alpha x)\right] = \alpha x \cdot B_0(\alpha x) \tag{D.10}$$

Hence, the right-hand side term of the eqn. D.9 can be rearranged to yield:

$$\begin{aligned} + \int \left[xB_1(\alpha x)\right] \cdot \left[\alpha x B_0(\alpha x)\right] \, dx &= \int \left[xB_1(\alpha x)\right] \cdot \frac{d}{dx}\left[xB_1(\alpha x)\right] \, dx \\ &= \frac{x^2 B_1^2(\alpha x)}{2} \end{aligned} \tag{D.11}$$

In the case of the $I_0(x)$, the D.9 becomes:

$$\int x I_0^2(\alpha x) dx = \frac{x^2}{2} \, I_0^2(\alpha x) - \int x^2 I_0(\alpha x) \cdot \left[\alpha I_1(\alpha x)\right] dx \tag{D.12}$$

Eqn. D.10 is also satisfied by $I_0(x)$, thus so is D.11:

$$+ \int \left[xI_1(\alpha x)\right] \cdot \left[\alpha x I_0(\alpha x)\right] \, dx = \frac{x^2 I_1^2(\alpha x)}{2} \tag{D.13}$$

Summarising, the results in the two cases is:

$$\int x B_0^2(\alpha x) dx = \begin{cases} \frac{x^2}{2}\left[B_0^2(\alpha x) + B_1^2(\alpha x)\right] & \text{for } B_0(x) = J_0(x), Y_0(x) \\ \frac{x^2}{2}\left[I_0^2(\alpha x) - I_1^2(\alpha x)\right] & \text{for } B_0(x) = I_0(x) \end{cases} \tag{D.14}$$

which concludes the demonstration.

Appendix E

Publications

Refereed Pubblications:

- M.N. Petrovich, F. De Monte, H.N. Rutt, "Analysis of heat flow in laser absorption calorimetry", *Int. J. Heat Mass Tran.*, in preparation.
- M.N. Petrovich, A Favre, D.W.Hewak, H.Rutt, A.C. Grippo, J.F. Gubeli III, K.C. Jordan, G.R. Neil, M.D. Shinn, "Near-IR absorption of *Ga:La:S* and *Ga:La:S:O* glasses by FEL-based laser calorimetry", *J. Non-cryst. Solids*, 2003, in print.
- A.K. Mairaj, M.N. Petrovich, Y.D. West, A. Fu, D.W. Harwood, L.N. Ng, T.M. Monro, N.G. Broderick, D.W. Hewak, "Advances in gallium lanthanum sulphide glass for optical fibre and devices", *SPIE Proceedings*, vol. 4204 (2001), 278.

Conference Presentations, Proceedings and other Publications:

- M.N. Petrovich, A. Favre, D.W.Hewak, H.Rutt, A.C. Grippo, J.F. Gubeli III, K.C. Jordan, G.R. Neil, M.D. Shinn, "Near-IR absorption of *Ga:La:S* and *Ga:La:S:O* glasses by FEL-based laser calorimetry", *International Symposium on Non-Oxide Glasses and New Optical Glasses (ISNOG XIX), Pardubice (Czech Republic) (2002).*
- K.M. Kiang, K. Frampton, T.M. Monro, M.N. Petrovich, R. Moore, J.H. Lee, Z. Yusoff, J. Tucknott, D.W. Hewak, H.N. Rutt, D.J. Richardson, "Extrusion of high nonlinearity single-mode holey optical fibers", *The American Ceramic Society, Glass & Optical Materials Division Fall Meeting, Pittsburgh (USA) (2002).*

- H.N. Rutt, M.N. Petrovich, M.D. Shinn, J.F. Gubeli III, K.C. Jordan, G.R Neil, "Calorimetric Measurement of near-IR optical absorption of *Ga:La:S* glass using JL-FEL", *LPC Meeting , Jefferson Lab, Newport News, VA, (USA) (2002).*

- M.N. Petrovich, H.N. Rutt, "The use of JL-FEL for near-IR absorbance measurements of *Ga:La:S* glasses", *Rank Prize Symposium on Applications of Free Electron Lasers, Grasmere (UK) (2001) (invited).*

- K.M. Kiang, A.K. Mairaj, M.N. Petrovich, D.W.Hewak, H.N.Rutt, "Photonic applications of sulphide glass optical fibres", *Photonics 2001, Glasgow (UK) (2001).*

- M.N. Petrovich, A.K. Mairaj, D.W. Hewak, H. N. Rutt, "Temperature dependence of reversible photodarkening in *Ga:La:S* and *Ga:La:S:O* glass fibres", *Proc. Int. Congr. Glass XIX, Edinburgh (UK) (2001), Vol.2, pag. 951.* Awarded the A.C. Owen Prize at the conference.

- D.W. Hewak, A.K. Mairaj, M.N. Petrovich, Y.D.West, "Application of novel glasses for the next generation of optical fibre devices", *Photonics 2000, Calcutta (2000) (invited).*

- A.K. Mairaj, M.N. Petrovich, D.J. Brady, D.H. Hewak, Y.D. West, T. Schweiz "Gallium lanthanum sulphide fibre for device fabrication in the infrared", *Photonics 2000, Manchester (UK) (2000).*

List of Figures

List of Tables

Bibliography

[1] R. Mears, L. Reekie, I. Jauncey, and D. Payne, "Low noise rare-earth doped fibre amplifier at 1.54 μm," *Electron. Lett.* **23**(19), pp. 1026–1028, 1987.

[2] G. Thomas, B. Shraiman, P. Glodis, and M. Stephens, "Towards the clarity limit in optical fibre," *Nature* **404**, pp. 262–264, 16 March 2000.

[3] A. Jha, X. Liu, A. Kar, and H. Bookey, "Inorganic glasses as Kerr-like media," *Curr. Opin. Solid State Mater. Sci.* **5**, pp. 475–479, 2001.

[4] V. Kokorina, *Glasses for infrared optics*, CRC Press, 2000.

[5] J. Sanghera and I. Aggarwal, *Infrared fiber optics*, CRC Press, 1998.

[6] D. Hewak, *Properties, processing and applications of glass and rare earth-doped glasses for optical fibres*, vol. 22 of *EMIS Datareviews Series*, INSPEC, 1998.

[7] H. Nasu, Y. Ibara, and K. Kubodera, "Optical third-harmonic generation from some high-index glasses," *J. Non-Cryst. Solids* **110**, pp. 229–234, 1989.

[8] C. Pedroso, E. Munin, A. Balbin Villaverde, J. Medeiros Neto, N. Aranha, and L. Barbosa, "High verdet constant $Ga{:}S{:}La{:}O$ chalcogenide glasses for magneto-optical devices," *Opt. Eng* **38**(2), pp. 214–219, 1999.

[9] I. Abdulhalim, C. Pannell, R. Deol, D. Hewak, G. Wylangowski, and D. Payne, "High performance acousto-optic chalcogenide glass based on Ga_2S_3-La_2S_3 systems," *J. Non-Cryst. Solids* **164&166**(2), pp. 1251–1254, 1993.

[10] G. Pfeiffer, M. Paesler, and S. Agarwal, "Reversible photodarkening of amorphous arsenic chalcogens," *J. Non-Cryst. Solids* **130**, pp. 111–143, 1990.

[11] K. Tanaka, "Photoinduced processes in chalcogenide glasses," *Curr. Opin. Solid State Mater. Sci.* **1**(4), pp. 567–571, 1996.

[12] Y. West, T. Schweizer, D. Brady, and D. Hewak, "Gallium lanthanum sulphide fibres for infrared transmission," *Fiber Integrated Opt.* **19**(3), pp. 229–250, 2000.

[13] P. France, *Fluoride glass optical fibres*, Blackie, 1989.

[14] R. Brückner, "Properties of vitreous silica," *J. Non-Cryst. Solids* **5**, pp. 123–175, 1970.

[15] N. Kapany and R. Simms, "Recent developments of infrared fiber optics," *Infrared Phys.* **5**, pp. 69–80, 1965.

[16] V. Kamensky, I. Scripachev, G. Snopatin, A. Pushkin, and M. Churbanov, "High power *As-S* glass fiber delivery instrument for pulsed YAG:*Er*," *Appl. Opt.* **37**(24), pp. 5596–5599, 1998.

[17] J. Sanghera and I. Aggarwal, "Active and passive chalcogenide glass optical fibres for IR applications: a review," *J. Non-Cryst. Solids* **256&257**, pp. 6–16, 1999.

[18] J. Sanghera, L. Shaw, L. Busse, V. Nguyen, J. Cole, R. Mossadegh, P. Pureza, R. Miklos, F. Kung, D. Talley, D. Roselle, and I. Aggarwal, "Infrared optical fibers and their applications," in *SPIE Proc. on Infrared Optical fibers and their applications*, **3849**, pp. 38–49, (Boston MA), 1999.

[19] V. Van Uitert and S. Wemple, "$ZnCl_2$ glass: a potential ultralow-loss optical material," *Appl. Phys. Lett.* **33**, pp. 57–59, 1978.

[20] S. Shibata, M. Horiguchi, K. Jinguji, S. Mitachi, T. Kanamori, and T. Manabe, "Prediction of loss minima in infra-red optical fibers," *Electron. Lett.* **17**(21), pp. 775–777, 1981.

[21] A. Vasilev, G. Devyatykh, E. Dianov, A. Guryanov, A. Lapter, V. Plotnichenko, Y. Pyrkov, G. Snopatin, I. Skripachev, M. Churbanov, and V. Shipunov, "Two-layer chalcogenide-glass optical fibers with optical losses below 30 dB/Km," *Quantum Electr.* **23**, pp. 89–90, 1993.

[22] J. Adam, "Lanthanides in non-oxide glasses," *Cem. Rev.* **102**(6), pp. 2461–2476, 2002.

[23] M. Asobe, "Nonlinear optical properties of chalcogenide glass fibres and their application to all-optical switching," *Opt. Fiber Technol.* **3**, pp. 142–148, 1997.

[24] A. Loireau-Lozac'h, M. Guittard, and J. Flahaut, "Verres formes par les sulfures L_2S_3 des terres rares avec le sulfure de gallium Ga_2S_3," *Mat. Res. Bull.* **11**(12), pp. 1489–1496, 1976.

[25] M. Guittard, , A. Loireau-Lozac'h, M. Pardo, and J. J. Flahaut, "Verres formes par le oxysulfures de terres rares Ln_2O_2S," *Mat. Res. Bul.* **13**(4), pp. 317–322, 1978.

[26] J. Flahaut, M. Guittard, and A. Loireau-Lozac'h, "Rare earth sulphide and oxysulphide glasses," *Glass Technol.* **24**, pp. 149–156, June 1983.

[27] M. Guittard, S. Jaulmes, A. Loireau-Lozac'h, A. Mazurier, F. Berguer, and J. Flahaut, "Etude du systeme La_2S_3-La_2O_3-Ga_2O_3-Ga_2S_3: description structurale des phases quaternaires et approche du diagramme de phase," *J. Solid State Chem.* **58**, pp. 276–289, 1985.

[28] M. Guittard, A. Loireau-Lozac'h, F. Berguer, S. Barnier, and J. Flahaut, "Verres du systeme La_2S_3-La_2O_3-Ga_2O_3-Ga_2S_3.," *J. Solid State Chem.* **62**, pp. 191–198, 1986.

[29] B. Cervelle, S. Jaulmes, P. Laruelle, and A. Loireau-Lozac'h, "Variation, avec la composition, des indices de refraction des verres de sulfures de lanthane et de gallium et indices de quelques verres apparentes," *Mat. Res. Bull.* **15**(2), pp. 159–164, 1980.

[30] G. Lucazeau, M. Barnier, and A. Loireau-Lozac'h, "Spectres vibrationnels, transitions electroniques et structures a courtes distances dans le verres: sulfures de terres rares - sulfure de gallium," *Mat. Res. Bull.* **12**, pp. 437–448, 1977.

[31] S. Benazeth, M. Tulier, A. Loireau-Lozac'h, H. Dexpert, P. Lagarde, and J. Flahaut, "An EXAFS structural approach of the lanthanum-gallium-sulphur glasses," *J. Non-Cryst. Solids* **110**, pp. 89–100, 1989.

[32] R. Reisfeld, A. Bornstein, J. Flahaut, M. Guittard, and Loireau-Lozac'h, "Absorption and fluorescence of Ho^{3+} in $La_2S_3 \cdot 3Ga_2S_3$," *Chem. Phys. Lett.* **47**, pp. 408–410, 1977.

[33] R. Reisfeld and A. Bornstein, "Absorption and emission spectra in chalcogenide glass of the composition $0.7Ga_2S_3 \cdot 0.27La_2S_3 \cdot 0.03Nd_2S_3$," *Chem. Phys. Lett.* **47**, pp. 194–196, 1977.

[34] R. Reisfeld and A. Bornstein, "Fluorescence of Er^{3+} doped $3La_2S_3 \cdot Ga_2S_3$ glasses," *J. Non-Cryst. Solids* **27**, pp. 143–145, 1978.

[35] A. Bornstein and R. Reisfeld, "Laser emission cross-section and threshold power for laser operation at 1077 and 1374 *nm*: chalcogenide mini-lasers doped with Nd^{3+}," *J. Non-Cryst. Solids* **50**(1), pp. 23–27, 1982.

[36] P. Kumta and S. Risbud, "Rare-earth chalcogenides: an emerging class of optical materials," *J. Mater. Sci.* **29**, pp. 1135–1158, 1994.

[37] P. Kumta and S. Risbud, "Novel glasses in rare-earth sulfide systems," *Am. Ceram. Soc. Bull.* **69**(12), pp. 1977–1984, 1990.

[38] P. Becker, M. Broer, V. Lambrecht, A. Bruce, and G. Nykolak, "Pr^{3+}:*La-Ga-S* glass: a promising material for 1.3 μm fiber amplfication," in *Proc. OSA Topical Meeting on Optical Amplifiers and Their Applications, Technical Digest*, **17, paper PD-5**, pp. 20–23, (Washington, DC), 1992.

[39] P. Becker, A. Bruce, D. DiGiovanni, and V. Lambrecht Jr., "Optical fiber amplifier and a glass therefor." US Patent Appl. n. 5,378,664, 1993.

[40] B. Aitken and M. Newhouse, "Gallium sulfide glasses." US Patent Appl. n. 5,392,376, 1994.

[41] D. Hewak, J. Medeiros-Neto, B. Samson, R. Brown, P. Jedrzejewshi, J. Wang, E. Taylor, R. Laming, G. Wylangowski, and D. Payne, "Quantum efficiency of praseodymium doped *Ga:La:S* glass for 1.3 μm optical fibre amplifiers," *IEEE Phot. Technol. Lett.* **6**(5), pp. 609–612, 1994.

[42] B. Samson, T. Schweizer, R. Laming, D. Hewak, and D. Payne, "Properties of dysprosium-doped gallium lanthanum sulphide fiber amplifiers operating at 1.3 μm," *Opt. Lett.* **22**(10), pp. 703–705, 1997.

[43] D. Hewak, R. Laming, D. Payne, and B. Samson, "Doped optical waveguide amplifier." US Patent Appl. n. 5,936,762, April 1994.

[44] D. Hewak, R. Moore, T. Schweizer, J. Wang, B. Samson, W. Brocklesby, D. Payne, and E. Tarbox, "Gallium lanthanum sulphide optical fibre for active and passive applications," *Electron. Lett.* **32**(4), pp. 384–385, 1996.

[45] T. Schweizer, D. Hewak, D. Payne, T. Jensen, and G. Huber, "Rare-earth doped chalcogenide glass laser," *Electron. Lett.* **32**(7), pp. 666–667, 1996.

[46] T. Schweizer, B. Samson, R. Moore, D. Hewak, and D. Payne, "Rare-earth doped chalcogenide glass fibre laser," *Electron. Lett.* **33**(5), pp. 414–416, 1997.

[47] D. Gill, R. Eason, C. Zaldo, H. Rutt, and N. Vainos, "Characterisation of Ga-La-S chalcogenide glass thin-film optical waveguides fabricated by pulsed laser deposition," *J. Non-Cryst. Solids* **191**, pp. 321–326, 1995.

[48] R. Li, D. Furniss, H. Bagshow, and A. Seddon, "The decisive role of oxide content in the formation and crystallisation behaviour of gallium-lanthanum-sulphide glasses," *J. Mater. Res.* **14**(6), pp. 2621–2627, 1999.

[49] D. Furniss and A. Seddon, "Extrusion of gallium lanthanum sulfide glass for fiber-optic preforms," *J. Mater. Sci. Lett.* **17**, pp. 1541–1542, 1998.

[50] T. Schweizer, *Rare-earth doped Gallium Sulfide glasses for mid-infrared fibre lasers.* PhD thesis, Optoelectronics Research Centre, University of Southampton, 1998.

[51] D. Brady, *Gallium sulphide based glasses for mid-infrared optical fibres.* PhD thesis, Optoelectronics Research Centre, University of Southampton, 1999.

[52] Z. Zhou, H. Nasu, T. Hashimoto, and K. Kamiya, "Third-order nonlinear optical properties of sulfide glasses La_2S_3-Ga_2S_3 binary and MS-La_2S_3-Ga_2S_3 ($MS = PbS$, Ag_2S and Na_2S) ternary glasses," *J. Ceram. Soc. Jpn.* **105**, pp. 1079–1085, December 1997.

[53] S. Smolorz, I. Kang, F. Wise, B. Aitken, and B. N.F., "Studies of optical nonlinearities of chalcogenide and heavy-metal oxide glasses," *J. Non-Cryst. Solids* **256&257**, pp. 310–317, 1999.

[54] J. Requejo-Isidro, A. Mairaj, V. Pruneri, D. Hewak, M. Netti, and J. Baumberg, "Self refractive nonlinearities in chalcogenide based glasses," *J. Non-Cryst. Solids* **317**, pp. 241–246, 2003.

[55] T. Monro, Y. West, D. Hewak, N. Broderick, and D. Richardson, "Chalcogenide holey fibres," *Electron. Lett.* **36**(24), pp. 1998–2000, 2000.

[56] J. Knight, T. Birks, P. Russell, and D. Atkin, "All-silica single-mode optical fibres with photonic crystal cladding," *Opt. Lett.* **21**, pp. 1547–1549, 1996.

[57] A. Siegman, *Lasers*, University Science, 1990.

[58] O. Svelto, *Principles of lasers*, Plenum, New York, 2nd edition ed., 1982.

[59] L. Riseberg and M. Weber, *Progress in optics.* E.Wolf ed., 1976.

[60] C. Layne, W. Lowdermilk, and M. Weber, "Multiphonon relaxation of rare-earth ions in oxide glasses.," *Phys. Rev. B* **16**(1), pp. 10–20, 1977.

[61] H. Toratani, T. Izumitani, and H. Kuroda, "Compositional dependence of nonradiative decay rate in Nd laser glasses," *J. Non-Cryst. Solids* **52**, pp. 303–313, 1982.

[62] Y. Durteste, M. Monerie, J. Allain, and H. Poignant, "Amplification and lasing at 1.3 μm in a praseodymium doped fluorozirconate fibre," *Electron. Lett.* **27**(8), pp. 626–628, 1991.

[63] Y. Miyajma, T. Sugawa, and Y. Fukasaku, "38.2 dB amplification at 1.3 μm and possibility of 0.98 μm pumping in Pr^{3+} doped fluoride fibres," *Electron. Lett.* **27**(19), pp. 1706–1707, 1991.

[64] Y. Ohishi, T. Kanamori, M. Shimizu, M. Yamada, Y. Terunuma, J. Temmyo, M. Wada, and S. Sudo, "Praseodymium-doped fiber amplifiers at 1.3 μm," *IEICE Trans. Commun.* **E77-B**, pp. 421–440, 1994.

[65] M. Shimizu, M. Yamada, M. Horiguchi, and T. Takeshita, "Erbium-doped fiber amplifiers with an extremely high gain coefficient of $11dB/m$," *Electron. Lett.* **26**, pp. 1641–1642, 1990.

[66] R. Reisfeld, "Fluorescence and nonradiative relaxations of rare earths in amorphous media and on high surface area supports: a review," *J. Electrochem. Soc.* **131**(6), pp. 1360–1364, 1984.

[67] R. Reisfeld, M. Eyal, and C. Jørgensen, "Comparison of laser properties of rare earths oxide and fluoride glasses," *J. Less-common Met.* **126**, pp. 187–194, 1986.

[68] D. Hewak, R. Deol, J. Wang, G. Wylangowski, J. Medeiros Neto, B. Samson, R. Laming, W. Brocklesby, D. Payne, A. Jha, M. Poulain, S. Otero, S. Surinach, and M. Baro, "Low phonon-energy glasses for efficient 1.3 μm optical fibre amplifiers," *Electron. Lett.* **29**(2), pp. 237–239, 1993.

[69] E. Taylor, B. Samson, D. Hewak, J. Medeiros Neto, D. Payne, S. Jordery, M. Naftaly, and A. Jha, "Cadmium mixed halide glass for optical amplification at 1.3 μm," *J. Non-Cryst. Solids* **184**, pp. 61–67, 1995.

[70] B. Dussardier, D. Hewak, B. Samson, H. Tate, J. Wang, and D. Payne, "Pr^{3+}-doped $Cs{:}Ga{:}S{:}Cl$ glass for efficient 1.3 μm optical fibre amplifiers," *Electron. Lett.* **31**(3), pp. 206–208, 1995.

[71] A. Van Osch, "Modelling of praseodymium-doped fluoride and sulfide fibre amplifiers for the wavelength region," tech. rep., EUT Report 95-E-294, 1995.

[72] M. Digonnet, "Closed-form expressions for the gain in three- and four-level laser fibers," *IEEE J. Quantum Electron.* **26**(10), pp. 1788–1796, 1990.

[73] P. Urquhart, "Praseodymium-doped fibre amplifiers: theory of 1.3 μm operation," *IEEE J. Quantum Electron.* **28**(10), pp. 1962–1965, 1992.

[74] C. Barnard, P. Myslinski, J. Chrostawski, and M. Kavehrad, "Analytical model for rare-earth doped fiber amplifiers and lasers," *IEEE J. Quantum Electron.* **30**(8), pp. 1817–1830, 1994.

[75] M. Dakss and W. Miniscalco, "A large signal and signal/noise ratio analysis for Nd^{3+}-doped fibre amplifiers at 1.3 μm," *SPIE Proc.* **1373**, pp. 111–124, 1990.

[76] E. Desurvire, *Erbium-doped fiber amplifiers*, Wiley-Interscience, 1994.

[77] R. Quimby and B. Aitken, "Effect of population bottlenecking in Pr fibre amplifiers with low phonon energy hosts," *IEEE Phot. Technol. Lett.* **11**(3), pp. 313–315, 1999.

[78] H. Yanagita, K. Itoh, E. Ishikawa, H. Aoki, and H. Toratani, "26 dB amplification at 1.31 μm in a novel $Pr^{3+}-$doped InF_3/GaF_3-based fibre," in *Proceedings OFC 1995*, **8 (Technical digest)** , pp. 331–334, (San Diego CA), 1995.

[79] R. Bartholomew, B. Aitken, and M. Newhouse, "Praseodymium-doped cadmium mixed halide glasses for 1.3 μm optical amplification," *J. Non-Cryst. Solids* **184**, pp. 229–233, 1995.

[80] K. Wei, D. Machewirth, J. Wenzel, E. Snitzer, and G. Sigel Jr., "$Pr^{3+}-$doped *Ge-Ga-S* for 1.3 μm fibre amplifiers," *J. Non-Cryst. Solids* **182**, pp. 257–261, 1995.

[81] H. Tawarayama, E. Ishikawa, K. Itoh, H. Aoki, H. Yanagita, K. Okada, K. Yamanaka, Y. Matsuoka, and H. Toratani, "Efficient amplification at 1.3 μm in a $Pr^{3+}-$doped *Ga-Na-S* fiber," in *Optical amplifiers and their applications OSA topical meeting*, pp. 141–143, 1997.

[82] K. Itoh, H. Yanagita, H. Tawarayama, K. Yamanaka, E. Ishikawa, K. Okada, H. Aoki, A. Shirakawa, Y. Matsuoka, and H. Toratani, "Pr^{3+} doped InF_3:GaF_3 based fluoride glass fibers and *Ga-Na-S* glass fibers for light amplification around 1.3 μm," *J. Non-Cryst. Solids* **256&257**, pp. 1–5, 1999.

[83] M. Schefler, J. Kirchhof, J. Kobelke, K. Schuster, and A. Schwuchow, "Increased rare-earth solubility in *As-S* glass," *J. Non-Cryst. Solids* **256&257**, pp. 59–62, 1999.

[84] V. Krasteva, D. Machewirth, and G. Siegel Jr., "$Pr^{3+}-$doped *Ge-S-I* glasses as candidate materials for 1.3 μm amplification," *J. Non-Cryst. Solids* **213&214**, pp. 304–310, 1997.

[85] Y. Ohishi, A. Mori, T. Kanamori, K. Fujiura, and S. Sudo, "Fabrication of praseodymium-doped arsenic sulfide chalcogenide fiber for 1.3 μm fiber amplifiers," *Appl. Phys. Lett.* **65**(1), pp. 13–15, 1994.

[86] B. Aitken and R. Quimby, "Rare-earth doped multicomponent ge-based sulphide glass," *J. Non-Cryst. Solids* **213&214**, pp. 281–287, 1997.

[87] J. Kobelke, J. Kirchhof, M. Scheffler, and A. Schwuchow, "Chalcogenide glass single mode fibres-preparation and properties," *J. Non-Cryst. Solids* **256&257**, pp. 226–231, 1999.

[88] S. Davey, D. Szebesta, R. Wyatt, W. Jordan, and A. Jha, "Properties of novel glasses for the optimisation of $Pr-$doped fluoride amplifiers," *SPIE Proceedings* **2073**, pp. 118–126, 1993.

[89] D. Brady, T. Schweizer, J. Wang, and D. Hewak, "Minimum loss predictions and measurements in gallium lanthanum sulphide based glasses and fibre," *J. Non-Cryst. Solids* **242**(2–3), pp. 92–98, 1998.

[90] D. Wood and J. Tauc, "Weak absorption tails in amorphous semiconductors," *Phys. Rev. B* **5**(8), pp. 3144–3151, 1972.

[91] J. Wang, J. Hector, D. Brady, D. Hewak, W. Brocklesby, M. Kluth, R. Moore, and D. Payne, "Halide-modified *Ga-La* sulphide glasses with improved fibre-drawing and optical properties for $Pr^{3+}-$doped fiber amplifiers at 1.3 μm," *Appl. Phys. Lett.* **71**, pp. 1753–1755, 1997.

[92] D. Hewak. EPSRC Longwave Project progress report, 1997.

[93] J. Hector, D. Hewak, J. Wang, R. Moore, and W. Brocklesby, "Quantum-efficiency measurements in oxygen-containing gallium lanthanum sulphide glasses and fibers doped with Pr^{3+}," *IEEE Phot. Technol. Lett.* **9**, pp. 443–445, April 1997.

[94] R. Brown, W. Brocklesby, D. Hewak, and B. Samson, "The effect of oxide on the spectroscopic properties of the praseodymium 1.3 μm transition in gallium-lanthanum-sulphide glass," *J. Lumin.* **66&67**, pp. 278–284, December 1996.

[95] B. Samson, D. Hewak, R. Laming, D. Payne, and W. Brocklesby, "Optical waveguide, waveguide amplifier and laser." US Patent n. 6,226,308, 1996.

[96] Y. Ohishi, T. Kanamori, T. Kitagawa, S. Takahashi, E. Snitzer, and G. Sigel Jr., "$Pr^{3+}-$doped fluoride fibre amplifier operating at 1.31 μm," in *Proc. OFC 1991*, p. PDP2, (San Diego CA), 1991.

[97] S. Carter, D. Szebesta, S. Davey, R. Wyatt, M. Brierley, and P. France, "Amplification at 1.3 μm in a $Pr^{3+}-$doped single-mode fluorozirconate fibre," *Electron. Lett.* **27**(8), pp. 628–629, 1991.

[98] T. Whitley, R. Wyatt, D. Szebesta, and S. Davey, "Towards a practical optical fibre amplifier," *Br. Telecom Technol. J.* **11**(2), pp. 115–127, 1993.

[99] H. Yamada, M. Shimizu, Y. Ohishi, J. Temmyo, M. Wada, T. Kanamori, and S. Sudo, "One-LD-pumped $Pr^{3+}-$doped fluoride fiber amplifier module with a signal gain of 23 dB," in *Tech. Digest of topical meeting on optical amplifiers and their applications*, pp. TuA1 240–243, Optical Society of America, (Washington DC), 1993.

[100] NTT Electric Corporation,, "www.nel-wdm.com."

[101] H. Yamada, M. Shimizu, Y. Ohishi, T. Kanamori, M. Horiguchi, S. Takahashi, J. Temmyo, and M. Wada, "15.1-dB-gain doped fluoride fiber amplifier pumped by high power laser modules.," in *Proc. ECOC '92 Vol. Mo A2*, pp. 49–52, (Berlin, Germany), 1992.

[102] M. Palazzi, "Study of the system Ga_3Na_2. existence of a glass-former region," *C.R. Acad. Sci. (Series II)* **299**(9), pp. 529–532, 1984.

[103] R. Li, D. Furniss, H. Bagshow, and A. Seddon, "Effects of the oxide content on the glass-forming ability of the Ga_2S_3-Na_2S_3 system," *J. Am. Ceram. Soc.* **81**(12), pp. 3353–3356, 1998.

[104] W. Miniscalco, L. Andrews, and B. Thompson, "1.3 μm fluoride fibre laser," *Electron. Lett.* **24**(1), pp. 28–29, 1988.

[105] M. Dakss and W. Miniscalco, "Fundamental limits on Nd^{3+}–doped fiber amplifier performance at 1.3 μm," *IEEE Phot. Technol. Lett.* **2**(9), pp. 650–652, 1990.

[106] E. Taylor, B. Samson, M. Naftaly, A. Jha, and D. Payne, "A 1300 nm Nd^{3+}-doped glass amplifier," in *Proc. ECOC 1998*, p. paper MoA09, ECOC'98, (Madrid, Spain), 1998.

[107] D. Harwood, *Towards a 1.31 μm planar neodymium doped fluoride glass waveguide amplifier.* PhD thesis, University of Southampton, Southampton, 2000.

[108] T. Sugawa, Y. Miyama, and T. Komukai, "10 dB gain and high saturation power in a Nd^{3+}–doped fluorozirconate fibre amplifier," *Electron. Lett.* **26**(24), pp. 2042–2044, 1990.

[109] D. Harwood, A. Fu, E. Taylor, R. Moore, Y. West, and D. Payne, "A 1317 nm neodymium doped fluoride glass waveguide laser," in *Proc. ECOC 2000*, paper 6.4.8 2000.

[110] A. Mori, Y. Ohishi, T. Kanamori, and S. Sudo, "Optical amplification with neodymium-doped chalcogenide glass fiber," *Appl. Phys. Lett.* **70**(10), pp. 1230–1232, 1997.

[111] D. Hewak, B. Samson, J. Medeiros Neto, R. Laming, and D. Payne, "Emission at 1.3 μm from dysprosium-doped Ga:La:S glass," *Electron. Lett.* **30**(12), pp. 968–969, 1994.

[112] K. Wei, D. Machewirth, J. Wenzel, E. Snitzer, and G. Sigel Jr., "Spectroscopy of Dy^{3+} in *Ge-Ga-S* glass and its suitability for 1.3-μm fiber-optical amplifier applications," *Opt. Lett.* **19**(12), pp. 904–906, 1994.

[113] B. Cole, L. Shaw, P. Pureza, R. Mossadegh, J. Sanghera, and I. Aggarwal, "Rare-earth doped selenide glasses and fibers for active applications in the near and mid-IR," *J. Non-Cryst. Solids* **256&257**, pp. 253–259, 1999.

[114] J. Heo, "Rare-earth doped chalcogenide glasses for wide-band fiber-optic amplifiers," in *Proc. ISNOG XIII Int. Symposium on non-oxide glasses and new optical glasses, Vol. 2*, pp. 467–473, (Pardubice (Czech Republic)), 2002.

[115] B. Samson, D. Hewak, R. Laming, and D. Payne, "Doped optical waveguide amplifier." US Patent n. 5,936,762, 1995.

[116] T. Schweizer, R. Goutaland, D. Martins, E.and Hewak, and W. Brocklesby, "Site-selective spectroscopy in dysprosium-doped chalcogenide glasses for 1.3 μm optical-fiber amplifiers," *J. Opt. Soc. Am. B* **18**(10), pp. 1436–1442, 2001.

[117] S. Tanabe, "Optical transitions of rare earth ions for amplifiers: how the local strusture works in a glass," *J. Non-Cryst. Solids* **259**, pp. 1–9, 1999.

[118] R. Stolen and E. Ippen, "Raman gain in glass optical waveguides," *Appl. Phys. Lett.* **22**(6), pp. 276–278, 1973.

[119] J. Auyeung and A. Yariv, "Spontaneous and stimulated raman scattering in low loss fibers," **QE-14**(5), pp. 347–352, 1978.

[120] M. Islam, "Raman amplification for telecommunications," *IEEE J. Sel. Top. Quant.* **8**(3), pp. 548–559, 2002.

[121] D. Gapontsev, S. Chernikov, and J. Taylor, "Fibre raman amplifiers for broadband operation at 1.3 μm," *Opt. Commun.* **166**, pp. 85–88, 1999.

[122] P. Thijs, L. Tiemeijer, J. Binsma, and T. van Dongen, "Progress in long-wavelength strained-layer $InGaAs(P)$ quantum-well semiconductor lasers and amplifiers," **30**(2), pp. 477–499, 1994.

[123] J. Bernard and M. Renaud, "Semiconductor optical amplifiers," *SPIE OE Magazine* , september 2001.

[124] S. Freiberg and P. Smith, "Nonlinear optical glasses for ultrafast optical switches," *IEEE J. Quantum Electron.* **QE-23**(12), pp. 2089–2094, 1987.

[125] S. Friberg, Y. Silberberg, M. Oliver, M. Andrejco, M. Saifi, and P. Smith, "Ultrafast all-optical switching in a dual-core fibre nonlinear coupler," *Appl. Phys. Lett.* **51**, pp. 1135–1137, 1987.

[126] S. Kawanishi, H. Takara, K. Uchiyama, M. Saruwatari, and T. Kitoh, "Fully time-division-multiplexed 100 *Gbit/s* optical transmission experiment," *Electron. Lett.* **29**, pp. 2211–12, 1993.

[127] E. Vogel, "Glasses as nonlinear photonic materials," *J. Am. Ceram. Soc.* **72**(5), pp. 719–724, 1989.

[128] N. Boling, A. Glass, and A. Owyoung, "Empirical relationships for predicting nonlinear refractive index changes in optical solids," *IEEE J. Quantum Electron.* **QE-14**, pp. 601–608, 1978.

[129] C. Wang, "Empirical relation between the linear and the third-order nonlinear susceptibilities," *Phys. Rev. B* **2**, pp. 2045–2048, 1970.

[130] M. Lines, "Oxide glasses for fast photonic switching: a comparative study.," *J. Appl. Phys.* **69**, pp. 6876–6884, 1991.

[131] C. Quemard, F. Smektala, V. Couderc, A. Barthelemy, and J. Lucas, "Chalcogenide glasses with high nonlinear optical properties for telecommunications," *J. Phys. Chem. Solids* **62**, pp. 1435–1440, 2001.

[132] J. Harbold, F. Wise, and B. Aitken, "Se-based chalcogenide glasses 1000 times more nonlinear than fused silica," in *Technical Digest, Conference on Lasers and Electro-Optics (CLEO 2001)*, pp. 14–15, (Washington, DC), 2001.

[133] V. Mizrahi, K. DeLong, G. Stegeman, M. Saifi, and M. Andrejco, "Two-photon absorption as a limitation to all-optical switching," *Opt. Lett.* **14**(20), pp. 1140–1142, 1989.

[134] M. Sheik-Bahae, D. Crichton Hutchings, D. Hagan, and E. Van Stryland, "Dispersion of bound electronic nonlinear refraction in solids," *IEEE J. Quantum Electron.* **27**(6), pp. 1296–1309, 1991.

[135] L. Canioni, M. Martin, B. Bousquest, and L. Sarger, "Precise measurements and analysis of linear and nonlinear optical properties of glass materials near 1.5 μm," *Opt. Commun.* **151**, pp. 241–246, 1998.

[136] D. Hall, M. Newhouse, N. Borrelli, W. Dumbaugh, and D. Weidman, "Nonlinear optical susceptibilities of high-index glasses," *Appl. Phys. Lett.* **54**, pp. 1293–1295, 1989.

[137] K. Bindra, H. Bookey, A. Kar, B. Wherret, X. Liu, and A. Jha, "Nonlinear optical absorption properties of chalcogenide glasses: observation of multi-photon absorption," *Appl. Phys. Lett.* **79**(19), pp. 1939–1941, 2001.

[138] N. Sugimoto, H. Kanbara, S. Fujiwara, K. Tanaka, Y. Shimizugawa, and K. Hirao, "Third-order optical nonlinearities and thier ultrafast response in Bi_2O_3-B_2O_3-SiO_2 glasses," *J. Opt. Soc. Am.* **B16**(11), pp. 1904–1908, 1999.

[139] K. Cerqua-Richardson, J. McKinley, B. Lawrence, S. Joshi, and A. Villenevue, "Comparison of nonlinear optical properties of sulfide glasses in bulk and thin film form," *Opt. Mater.* **10**, pp. 155–159, 1998.

[140] J. Harbold, F. Ilday, F. Wise, J. Sanghera, V. Nguyen, L. Shaw, and I. Aggarwal, "Highly nonlinear *As-S-Se* glasses for all-optical switching," *Opt. Lett.* **27**(2), pp. 119–121, 2002.

[141] J. Harbold, F. Ilday, F. Wise, and B. Aitken, "Highly nonlinear *Ge-As-Se* and *Ge-As-S-Se* glasses for all-optical switching," *IEEE Phot. Technol. Lett.* **14**(6), pp. 822–824, 2002.

[142] G. Lenz, J. Zimmermann, K. T., M. Lines, H. Hwang, S. Spälter, R. Slusher, S. Cheong, J. Sanghera, and I. Aggarwal, "Large kerr effect in bulk *Se*–based chalcogenide glasses," *Opt. Lett.* **24**(4), pp. 254–256, 2000.

[143] A. Belykh, O. Efimov, L. Glebov, Y. Matveev, A. Mkryukov, M. Mikhailov, and K. Richardson, "Photo-structural transformation of chalcogenide glasses under non-linear absorption of laser radiation," *J. Non-Cryst. Solids* **213&214**, pp. 330–335, 1995.

[144] K. Kikuchi, K. Taira, and N. Sugimoto, "Highly nonlinear bismuth oxide-based glass fibres for all-optical signal processing," *Electron. Lett.* **38**(4), pp. 166–167, 2002.

[145] M. Onishi, T. okuno, S. Ishikawa, N. Akasaka, and M. Nishimura, "Highly nonlinear dispersion shifted fiber and its application to broadband wavelength converters.," in *Proc. ECOC-IOOC '97*, p. paper TU2C, (Edinburgh, UK), 1997.

[146] T. Monro, K. Furusawa, J. Lee, J. price, Z. Yusuff, J. Baggett, and D. Richardson, "Advances in holey fibres," in *Photonics West*, (San Francisco), 2003.

[147] T. Monro, K. Kiang, J. Lee, K. Frampton, Z. Yusoff, R. Moore, J. Tucknott, D. Hewak, H. Rutt, and D. Richardson, "High nonlinearity extruded single-mode holey optical fibers," in *Proc. OFC '02*, (Anaheim), 2002.

[148] M. Asobe, T. kanamori, and K. kubodera, "Applications of highly nonlinear chalcogenide fibres in ultrafast all-optical switches," *IEEE J. Quantum Electron.* **29**(8), pp. 2325–2333, 1993.

[149] S. Benazeth, M. Tulier, H. Dexpert, M. Guittard, and D. Carre, "Chaclogenide and oxichalcogenide glasses: evolution of the gallium surrounding with the oxigen content," *J. Phys.-Paris* **47**(12,C8), pp. C8–419–C8–422, 1986.

[150] M. Scheffler, J. Kirchhof, J. Kobelke, K. Schuster, and A. Schwuchow, "Optical and thermal properties of rare earth containing low phonon energy glasses," *SPIE Proc.* **3416**, pp. 89–98, 1998.

[151] M. Guittard, P. Fourcroy, J. Flahaut, and A. Chilouet, "Etude du systeme La_2S_3-Al_2S_3. diagramme de phase-verres, preparation, mechanisme de recrystallisation," *Ann. Chim.* **1**, pp. 47–53, 1976.

[152] J. Wang, D. Hewak, W. Brocklesby, and D. Payne, "Mofification of binary Ga_2S_3-La_2S_3 glass by the addition of a thord component," in *Proc. of the 10th international symposium on non-oxide glasses*, pp. 8–13, (Corning NY), 1996.

[153] K. Kadono, H. Higuchi, M. Takahashi, Y. Kawamoto, and H. Tanaka, "Upconversion luminescence of Ga_2S_3-based sulfide glasses containing Er^{3+} ions," *J. Non-Cryst. Solids* **184**, pp. 309–13, 1995.

[154] "GOAL PROJECT - glasses for amplifiers and lasers," 1992-1994.

[155] "LONGWAVE Project - LINK Photonics Programme," 1997–1999.

[156] R. Li and A. Seddon, "Gallium-lanthanum-sulfide glasses: a review of the recent crystallisation studies," *J. Non-Cryst. Solids* **256&257**, pp. 17–24, 1999.

[157] E. Mamolejo, E. Granado, O. Alves, C. Cesar, and L. Barbosa in *Proceedings of the XVIII International Congress on Glass*, pp. 34–38, (San Francisco), 1998.

[158] S. Morgan, D. Furniss, and A. Seddon, "Lanthanum fluoride addition to gallium-lanthanum-sulphide glasses," *J. Non-Cryst. Solids* **203**, pp. 135–142, 1996.

[159] "www.webelements.com."

[160] J. Goodyear and G. Steigmann, "The crystal structure of α-Ga_2S_3," *Acta Cryst.* **16**, pp. 946–949, 1963.

[161] A. Kuhn and A. Chevy, "Refinement of the 2H *GaS* β-type," *Acta Cryst.* **B32**, pp. 983–984, 1975.

[162] R. Jenkins and R. Snyder, *Introduction to X-Ray Powder Diffractometry*, Wiley, 1996.

[163] A. Clare, "Structure and properties of rare earth gallium sulfide glasses," *Key. Eng. Materials* **94&95**, pp. 81–108, 1994.

[164] J. Wang, "Glass viscosity and structural relaxation by parallel plate rheometry using a thermal mechanical analyser," *Mater. Lett.* **31**, pp. 99–103, 1997.

[165] S. Wilson and D. Poole, "Glass viscosity measurements by parallel plate rheometry," *Mater. Res Bull.* **25**(1), pp. 113–118, 1990.

[166] M. Weinberg, "An assesment of glass stability criteria," *Phys. Chem. Glasses* **35**(3), pp. 119–123, 1994.

[167] S. Morgan, I. Reaney, R. Buckley, D. Furniss, and A. Seddon, "Crystallization of gallium lanthanum sulfide glasses," *J. Am. Ceram. Soc.* **81**(7), pp. 1913–1918, 1998.

[168] I. Reaney, S. Morgan, R. Li, and A. Seddon, "Transmission electron microscopy studies of $70Ga_2S_3$-$30La_2S_3$," *J. Non-Cryst. Solids* **256&257**, pp. 149–153, 1999.

[169] E. Dianov, V. Shiryaev, A. Izyneev, G. Plotnichenko, and M. Churbanov, "Crystallization kinetics of praseodymium-doped $(Ga_2S_3)_{0.7}(La_2S_3)_{0.3}$ glass," *Inorg. Mater.* **33**(9), pp. 975–977, 1997.

[170] H. Takebe, D. Brady, D. Hewak, and K. Morinaga, "Thermal properties of Ga_2S_3-based glasses and their consideration during fibre drawing," *J. Non-Cryst. Solids* **258**, pp. 239–243, 1999.

[171] E. Roeder, "Extrusion of glass," *J. Non-Cryst. Solids* **5**, pp. 377–388, 1970.

[172] R. Driver, G. Leskovitz, L. Curtiss, D. Moynihan, and L. Vacha, "The characterisation of infrared transmitting optical fibres," *Mat. Res. Soc. Symp. Proc.* **172**(6), pp. 169–175, 1990.

[173] A. Borghesi and G. Guizzetti, *Handbook of optical constants of solids II*, ch. 4, Graphite. Academic Press, E.D. Palik (ed) ed., 1991.

[174] D. Pinnow and T. Rich, "Development of a calorimetric method for making precise optical absorption measurements," *Appl. Opt.* (5), pp. 984–992, 1973.

[175] U. Willamowski, T. Gross, D. Ristau, and H. Welling, "Calorimetric measurement of optical absorption and transmissivity with sub ppm sensitivity," in *Proc. specification, production and testing of optical components and systems*, pp. 148–158, (Glasgow, UK), 1996.

[176] T. Rich and D. Pinnow, "Total optical attenuation in bulk fused silica," *Appl. Phys. Lett.* **20**(7), pp. 264–266, 1972.

[177] ISO 11551, "Test method for absorbance of optical laser components." International Organisation for Standardization, Geneve, Switzerland, 1997.

[178] A. O'Keefe and D. Deacon, "Cavity ringdown optical spectrometer for absorption measurements using pulsed laser sources," *Rev. Sci. Instrum.* **59**(12), pp. 2544–2551, 1988.

[179] A. Boccara, D. Fournier, W. Jackson, and N. Amer, "Sensitive photothermal deflection technique for measuring absorption in optically thin media.," *Opt. Lett.* **5**(9), pp. 377–379, 1980.

[180] M. Baesso, J. Shen, and R. Snook, "Mode-mismatched thermal lens determination of temperature coefficient of optical path length in soda lime glass at different wavelengths," *J. Appl. Phys.* **75**(8), pp. 3732–3737, 1994.

[181] A. Ångström *Philos. Mag.* **25**, p. 130, 1863.

[182] P. Sidles and G. Danielson, "Thermal diffusivity of metals at high temperature," *J. Appl. Phys.* **25**(1), pp. 58–66, 1954.

[183] G. R. Niel, S. Benson, G. Biallas, J. Gubeli, K. Jordan, S. Myers, and M. Shinn, "Second harmonic FEL oscillation," *Phys. Rev. Lett.* **87**(8), pp. 084801-1–4, 2001.

[184] B. Steiger, U. Pfeifer, P. Meja, U. Broulik, and V. Neumann, "Practicability of absorption measurements according to ISO/DIS 115511," *SPIE Proceedings* **2870**, pp. 495–501, 1996.

[185] E. Bernal, "Heat flow analysis of laser absorption calorimetry," *Appl. Opt.* **14**(2), pp. 314–321, 1975.

[186] U. Willamowski, D. Ristau, and E. Welsch, "Measuring the absolute absorptance of optical laser components," *Appl. Opt.* **37**(36), pp. 8362–8370, 1998.

[187] M. N. Özisik, *Heat conduction*, Wiley, 1st edition ed., 1980.

[188] G. Arfken and H. Weber, *Mathematical methods for physicists*, Academic Press, 2001.

[189] I. Gradshteyn and I. Ryzhik, *Table of Integrals, Series and Products*, Academic Press, 1994.

[190] F. De Monte, "Unsteady heat conduction in two-dimensional two slab-shaped regions. exact closed-form solution and results.," *Int. J. Heat Mass Transfer* **46**, pp. 1455–1469, 2003.

[191] V. Vodicka, "Wärmeleitung in geschichteten kugel- und zylinderkörpern," *Schweiz. Arch.* **10**, pp. 297–304, 1950.

[192] S. Lima, T. Catunda, M. Baesso, L. Vila, Y. Messadeq, E. Stucchi, and S. Ribeiro, "Thermal-optical properties of *Ga:La:S* glasses measured by the thermal lens technique," *J. Non-Cryst. Solids* **247**, pp. 222–226, 1999.

[193] T. Kanamori, Y. Terunuma, S. Takahashi, and T. Miyashita, "Transmission loss characteristics of $As_{40}S_{60}$ and $As_{38}Ge_5Se_{57}$ glass unclad fibres," *J. Non-Cryst. Solids* **69**(2–3), pp. 231–242, 1985.

[194] J. Tauc, *Amorphous and liquid semiconductors*, Plenum Press, New York, 1974.

[195] K. Tanaka, "Photoinduced fluidity in chalcogenide glasses," *C.R. Chimie* **5**, pp. 805–811, 2002.

[196] D. Pinnow, T. Rich, F. Ostermayer, and M. DiDomenico, "Fundamental optical attenuation limits in the liquid and glassy state with application to fiber optical waveguide devices," *Appl. Phys. Lett.* **22**, pp. 527–529, May 1973.

[197] M. Lines, "Scattering losses in optic fiber materials (I. A new parametrization)," *J. Appl. Phys.* **55**(11), pp. 4052–4057, 1984.

[198] J. Sanghera, V. Nguyen, P. Pureza, R. Miklos, F. Kung, and A. I.D., "Fabrication of long lengths of low-loss IR transmitting $As_{40}S_{60-x}Se_x$ glass fibres," *J. Lightwave Technol.* **14**, pp. 743–748, May 1996.

[199] J. Nishii, S. Morimoto, R. Yokota, and T. Yamagishi, "Transmission loss of *Ge-Se-Te* and *Ge-Se-Te-Tl* glass fibers," *J. Non-Cryst. Solids* **95–96**, pp. 641–646, December 1987.

[200] P. Klocek and L. Colombo, "Index of refraction, dispersion, bandgap and light scattering in *Ge-Se* and *Ge-Sb-Se* glasses," *J. Non-Cryst. Solids* **93**, pp. 1–16, 1987.

[201] E. Dianov, V. Mashinsky, V. Neustruev, O. Sazhin, A. Guryanov, V. Khopin, N. Vechkanov, and S. Lavrishchev, "Origin of the excess loss in single-mode optical fibres with high geo_2–doped silica core," *Opt. Fiber Technol.* **3**, pp. 77–86, 1997.

[202] P. Schultz, "Optical absorption of the transition elements in vitreous silica," *J. Am. Ceram. Soc.* **57**(7), pp. 309–313, 1974.

[203] K. Beales, C. Day, W. Duncan, J. Midwinter, and G. Newns, "Preparation of sodium borosilicate glass fibre for optical communication," *Proc. IEEE* **123**(6), pp. 591–596, 1976.

[204] Y. Ohishi, S. Mitachi, T. Kanamori, and T. Manabe, "Optical absorption of 3d transition metal and rare earth elements in zirconium fluoride glasses," *Phys. Chem. Glasses* **24**(5), pp. 135–140, 1983.

[205] K. Fox, T. Furukawa, and W. White, "Transition metal ions in silicate melts. Part 2. Iron in sodium silicate glasses," *Phys. Chem. Glasses* **23**(5), pp. 169–178, 1982.

[206] T. Nakai, Y. Mimura, O. Shinbori, and H. Tokiwa, "Redox states and absorption losses of 3d transition metals in fluoride glasses," *Jpn. J. Appl. Phys.* **24**(9), pp. L714–L716, 1985.

[207] V. Felice, B. Dussardier, J. Jones, G. Monnom, and D. Ostrowsky, "Chromium-doped silica optical fibres: influence of the core composition on the Cr oxidation states and crystal field," *Opt. Mater.* **16**, pp. 269–277, 2001.

[208] C. Nelson and W. White, "Transition metal ions in silicate melts. Part 3. Nickel in quenched oxide glasses," *Phys. Chem. Glasses* **34**(5), pp. 219–225, 1993.

[209] Shiva Technologies Europe. private communication, 2000.

[210] V. Nguyen, J. Sanghera, F. Kung, P. Pureza, and I. Aggarwal, "Very large temperature-induced absorptive loss in high Te-containing chalcogenide fibres.," *J. Lightwave Technol.* **18**(10), pp. 1395–1401, 2000.

[211] J. Pankove, *Optical processes in semiconductors*, Dover, New York, 1971.

[212] V. Nguyen, J. Sanghera, F. Kung, I. Aggarwal, and I. Lloyd, "Effect of temperature on the absorption loss of chalcogenide glass fibers," *Appl. Opt.* **38**(15), pp. 3206–3213, 1999.

[213] I. Inagawa, S. Morimoto, T. Yamashita, and I. Shirotani, "Temperature dependence of transmission loss of chalcogenide glass fibers," **36, Part 1**(4A), pp. 2229–2235, 1997.

[214] K. Shimakawa, A. Kolobov, and S. Elliot, "Photoinduced effects and metastability in amorphous semiconductors and insulators," *Adv. Phys.* **44**(6), pp. 478–588, 1995.

[215] V. Zhdanov, B. Kolomiets, V. Lyubin, and V. Malinovsky, "Photoinduced optical anysotropy in chalcogenide vitreous semiconducting films," *Phys. Stat. Sol.* **A52**, pp. 621–626, 1979.

[216] T. Schweizer and W. Brockesby. ORC Internal Report, 1998.

[217] K. Shimakawa, S. Inami, T. Kato, and S. Elliot, "Origin of photoinduced metastable defects in amorphous chalcogenides.," *Phys. Rev. B* **46**(16), pp. 10062–10069, 1992.

[218] A. Chandonnet, P. Laperle, S. LaRochelle, and R. Vallee, "Photodegradation of fluoride glass blue fiber laser," *SPIE Proc.* **2998**, pp. 70–81, 1997.

[219] M. Iovu, S. Shutov, and M. Popescu, "Relaxation of photodarkeing in amorphous *As-Se* films doped with metals," *J. Non-Cryst. Solids* **299-302**, pp. 924–928, 2002.

[220] A. Ganjoo, K. Shimakawa, K. Kitano, and E. Davis, "Transient photodarkening in amorphous chalcogenides," *J. Non-Cryst. Solids* **299-302**, pp. 917–923, 2002.

[221] M. Asobe, T. Ohara, I. Yokohama, and T. Kaino, "Fabrication of bragg grating in chalcogenide glass fibre using the transverse holographic method," *Electron. Lett.* **32**(17), pp. 1611–1613, 1996.

[222] C. Meneghini and A. Villenevue, "As_2S_3 photosensitivity by two-photon absorption: holographic gratings and self-written channel waveguides," *J. Opt. Soc. Am.* **B15**(12), pp. 2946–2950, 1998.

[223] A. Ljungstrom and T. Monro, "Light-induced self-writing effects in bulk chalcogenide glass," *J. Lightwave Technol.* **20**(1), pp. 78–85, 2002.

[224] M. Broer, D. Krol, and D. DiGiovanni, "Highly nonlinear near-resonant photodarkening in a thulium-doped aluminosilicate glass fibre.," *Opt. Lett.* **18**(10), pp. 799–801, 1993.

[225] T. Schweizer, J. Hector, D. Brady, J. Wang, D. Hewak, W. Brocklesby, and D. Payne, "Visible upconversion in rare-earth doped gallium lanthanum sulphide based glasses," in *Proc. CIMTEC '98, paper SX-2:L02*, (Florence, Italy), 1998.

[226] E. Dianov, I. Bufetov, A. Frolov, V. M. Mashinsky, V. Plotnichenko, M. Churbanov, and G. Snopatin, "Catastrophic destruction of fluoride and chalcogenide optical fibres," *Electron. Lett.* **38**(15), pp. 783–784, 2002.

[227] S. Lima, A. de Camargo, L. Nunes, T. Catunda, and D. Hewak, "Fluorescence quantum efficiency measurements of excitation and nonradiative deexcitation processes of rare earth 4f-states in chalcogenide glasses," *Appl. Phys. Lett.* **81**(4), pp. 589–591, 2002.

[228] K. Tanaka, "Sub-gap excitation effects in As_2S_3 glass," *J. Non-Cryst. Solids* **266&269**, pp. 889–893, 2000.

[229] K. Tanaka, "Two-photon absorption spectroscopy of As_2S_3 glass," *Appl. Phys. Lett.* **80**(2), pp. 177–179, 2002.

[230] R. Baltraneyunas, Y. Vaikus, and V. Gavryushin, "Light absorption by nonequilibrium, two-photon-generated, free and localized carriers in ZnTe single crystals," *Sov. Phys. JETP* **60**, pp. 43–48, 1984.

[231] S. Gu, S. Ramachandran, E. Reuter, D. Turnbull, J. Verdeyen, and S. Bishop, "Novel broad-band excitation of Er^{3+} luminescence in chalcogenide glasses," *Appl. Phys. Lett.* **66**(6), pp. 670–672, 1995.

[232] S. Gu, D. Turnbull, and S. Bishop, "Broad-band excitation of Pr^{3+} luminescence by localized gap state absorption in $Pr : As_{12}Ge_{33}Se_{55}$ glass," *IEEE Phot. Technol. Lett.* **8**(2), pp. 260–262, 1996.

[233] S. Jetschke, A. Schwuchow, J. Kobelke, K. Schuster, and J. Kirchhof, "Gain, damage, and recovery at 1.3 μm in Pr^{3+}-doped arsenic sulfide fibers," *SPIE Proc.* **4645**, pp. 26–34, 2002.

[234] M. Asobe, H. Itoh, T. Miyazawa, and T. Kanamori, "Efficient and ultrafast all-optical switching using high Delta n, small core chalcogenide glass fibre," *Electron. Lett.* **29**(22), pp. 1966–1968, 1993.